EXPLORING INFRARED-BRIGHT SOURCES DETECTED BY THE SOUTH POLE TELESCOPE
-
LENSING GALAXIES AND THE MOST MASSIVE STRUCTURES IN THE UNIVERSE

by

Kaja M. Rotermund

Submitted in partial fulfillment of the requirements
for the degree of Doctor of Philosophy

at

Dalhousie University
Halifax, Nova Scotia
April 2020

To Shackle & Mali

Table of Contents

List of Tables

List of Figures

Abstract

The work in this thesis presents advances in the field of astrophysics - exploring the exciting (and unexpected) secondary science from millimetre-wave cosmology experiments as well as the development of a novel cold-readout system that improves the sensitivity of said experiments. The South Pole Telescope, whose primary science objectives include measuring the temperature anisotropy and polarization of the cosmic microwave background, conducted a $2,500$ deg^2 survey and detected a population of rare, bright, high-redshift, dusty, star-forming galaxies whose light is frequently magnified and distorted by gravitational lensing, a phenomenon predicted by Einstein. In Chapter 2 we explore the gravitational lenses - massive, passively evolving elliptical galaxies. Multi-band photometric imaging allows us to determine a redshift distribution for the lenses and estimate astrophysical properties such as galaxy type (using a variety of diagnostics) as well as stellar mass and Einstein mass. In Chapter 3 we focus on SPT2349-56, an even rarer unlensed object at high-redshift identified by the South Pole Telescope survey. It was determined to be a uniquely dense proto-cluster, the core of which contains 14 individual dusty, star-forming galaxies. We apply a modified black-body to multi-band photometry in an effort to constrain dust temperatures, we estimate star formation rates using three different tracers, and determine stellar, gas, and dynamical masses for the individual galaxies as well as consider them in the context of the greater proto-cluster. Finally in Chapter 4 we delve into updating an integral component of the cold-readout electronics critical to increasing the sensitivity of observations. We discuss the design considerations, fabrication techniques and challenges, and device assembly for planar lithographed superconducting capacitor-inductor resonator pairs. This work was initially done with the POLARBEAR-2 receiver in mind (another cosmic microwave background polarimetry experiment). However, modified designs have since been implemented in next-generation South Pole Telescope receivers as well. Each chapter contains its own conclusions, leaving Chapter 5 to conclude the thesis with future outlooks for the researched advanced here.

List of Abbreviations and Symbols Used

$'$	Arcminute (unit) [$1' = 1/60$ deg], angular measurement.
$''$	Arcsecond (unit) [$1'' = 1/3600$ deg], angular measurement.
β	Dust emissivity index (unitless), generally $\beta \approx 1 - 2$.
θ_{E}	Einstein radius given in arcsec, radius of the Einstein ring.
ν	Frequency in units of Hz.
σ	Velocity dispersion given in km s^{-1}.
$\tan\delta$	Loss tangent of a dielectric material (unitless).
τ_ν	Frequency-dependent dust opacity (unitless).
Ω_Λ	Ratio of the dark energy density to the critical density [$\Omega_\Lambda = 0.730$].
Ω_{M}	Ratio of the baryonic matter density to the critical density [$\Omega_{\mathrm{M}} = 0.270$].
C	Capacitance in units of F.
C_ℓ	Angular power spectrum.
D_L	Luminosity distance given in pc, a measurement of astronomical distances determined from the object's absolute and apparent magnitude.
f	Frequency in units of Hz.
$H_\circ$	Hubble constant [$H_\circ = 71$ km s^{-1} Mpc^{-1}].
h	Planck constant [$h = 6.625 \times 10^{-27}$ erg s].
Jy	Jansky (unit) [1 Jy $= 1 \times 10^{-26}$ W Hz^{-1} m^{-2}], spectral flux density.
$k_{i,j}$	Coupling coefficient between two inductors.
k	Boltzmann constant [$k = 1.38 \times 10^{-16}$ erg K^{-1}].
$\vec{k}$	Wavevector, indicates the direction of propagating electromagnetic radiation.
L	Inductance in units of H.

$L_\odot$	Solar luminosity (unit) [$L_\odot = 3.846 \times 10^{26}$ W], power radiated by the sun.
$L_{\rm IR}$	Infrared luminosity given in $L_\odot$, power radiated across $8 - 1100\,\mu$m.
L_ν	Luminosity given in $L_\odot$, power radiated at a given frequency, intrinsic brightness of an object.
$M_{\rm dyn}$	Dynamical mass given in $M_\odot$, "total" mass of a galaxy.
$M_{\rm E}$	Einstein mass given in $M_\odot$, mass within the Einstein radius.
$M_{\rm gas}$	Gas mass given in $M_\odot$, mass of intragalactic gas.
$M_{i,j}$	Mutual inductance between two inductors.
M^*	Stellar Mass given in $M_\odot$, total mass of stars within a galaxy.
$M_\odot$	Solar mass (unit) [$M_\odot = 1.989 \times 10^{30}$ kg], mass of the sun.
pc	Parsec (unit) [1 pc $= 3.086 \times 10^{16}$ km], astronomical distance.
$R_{\rm bolo}$	Resistance of the TES bolometer in units of Ω.
S_ν	Flux density given in Jy, detected energy per unit area per unit time at a given frequency - apparent brightness of an object.
T	Temperature given in K.
$T_{\rm dust}$	Dust Temperature given in K of interstellar dust, generally $T_{\rm dust} = 30 - 100$ K for cold diffuse medium.
z	Redshift, $1 + z = {\lambda_{\rm observed}}/{\lambda_{\rm emitted}}$.
Ca K & H	Singly-ionized calcium absorption doublet still referred to by the Fraunhofer K and H letters $\lambda_{\rm rest} = 3,933$ & $3,968$ Å.
[C II]	Singly ionized carbon, forbidden $^2P_{3/2} - {}^2P_{1/2}$ transition $\nu_{\rm rest} = 1,900.5$ GHz ($\lambda_{\rm rest} = 157.7\,\mu$m).
CO	Carbon monoxide, rotational transitions $J = 2 \rightarrow 1$: $\nu_{\rm rest,\,CO(2-1)} = 230.538$ GHz and $J = 4 \rightarrow 3$: $\nu_{\rm rest,\,CO(4-3)} = 461.041$ GHz.
H_2O	Water molecule, para (anti-parallel alignment of the nuclear spins of the two hydrogen atoms) $2_{11} - 2_{02}$ transition $\nu_{\rm rest} = 752.051$ GHz.

H I	Neutral hydrogen, hyperfine transition $\nu_{\rm rest} = 1.420$ GHz ($\lambda_{\rm rest} = 21$ cm), ionization energy $E = 13.6$ eV (corresponds to photons with $\lambda < 91.2$ nm).
H II	Singly ionized hydrogen, Hα Balmer transition n = 3 $\rightarrow$ 2 $\lambda_{\rm rest} = 656.3$ nm.
H_2	Molecular hydrogen.
[N II]	Singly ionized nitrogen, forbidden $^3P_1 - {}^3P_0$ transition $\nu_{\rm rest} = 1,461$ GHz ($\lambda_{\rm rest} = 205.3\,\mu$m).
[O II]	Singly ionized oxygen, forbidden doublet $^2D_{3/2} - {}^4S_{3/2}$ transition $\lambda_{\rm rest} = 3,726$ Å and $^2D_{5/2} - {}^4S_{3/2}$ transition $\lambda_{\rm rest} = 3,729$ Å.
[O III]	Doubly ionized oxygen, forbidden $^1D_2 - {}^3P_2$ transition $\lambda_{\rm rest} = 5,007$ Å.
2MASS	Two Micron All Sky Survey.
ACTpol	Polarization-sensitive receiver on the Atacama Cosmology Telescope.
AdvACT	Advanced polarization-sensitive receiver on the Atacama Cosmology Telescope.
AGN	active galactic nucleus.
ALMA	Atacama Large Millimeter/submillimeter Array.
APEX	Atacama Pathfinder EXperiment.
ATCA	Australia Telescope Compact Array.
BELLS	BOSS Emission-Line Lens Survey.
BICEP2	Background Imaging of Cosmic Extragalactic Polarization.
BOSS	Baryon Oscillation Spectroscopy Survey.
CASA	Common Astronomy Software Applications package.
CIB	cosmic infrared background.
CIGALE	Code Investigating GALaxy Emission.
CLASS	Cosmic Lens All-Sky Survey.
CMB	cosmic microwave background.
COB	cosmic optical background.

COBE	COsmic Background Explorer.
CT	cross talk.
DAN	digital active nulling.
DASI	Degree Angular Scale Interferometer.
Dec	Declination, coordinate on the celestial sphere equivalent to latitude.
DECam	Dark Energy CAMera.
DES	Dark Energy Survey.
DM	dark matter.
DSFG	dusty, star-forming galaxy.
EAZY	Easy and Accurate Z-phot from Yale.
ESO	European Southern Observatory.
ESR	equivalent series resistance.
EW	equivalent width.
FDM	frequency-domain multiplexing.
F2	FLAMINGOS-2.
FORS2	FOcal Reducer/low dispersion Spectrograph 2.
FWHM	full width at half max.
GAIA	Graphical Astronomy and Image Analysis Tool.
Gemini-S	Southern Gemini Observatory.
GMOS	Gemini Multi-Object Spectrographs.
H-ATLAS	*Herschel*-Astrophysical Terahertz Large Area Survey.
HerMES	*Herschel* Multi-tiered Extragalactic Survey.
Herschel	*Herschel Space Observatory*.
HTT	Huan Tran Telescope.
HST	*Hubble Space Telescope*.
HyperZ	Photometric redshift code based on SED fitting.
IMF	initial mass function.
IRAC	Infrared Array Camera.
IRAF	Image Reduction and Analysis Facility.
IRAM	Institut de Radio Astronomie Millimetrique.

IRAS	Infrared Astronomical Satellite.
ISAAC	Infrared Spectrometer And Array Camera.
ISM	interstellar medium.
JCMT	James Clerk Maxwell Telescope.
JVAS	Jodrell Bank Very Large Array.
Keck Array	Suit of cosmic microwave background polarimetry telescopes, each duplicates of the BICEP2 telescope.
LABOCA	Large APEX BOlometer CAmera.
MAMBO	MAx-Planck Millimeter BOlometer.
MBB	modified black-body.
MS	main sequence.
NASA	National Aeronautics and Space Administration.
NIST	National Institute for Standards and Technology.
NOAO	National Optical Astronomy Observatory.
O & B type	Stellar spectral type classifications. O & B stars are young (short-lived), hot (effective surface temperatures $> 10,000$ K), and massive ($\gtrsim 20$ $M_\odot$).
PAH	polycyclic aromatic hydrocarbon.
POLARBEAR	Cosmic microwave background polarimetry experiment.
POLARBEAR-2	Cosmic microwave background polarimetry experiment - second generation.
RA	Right Ascension, coordinate on the celestial sphere equivalent to longitude.
RMS	root mean square.
SCUBA	Submillimeter Common-User Bolometer Array.
SDSS	Sloan Digital Sky Survey.
SED	spectral energy distribution.
SEM	scanning electron microscope.
SEXTRACTOR	Source Extractor, "A program that builds a catalogue of objects from an astronomical image." `https://sextractor.readthedocs.io/en/latest/Introduction.html`.

SFR	star formation rate.
SLACS	Sloan Lens Advanced Camera for Surveys.
SMA	Submillimeter Array.
SMG	sub-millimetre galaxy.
SNR	signal-to-noise ratio.
SPIRE	Spectral and Photometric Imaging Receiver.
Spitzer	*Spitzer Space Telescope*.
SPT	South Pole Telescope.
SPT-3G	Polarization-sensitive receiver on the South Pole Telescope - third generation.
SPTpol	Polarization-sensitive receiver on the South Pole Telescope.
SPT-SZ	Three-frequency receiver on the South Pole Telescope conducting a survey of the Sunyaev-Zel'dovich effect.
SQUID	superconducting quantum interference device.
SWarp	"A program that re-samples and co-adds together FITS images sing any arbitrary astrometric projection defined in the WCS standard." `https://www.astromatic.net/software/swarp`.
SZ	Sunyaev-Zel'dovich effect.
TES	transition edge sensor.
USNO	United States Naval Observatory.
VLA	Very Large Array.
VLT	Very Large Telescope.
WFC3	Wide Field Camera 3.
WMAP	Wilkinson Microwave Anisotropy Probe.
X-shooter	Single-object, intermediate resolution, UV-NIR spectrograph.

Acknowledgements

The number of people who deserve my sincerest gratitude is seemingly endless. First and foremost I would like to thank my family - Harm, Caryl, Meike and Brenden, Lina, Janso and of course Grandpa, who have always encouraged me and motivated me both academically and personally. To my Lake George family, thank you for reminding me of the important things in life - a calm lake, a roaring campfire, and some s'mores.

I would like to thank my supervisor, Scott Chapman, for his guidance and support throughout the many years of my PhD. The opportunities he has given me are immeasurable - conducting observations with pioneering sub-mm telescopes in Hawaii, using state of the art instruments to design, fabricate, and test critical hardware for CMB telescopes at both UC Berkeley and NRC-HIA, and introducing me to amazing scientists around the world. I would also like to extend my deepest appreciation to the members of the SPT-SMG collaboration, the POLARBEAR-2 team, and the scientists at NRC-HIA for the many discussions helping me form a clearer and broader picture of the science.

A special thank you to my committee members, Ted Monchesky and Phil Bennett, as well as Ian Hill and Stephen Payne for their comments and suggestions along the way.

Lastly, I would be remiss if I didn't thank my lab-mates, Colin Ross, Kevin Lacaille, Tim Miller, and Ryan Perry, as well as fellow basement dwellers of the Dunn, David Kalliecharan and Simon Meynell. They have provided much needed support as well as the occasional yet necessary distractions. You have all been, and continue to be, great friends.

This research was supported in part by the Natural Sciences and Engineering Research Council of Canada (NSERC).

Chapter 1

Introduction

In 1929 Edwin Hubble discovered that the universe was expanding, which promptly led to the conclusion that at earlier times the universe was smaller. When taken to its limit, this would suggest that the universe originated from a single point. Within the next couple of decades George Gamow, Robert Herman, and Ralph Alpher concluded that the universe must have also been hotter and denser. Thus the Hot Big Bang model was born - the universe began with a Big Bang at which point it was filled with a hot, dense plasma (with temperature $T > 10^{12}$ K) in which electrons, quarks, and other elementary particles soon formed followed by protons and neutrons, all within the first second after the Big Bang. A high electron number density resulted in a mean free path so short that photons were "trapped" within the plasma, no light being able to escape. As the universe continued to expand and cool, protons and neutrons combined into deuterium nuclei from which helium nuclei fused once $T \sim 10^9$ K was reached, < 300 s after the Big Bang.

As the temperature continued to lower and reached $T \sim 3,000$ K, $\sim 400,000$ years after the Big Bang, neutral hydrogen became energetically favourable and hydrogen and helium nuclei "recombined" with electrons to form neutral elements. This period is known as the recombination epoch. At this point the number density of free electrons was finally low enough that photons "decoupled" from the baryonic matter, *i.e.* photons no longer perpetually scattered off electrons, and they were able to travel freely through space. This earliest light radiates isotropically and can be observed at microwave wavelengths, it is known as the cosmic microwave background (CMB). Due to the continued expansion and cooling of the universe, the CMB is observed as a near-perfect black-body radiating at a temperature of $T_{\rm CMB} = 2.726 \pm 0.010$ K (Mather et al. 1994). Fig. 1.1 is a full-sky image of the temperature anisotropies of the CMB with a temperature range of $\pm\, 200\, \mu$K compiled by the National Aeronautics and Space Administration (NASA) and the Wilkinson Microwave Anisotropy Probe

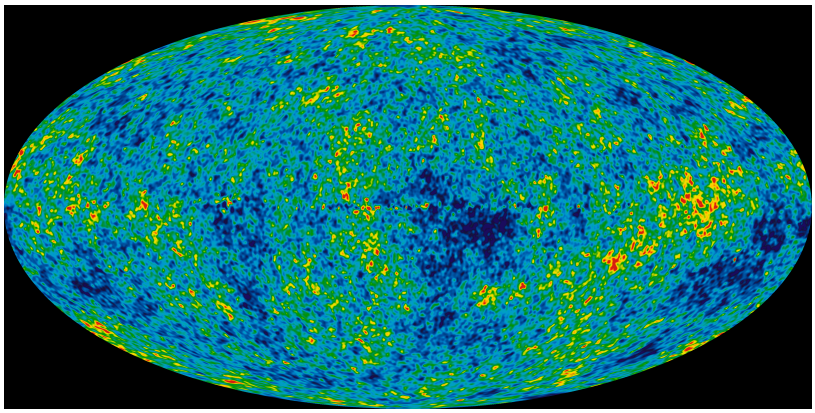

Figure 1.1: WMAP full-sky image of the temperature anisotropies of the CMB, temperature range $\pm 200\,\mu$K. Image credit: NASA / WMAP Science Team.

(WMAP) science team using many years of observations.

The CMB is a relic of the Big Bang in which critical information about the earliest evolutionary stages of the universe is imprinted. One of the biggest surprises about the CMB was the remarkable uniformity of its temperature across the entire sky, with anisotropies on the order of $\Delta T/T \sim 10^{-5}$ K (Schneider 2006), as was confirmed by observations conducted with the COsmic Background Explorer (COBE) satellite by Mather et al. in 1994. The uniformity of the CMB temperature led to the so-called "horizon problem" in which two photons that should not have been in causal contact with each other when they originated from the CMB, *i.e.* they were separated to such a degree that they could not share information, are in fact in thermal equilibrium. This problem was solved by the suggestion of an inflationary period a mere 10^{-25} s after the Big Bang. The original inflation theory was developed by Alan Guth, Andrei Linde, Paul Steinhardt, and Andy Albrecht in the 1980's - the universe began small, the entirety of space in causal contact and through a brief period ($< 10^{-32}$ s) of exponential expansion, inflated in size by a factor of 10^{26} followed by the regular expansion we observe today. Thus the relative homogeneity of the temperature is preserved.

A further consequence of the rapid inflationary epoch is the dramatic growth of small quantum fluctuations in density to all angular sizes. The dark matter (DM) in our universe began as a near-homogenous distribution with slight over-densities

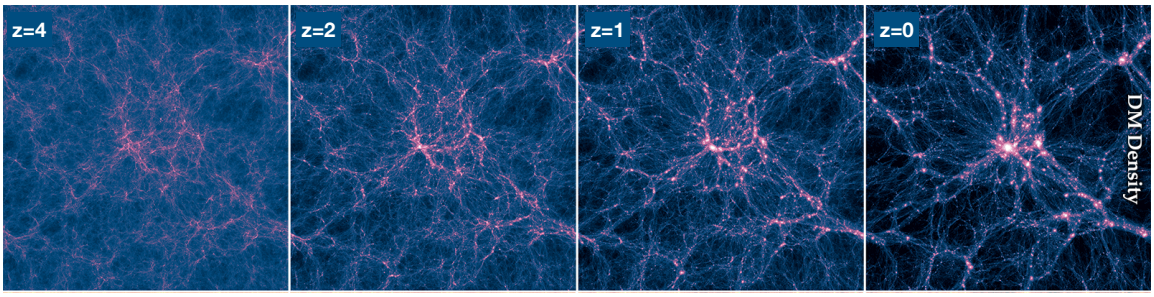

Figure 1.2: Projection of the dark matter density at four different redshifts. Image credit: Illustris Collaboration.

caused by quantum fluctuations. While the true nature of dark matter is still unknown, it interacts gravitationally with baryonic matter and outweighs it roughly by a factor of six. Due to the effects of gravity, matter is continuously attracted to these over-densities, growing both in size and contrast with respect to surrounding space even as the universe expands. The Illustris Collaboration simulated the dark matter density and its evolution from early-times in our universe to the present day. Four snapshots, at redshifts $z = 4$, 2, 1, and 0 are shown in Fig. 1.2. As time passes, the dark matter density converges into nodes of over-densities - massive DM halos, connected via a filamentary structure that is surrounded by large voids (*e.g.* Overzier 2016). This is often referred to as the "cosmic web." It is towards dark matter nodes and filaments that gas gravitates, in the coldest regions eventually leading to the collapse into dense cores resulting in the formation of stars (Lacey and Cole 1993) and galaxies and, in the largest over-densities, to clusters of galaxies.

1.1 An Overview of Galaxies

Due to the expansion of the universe, as light emitted from an object travels through space, its wavelength will increase, *i.e.* it gets redshifted (Schneider 2006). This is a Doppler shift caused by the expansion of space itself. The redshift, z, is defined as the shift in wavelength between the emitted light (rest-frame) and the observed light,

$$z \equiv \frac{\lambda_{\rm obs} - \lambda_{\rm rest}}{\lambda_{\rm rest}} \qquad \rightarrow \qquad 1 + z = \frac{\lambda_{\rm obs}}{\lambda_{\rm rest}}. \tag{1.1}$$

The spectral emission/absorption features of elements are well understood in the lab and so redshifts determined from the spectroscopic analysis of galaxies, termed

"spectroscopic redshifts," are considered robust. Objects at greater distances have larger redshifts as the light-travel time and thus the observed wavelength are longer. Consequently, light from higher redshift objects is older. They are, however, a relic from when the universe was younger - redshift and time are non-linearly related to each other. A redshift of zero is the local, present universe at an age ~ 13.8 Gyrs. At $z = 1$ the universe was only ~ 5.9 Gyrs old, just under half its current age. Objects at $z > 1$ are considered high-redshift objects. The CMB is at $z \sim 1,100$ and displays a snapshot of the universe at the young age of $400,000$ yrs.

1.1.1 Galaxy Formation and Growth

Many different types of galaxy populations exist. In 1926 Hubble, having recently measured the distance to Andromeda and for the first time definitively categorizing it as a galaxy, invented a classification scheme in which he characterized galaxies by their morphological shapes. The two main types were ellipticals and spirals, differentiated from each other by their egg- or disc-like shape, respectively. These two classes of galaxies were further subdivided depending on either the ellipticity or the tightness of spiral arms in the disc. Hubble's sequence is now considered too simplistic, the number of known galaxies having increased exponentially from just several hundred in the late 1920s. Regardless, the general classifications are still used today.

Different galaxy populations have varying properties and, importantly, they also have different formation histories. While it is still an open question as to how the first galaxies formed, consensus lies in a hierarchical growth model. In hierarchical growth smaller galaxies and their accompanying dark matter halos merge to form more massive galaxies. Mergers can either occur between two galaxies of comparable mass - typically two disc galaxies merge to form an elliptical galaxy, or a smaller galaxy can merge into a more massive galaxy, in which case the more massive galaxy may retain its original shape, either as a disc or an elliptical (Lacey and Cole 1993). The critical aspect of hierarchical growth models is the build-up of dark matter halos.

The merger of two galaxies leads to their gas clouds colliding, which triggers the formation of new stars. Stars are classified by their spectral type, which is defined by the star's effective surface temperature and is a function of the star's luminosity. There are seven basic spectral types (labelled O, B, A, F, G, K, and M in decreasing

order of temperature) that are sometimes subdivided further. O & B type stars are massive, yet short-lived, and have temperatures upwards of $10,000$ K. They radiate in the ultra-violet (UV) and blue-optical range of the electromagnetic spectrum. Less massive stars (*i.e.* K & M type stars) have much longer lifetimes and have significantly lower surface temperatures and therefore radiate at longer red-optical and near-infrared (near-IR) wavelengths.

The luminosity of an object is its power output and is measured in units of solar luminosities ($\mathrm{L}_\odot = 3.846 \times 10^{26}$ W), the power radiated by our Sun. It is an intrinsic property that is frequently measured either at a specific frequency or over a range of frequencies. The IR luminosity, L_{IR}, is measured in the rest frame from $8 - 1,100\,\mu$m, the range over which dust radiates thermally due to the absorption of UV photons. Dust grains are introduced into a galaxy via the death of massive stars - a collapse of the star's core frequently followed by an energetic explosion. This releases numerous heavy elements back into the gas clouds within the galaxy. Some of these, generally carbon and silicates, combine into small dust grains. In the local universe, the population of galaxies whose L_{IR} falls within the range $11 \leq \log\left(L_{\mathrm{IR}}/\mathrm{L}_\odot\right) < 12$ are coined "luminous IR galaxies," whereas "ultra-luminous IR galaxies" have IR luminosities in excess of this range, $\log\left(L_{\mathrm{IR}}/\mathrm{L}_\odot\right) \geq 12$ (Sanders and Mirabel 1996). IR luminosities at these scales implies a substantial dust component to the galaxy as well as high star formation rates, the rate with which stars are formed, to heat the dust.

The total radiation of all objects in the universe in the optical and infrared regimes are called the cosmic optical background (COB) and cosmic infrared background (CIB), respectively. Despite dust making up a very small fraction of the mass within a galaxy, less than 1 % by some estimates (Sandstrom et al. 2013), observations of local galaxies found the infrared output to be approximately a third of the optical output (Lagache et al. 2005). Surprisingly, with the advent of the COBE (Puget et al. 1996; Hauser et al. 1998) and the first measurements of the CIB, the optical and infrared background radiation were found to be equal. Fig. 1.3 taken from Dole et al. (2006) shows the total power output of the universe over 6 decades of the electromagnetic spectrum. For each regime the approximate brightness (in nW m^{-2} sr^{-1}) is listed. The discrepancy in the infrared output between observations of

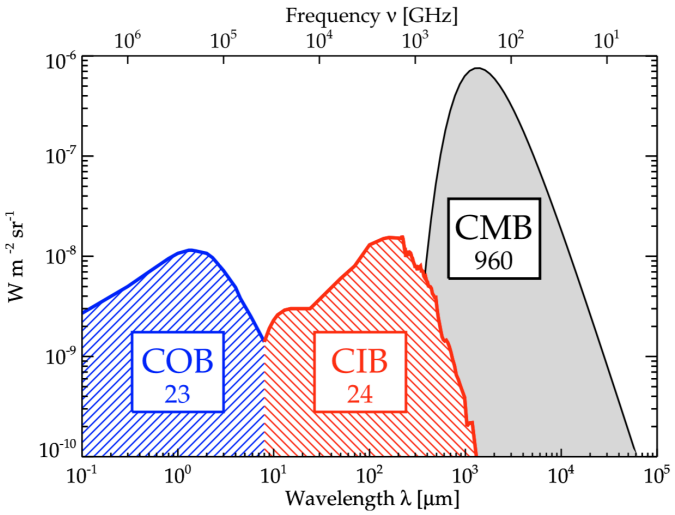

Figure 1.3: Total power output of the background radiation of the universe over six decades of the electromagnetic spectrum. The three main regimes, cosmic optical background (COB), cosmic infrared background (CIB), and cosmic microwave background (CMB), are highlighted and their approximate brightness in nW m^{-2} sr^{-1} given. Figure taken from Dole et al. (2006).

local galaxies and the total IR background radiation implies that the number of IR-luminous galaxies observed in the local universe are not enough to identify all source of IR radiation. This can only be rectified if IR sources become more numerous at greater distances (Lagache et al. 2005). The implication being a strong evolution of IR-luminous galaxies with redshift, thereby making them a critical component in early build-up of galaxies (Lagache et al. 2005).

One evolutionary sequence that has remained popular was proposed by Sanders et al. (1988). They studied 324 IR-bright galaxies that were discovered in the Infrared Astronomical Satellite (IRAS) Bright Galaxy Survey, which covered $\sim 14,500$ deg^2 initially, roughly 35 % of the sky. The total bolometric luminosity, the power output of a galaxy measured over all wavelengths, for these IR-bright galaxies were comparable if not in excess of the bolometric luminosities of the brightest optical galaxies. Furthermore, they found a majority of galaxies in their sample displayed clear evidence of either ongoing or recent mergers. Sanders et al. (1988) proposed a model in which they identified several stages in the merger of two disc galaxies. A major merger of two gas-rich galaxies triggers a period of intense star formation

due to the collision of gas clouds within the galaxies. These periods of high star formation rates are coined starburst events and are generally short lived as they follow the collision time of a galaxy, several million years (Sanders et al. 1988). As a comparison, the lifetime of a star such as our sun can be upwards of several billion years. The starburst event coincides with an IR-luminous phase, in which dust is thermally excited either via collisions or UV radiation from the young, hot stars. As the merger progresses, gas begins to funnel into the merger nucleus, which becomes an active galactic nucleus (AGN). Sanders et al. (1988) suggest that if a black hole did not previously exist in one or both of the merging galaxies, conditions would be sufficiently met to form a black hole at this time. It is now commonly accepted that at the centre of every galaxy is a supermassive black hole. As gas continues to accrete into the AGN it grows until it becomes large enough to feed back on the galaxy. AGN feedback is a complex process in which energy is re-deposited into the galaxy via radiation from the AGN. The source of this radiation can either be the accretion process itself or outflows, the ejection of material from the AGN. Importantly both methods of AGN feedback affect the galaxy evolution as gas is either expelled from the galaxy (outflows) or heated (radiation) so that the fuel for star formation (cold, dense gas) is depleted. This effectively results in the quenching of further AGN growth, which consequently may lead to a renewed starburst and IR-luminous phase. The burst-quench cycle can occur several times during the merger process. Once all the gas and dust has been cleared from the galaxy, the AGN is no longer "active" and a "simple" supermassive black hole is left behind. The resulting massive galaxy is a quiescent elliptical with a now old stellar population. Sanders et al. (1988) suggest that a similar model can apply to the collision of any two galaxies as long as at least one is host to a significant gas cloud. The intensity of the IR-luminous phase would simply be dimmer if the merger were to occur between a gas-rich and a gas-poor galaxy instead of between two gas-rich galaxies.

1.1.2 Dusty, Star-Forming Galaxies

Dusty, star-forming galaxies (DSFGs) are a class of galaxies that are host to massive gas and dust reservoirs. This has two implications - high star formation rates, some

of the largest ever observed, and significant thermal dust emissions due to the absorption of energetic UV photons from young stars and the subsequent re-radiation at longer wavelengths. The classification of a galaxy as a DSFG relies primarily on the significant presence of thermal dust radiation. The local ($z \ll 1$), IR-bright merging systems studied by Sanders et al. (1988) are one population of galaxy that fall within the umbrella of DSFGs.

In the distant, high-z ($z > 1$) universe, the thermal IR radiation is redshifted into the sub-millimetre (sub-mm) and millimetre (mm) regimes. Galaxies originally discovered in the sub-mm are named sub-millimetre galaxies (SMGs) and are another subclass of DSFGs. Due to their large dust content they are largely obscured from view in the optical and near-IR and were, until recently, undetected. SMGs were first discovered in the late 1990s in a systematic survey of the CIB conducted by the Submillimeter Common-User Bolometer Array (SCUBA) (Smail et al. 1997) on the James Clerk Maxwell Telescope (JCMT) and by the MAx-Planck Millimeter BOlometer (MAMBO) camera (Bertoldi et al. 2000) on the Institut de Radio Astronomie Millimetrique (IRAM) telescope. SCUBA conducted its survey at 850 μm (345 GHz), which is an atmospheric transmission window, thereby allowing for observations with high sensitivity (atmospheric transmission windows are discussed in greater detail in Section 1.3).

The importance of SMGs in regard to galaxy evolution at high redshift became evident in early observations that suggested they were sites of significant star formation, which had previously been obscured from view in the optical (Blain et al. 1999). A great effort was immediately made to learn more about the elusive SMGs. They were found to be massive systems (Swinbank et al. 2004; Greve et al. 2005; Tacconi et al. 2006) peaking at $z \sim 2$ (Chapman et al. 2005; Pope et al. 2005) with disturbed morphologies suggesting ongoing major mergers (Chapman et al. 2003b; Conselice et al. 2003). Lilly et al. (1999) hypothesized that SMGs are likely the progenitors to the population of massive ellipticals seen at lower redshift. This theory is consistent with the evolutionary sequence described by Sanders et al. (1988) as well as by observations that suggest similar number densities for the two populations (Swinbank et al. 2006) and has become the prevailing theory to date.

Early observations in the sub-mm regime suffered from poor spatial resolution.

For a circular aperture, the resolution θ (in radians) is dependent on the choice of wavelength λ and the aperture diameter D, $\theta = 1.22\,\lambda/D$. The JCMT has a diameter of 15 m and is the world's largest single-dish telescope specifically designed for sub-mm observations. Observations conducted at 850 μm have a spatial resolution of $\sim 14''$ (1 deg = 60 arcminutes [$'$] = 3600 arcseconds [$''$]). The *Hubble Space Telescope* (*HST*) on the other hand, despite having a significantly smaller aperture, a diameter of just 2.4 m, operates in the UV, optical, and near-IR. Its spatial resolution when observing in the optical, at 630 nm for example, would be $\sim 0.07''$, an improvement of two orders of magnitude. Consequently, in deep optical surveys conducted by the *HST* on the order of $\sim$ 10 galaxies are often detected within a single SCUBA beam. This means that determining the optical counterpart to a sub-mm detection is difficult. The term "counterpart" refers to the same galaxy observed at different wavelengths.

The solution for the (sub-)mm regime lies in interferometric observations. Interferometric telescopes consist of an array of single-dishes separated over great distances, effectively increasing the telescope diameter, thereby dramatically improving the spatial resolution. Initially the Very Large Array (VLA), an interferometer operating in the radio frequency range, was used to identify radio counterparts to SMGs, which in turn helped narrow down possible optical counterparts. Unfortunately, a significant fraction of SMGs are either undetected ($\sim$ 25 %) or have more than one potential counterpart ($\sim$ 10 %) at radio frequencies (Ivison et al. 2002; Chapman et al. 2005). Since the advent of the Atacama Large Millimeter/submillimeter Array (ALMA) in 2011, significant advancements have been made. ALMA is an interferometer located on the Chajnantor plateau in the Atacama Desert of northern Chile. It is capable of using up to 66 dishes in either compact or extended configurations, the baseline varying between 160 m and 16 km. 54 of the dishes are 12 m in diameter and the remaining 12 dishes are 7 m in diameter. As the name suggests, it observes in the millimetre and sub-millimetre regimes, covering a range from 0.3 mm to 3.6 mm, and is therefore ideal for observing SMGs. The resolution at its most compact configuration is $\sim 1.4''$, using 870 μm as an example observing wavelength. This improves to a remarkable $\sim 0.014''$ at its most extended configuration. With resolutions like these, identifying counterparts in the optical is no longer a problem.

1.1.3 Quiescent Elliptical Galaxies

Elliptical galaxies, also known as "early-type" galaxies as they were originally thought to be the first galaxies formed, are some of the most massive galaxies observed. They are host to an old stellar population and contain little-to-no interstellar gas or dust. Local ellipticals are observed via the direct emission from their old stellar population in the red-optical regime. At high-z, this emission is redshifted into the near-IR. The lack of interstellar gas and dust means thermal dust radiation in the rest-frame IR (or redshifted into the sub-mm) is not observed. Furthermore, new star formation cannot occur. Ellipticals are therefore considered a passively evolving population, *i.e.* no further growth occurs unless it interacts or merges with a gas-rich galaxy.

The lack of gas and dust also results in a distinct absence of spectral emission features and absorption lines that are weak (discussed further in Sect. 1.2.3). Determining spectroscopic redshifts is therefore frequently not feasible. Multi-band photometry is commonly used in its stead. However, photometric redshifts (discussed further in Chapter 2) are generally not as robust as those determined spectroscopically.

Multi-band photometry is the measurement of the brightness of light radiated by a galaxy across multiple wavelengths, or bands. Historically, photometry measurements for high-z sources are quoted as a flux, the power detected per unit area at a given frequency, given in units of Jansky (1 Jy $= 1 \times 10^{-26}$ W Hz^{-1} m^{-2}), while magnitudes are used for low-z sources. Both flux and magnitude are a measure of the apparent brightness of an object. The magnitude scale is logarithmic and is inversely related to the brightness, *i.e.* brighter objects have smaller magnitudes. An increase in brightness by a factor of 10 results in a decrease in magnitude by 2.5.

The evolutionary connection between high-z SMGs and lower-redshift ellipticals has been commonly accepted since its initial suggestion despite only circumstantial evidence existing to back it up. One compelling argument backed up by observations, as previously stated, is the suggestion that SMGs and ellipticals have similar number densities (Swinbank et al. 2006), *i.e.* the number of SMGs in a volume at high-z is similar to the number of ellipticals in the same volume at lower z. Another argument is the evolutionary track proposed by Sanders et al. (1988) in which epochs of high star formation rates are triggered by major mergers, observed as SMGs, that eventually result in quiescent, massive ellipticals. Furthermore, the stellar masses, M^*, *i.e.* the

cumulative mass of all stars in the galaxy in units of solar mass ($M_\odot = 1.989 \times 10^{30}$ kg), of SMGs and ellipticals are also suggestive of an evolutionary sequence. Despite the determination of stellar mass in SMGs suffering from relatively large systematic uncertainties, they are believed to be the most massive galaxies at their redshift, with stellar masses ranging from $M^* \sim 5 \times 10^{10} - 9 \times 10^{11}$ $M_\odot$ (*e.g.* Borys et al. 2005; Dye et al. 2008; Michałowski et al. 2010, 2012; Hainline et al. 2011). Ellipticals in contrast have stellar masses an order of magnitude larger $M^* \sim 10^{11} - 10^{12}$ $M_\odot$ (*e.g.* Auger et al. 2009; Brownstein et al. 2011), consistent with continuing growth of the SMG until its gas reservoir is depleted. There is therefore significant evidence that SMGs are the progenitors, *i.e.* the forebears, to ellipticals.

1.2 The Spectral Energy Distribution

A galaxy emits radiation across a wide range of wavelengths. The energy output as a function of wavelength, or frequency, of a galaxy is referred to as the spectral energy distribution (SED). Each population of galaxies has a characteristic shape to its SED. This shape is dependent on which sources of radiation are dominant for that population of galaxies. The primary factors that impact the SED shape are the relative radiation of both the young and old stellar populations and the thermal dust radiation with respect to each other, as well as the wavelength of the peak of the thermal dust. Fig. 1.4, taken from Galliano (2004), displays the SED from the UV to the millimetre for four different galaxies (named CFRS14.1139, M82, M101, and NGC5018). They are well-studied galaxies and are representative of their galaxy type: ultra-luminous IR galaxies, starbursts, discs, and ellipticals, respectively. The coloured SEDs in Fig. 1.4 are models that have been fit to the observations of each galaxy (black crosses) and are all shifted into the rest-frame to facilitate a comparison of the intrinsic spectra.

For all SEDs essentially zero emission is observed short-ward of 91.2 nm. This is known as the Lyman break. The Lyman-α absorption of hydrogen from the ground state into the first exited state occurs at $1,216$ Å, a ubiquitous feature in all SEDs. Absorption of shorter wavelength photons (*i.e.* higher energy photons) results in excitations into higher excited states and eventually to the ionization of hydrogen. Neutral hydrogen's ionization energy is 13.6 eV, corresponding to a wavelength of 91.2 nm.

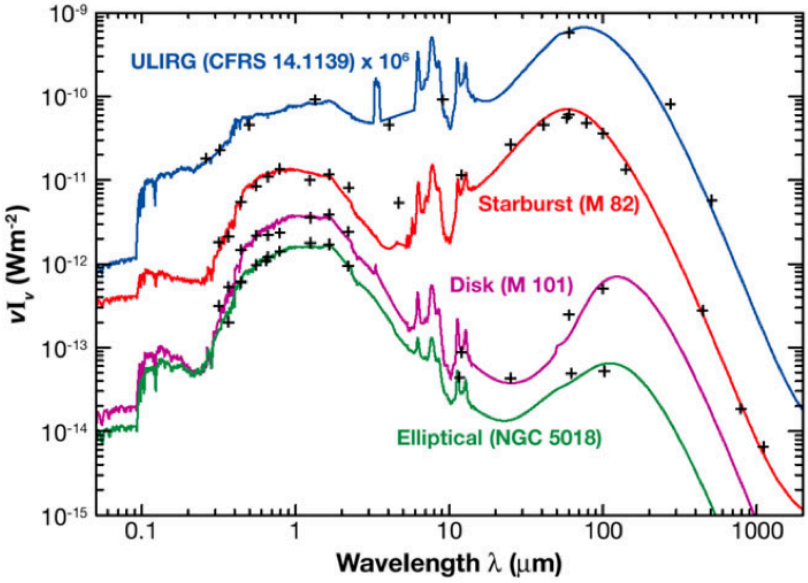

Figure 1.4: Spectral energy distributions for four different galaxies representative of their galaxy population - ultra-luminous IR galaxies, starbursts, discs, and ellipticals, across five decades in wavelength - from the UV to the millimetre. Observations to which the modelling was fit are shown as black crosses. Figure taken from Galliano (2004).

The sheer abundance of neutral hydrogen in the universe is so large that virtually all photons with $\lambda < 91.2$ nm are absorbed (Schneider 2006). The probability of these short wavelength photons escaping from a galaxy is therefore low, resulting in the observed suppression, or "break," in the SED short-ward of 91.2 nm.

As briefly mentioned in the previous section, young stars, old stars, and dust all radiate at different wavelengths. Young, hot stars, with surface temperatures upwards of $50,000$ K (Schneider 2006), radiate in the UV and blue-optical range. These O & B type stars are also the most massive and luminous. However, they are short-lived. In actively star forming galaxies the young O & B type stars dominate the emitted radiation. This is the small bump seen in Fig. 1.4 at $0.1-0.2\,\mu$m. Counterintuitively, the UV radiation of ellipticals appears to be quite pronounced. This is referred to as the "UV-upturn," an increase in flux with decreasing wavelength. Recent studies have shown that this upturn is primarily caused by extreme horizontal branch stars (*e.g.* Han et al. 2007; Conroy 2013) These are sub-luminous B type stars believed to have masses around 0.5 $M_\odot$ (Han et al. 2007, & references therein). Their population

Table 1.1: Features in the spectral energy distribution. Wavelengths are given in the rest-frame.

Feature	Cause	Wavelength
Lyman break	Abundance of intervening neutral hydrogen (ionization energy $E = 13.6$ eV) results in virtually all photons with $\lambda < 91.2$ nm being absorbed.	$< 0.0912\,\mu$m
Lyman-α absorption	The absorption of photons with $\lambda = 1,216$ Å excites neutral hydrogen from its ground state into its first exited state.	$0.1216\,\mu$m
Young stellar pop. bump	Young, hot stars with surface temperatures $> 50,000$ K radiate in the UV and blue-optical.	$\sim 0.1{-}0.2\,\mu$m
Old stellar pop. bump	Older, colder stars with surface temperatures $\sim 3,500$ K radiate in the red-optical and near-IR.	$\sim 0.3 - 3\,\mu$m
4,000 Å break	A number of overlapping metal absorption lines (*i.e.* calcium K & H as well as other metals) stemming from the atmospheres of older stars exist at $\leq$ 4,000 Å resulting in a blanket absorption of high-energy photons. A lack of young, hot O & B type stars in ellipticals further enhances the break.	$0.4\,\mu$m
1.6 μm bump	Arises due to the H^- ion in stellar atmospheres, the opacity of which is at a minimum at 1.6 μm. Associated with the old stellar population.	$1.6\,\mu$m
PAH spikes	Emission from neutral and ionized polycyclic aromatic hydrocarbons (PAH), organic compounds comprised purely of carbon and hydrogen.	$\sim 5 - 20\,\mu$m
Thermal dust bump	Thermal emission in the far-IR by cold interstellar dust after the absorption of energetic UV photons.	$\sim 30{-}800\,\mu$m

synthesis is still an ongoing debate, however, will not be discussed further here.

Older, colder stars with surface temperatures closer to 3,500 K (Schneider 2006) radiate at longer red-optical and near-IR wavelengths. Less massive stars are less luminous but they are longer-living, thus significantly more low mass stars exist. In older galaxies, such as ellipticals, the radiation from low-mass stars as well as red giants dominates. This is the significantly larger bump centred on 1 μm in Fig. 1.4.

Dust presents itself as the third bump in the SED centred around 100 μm. The thermal far-IR radiation of dust is a consequence of heating by young, hot stars. The wavelength of the peak of the thermal dust radiation is dependent on the temperature of the dust. The presence of dust in a galaxy further manifests itself in two ways:

1) it acts to decrease the emission in the UV as it obscures the young stars, and 2) its own thermal radiation in the far-IR increases with increasing dust content. For example, ultra-luminous IR galaxies and starbursts have high dust content and so their UV emission is obscured by the presence of dust resulting in a lower UV emission relative to the far-IR. On the contrary, ellipticals, which barely have any dust content, have low far-IR emissions in comparison to the UV, which while low overall, is not obscured.

The spiked features around 10 μm are a product of polycyclic aromatic hydrocarbons (PAHs), organic compounds comprised purely of carbon and hydrogen (Puget and Léger 1989). They are mentioned for completeness but will not be discussed further. The various features of the SED mentioned here, as well as a few additional ones mentioned later, are tabulated in Table 1.1.

1.2.1 Modelling Thermal Dust Radiation as a Modified Black-Body

The thermal re-radiation of starlight by dust is commonly modelled as a modified black-body (MBB). This can take various forms (see Casey et al. 2014). The simplest models modify the Planck function, $B_\nu(T) = \frac{2h\nu^3}{c^2}\frac{1}{e^{h\nu/kT}-1}$, by a term containing the dust opacity, τ_ν. Here ν is the frequency in Hz, T is the temperature in K, $h = 6.625 \times 10^{-27}$ erg s is the Planck constant, and $k = 1.38 \times 10^{-16}$ erg K^{-1} is the Boltzmann constant. The thermal dust radiation is observed relative to the ever-present CMB black-body radiation (*e.g.* da Cunha et al. 2013), emitting at ~ 2.7 K,

$$S_\nu = A\left(\frac{\lambda}{\lambda_0}\right)^2 \left[\left(1 - e^{-\tau_\nu}\right) B_\nu(T_{\rm dust}) + e^{-\tau_\nu} B_\nu(T_{\rm CMB})\right], \tag{1.2}$$

where S_ν is the frequency-dependent flux density (in units of Jy) - the amount of energy per area that reaches the detectors. The flux density decreases with the square of the distance, it is the apparent brightness of an object. A is an arbitrary normalization factor and λ_0 is the wavelength (in units of m) at which the dust opacity is 1. The dust opacity is wavelength-dependent and is a power-law of the spectral dust emissivity index, β, such that $\tau_\nu = (\lambda/\lambda_0)^{-\beta} = (\nu/\nu_0)^\beta$. By definition, the spectral dust emissivity index is the slope of the logarithmic relation of the opacity with wavelength. The absorption of radiation by interstellar dust, and thus opacity, is a

complex function of a number of grain properties including composition, structure, physical nature, and morphology (Yang 2007). The dust emissivity index, which characterizes the dependence of opacity, or absorption, on wavelength, is therefore equally a function of these properties. Interstellar dust (primarily silicates, carbonateous grains, and ice) exists with a range of properties, β therefore is an average value for the entire galaxy. It is determined empirically from observations of the cold dust within galaxies. The review done by Casey et al. (2014) found that most data indicates $\nu_0 = 1.5$ THz whereas β is typically assumed to be 1.5 with some work finding it to vary from $\beta \approx 1 - 2$. We chose to set $\nu_0 = 3$ THz ($\lambda_0 = 100\,\mu$m) and $\beta = 2$, as was done by Greve et al. (2012) and Strandet et al. (2016) in their modelling of the thermal dust emission for the SPT-SMG sample.

The wavelength dependence of the dust opacity stems from the effectiveness with which dust absorbs radiation. Shorter wavelengths, such as the UV and blue-optical, are efficiently absorbed (or scattered) by dust, while longer wavelengths are less affected. In the cold, diffuse medium between stars, the interstellar dust heats to only $\sim 30 - 100$ K upon the absorption of UV radiation. At these low temperatures, the resulting thermal dust radiation occurs in the far-IR regime ($\sim 30 - 100\,\mu$m) following Wien's displacement law, $\lambda_{\rm peak} T = 2.898 \times 10^{-3}$ m K, where $\lambda_{\rm peak}$ is the wavelength of the peak of the black-body in m and T is the temperature in K. Interstellar dust comes in a range of sizes. However, grain size typically remains below $0.3\,\mu$m. For light whose wavelength is substantially larger than the particle off of which it scatters, generally the wavelength must be at least $\sim 10\times$ the grain size, the intensity I of the scattered light has a strong inverse-dependence on wavelength, $I \propto \lambda^{-4}$. This is known as Rayleigh scattering - the intensity of the scattered light drops off quickly with increasing wavelength. Alternatively, shorter wavelength light is scattered preferentially and longer wavelength light passes the dust grain without scattering. The thermal dust radiation in the far-IR, especially the longer wavelength radiation, can therefore escape the galaxy unimpeded. At longer wavelengths (*i.e.* at sub-mm and mm wavelengths), in the optically thin regime where $\tau_\nu \ll 1$, the $(1 - e^{-\tau_\nu})$ term in eq. 1.2 reduces to ν^β. Additionally Planck's function can be approximated by the Rayleigh-Jeans form, $B_\nu(T_{\rm dust}) \propto \nu^2$. The flux at long wavelengths from the source

itself, the first term in eq. 1.2, therefore takes the form

$$S_\nu \propto \nu^{2+\beta}. \tag{1.3}$$

In this way, β governs the long wavelength regime, known as the Rayleigh-Jeans tail, while the peak wavelength and width of the MBB are determined by $T_{\rm dust}$ and the normalization ν_0. The CMB term simply applies a small correction.

1.2.2 Negative K-correction

Sub-mm observations sample the peak of the dust continuum, the shape of which has greatly enhanced the study of SMGs. As the redshift of an SMG increases the observed SED shifts to longer wavelengths. Consequently, the observed-wavelength (if $> 250\,\mu$m) samples higher on the dust continuum (Blain et al. 2002), *i.e.* samples at shorter rest-wavelengths. A brighter region of the SED is therefore observed. This phenomenon is known as negative K-correction and works to negate the effects of cosmological dimming, the expected decrease in brightness of an object as it moves further away. Generally, K-correction is the adjustment made to the flux density, S_ν, for high-z objects and is dependent on the shape of the SED at the frequency of interest (Schneider 2006). Negative K-correction means the object appears brighter despite being at a higher redshift. This effect is shown in Fig. 1.5, which plots "the predicted flux density of a dusty galaxy as a function of redshift in various sub-mm atmospheric windows" (Blain et al. 2002). At wavelengths $> 250\,\mu$m the negative K-correction begins to take affect. At $\lambda \sim 850\,\mu$m the flux density remains virtually unchanged over the wide range $1 < z < 10$. The sub-mm flux is therefore independent of redshift. This means that an SMG at $z \sim 10$ can be detected just as readily as the same galaxy at $z \sim 1$.

1.2.3 The Interstellar Medium

On top of the baseline SED whose shape is determined by the galaxy's stellar population and the prevalence of dust, or lack thereof, spectral features can be observed as well. Spectral features, either in the form of absorption or emission lines, stem from the interstellar medium (ISM).

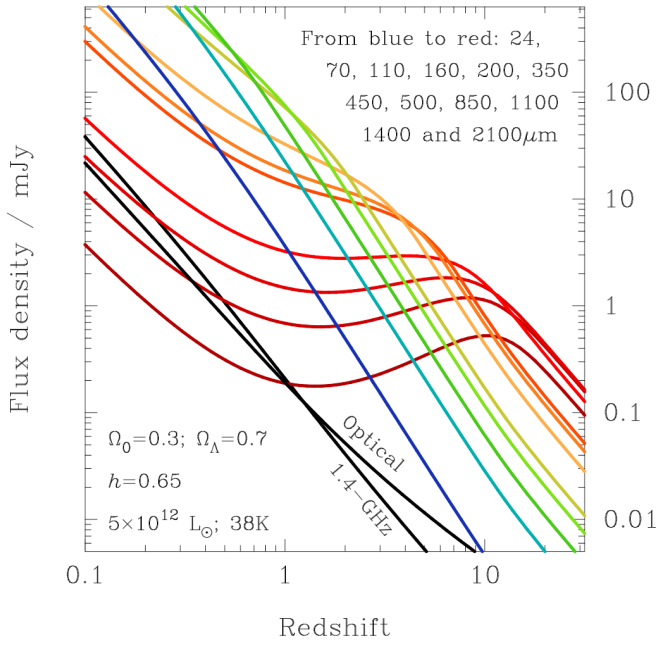

Figure 1.5: "The predicted flux density of a dusty galaxy as a function of redshift in various sub-mm atmospheric windows" (Blain et al. 2002). Negative K-correction is observed at wavelengths $> 250\,\mu$m. Figure taken from Blain et al. (2002).

The ISM is the low density material that fills the space between stars in a galaxy. It is comprised predominantly of gas (~ 99 %) of which 70.4 % by mass is hydrogen, 28.1 % is helium, and 1.5 % are gaseous metals (Ferrière 2001, & references therein). The remaining ~ 1 % of the ISM are dust grains containing metals. Metals are defined as any element beyond helium and are formed via fusion predominantly in stellar cores. Trace amounts of these metals are released back into the ISM during supernova, the highly energetic explosion of a massive star upon its death. Emission lines produced by the spontaneous decay of metals from various excited states originate from different regions in the ISM.

The ISM is non-uniform and exists in three primary forms - the cold, warm, and hot phase. The density for each phase varies inversely with the temperature. Table 1.2 lists approximate number densities in cm^{-3} and temperature ranges in K for each of the primary phases. The warm neutral phase ($T \sim 6,000$ K) is by far the most abundant ($\sim 30 - 60$ % by volume) and largely contains neutral hydrogen, H I. Molecular hydrogen, H_2, can only be found in the cold phase. Here the high densities

Table 1.2: Various phases of the ISM

Phase	Number Density [cm^{-3}]	Temperature [K]
cold	$> 10 - 100$	$30 - 100$
warm	0.3	10^{3-4}
hot	$0.01 - 0.001$	10^{5-6}

provide the necessary shielding from UV radiation to prevent the photodissociation of H_2 (Abgrall et al. 1992). Necessarily, in the low density ISM, hydrogen ionizes easily to singly ionized hydrogen, H II. The abundance, density, and temperature of interstellar gas are some of the key parameters that dictate star formation and play a critical role in galaxy evolution.

Energy Transitions

There are three basic types of energy transitions a molecule can experience - electronic, vibrational, and rotational. They are quantized and occur in vastly different wavelength regimes - UV-visible, IR, and microwave, respectively. Different components of the ISM as well as physical and chemical processes within the ISM can be traced by a variety of rotational and vibrational transitions of interstellar molecules.

Molecular hydrogen is the most abundant molecule in the universe. A schematic of the basic energy levels of H_2 (as presented by Pak et al. (2003)) is shown in Fig. 1.6. H_2 plays a key role in regulating star formation processes (Habart et al. 2005). Stars are formed in cold molecular gas clouds in which the collapse into a proto-star is triggered by compressions caused by shock waves. The density and temperature of H_2 are critical properties of a molecular gas cloud that determine if star formation can occur, the cooling of the ISM is in large part attributed to H_2 itself (Habart et al. 2005). Despite the abundance and importance of H_2, it is a challenging molecule to observe. Its electronic transitions are in the UV, to which our atmosphere is opaque. Such observations would therefore need to be conducted from space. To further complicate matters, the photodissociation of H_2 occurs via the absorption of UV radiation. H_2 initially transitions into the vibrational levels of either the $B^1\Sigma_u^+$ or $C^1\Pi_u$ excited electronic states, followed by the emission (either via the Lyman or Werner system respectively) into the vibrational continuum (denoted by H+H,

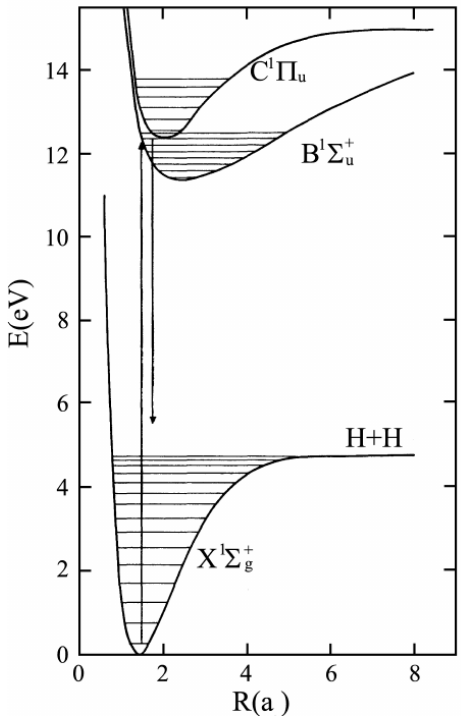

Figure 1.6: Energy levels of molecular hydrogen as a function of internuclear separation R in Å. The electronic ground state is denoted by $X^1\Sigma_g^+$, where H+H shows the dissociation energy, *i.e.* the vibrational continuum of the ground state. The first and second electronic excites states are denoted by $B^1\Sigma_u^+$ and $C^1\Pi_u$. Vibrational energy levels for each electronic state are shown as horizontal lines. Image taken from Pak et al. (2003) (adapted from reference within).

two neutral hydrogen atoms, in Fig. 1.6) of the ground electronic state $X^1\Sigma_g^+$, at which point it dissociates. The absorption of UV photons, which are ubiquitous in space, is therefore an efficient mode of H_2 destruction in the ISM (Dalgarno and Stephens 1970, & references therein). Vibrational transitions of H_2 generally do not exist, as molecular clouds are so cold ($10 - 20$ K) that even excitations into the lowest vibrational levels cannot occur. The rovibrational (transitions involving both rotational and vibrational states) and rotational excitations of H_2 stem from weak quadrupole transitions as H_2 is a homonuclear diatomic molecule and therefore has no permanent electric dipole moment (*i.e.* H_2 is non-polar). Emission features associated with such transitions are thus typically too weak to observe (Habart et al. 2005).

The second-most abundant molecule in the ISM after H_2 is carbon monoxide, CO. CO exists in the same environments as H_2 and is therefore frequently used as a proxy to H_2. It has a non-zero electric dipole moment and is easily excited by collisions

with H_2. The rotational transitions are identified by the rotational quantum number, J. For example, the emission stemming from the transition of CO's rotational level $J = 4 \rightarrow 3$ is denoted as CO(4-3). The energy associated with a rotational transitions is of the form $E_{\rm rot} \propto J(J+1)$. The abundance of CO means that its rotational lines are the brightest emission features in the (sub-)mm. With the advent of ALMA, CO lines have become the most ubiquitously used emission features in determining robust, spectroscopic redshifts for SMGs.

Water (H_2O) too is an abundant molecule in the ISM. Rotational water lines are thought to be excited by the absorption of far-IR photons from thermal dust emission and therefore trace the ISM's compact, warm and dense regions (Yang et al. 2013; González-Alfonso et al. 2010). Specifically, either young, hot stars or an AGN are required to excited H_2O. Water lines are therefore a powerful diagnostic of a galaxy's far-IR radiation generated by newly formed stars and are believed to be a tracer of both the physical extent of star forming regions as well as of the star formation rate (SFR) (Yang et al. 2016). The primary challenge in observing the H_2O emission lines is Earth's atmosphere. However, for high-z galaxies some of H_2O's rotational transitions are serendipitously redshifted into an atmospheric transmission window, enabling their observation.

In addition to the various energy levels discussed above, fine structure lines exist as well. The fine structure splitting of an energy level is caused by spin-orbit coupling - the interaction between the electron's spin angular momentum and the orbital angular momentum of the nucleus as perceived by the electron. (The perceived motion of the nucleus generates a magnetic field that interacts with magnetic dipole moment of the electron.) A small energy difference exists between different alignments of the electron spin and its orbital motion, thereby splitting the energy level. Fine structure transition lines such as those from singly ionized carbon ([C II] $\lambda_{\rm rest} \sim 158\,\mu$m) and singly ionized nitrogen ([N II], $\lambda_{\rm rest} \sim 205\,\mu$m) are at (sub-)mm wavelengths when redshifted by $z \sim 2-4$ (and therefore accessible to us) and offer important insight into properties of the ISM in high redshift galaxies where more traditional optical and UV line diagnostics are redshifted past the near-IR atmospheric transmission windows and are no longer accessible (*e.g.* Nagao et al. 2012). [C II] is one of the strongest lines in the far-IR and is therefore frequently used in redshift determinations

of SMGs instead of the popular CO lines (Sargsyan et al. 2012). Due to their low dust attenuation, fine structure lines can still be observed in the far-IR where thermal dust emission dominates and offer insight into the density and ionization of gas clouds (*e.g.* Pavesi et al. 2016; Nagao et al. 2012).

[C II] is also another important coolant of the ISM. Photodissociation regions are neutral regions of the ISM surrounding sites of recent star formation in which the density is low enough for UV photons from young, hot stars to penetrate and heat the dust. In turn, thermal dust radiation heats the gas. However, collisions with photo-electrons emitted by dust, most commonly by PAHs, excite the ground state of [C II] into its upper fine-structure level, eventually leading to radiative decay into the lower fine-structure level. The strong emission line of [C II] therefore cools the gas of photodissociation regions and is thought to be another useful tracer of the star formation rate (*e.g.* Maiolino et al. 2005; Stacey et al. 2010; Gullberg et al. 2015).

Insight into other physical properties such as gas temperature, density, mass, *etc.* can be gleaned by comparing the intensities of various fine-structure lines (Decarli et al. 2014). As discussed, some of the atoms and molecules that are the source of fine-structure lines are crucial to the cooling of the ISM. Seeing as cold, dense gas is required for star formation, they can therefore be used as diagnostics of star formation rates. Star formation rates play a significant role in the absolute intensities of all emission lines, as they are powered by the absorption of UV photons emitted by young, hot stars. Besides identifying the wavelength of an emission line, the width can provide interesting diagnostics as well. The width, or the velocity dispersion, σ, is primarily broadened by the motion of the ISM. The more turbulent the system, the broader the lines. The physical properties, such as star formation rates and various masses, that can be determined from the intensities and velocity dispersions of fine-structure lines will be discussed in greater detail in subsequent chapters.

For completeness, hyper-fine splitting of energy levels can occur too. They arise due to the interactions of the electron spin with the nuclear spin. The most common example of this is the 21 cm spin-flip line of neutral hydrogen. The energy of H I is slightly higher when the electron and proton spin are parallel as opposed to anti-parallel. When the electron spin spontaneously flips from the parallel (higher energy) to anti-parallel (lower energy) state a photon with $\lambda \sim 21$ cm is radiated.

The abundance of neutral hydrogen makes the 21 cm line the strongest feature in a spectrum, however it is well past the range of interest for this work.

Emission lines in the sub-mm are clearly a critical component in the study of SMGs. Sub-mm emission lines are a product of spontaneous decay from an excited state after the absorption of energetic UV photons, the UV photons consequently cannot escape the optically thick ISM. The sub-mm photons emitted are, however, able to escape the galaxy relatively unimpeded as the sub-mm opacity is several orders of magnitude lower. Attenuation, via absorption or scattering, is most prevalent when the dust grain size and the wavelength of incident light are comparable. Long wavelength radiation therefore travels freely through the galaxy. In contrast, shorter wavelength radiation, *i.e.* in the optical and near-IR, suffers from attenuation. Spectroscopic analysis in these more traditional optical wavelengths is therefore significantly more challenging. This is especially true for elliptical galaxies, in which the gas and dust content is so low that the emission features are often hard to detect above the noise of the baseline SED. Instead, absorption lines from the old stellar population are commonly observed. While emission lines stem from the diffuse gas surrounding stars and their intensity is powered by the isotropic radiation of said stars, only line-of-sight absorption features measured relative to the star's continuum can be detected and are therefore typically weaker than emission lines.

1.3 The South Pole Telescope

The South Pole Telescope is a 10 m diameter telescope located at the geographic South Pole at the Amundsen-Scott South Pole Station on the Antarctic Plateau. Its geographic location is important in numerous ways, primarily because of its superior atmospheric conditions. Water vapour in the atmosphere is the dominant source of opacity in the IR and sub-mm regimes. It absorbs radiation from the sky to varying degrees depending on the wavelength of incoming radiation, preventing certain radiation from passing through the atmosphere completely. At radio frequencies for example, the atmosphere is fully transparent. At wavelengths shorter than the UV and for most of the far-IR the atmosphere is almost completely opaque and observations need to be conducted using space-borne telescopes. The optical, key near-IR

regimes, and critically some sub-mm wavelengths fall within atmospheric transmission windows - wavelength ranges in which the transmission of radiation is considered high enough for observations. In the sub-mm specifically these transmission windows are narrow and still only transmit a fraction of the incoming radiation. Sites with low and stable water vapour content in the atmosphere are therefore crucial for observations. Three such popular sites are Mauna Kea in Hawaii, the Atacama Desert in northern Chile, and the South Pole. All three sites are at high altitude and are cold and dry, resulting in some of the lowest water vapour content around the world. The South Pole, the coldest and driest of these sites, additionally benefits from the circumpolar nature of apparent motion in the sky, *i.e.* the apparent motionlessness of the sky. Due to its location beneath the celestial south pole, observations do not have to contend with objects rising and setting.

SPT was originally designed to conduct a large-area survey ($\sim 4,000$ deg^2) searching for massive clusters of galaxies (massive, gravitationally bound structures containing > 50 galaxies) via the Sunyaev-Zel'dovich (SZ) effect. The SZ effect is the up-scattering of low-energy CMB photons via interactions with high-energy intracluster electrons in a process known as inverse Compton scattering. Conservation of CMB photon numbers dictates that while more photons have higher frequencies (frequencies above the peak of the CMB Planck distribution), at lower frequencies there must be a corresponding deficit of photons. Large-scale surveys search for "shadows" against the CMB by comparing maps of the sky at different frequencies. Fig. 1.7 is a 150 deg^2 map of the CMB as observed by SPT (image adapted from a presentation given by Bradford Benson and the SPT Collaboration). The green circles identify shadows against the CMB, thus pointing to massive galaxy clusters.

The sensitivity, selection wavelengths (3 mm, 2 mm and 1.4 mm), and beam size ($\sim 1'$) make SPT an ideal instrument in identifying high-z SMGs. From just a small section of the total survey, 87 deg^2, Vieira et al. (2010) detected almost 200 point sources above 4.5σ at 1.4 mm and 2 mm. (4.5σ refers to a signal $4.5\times$ the standard deviation of the normal distribution of the noise. Detections at 3σ significance are considered highly likely whereas 5σ detections are deemed robust.) The yellow circles in Fig. 1.7 identify some of these point sources. The simultaneous detection in two

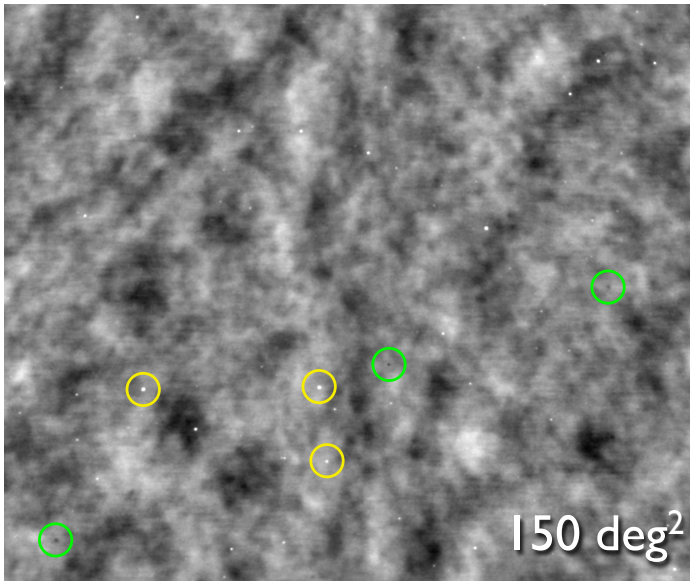

Figure 1.7: 150 deg^2 SPT map of the CMB. Green circles identify shadows against the CMB indicating the detection of a galaxy cluster. Yellow circles identify point sources - active galactic nuclei (at $\sim$ 75 %) or high-z dusty, star-forming galaxies (at $<$ 25 %). Image credit: Bradford Benson and SPT Collaboration.

bands allows for the separation of sources into two distinct populations - synchrotron-emission dominated sources and dusty, star-forming galaxies.

Synchrotron emission, the non-thermal emission from electrons accelerated through a magnetic field, is a hallmark of an active galactic nucleus and results in the mm regime of the SED being either flat or increasing with increasing wavelength, *i.e.* synchrotron-dominated sources will have the same brightness or are dimmer at 1.4 mm as compared to at 2 mm. Approximately 75 % of the sources detected by SPT fall within this category, the majority of which match with counterparts in external radio catalogues. These sources will not be discussed further.

The remaining $\sim$ 25 % of sources decrease in brightness as wavelength increases from 1.4 mm to 2 mm, a clear indication of thermal dust emission (refer back to Section 1.2). A small subset of these are local, low-redshift ($z \ll 1$) galaxies previously detected in optical surveys and are therefore discarded. Lastly, a flux cut is applied to the remaining sources. Sources with a 1.4 mm flux greater than 20 mJy are kept. Unlensed sources of this brightness at high-redshift are exceptionally rare. It is therefore expected that a predominant component are gravitationally lensed

(Blain 1996; Negrello et al. 2007; Hezaveh and Holder 2011). A detailed discussion on gravitational lensing will be presented in Chapter 2. The resulting sample consists of 47 previously undetected high-z sources dominated by thermal dust emission (Vieira et al. 2010). They are referred to as the SPT-SMG sample from here on.

Since the original discovery of the SPT-SMG sample by Vieira et al. (2010), $2,500$ deg^2 of the southern sky have been surveyed across all three SPT bands and the sample size has increased to ~ 90 SMGs (*e.g.* Mocanu et al. 2013). Extensive spectroscopic follow-up observations to determine redshifts were immediately conducted using ALMA (Weiß et al. 2013; Strandet et al. 2016). Additionally, high-resolution imaging by ALMA confirmed image morphologies unique to gravitational lensing for the majority of the sample (Vieira et al. 2013). This subsequently led to efforts in creating models of the gravitational lensing systems (Hezaveh et al. 2013; Spilker et al. 2016). Follow-up observations in the red-optical and near-IR detect massive ellipticals in the foreground of gravitationally lensed SMGs, thereby identifying them as candidate lenses of the system. Chapter 2 focuses on these lenses.

In Chapter 3 I analyze one of the rarer objects found in the SPT-SMG survey in more detail, SPT2349-56. Unlike the majority of the SMGs in the sample, SPT2349-56 was confirmed to be an unlensed, yet high-redshift object. At $z \sim 4.3$, we are observing SPT2349-56 approximately 1.35 billion years after the Big Bang. High-resolution imaging identified 14 individual SMGs, all part of a so-called "protocluster." This chapter considers several astrophysical properties of these 14 sources.

In order to observe objects that are either at higher redshifts or are simply faint, measurement sensitivities need to improve. Sensitivity improvements by several orders of magnitude are particularly needed in observations of the CMB polarization, another primary science objective of SPT (Carlstrom et al. 2011). Chapter 4 therefore changes perspectives and focuses on improvements that can be made to the cold-readout electronics of telescopes in an effort to increase their sensitivity. Specifically, planar lithographed superconducting inductor-capacitor resonators are considered.

Lastly, Chapter 5 summarizes this thesis, placing the previous research results into context with ongoing efforts in their respective fields.

Chapter 2

A Redshift Survey of the Gravitational Lenses Discovered by the South Pole Telescope

This chapter discusses the lenses of the gravitational lensing systems in the South Pole Telescope (SPT)-sub-millimetre galaxy (SMG) sample. Extensive follow-up observations in the optical and near-infrared have been conducted in order to determine accurate redshifts for the lenses and to characterize numerous physical parameters such as galaxy morphology (*i.e.* galaxy type and shape) and galaxy masses, placing them into context with other surveys of gravitational lenses. Sect. 2.1 introduces gravitational lensing theory, different methods of determining redshift, the SPT-SMG sample in more detail, and the motivation behind studying the lenses. In Sect. 2.2, 2.3, and 2.4 the imaging, spectroscopic, and ancillary data is presented respectively. Sect. 2.5 briefly outlines the three primary surveys used as comparison samples and Sect. 2.6 details the results, discussing the numerous physical properties explored. Sect. 2.7 concludes the discussion of gravitational lenses.

2.1 Introduction

2.1.1 Gravitational Lensing

Gravitational lensing is the bending, magnification, and distortion of light from a distant galaxy by the gravitational potential of a massive object in the foreground. There are two types of gravitational lensing - weak and strong lensing. Weak gravitational lensing is a slight distortion in the image of a background object. It is typically caused by a diffuse gravitational potential in the foreground, *i.e.* dark matter halos of galaxy clusters, or a poor alignment with a single massive galaxy in the foreground. Weak lensing can only be detected by statistical averaging of many background sources, as it is too weak to detect in any one galaxy by itself (Schneider 2006). It has been used

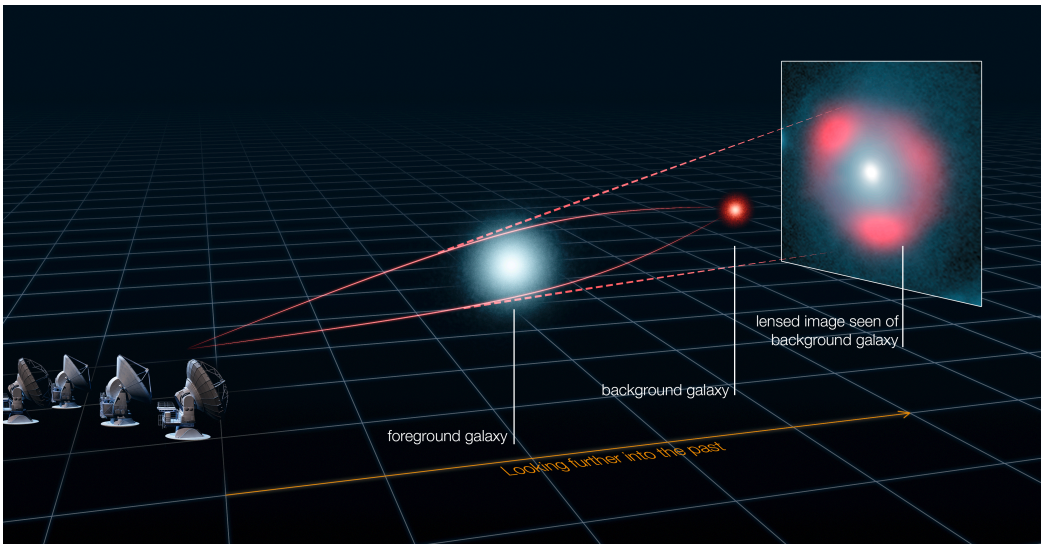

Figure 2.1: Schematic depicting the effects of gravitational lensing. Light from a distant background galaxy is bent, magnified, and distorted as it travels past the gravitational potential of a massive object in the foreground, acting as a lens. Image credit: ALMA (ESO/NRAO/NAOJ), L. Calçada (ESO), Y. Hezaveh et al.

to great effect in detecting galaxy clusters and is crucial in determining accurate constraints on cosmological parameters needed when modelling the origin and growth of the universe. Specifically, weak lensing of the cosmic microwave background (CMB) probes the spatial distribution of dark and light matter in our universe out to the greatest distances (Bartelmann and Maturi 2017, & references therein).

Conversely, strong gravitational lensing is the result of lensing by a foreground object with a dense core, *i.e.* a single massive elliptical galaxy. Fig 2.1 (image credit: ALMA (ESO/NRAO/NAOJ), L. Calçada (ESO), Y. Hezaveh et al.) is a schematic depicting the effects of strong gravitational lensing. The observed image of the distant galaxy is magnified and highly distorted - in cases with good lens-source alignment into arcs or rings referred to as Einstein rings. The serendipitous alignment of a distant galaxy with a massive foreground galaxy allows for the observation of the distant galaxy when it would otherwise be too faint to detect or have a signal-to-noise ratio too low for detailed, statistically significant analysis. In this work, we focus on strong gravitational lensing. From here on the distant object being lensed will be referred to as the "source" and the massive object in the foreground responsible for the lensing as the "lens."

Historical Perspective

Strong gravitational lensing is a direct prediction of Albert Einstein's theory of general relativity in which the geometry of spacetime is affected by matter and radiation. A massive object will distort spacetime, creating a gravitational potential well through which the light travel path is affected. Originally stars within our galaxy were considered as potential gravitational lenses. However, Fritz Zwicky in 1937, determined they were not massive enough to create a visible effect. Instead, Zwicky was the first to predict a visible effect of strong lensing via extragalactic nebulae, massive clouds of gas and dust outside of our Milky Way. He suggested two key consequences of such galactic-scale lensing: 1) the image of the distant object would appear as a ring. He considered the most massive and concentrated nebulae known and hypothesized that the deflection from line of sight may be up to 0.5 arcminutes. 2) The apparent brightness of the ring could be up to a factor of 100x brighter than the intrinsic brightness of the object, while the surface brightness remains unchanged. This would require near perfect alignment along the line of sight of the source and the lens.

In 1979 Dennis Walsh and his colleagues made the first observation of strong gravitational lensing. They discovered two quasi-stellar objects (high-z galaxies that have spectra very similar to blue stars) separated by less than $6''$ with the same redshift, similar magnitude, and whose spectra clearly identified the two as being physically associated with one another. In their discussion they considered the possibility that the two objects are images of the same source through the effects of gravitational lensing while also stating the low probability of the necessary chance alignment of a massive foreground object with their quasi-stellar objects (Walsh et al. 1979).

Since this first discovery of strong gravitational lensing, the search for the serendipitous alignment of two massive objects has been ongoing. The effect is not a frequent occurrence and requires expensive large-field surveys for initial detections. Early surveys, such as the Cosmic Lens All-Sky Survey (CLASS) (Myers et al. 2003) and the Jodrell Bank Very Large Array (JVAS) gravitational lens survey (King and Browne 1996), were conducted using radio frequencies and resulted in a sample of ~ 80 strong lensing systems. These surveys were necessarily biased towards detecting sources with strong radio components. More recently, follow-up surveys were conducted for candidates initially selected from the Sloan Digital Sky Survey (SDSS) using the Sloan

Lens Advanced Camera for Surveys (SLACS) (Bolton et al. 2006; Bolton et al. 2008) and the SDSS-III Baryon Oscillation Spectroscopy Survey (BOSS) (Eisenstein et al. 2011), specifically the BOSS Emission-Line Lens Survey (BELLS) (Brownstein et al. 2011). These endeavours more than doubled the number of confirmed lenses. The SLACS and BELLS surveys will be discussed in greater detail in Section 2.5 as they form the basis for the comparison sample to our own lenses.

Gravitational Lensing Theory

In a gravitational lensing system, the source sometimes appears as either a ring or an arc around the foreground lens. The radius of such a lensed ring or arc, known as the Einstein radius, $\theta_{\rm E}$, is a consequence of the geometry of the lensing system as well as the mass of the lens.

The geometry of a typical lensing system is shown in Fig. 2.2 and is based on the one presented by Narayan and Bartelmann (1996) in "Lectures on Gravitational Lensing." Here the source, S, is a distance $D_{\rm s}$ away from the observer, O, and the lens, L, is a distance $D_{\rm l}$ away from the observer. The distance between the lens and the source is $D_{\rm ls}$, where in general $D_{\rm ls} \neq D_{\rm s} - D_{\rm l}$. The optical axis is defined as the line-of-sight from the observer through the centre of the lens, the horizontal dashed line in Fig. 2.2(a). The thickness of the lens along the line-of-sight can safely be

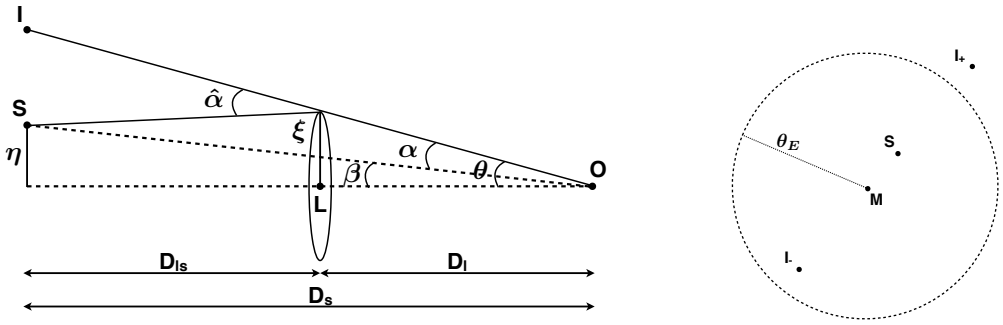

(a) Side view

(b) Front view

Figure 2.2: Geometry of a typical lensing system. (a) Side view. Light from the source S is deflected by an angle $\hat{\alpha}$ at the lens before reaching the observer O and appearing as an image at location I. (b) Front view. A lens of mass M and an Einstein radius of $\theta_{\rm E}$ doubly images the source at $\rm I_+$ and at $\rm I_-$.

assumed to be negligibly small as compared to the distances D_l and D_s. The physical situation is therefore one of a geometrically thin lens.

The distances in this picture are angular diameter distances and have units of megaparsec (1 pc $= 3.086 \times 10^{16}$ km). The angular diameter distance is the ratio of the physical extent of an object (*i.e.* the radius of an object) to its angular size (*i.e.* the angle that that radius subtends as seen by the observer). Angular diameter distances are therefore defined using the small angle approximation. This is a reasonable assumption to make as the physical size of the lens, ξ, or the distance from the optical axis at which the light ray is deflected (*i.e.* the impact parameter), as well as the distance of the source to the optical axis, η, are significantly smaller than either distances D_l or D_s. We can therefore define $D_\mathrm{l} = \xi/\theta$ and $D_\mathrm{s} = \eta/\beta$, where θ is the angle subtended by ξ and similarly β is the angle subtended by η, as seen by the observer. The angle $\hat{\alpha}$ in Fig. 2.2(a) is the deflection angle, the angle by which a light ray emitted from the source is deflected when it passes the lens at its impact parameter. The image is therefore observed at a distance further from the optical axis than the source. The distance of the image from the optical axis can be expressed either by the angle that it subtends from the observer's perspective, θ, or by the sum of the distance from the optical axis to the source and the distance from the source to the image, both expressed in terms of the angles they subtend,

$$\theta D_\mathrm{s} = \beta D_\mathrm{s} + \hat{\alpha} D_\mathrm{ls}. \tag{2.1}$$

Dividing both sides by D_s, we can define the reduced deflection angle $\alpha \equiv (D_\mathrm{ls}/D_\mathrm{s})\,\hat{\alpha}$ so that we are left with the simple equation $\beta = \theta - \alpha$. This is referred to as the lens equation.

General relativity can be used to find the angle of deflection of a photon as it travels past a gravitational potential. As Einstein predicted, the deflection angle is a factor of 2 larger in general relativity than in Newtonian physics. The angle of deflection is given by

$$\hat{\alpha}(\xi) = \frac{4GM(\xi)}{c^2 \xi}, \tag{2.2}$$

where G is the gravitational constant, $M(\xi)$ is the mass enclosed within the radius ξ,

and c is the speed of light. The reduced deflection angle then becomes:

$$\alpha(\xi) = \frac{D_{\rm ls}}{D_{\rm s}} \frac{4GM(\xi)}{c^2 \xi}. \tag{2.3}$$

ξ and θ are geometrically related through $\tan\theta = \xi/D_{\rm l}$, which, when using the small angle approximation becomes $\xi = D_{\rm l}\theta$. This and equation 2.3 can be substituted into the lens equation to produce the following relation:

$$\beta(\theta) = \theta - \frac{D_{\rm ls}}{D_{\rm l} D_{\rm s}} \frac{4GM(\theta)}{c^2 \theta}. \tag{2.4}$$

If the source lies on the optical axis, we set $\beta = 0$. For simplicity, we can approximate the lens as a point mass. Equation 2.4 then becomes:

$$\theta_{\rm E} = \left[\frac{D_{\rm ls}}{D_{\rm l} D_{\rm s}} \frac{4GM_{\rm E}}{c^2} \right]^{\frac{1}{2}}, \tag{2.5}$$

where $\theta_{\rm E}$ is referred to as the Einstein radius (units of radians). It is a critical parameter of gravitational lensing that is defined by the Einstein mass, $M_{\rm E}$, of the lens and the geometry of the lensing system. The Einstein mass is the total mass (baryonic matter and dark matter combined) enclosed in a sphere with radius $\theta_{\rm E}$.

In this on-axis configuration, the lensing system is symmetric and the image of the source will appear as a perfect circle centred on the lens. In general though, the source does not lie on the optical axis. The general lens equation for a point mass can therefore be written as, $\beta(\theta) = \theta - \theta_{\rm E}^2/\theta$. This is a quadratic equation of θ and we find that the source will be imaged twice,

$$\theta = \frac{1}{2} \left(\beta \pm \sqrt{\beta^2 + 4\theta_{\rm E}^2} \right), \tag{2.6}$$

where it is common to observe a bright image and a fainter counter image, labelled $\rm I_+$ and $\rm I_-$ in Fig. 2.2(b). While gravitational lensing distorts and magnifies the light emitted by a source, the surface brightness (the flux per unit area) remains constant. The magnification is therefore the ratio of the area of the image to that of the source. The distortion of the image is a result of light bundles being differentially deflected as they pass the lens with slightly different impact parameters.

2.1.2 Redshifts

Confirming the redshift of an object is integral to the analysis of its intrinsic properties and can be accomplished either via spectroscopic or photometric methods. The most robust method is through spectral analysis; matching observed wavelengths of features in the spectrum with known rest wavelengths and applying Eq. 1.1, $(1+z) = {}^{\lambda_{\rm obs}}/_{\lambda_{\rm rest}}$. For galaxies with high gas and dust content and active star formation, strong emission lines from either the ionized or molecular gas are ubiquitous. Some of the strongest and most commonly used features for this method are the multitude of CO transition lines. Unfortunately, galaxies with low gas and dust content (*i.e.* ellipticals) will not have strong emission lines and so spectral analysis must frequently rely on the weaker stellar absorption features. Furthermore, as the redshift rises, galaxies typically become fainter and spectral absorption lines become increasingly more difficult to detect. Lastly, spectral analysis is also costly. In spectroscopy, incident light gets broken up into spectral components and therefore requires substantially more telescope time to achieve the same continuum signal-to-noise ratio (SNR) as imaging.

An alternative option is to determine a photometric redshift, *i.e.* use the photometry (measurements of the radiated power) of the galaxy to estimate a redshift. Baum (1962) was the first to suggest such a technique. He imaged and determined the photometry in 9 bands, *i.e.* at 9 different wavelengths, for 6 elliptical galaxies in a cluster of unknown redshift as well as for 3 ellipticals in a cluster of known redshift. By averaging the photometry and creating a spectral energy distribution (SED) for each cluster and comparing them to each other, he was able to infer a redshift for the cluster whose redshift was previously unknown.

A critical component of the comparison lay in identifying the $4,000$ Å break in the SED. The rest-frame optical region of the SED is a superposition of the black-body spectra from all the stars within the galaxy at varying temperatures and ages. This results in a bump in the SED with a fairly flat top, refer back to Fig. 1.4. However, for a sufficiently old stellar population ($> 10^8$ yrs.) the hottest black-body spectra of young, hot O & B type stars (peaking in the UV) are missing. Furthermore, the presence of metals in the atmospheres of older stars is increased. A number of overlapping metal absorption lines (including calcium K & H, the singly-ionized calcium doublet still referred to by the Fraunhofer K and H letters) exist at $< 4,000$

Å resulting in a blanket absorption of high-energy photons superposed onto the multi-temperature stellar spectra. The SEDs therefore display a sharp break at $4,000$ Å, already on the downward slope of the bump associated with the old stellar population. The flux at longer wavelengths is substantially larger than that at shorter wavelengths (Schneider 2006). By identifying the location of the $4,000$ Å break in a galaxy's SED, the redshift can be determined. To do so with some accuracy though, the galaxy's photometry must be sampled over the optical and near-IR at sufficiently frequent intervals.

Another source that causes a similar feature in the SED that is often used to determine photometric redshifts is the Lyman break, discussed in the introduction (Sect. 1.2). It is expected that galaxies at higher redshifts will display a stronger Lyman break as more intergalactic hydrogen exists between it and the observer to absorb these short-wavelength photons (Schneider 2006).

Since these early methods of using multi-band photometry to locate significant features in the SED, more rigorous techniques have been created where SED templates are fit to the photometry. This generally requires an assumption about the type of galaxy in question, as the templates are average SEDs for varying galaxy populations. At its most basic, the appropriate template can be shifted in wavelength from the rest-frame until the photometry is aligned with the template. The shift is equal to $1+z$. Within a galaxy population, however, variations to the SED are caused by age, metallicity - the mass fraction of heavier elements (any element past hydrogen) to hydrogen, reddening - the scattering of blue light by interstellar dust, dust content, etc. More sophisticated fitting can take these variations into account. Many SED fitting packages are available online, *e.g.* Easy and Accurate Z-phot from Yale (EAZY) (Brammer et al. 2008), HyperZ (Bolzonella et al. 2000), and Code Investigating GALaxy Emission (CIGALE) (Noll et al. 2009). While these packages all vary to certain degrees, the core concept is a minimization procedure between the SED template and the multi-band photometry while taking various parameters of the galaxy into account. These fitting packages contain large libraries of SED templates and either single or multiple templates can be fit to match the photometry. The more the input parameters are constrained, the more accurate the result can be. Alternatively, some key galactic parameters that can be ascertained through the

fitting procedure are IR luminosity, stellar mass, dust mass, and dust temperature. Fortunately, photometry from the entire electromagnetic spectrum is not required as the various galaxy parameters manifest themselves in specific features within a given wavelength regime. Thus strategic photometry sampling over a specific wavelength range with enough resolution to identify changes in the SED shape can inform on a given parameter. Unfortunately observing a galaxy in a sufficient number of bands is time consuming and can frequently require observations from multiple telescopes. In addition, systematic errors on top of measurement errors of the photometry between different bands from different telescopes can lead to highly misleading results - error weighting can only compensate for so much. Finally, the large multi-parameter space of the fitting procedures, while sometimes useful, is often unjustified and can introduce degeneracies in the results. For these reasons, multi-band SED fitting with limited information can produce results that should not be trusted.

As an alternative to multi-band SED fitting, single-band photometric redshifts can frequently be more informative. The $K - z$ relation is one example. The $K - z$

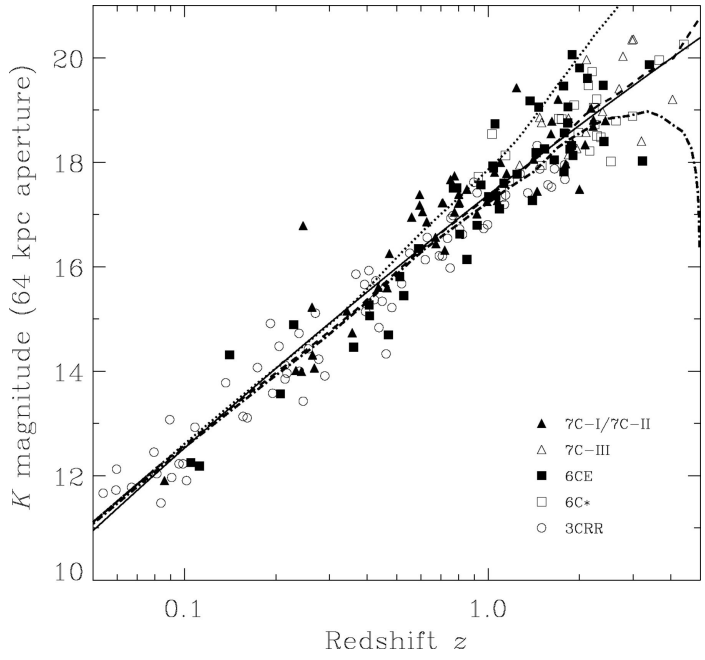

Figure 2.3: The $K - z$ relation for radio galaxies from several surveys across the redshift range $0 < z < 5$. The solid line is the second-order polynomial fit to the data. Dashed and dotted curves represent the predicted luminosities for a a variety of different models. Figure taken from Willott et al. (2003).

relation is a tight empirical correlation that was found between the K-band magnitude (centred at 2.16 μm) and the redshift of radio loud galaxies, galaxies with substantial emission in the radio wavelengths caused by synchrotron radiation. Lilly and Longair (1984), for example, studied 83 radio galaxies spanning the redshift range $0 < z < 1.7$ and found the $K - z$ relation to be well defined with a dispersion that remained approximately constant even for redshifts past unity. Studies of radio galaxies at low redshift ($z < 0.2$) have found these radio sources to be bright, massive ellipticals (Bettoni et al. 2001). De Breuck et al. (2002) found the $K - z$ relation to hold even for redshifts out to $z \sim 5$. They found the loudest radio sources identify the most massive galaxies across all redshifts, strongly suggesting that radio sources are massive ellipticals even at high-z. Willott et al. (2003) suggested that radio galaxies are a population of galaxies in which the bulk of the star formation occurred at high-redshift ($z > 5$) and continued to evolve passively from then on as massive ellipticals. Fig. 2.3 (taken from Willott et al. 2003) shows the K-band magnitudes (K, unit-less) for radio galaxies from several surveys as a function of redshift. They found the best fit to be a second-order polynomial relation in $\log z$ (solid line in Fig. 2.3),

$$K = 17.37 + 4.53 \log z - 0.31(\log z)^2. \tag{2.7}$$

They too found the dispersion of the relation to remain roughly constant at $\sigma \sim 0.57 - 0.6$ across the entire redshift range. Willott et al. (2003) remark on the incredible similarity between their empirical fit and the predicted evolution of the K-band magnitude with redshift for a galaxy that formed all its stars instantaneously at $z = 10$, evolving passively from then on (dashed curve in Fig. 2.3). While the $K - z$ relation has no physical meaning, it can be used to estimate redshifts if the K-band magnitude is known (*e.g.* Schmidt et al. 2006). An empirical relation derived from radio loud galaxies has thus become a single-band redshift proxy for ellipticals.

2.1.3 SPT-SMG

The SPT-SMG sample is a group of dusty, star-forming galaxies that are luminous in the sub-mm and were first discovered by the South Pole Telescope (Carlstrom et al. 2011; Vieira et al. 2010). The $2,500$ deg^2 SPT survey was one of the first wide-field

surveys conducted in the sub-mm that enabled the blind search of SMGs as opposed to targeting observations at galaxy clusters or searching within radio surveys. The SPT survey furthermore benefited immensely from the effects of negative K-correction, where the rising dust spectrum compensates for any cosmological dimming. SMGs in the SPT survey are therefore selected independent of their redshift (Vieira et al. 2013). The 4.5σ detection limit ($S_{1.4\,\mathrm{mm}} > 20$ mJy) of the SPT-SMG sample ensures that the majority are magnified due to gravitational lensing. Specifically, the lensing occurs predominantly via galaxy-galaxy lensing (*i.e.* the lens is a single massive galaxy) as opposed to being lensed by a dense group or a dense cluster of galaxies. The combination of the above factors results in a more statistically complete SMG sample that spans a much larger redshift range than previous surveys. The redshift completeness along with the long-wavelength selection and the benefits from gravitational lensing makes the SPT-SMG sample so powerful and unique. Consequently, it is likely that the redshift distribution of the lenses in the SPT-SMG lensing systems are less biased towards low redshifts and the most massive lenses, and present a more complete distribution compared to previous surveys conducted.

2.1.4 Motivation

The serendipitous alignment of galaxies that results in gravitational lensing has lead to the quickly advancing field studying dusty, star-forming galaxies otherwise too distant and faint to study in detail. While the magnification and flux amplification have made it easier to observe SMGs, they also pose as hurdles in the analysis of the intrinsic, physical properties of the galaxy. The distorted and magnified images need to be reconstructed in the source-plane. Consequently a large, ongoing effort has been made in creating models that will accurately reproduce magnification factors and image morphologies (*e.g.* Hezaveh and Holder 2011; Spilker et al. 2016). This will ultimately allow for a "de-lensing" of the source so that further analysis of the SMGs can be done using their intrinsic properties instead of the lensed ones. To do so, lensing models require a detailed understanding of the lenses so that SMGs can be accurately de-lensed. The primary concerns of models in regard to the lenses are the lens mass and lens redshift. Mass distribution within the lens can also play a role in the lensing effectiveness. Importantly, the mass distribution of the lens is affected

greatly by the dark matter distribution. Characterizing the lenses is therefore not only required for the analysis of lensed SMGs, lenses are also great laboratories in which to study dark matter.

We find the lenses in these systems to predominantly be elliptical galaxies that are evolving passively, *i.e.* no longer forming stars. Elliptical galaxies are some of the most massive galaxies in the local universe and are therefore an interesting population in their own right to study. Learning more about their evolutionary track is critical in understanding the build-up of mass in the universe. Ellipticals are likely the natural evolutionary progression of SMGs and so gravitational lensing identifies two populations of galaxies seemingly as different as night and day, that are potentially snapshots of the same population simply at different evolutionary stages.

We study these massive elliptical galaxies and hypothesize that the SPT selected lenses represent a more comprehensive view of gravitational lenses as compared to other recent surveys (such as SLACS, BELLS, and the Herschel-subsample). The focus of this project is the analysis of the SPT lenses, determining their redshift distribution as well as other astrophysical properties, and their comparison to other samples.

2.2 Imaging

2.2.1 Observations

Obtaining a complete set of multi-band photometry as well as spectroscopy is crucial for a rigorous analysis of the lenses. From past surveys it has been shown that the majority of objects that facilitate strong gravitational lensing are massive elliptical galaxies with redshifts spanning a fairly wide range, $0.06 \lesssim z \lesssim 1.4$ (Bolton et al. 2006; Brownstein et al. 2011; Bussmann et al. 2013). Elliptical galaxies, due to their lack of dust, emit most strongly in the visible spectrum as this is the range in which stars predominantly radiate. A near universal bump at 1.6 μm in the rest-frame spectrum of all but the youngest of galaxies exists. This bump arises due to the H^- ion in stellar atmospheres, the opacity of which is at a minimum at 1.6 μm (John 1988), thereby leading to a peak in emission. For ellipticals the 1.6 μm bump is the brightest part of the spectrum (refer back to Fig. 1.4). For moderate redshifts, as is

expected for our ellipticals, this peak shifts further into the near-IR.

Observing the lenses in the $J-$ and $K-$bands (1.24 μm and 2.16 μm respectively) using either the Infrared Spectrometer And Array Camera (ISAAC) on the Very Large Telescope (VLT) located in the Atacama Desert of northern Chile or alternatively using the FLAMINGOS-2 (F2) camera on the Gemini-S Telescope located on Mauna Kea in Hawaii, USA should therefore capture the most luminous wavelengths of the lens' radiation. For the most redshifted ellipticals, the peak will shift as far as the Infrared Array Camera (IRAC) channels (CH1 and CH2 are at 3.55 μm and 4.49 μm respectively) on *Spitzer* (a space-borne observatory) in the mid-IR, while the lowest redshift ellipticals or potentially the bluest (*i.e.* those with a slightly younger stellar population) will continue to emit strongly in the optical. $G-$ and $R-$bands (0.47 μm and 0.64 μm respectively) can be used to cover the optical range on either the FOcal Reducer/low dispersion Spectrograph 2 (FORS2) on the VLT, the Gemini Multi-Object Spectrographs (GMOS) on Gemini-S, or the Dark Energy CAMera (DECam) on the Blanco 4-m telescope (located on the Cerro Tololo mountaintop in the Chilean Andes) for the Dark Energy Survey (DES). For a small sub-sample of the the SPT lenses we also made use of near-IR imaging from the Wide Field Camera 3 (WFC3) on the *Hubble Space Telescope* (*HST*) (another space-borne observatory). This selection of data provides a snapshot of the lens' radiation across a wide range of key wavelengths in the optical, near-IR, and mid-IR. Table 2.1 lists the telescope, instrument, and band with corresponding central wavelengths that were used to obtain photometry for our lenses.

A priority throughout this research has been to obtain a complete set of $K-$band imaging for all lenses. Given the expected redshift range of the lenses, their luminosities are likely to peak in the near-IR and so detecting them in the $K-$band is more probable than at shorter wavelengths. For this work, we have obtained photometric imaging in the $G-$, $R-$, $J-$ and $K-$bands, where appropriate. Access to *HST*, *Spitzer*, and DES imaging was granted, but not obtained exclusively for this work.

2.2.2 Data Reduction

Frequently data is released to the user after it has been processed through a data reduction pipeline. If the reduction is not adequate or it was not done, the user

Table 2.1: Summary of the multi-band photometry obtained for the SPT lenses across the optical, near-IR, and mid-IR. Note: In the case of slightly varying central wavelengths a " † " or " ‡ " identifies the corresponding telescope and instrument.

Telescope	Instrument	Band	λ (μm)
VLT	FORS2	G	0.47 (0.475†) [0.4720‡]
(†Gemini-S)	(†GMOS)	R	0.64 (0.63†) [0.6415‡]
[‡Blanco]	[‡DECam]	I	0.80 [0.7835‡]
HST	WFC3	F110	1.150
		F140	1.400
		F160	1.545
VLT	ISAAC	J	1.24
Gemini-S	FLAMINGOS2	K	2.16 (1.98-2.32†)
(†Magellan)	(†MMIRS)		
Spitzer	IRAC	CH1	3.550
		CH2	4.493

can manually do the reductions themselves or find an appropriate pipeline. Most data reduction procedures rely on the Image Reduction and Analysis Facility (IRAF) command *imcombine*. IRAF is a terminal-based software written by the National Optical Astronomy Observatory (NOAO) designed specifically for the reduction of astronomical images. The *imcombine* command allows you to combine/stack images in a variety of different ways and is the workhorse of most reduction pipelines. While the details of the data reduction process can vary, the basic principles remain the same. Here we briefly outline the steps used in reducing astronomical images.

Besides the science frames, there are two additional types of images that are required such that proper corrections can be applied during the data reduction process - dark frames and flat fields.

Dark frames are taken by shielding the sensors of any incoming light. Despite the lack of an incoming signal, thermal excitations on some pixels will lead to a charge build up. These so-called "hot pixels" can be as bright as some of the fainter sources in the science frames. Applying a simple threshold to the science frames can therefore lead to loss of information. Dark frames must have longer integration times than the science frames so that adequate charge build up can occur. While multiple shorter-integration-time dark frames can be combined to create a master dark frame, it is important to ensure that the noise of the dark frame remains less than that of the science frames, as it will otherwise increase the noise of the final product.

Flat fielding is the process of removing any pixel-to-pixel optical defects either due to variations in sensitivity, vignetting, scratches, dust, *etc.*. Flat fields can be taken of either a bright, out-of-focus light source or of the dusk or dawn sky. Typically multiple flat fields are taken and averaged to create a master flat field. From the flat fields a bad pixel mask can be created. This is a boolean image in which "bad" pixels are set to 1 and everything else is at 0. Bad pixels are flagged if the ratio between two flat fields is above a certain threshold from the median ratio, thereby suggesting an inappropriate response of the pixel. After the bad pixel mask is applied to the science frames, a linear interpolation of neighbouring pixels is frequently used to assign a new flux to the previous bad pixel.

Background sky subtractions are an additional important step in data reduction procedures especially in the near-IR in which the sky is quite bright. A simple method in which to create a background sky image is to stack the science images without the proper astrometry offsets. In this way an image of the background sky is created in which sources are averaged out. The background sky can then be subtracted from the science frames. Frequently a two step process is applied in which the previous step is followed by detecting and masking all objects in the science frames before stacking them once again without the proper astrometry offsets to create a second background sky image which subsequently gets subtracted from the science frames as well.

The general order in which data reduction occurs is as follows: 1) Combine dark frames to create a master dark. 2) Subtract the master dark from all science frames. 3) Combine flat fields to create a master flat. 4) Create a bad pixel mask from the flat fields. 5) Mask bad pixels in the science frames and in the master flat field. 6) Divide the science frames by the master flat field. 7) Subtract the background sky from the science frames. 8) Align the science frames with proper astrometry offsets and stack/combine them into the final product.

A large number of observations used in this work were reduced either by a pipeline prior to release to the user or by other members of the SPT-SMG collaboration before this work was started. All $J-$ and $K-$band data taken with the F2 camera on Gemini-S were reduced for this work specifically.

2.2.3 Astrometry Calibration

Astrometry calibrations, *i.e.* the positioning in the sky, are a critical initial step in photometry measurements after the data has been reduced. These calibrations are the matching of the right ascension (RA) and declination (Dec) of bright objects to their known position in the sky. RA and Dec are the coordinates on the celestial sphere that match Earth's longitude and latitude. One full rotation of Earth about its axis (*i.e.* in longitude) is 360° and takes 24 hrs. Therefore 1 hr of RA is equivalent to 15°. RA is given in hours, minutes, and seconds of time in the format hh:mm:ss while Dec is given in degrees, minutes, and seconds of arc in the format dd:mm:ss in the same way that latitudes are. RA values will always be positive whereas Dec values can be either positive or negative, *i.e.* north or south respectively of the celestial equator. The SPT sample of SMGs were named by their abbreviated position in the sky. They follow the template SPTXXXX-YY, where XXXX is the RA in hours and minutes and -YY is the Dec in degrees. Here the Dec is always negative as SPT observed the night sky from the South Pole and therefore can only access negative declinations.

Identifying the same object in multiple images taken with numerous telescopes across many different bands relies heavily on proper astrometry calibrations. Mismatched astrometry can lead to the misidentification of the object of interest. Poor alignment can also result in truncated light measurements. Astrometry calibrations are therefore a crucial first step. For this project they were done in one of two ways depending on the image.

For new $J-$ and $K-$band data that we observed using F2 on Gemini-S, for which the reduced images had no assigned coordinate system, an online tool was used (Principle Investigators: D. W. Hogg and D. Lang, `http://nova.astrometry.net`). Images with unknown coordinates can be uploaded and their "astrometry engine" will return the proper celestial coordinates to your image.

For the remainder of our data the images already had an assigned coordinate system. However, the astrometry frequently had to be calibrated manually. This was done using Graphical Astronomy and Image Analysis Tool (GAIA) (the "Graphical Astronomy and Image Analysis Tool") developed by the European Southern Observatory (ESO). It is an interactive image display tool which can be used to, among

other things, manipulate astronomical images and extract data. Manual astrometry calibrations consist of loading external catalogues containing the coordinates of known objects within the field of the image and shifting the image, "tweaking" the astrometry, so that the image coordinates and the catalogue coordinates of the known objects match. This is a manual, time consuming process, as the astrometry for each field has to match across all bands.

2.2.4 Photometry Calibration

Photometric calibrations are the next step in preparing useful images. Photometry is the science pertaining to the measurement of light intensity, the apparent brightness, of an object. Telescopes measure the flux density, the energy per unit area per unit time at a given frequency, of an object. In each wavelength band the transmission of light varies due to Earth's atmosphere, as discussed previously. The flux, or photometry, must therefore be calibrated. For some telescopes in some bands the raw data is stacked and photometrically calibrated before being released to the user. In the optical and near-IR this is generally not the case as the variability of the atmosphere is too great. The raw data must therefore be reduced by the user and both astrometrically and photometrically calibrated.

Historically, the brightness of objects in the optical range were defined by their magnitude instead of by a flux. The magnitude of an object is an inverse logarithmic scale of the flux of an object, where a decrease in brightness by a factor of 100 corresponds to an increase in magnitude of 5.0. Each difference in magnitude of +1.0 is therefore a factor of $\sqrt[5]{100} = 2.512$ fainter. The apparent magnitude at a given frequency, m_ν, and the flux density, S_ν, of an object are related via $m_\nu = -2.5 \log_{10} ({}^{S_\nu}/_{S_{\nu,0}})$, where $S_{\nu,0}$ is the reference flux for that frequency. The reference flux is telescope- and wavelength-dependent and corresponds to an apparent magnitude of zero. On the magnitude scale it is therefore referred to as the "zero point." The zero point is the parameter used to calibrate the image photometry to a universal magnitude system. Traditionally the star Vega has been used as the calibration star, as it is one of the brightest stars in the northern hemisphere. In the Vega magnitude system, the apparent magnitude of Vega is defined to be zero.

The AB magnitude system is another magnitude scale which has gained popularity over the years. Unlike the Vega scale which is relative to the brightness of the star Vega, the AB scale is an absolute scale and is based on flux measurements, $m_{\rm AB} = -2.5\log_{10}(S_\nu) - 48.60$ where S_ν is given in units of $\mathrm{erg\,cm^{-2}\,s^{-1}\,Hz^{-1}}$. For this work, the AB scale was used.

Zero Point Calibrations

External catalogues are once again used in this calibration step. The magnitudes of multiple objects in our images are compared to the magnitudes of the same objects in public catalogues. Any discrepancies between our magnitudes and the catalogue magnitudes results in a necessary adjustment of the zero point for our images. Approximately 10 objects were typically averaged over. Occasionally fewer objects had to be used as the external catalogues were limited in the number of objects that overlapped with our image. Once again, this is a manual, time consuming process.

The United States Naval Observatory (USNO) published a catalogue of objects observed in various optical bands. We therefore used the USNO catalogue when calibrating our $G-$ and $R-$band images. The Two Micron All Sky Survey (2MASS) was conducted in the near-IR. It was used to calibrate our $J-$ and $K-$band images.

For ground based telescopes, the zero point may vary slightly from night to night due to changing atmospheric conditions. While some variability is expected in the zero point, it should remain fairly consistent. Fig. 2.4 is a histogram of our zero points across the optical and near-IR bands we observed in. A gaussian was fit to each band and the mean and standard deviation of the gaussian are shown in the legend. For the near-IR bands, we find that observations conducted with ISAAC have a much narrower distribution of zero points compared to those conducted using F2. This is true both in the $J-$ and $K-$bands.

The large spread in $R-$band zero points when using the USNO catalogue for calibrations is indicative of poor calibration. While we tried to average over ~ 10 objects, the USNO catalogue frequently had significantly fewer objects available within the field of view of our image. This resulted, in some cases, in calibrations being done using just 2-3 objects. Furthermore, objects in the USNO catalogues are often saturated in our own images due to long exposure times. USNO calibrations are therefore

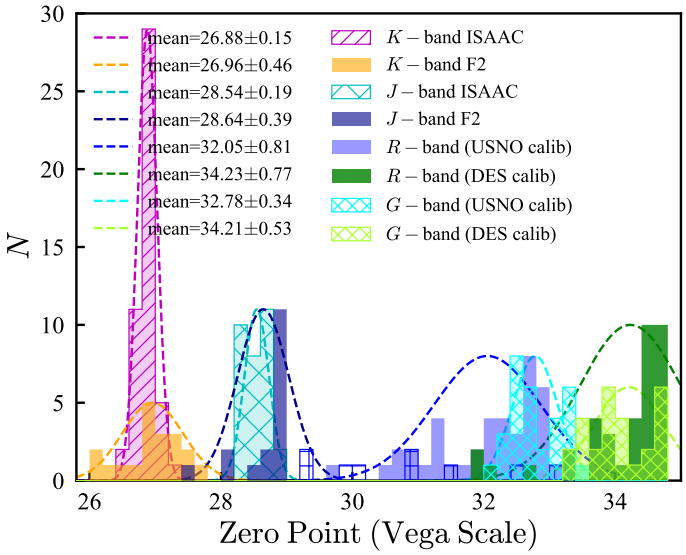

Figure 2.4: Zero point analysis. Near-IR bands are calibrated against 2MASS. Optical bands were originally calibrated to the USNO catalogue and later against DES.

unreliable for our $G-$ and $R-$bands. For this reason we switched to calibrating our images against DES images. While the photometric calibration of the DES images is uniform across its wide field, the images themselves are not deep and are unlikely to detect our fainter lenses. We therefore continue to use FORS2 $G-$ and $R-$band imaging for object detections, but calibrate them photometrically against the DES images. If FORS2 imaging is not available we include the DES imaging, as well as $i-$band DES imaging for all lenses.

Both the USNO and the 2MASS catalogues are in the Vega scale. Any measurements made using images calibrated to these catalogues must therefore be converted to the AB scale. DES as well as *Spitzer* images are calibrated to a common zero point on the AB scale before being released to the user. No further adjustments need to be made to these measurements. *HST* images are also released with a common zero point, this one on the ST scale. The ST scale is equivalent to the AB scale except that the flux density is expressed as the flux per unit wavelength (ST) as opposed to the flux per unit frequency (AB). It is important to note that the conversion from one scale to another is band-dependent. The difference in magnitude between the Vega, ST, and AB scale (where appropriate) are presented in Table 2.2.

Table 2.2: Image calibration and magnitudes conversion.
$m_{\rm Vega} = -2.5\log_{10}(S_\nu/S_{\rm Vega,0})$ $\quad [S_\nu] = [S_{\rm Vega,0}]$
$m_{\rm AB} = -2.5\log_{10}(S_\nu) - 48.60$ $\quad [S_\nu] = {\rm erg\,cm^{-2}\,s^{-1}\,Hz^{-1}}$
$m_{\rm ST} = -2.5\log_{10}(S_\lambda) - 21.10$ $\quad [S_\lambda] = {\rm erg\,cm^{-2}\,s^{-1}\,\AA^{-1}}$

Telescope	Band	Calibration system	$m_{\rm AB} - m_{\rm calibration}$
VLT/Gemini-S	G	Vega	-0.08
	R		0.21
DES	g & r & i	AB	-
HST	F110	ST	-1.62
	F140		-2.03
	F160		-2.24
VLT/Gemini-S	J	Vega	0.91
	K		1.85
Spitzer	CH1 & CH2	AB	-

Effects of Aperture and Source Size

In addition to proper calibrations, photometry measurements are dependent on aperture size. The aperture size is the diameter of the circle, usually given in number of pixels, centred on the object within which the light is measured. Determining the proper aperture size is crucial for accurate measurements. If the aperture is too small, light from the source will be truncated. Conversely, if the aperture size is too large, light from neighbouring sources may be inadvertently included. Furthermore, aperture sizes that are too large result in detections with decreased signal-to-noise values because of the increase in background noise being included in the object's flux. Determining the optimal aperture size is therefore critical.

Source-Extractor (SExtractor) is the leading program in the field that scans astronomical images, detects sources, and builds a catalogue of extracted parameters, including magnitudes (Bertin and Arnouts 1996). SExtractor and it's input configuration will be discussed in greater detail in Sect. 2.2.5. Here we will briefly discuss the different methods in which it extracts magnitudes for a source as outlined in the SExtractor user's manual v2.13 by Bertin.

There are four methods in which the magnitude of an object can be measured: isophotal, corrected-isophotal, fixed-aperture, and automatic-aperture. Isophotal magnitudes ($m_{\rm iso}$) are calculated by integrating all pixels above a certain detection threshold. This method yields magnitudes that are numerically larger (*i.e.* dimmer)

than the true magnitude due to a loss of flux in the wings of the object. However, the intensity profile of a star can be roughly approximated as a Gaussian, so the isophotal magnitude can be corrected ($m_{\rm isocor}$) to include the flux from the wings. This method is not very accurate for objects that do not fit a Gaussian profile well, and so is, for the most part, not used. The fixed aperture magnitude ($m_{\rm aper}$) is measured by integrating the flux of each pixel within a user-defined circular aperture. It is important for the user to input an aperture size that will encompass the whole object, without including neighbouring objects. Neighbouring objects that do fall within the aperture will be masked. Unfortunately, the reliability of this process is not quantified. Pixels within the aperture that fall below the background noise will be subtracted from the measured magnitude. The magnitude measured using the automatic aperture ($m_{\rm auto}$) is the most robust method. Here the objects are convolved with a Gaussian seeing and the aperture size is defined by the Kron radius (kr), where a Kron factor of $k = 2$ will include $\geq 90\%$ of the flux and a factor of $k = 2.5$ will include $\geq 94\%$ of the flux. The method remains just as reliable for objects with ellipticity.

Different types of analysis emphasize different aspects of the detected light. For example, galaxies will frequently have different morphologies, shapes and sizes, in different bands. Sometimes it may therefore be beneficial to measure the detected light in a defined physical region. Detecting 100% of the light is therefore not always the appropriate approach. However, it is critical to remain consistent within the analysis. In our analysis, comparing the detected light across multiple bands, it is important to measure the total light. To ensure that we are doing so we perform a curve of growth analysis. This consists of measuring the magnitude within an aperture as we increase the aperture size. Two example curve of growth plots are shown in Fig. 2.5 for SPT0103-56 and SPT0418-47. As we increase the aperture size, the magnitude initially decreases (*i.e.* the source is becoming brighter) since we are including more and more of the source in the measurement. Once the aperture encompasses the entirety of the source, we observe a plateau in the curve of growth line (as seen in the data in Fig. 2.5).

Magnitudes (horizontal dashed lines) and the corresponding aperture sizes (vertical dashed lines) for the isophotal (cyan) and automatic (magenta) methods have been overlain, as well as a full width at half max (FWHM) (black) magnitude and a

magnitude corresponding to the plateau (blue) of the curve. The plateau was determined by finding the data point whose following data point was within 0.1% of its own magnitude. This method is fairly ad hock, but does provide a good estimate of the total magnitude. For the 7 sources for which this analysis was done (only two shown), $m_{\rm iso}$ repeatedly suggested a fainter source than $m_{\rm plateau}$. Conversely, $m_{\rm auto}$ was comparable to $m_{\rm plateau}$.

In fact, finding the difference between $m_{\rm auto}$ and $m_{\rm plateau}$ and averaging across the four sources that were relatively isolated from their nearest neighbour, we find negligibly small deviations between the two magnitudes, $m_{\rm auto} - m_{\rm plateau} = 0.060 \pm 0.015$. For the remaining three sources where the immediate surroundings were more densely populated with additional objects, the difference between $m_{\rm auto}$ and $m_{\rm plateau}$ was larger, $m_{\rm auto} - m_{\rm plateau} = 0.17 \pm 0.15$, although still relatively small. This curve of growth analysis shows that $m_{\rm auto}$ is a good approximation of $m_{\rm plateau}$, the total

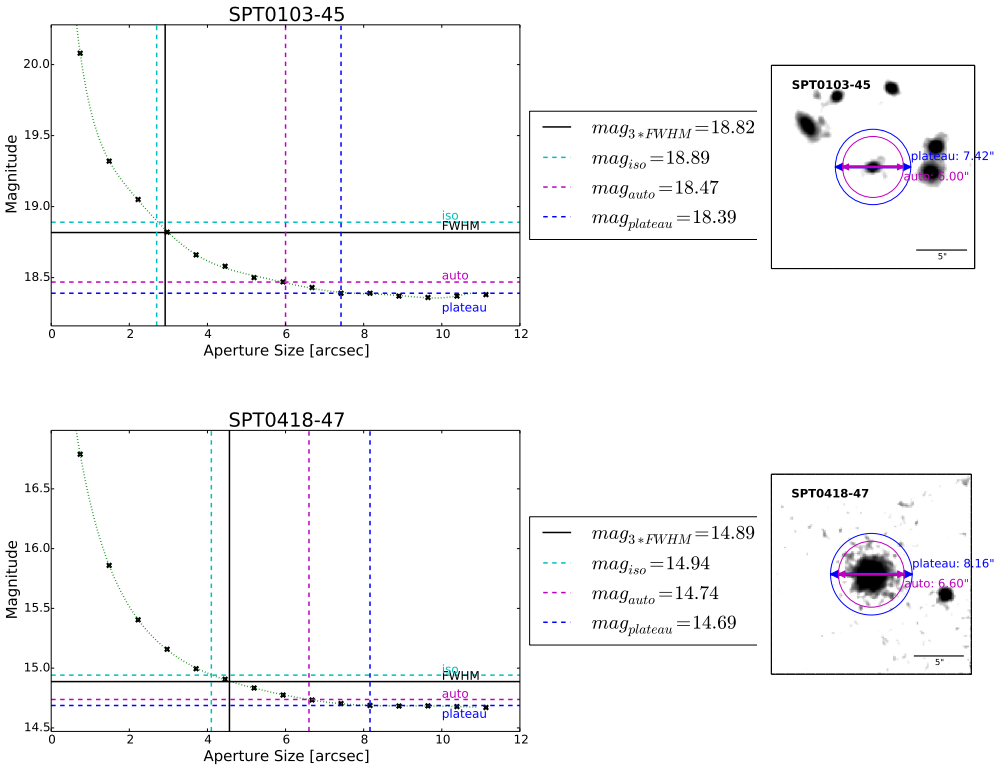

Figure 2.5: Example curve of growth analysis for a crowded field (SPT0103-45) and an isolated field (SPT0418-47). $m_{\rm iso}$ and $m_{\rm auto}$ are SExtractor parameters, $m_{\rm plateau}$ is calculated from the curve of growth line, and $m_{\rm 3*FWHM}$ is the magnitude within an aperture the size of 3*FWHM.

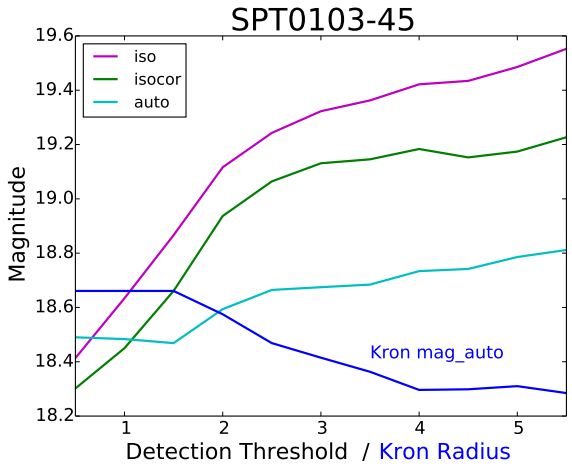

Figure 2.6: Detection threshold analysis for isophotal, corrected-isophotal, and automatic aperture magnitudes. For the automatic aperture, a similar analysis was done for an increasing Kron radius while the detection threshold was kept constant at 1.5.

magnitude, especially in the case of isolated sources. For more crowded fields, it is important to remain vigilant when measuring magnitudes.

For further analysis, we compared how $m_{\rm iso}$, $m_{\rm isocor}$ and $m_{\rm auto}$ are affected by detection thresholds, see Fig. 2.6. As the detection threshold increases, so does the magnitude for all three of the methods, indicating more and more flux is being left out, as is expected. We do, however, see that $m_{\rm auto}$ is less affected by detection thresholds than either $m_{\rm iso}$ or $m_{\rm isocor}$. This emphasizes that $m_{\rm auto}$ is a more reliable method in determining magnitudes, especially for dim objects. We have also plotted the effects on $m_{\rm auto}$ as the Kron radius is increased (blue) while keeping the detection threshold constant at 1.5. Here, increasing the Kron radius decreased the magnitude, *i.e.* a brighter source. This is to be expected as larger Kron radii should include larger percentages of the flux. The intersection of the two $m_{\rm auto}$ curves, suggests that a detection threshold and a Kron radius both between 1.5 and 2.5 is best. For this work, we have chosen to keep the detection threshold and the Kron radius at their respective default values, 1.5 and 2.5, while using $m_{\rm auto}$ as the "total" magnitude.

2.2.5 Extracting Photometry

We use the program SExtractor to create a catalogue of sources for each image. SExtractor has a dual-imaging mode, in which one image is the detection image

and a second image is the measurement image. For this method, sources are detected in the first images, the locations and aperture sizes are then duplicated for the second image, in which the magnitudes are subsequently measured and recorded. In this way, the created catalogue contains magnitudes of the measurement image while source locations are identical to those of the detection image. This is useful when observing an object in multiple bands - we are able to detect the object using the same location and aperture size across all images. To use SExtractor in dual-image mode, the two images need to be of the same size and shape, and, importantly, have the same pixel scaling. The pixel scale refers to the number of arcseconds per pixel in the image. If the pixel scale is the same, the aperture will cover the same physical extent in both images. It is therefore critical to manipulate the images first so that they have the same size, shape, and pixel scale.

SWarp

SWarp is a program that, among other capabilities, can regrid (resample) images to any arbitrary astrometric projection (Bertin et al. 2002), *i.e.* to any arbitrary pixel scale. This is crucial when using SExtractor in dual-imaging mode, the pixel scale, size, and shape of the two images need to be the same. SWarp is a program that can do all three simultaneously. We can manually set the image centre, by providing the coordinates (RA and Dec) to the object of interest for example (*i.e.* the lens), specify the number of pixels in the x and y direction to set the size and shape, and set the desired pixel scale for the output image. It is important to note that while the total flux of a source is conserved when changing the pixel scale, the flux per pixel is not. It is therefore important that the aperture size encompasses the entire source in all bands and does not truncate pixels and thus the flux. To ensure this, the detection image should be the one in which the physical extent of the source is greatest.

SExtractor

As mentioned earlier, SExtractor scans astronomical images, detects sources, and builds a catalogue of extracted parameters, including magnitudes (Bertin and Arnouts 1996). We use SExtractor in dual-imaging mode, detecting sources in one image and measuring magnitudes in another.

The majority of the configuration parameters are left at their default values, only a few are adjusted. Configuration parameters that are set to a common value across all bands when running SExtractor are the detection threshold (the number of standard deviations above the background that triggers a detection), the minimum detection area (the minimum number of adjacent pixels above the threshold required for a detection), the analysis threshold (the threshold above the background for FWHM determinations and galaxy separation), the pixel scale, and the Kron radius.

Parameters that vary from camera to camera are the gaussian filter applied to facilitate detections of faint objects and the seeing FWHM (the FWHM of the point spread function and therefore the best angular resolution achievable by the detector). The parameter that varies from image to image is the zero point. The $K-$band configuration file can be found in Appendix B as an example.

2.3 Spectroscopy

1D spectra were extracted from spectroscopic measurements for 25 lenses. These observations were conducted using the X-shooter camera on the VLT. X-shooter is a multi-wavelength ($300 - 2,500$ nm), intermediate resolution ($R \sim 4,000 - 17,000$, depending on wavelength and slit width) single-object spectrograph (Vernet et al. 2011). The spectra for our lenses are in Appendix C (left column). The observations and extraction of 1D spectra were done prior to this work.

As discussed earlier, elliptical galaxies are unlikely to have many emission features as there is a lack of dust in the interstellar medium. Furthermore absorption lines are likely to be faint. However, a couple of key absorption features should be detectable. These include the calcium H & K lines just below 400 nm and the G-band break at around 430 nm. These two sets of absorption features are the most commonly used in determining spectroscopic redshifts for ellipticals.

The [O II] line is the one emission feature that was considered in this work in detail, as it lies at 372.7 nm and, if present, is redshifted into our spectra. A strong [O II] line has been shown to suggest elevated star formation rates (*e.g.* Ly et al. 2012). The presence of a strong [O II] line could therefore indicate that the lens is not a passively evolving elliptical. We have searched our spectra for the [O II] line, fitting a gaussian if possible and extracting the equivalent width of the feature. The

gaussian fit of the [O II] line can also be found in Appendix C (right column). Further discussion of the equivalent width of the [O II] line will be done in Sect. 2.6.2.

2.4 Ancillary Data

The SPT-SMG sample is a source selected sample, *i.e.* SMG candidates are identified in the sub-mm. Unfortunately, SPT's resolution is poor, at $\sim 1'$. Most galaxies at redshifts $z \gtrsim 0.05$ will therefore likely appear as point sources and the possibility of misidentification is non-negligible (Vieira et al. 2010). Higher resolution imaging was therefore required and extensive follow-up observations on numerous telescopes were commissioned. With the advent of Atacama Large Millimeter/submillimeter Array (ALMA) (an interferometric telescope located in the Atacama Desert of Chile), high spatial resolution imaging ($\sim 1''$, a factor of $60\times$ better than SPT) as well as spectroscopic data were taken (Vieira et al. 2013; Weiß et al. 2013; Strandet et al. 2016). The tell-tale Einstein rings were observed in the imaging and redshifts determined from the spectra. With precise ALMA locations, follow-up observations in the optical and near-IR could be conducted to search for possible optical counterparts to complete the gravitational lensing picture. In this work, only lenses whose accompanying SMG was imaged by ALMA are considered. Additionally the lens must have been observed in the $K-$band specifically (with the exception of four lenses). The resulting SPT sample consists of 56 gravitational lenses.

2.5 Comparison Samples

2.5.1 SLACS

The Sloan Lens Advanced Camera for Surveys sample is selected spectroscopically from the magnitude-limited SDSS database. Selection criterions are an absorption-dominated continuum at lower redshifts and nebular emission lines such as the Balmer Series, [O II] $3,727$ Å, and [O III] $5,007$ Å lines at higher redshifts (Bolton et al. 2008). Additional requirements are clear features characteristic to strong lensing in the imaging. Their photometric analysis relies on *HST* $I-$band imaging, with further *HST* optical and near-IR imaging available for a subset of the sample. The complete SLACS sample consists of 85 "certain" lenses and 13 "likely" lenses, as of their Paper

IX (Auger et al. 2009). A benefit of their spectroscopic selection process is that the lens and source redshift are immediately known. SLACS lens redshifts range from 0.063 to 0.513 with a median redshift of 0.19 (Auger et al. 2009). Unfortunately, the magnitude-limited nature of the parent SDSS database results in a systematic relation between the lens redshift and mass: galaxies must be more luminous (and therefore more massive) at higher redshifts in order to be detected. The elimination of this bias is a primary benefit of the SPT sample to the SLACS sample.

2.5.2 BELLS

The BOSS Emission-Line Lens Survey was initiated by the SDSS-III collaboration and is therefore in many ways an extension of the SLACS sample selected from SDSS-I. Data reduction methods, lens modelling techniques, and lens candidate selection procedures and classifications are similar between SLACS and the BELLS. The primary difference is that BELLS probes higher-redshift lenses ($0.4 \lesssim z_{\rm lens} \lesssim 0.7$) and consequently higher-redshift sources ($z_{\rm source} \lesssim 1.52$) Brownstein et al. (2011). However, *HST* $I-$band imaging identifies the lenses to span the same stellar mass range as the SLACS sample (10^{11} $\mathrm{M}_{\odot} \lesssim M^{*} \lesssim 10^{12}$ $\mathrm{M}_{\odot}$). The BELLS and SLACS sample therefore trace the evolution of a single massive galaxy population. Of the 44 lens candidates in BELLS, 25 are identified as grade A lenses (multiply imaged) and 11 as grade B lenses (multiply imaged but with faint or contaminated counterparts).

2.5.3 Herschel Space Telescope lensed SMG Sample

The *Herschel* Space Telescope conducted two surveys, *Herschel*-Astrophysical Terahertz Large Area Survey (H-ATLAS) and *Herschel* Multi-tiered Extragalactic Survey (HerMES), from which 104 lens candidates were selected. The Submillimeter Array (SMA) subsequently confirmed 30. Both *Herschel* surveys were conducted in the sub-mm with a flux cut-off of $S_{500\,\mu\mathrm{m}} > 100$ mJy for lens candidates. Both the SMA sub-sample and the *Herschel* sample in general, unlike SLACS, are source-selected. This means that they are able to probe lenses at higher redshifts as well as less massive lenses. Lens-selected samples (*i.e.* optical surveys such as SLACS and BELLS) are inherently biased towards brighter lenses than source-selected samples (*i.e.* sub-mm surveys such as *Herschel* and our own SPT survey) (Bussmann et al. 2013). A major

consequence of observing higher redshift lenses though, is the difficulty in obtaining spectroscopic redshifts for lenses above $z > 1$.

2.6 Results

In this section the redshifts and various astrophysical parameters of the 56 lenses will be discussed and placed into context with the comparison samples just mentioned. The analysis focuses on 1) the redshift distribution and lensing geometry, 2) identifying the galaxy type - *i.e.* is there any evidence to suggest the lens is something other than a passively evolving elliptical galaxy? and 3) the mass composition (*i.e.* light-to-dark matter ratios) and respective mass distributions.

Thumbnails of the calibrated multi-band imaging for each lens can be found in Appendix D, an example of which is shown in Fig. 2.7. In the top left corner of each thumbnail, the camera and band of the grey-scale image of the lens are identified. The blue-green ALMA contours of the SMG identify the lens as the object the contours are centred on and frequently display the tell-tale signs of gravitational lensing - Einstein rings or arcs with counter-images. While the presence of such features is a clear sign of gravitational lensing, the lack of them does not preclude a lensing system. Poor alignment along the line-of-sight can lead to counter-images too faint to detect. For $G-$ and $R-$band, FORS2 images are displayed if available otherwise DES images are used.

The extracted AB-magnitudes from observations commissioned for this work or by the SPT-SMG collaboration are reported in Table 2.3. If the lens was not detected, the image background is reported as a lower limit. DES photometry for $g-$, $r-$, and $i-$band can be found in Appendix E.

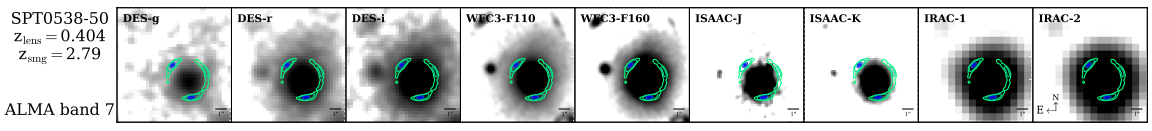

Figure 2.7: Example multi-band thumbnail imaging in grey-scale, for SPT0538-50. ALMA contours (blue-green) of the SMG are overlain and identify the lens as the object it is centred on.

Table 2.3: Multi-band photometry, $m_{\rm AB}$. Note: See Table 2.2 for definition of the photometric bands.

ID	G	R	J	K_s	CH1	CH2
SPT0002-52	-	> 23.61	-	19.2 ± 0.03	-	-
SPT0020-51	23.8 ± 0.04	-	20.1 ± 0.1	19.2 ± 0.06	-	19.4 ± 0.2
SPT0027-50	-	> 23.70	21.5 ± 0.3	19.7 ± 0.07	-	18.6 ± 0.1
SPT0103-45	> 24.72	23.2 ± 0.06	21.6 ± 0.2	20.2 ± 0.06	18.6 ± 0.1	18.3 ± 0.1
SPT0106-64	-	-	18.8 ± 0.04	18.5 ± 0.03	-	-
SPT0109-47	> 25.96	23.1 ± 0.03	-	20 ± 0.05	-	-
SPT0113-46	> 24.52	22.7 ± 0.04	20 ± 0.09	19 ± 0.03	18.6 ± 0.1	18.7 ± 0.2
SPT0114-59	-	-	21.8 ± 0.1	21.1 ± 0.2	-	-
SPT0125-47	21.4 ± 0.003	19.9 ± 0.001	17.9 ± 0.01	17.3 ± 0.009	17.7 ± 0.1	17.6 ± 0.09
SPT0125-50	-	20.8 ± 0.006	18.7 ± 0.04	18 ± 0.02	18.4 ± 0.1	18.6 ± 0.1
SPT0147-64	-	-	20.5 ± 0.06	19.8 ± 0.06	-	-
SPT0150-59	-	-	21.3 ± 0.05	20.2 ± 0.06	-	-
SPT0155-62	-	-	> 22.76	22 ± 0.1	-	-
SPT0202-61	-	> 24.28	21.2 ± 0.1	20.4 ± 0.07	-	-
SPT0243-49	> 24.39	23.8 ± 0.05	> 21.74	21.1 ± 0.2	20.8 ± 0.4	20.7 ± 0.4
SPT0245-63	20.9 ± 0.003	19.8 ± 0.002	-	17.8 ± 0.01	-	-
SPT0300-46	> 25.04	> 22.38	-	> 18.36	-	-
SPT0311-58	-	-	-	22.3 ± 0.4	21.2 ± 0.005	21.4 ± 0.006
SPT0319-47	> 24.11	-	21 ± 0.2	20.5 ± 0.1	20.1 ± 0.3	19.9 ± 0.3
SPT0345-47	-	-	23.3 ± 0.6	23 ± 0.6	-	-
SPT0346-52	-	> 23.58	> 23.55	21.6 ± 0.3	20.8 ± 0.4	20.4 ± 0.3
SPT0403-58	23.4 ± 0.04	23 ± 0.03	-	21.5 ± 0.1	-	-
SPT0404-59	> 25.15	23.8 ± 0.04	-	20.9 ± 0.1	-	-
SPT0418-47	-	19.4 ± 0.003	17.7 ± 0.02	17.5 ± 0.02	18 ± 0.1	18.1 ± 0.1
SPT0441-46	> 24.48	22.4 ± 0.01	20 ± 0.07	19.1 ± 0.03	19.1 ± 0.2	19.6 ± 0.2
SPT0452-50	> 24.89	> 24.10	-	20.5 ± 0.1	-	-
SPT0459-58	-	23.7 ± 0.09	21.1 ± 0.2	> 19.82	20.7 ± 0.4	20.4 ± 0.3
SPT0459-59	-	22.7 ± 0.06	-	19.5 ± 0.04	19 ± 0.2	19.2 ± 0.2
SPT0512-59	-	-	20.1 ± 0.1	18.6 ± 0.03	-	17.7 ± 0.1
SPT0516-59	-	-	21.6 ± 0.07	20.5 ± 0.09	20 ± 0.3	20 ± 0.3
SPT0529-54	-	-	-	-	-	17 ± 0.07
SPT0532-50	-	-	22 ± 0.2	20.1 ± 0.04	20.1 ± 0.3	-
SPT0538-50	-	-	18 ± 0.01	17.3 ± 0.008	17.6 ± 0.1	17.5 ± 0.09
SPT0544-40	-	-	22 ± 0.08	20.8 ± 0.04	-	-
SPT0551-48	> 26.38	> 24.13	20.9 ± 0.04	19.3 ± 0.05	-	-
SPT0552-42	-	> 23.36	21.3 ± 0.09	> 19.11	-	-
SPT0555-62	-	-	18.7 ± 0.009	17.8 ± 0.009	-	-
SPT0604-64	-	19.4 ± 0.006	18.1 ± 0.008	17.5 ± 0.01	-	-
SPT0625-58	-	> 22.98	21.1 ± 0.06	20.1 ± 0.07	-	-
SPT2008-58	-	-	20.3 ± 0.02	20.4 ± 0.06	-	-
SPT2031-51	> 24.48	22.4 ± 0.01	20 ± 0.1	19 ± 0.03	18.6 ± 0.2	18.4 ± 0.1
SPT2048-55	> 26.02	> 24.52	-	20.9 ± 0.09	-	-
SPT2101-60	-	-	18.6 ± 0.01	17.9 ± 0.01	-	-
SPT2103-60	-	23.4 ± 0.03	20.3 ± 0.1	19.2 ± 0.04	19 ± 0.2	-

ID	G	R	J	K_s	CH1	CH2
SPT2132-58	-	-	20.9 ± 0.1	20.4 ± 0.08	-	-
SPT2134-50	> 24.42	22.6 ± 0.03	19.8 ± 0.07	18.9 ± 0.03	18.7 ± 0.2	18.7 ± 0.1
SPT2146-55	> 25.05	> 24.94	21.9 ± 0.4	21 ± 0.1	19.8 ± 0.3	19.6 ± 0.2
SPT2147-50	> 25.02	22.4 ± 0.02	19.6 ± 0.1	18.9 ± 0.06	18.6 ± 0.1	18.7 ± 0.2
SPT2307-50	-	-	-	20.8 ± 0.2	20.6 ± 0.03	20.8 ± 0.04
SPT2311-54	-	-	-	-	20.1 ± 0.3	20 ± 0.3
SPT2319-55	-	-	20.9 ± 0.1	20 ± 0.07	20.4 ± 0.3	20.5 ± 0.3
SPT2335-53	> 25.59	> 24.34	-	21.9 ± 0.4	22.2 ± 0.05	22.2 ± 0.05
SPT2340-59	18.2 ± 0.001	17.4 ± 0.001	-	16.2 ± 0.009	16.1 ± 0.05	16.5 ± 0.05
SPT2349-50	22.8 ± 0.009	21.4 ± 0.006	19 ± 0.04	18.7 ± 0.03	19.4 ± 0.01	19.1 ± 0.01
SPT2354-58	-	18.8 ± 0.003	18.4 ± 0.02	18 ± 0.03	18.2 ± 0.1	17.8 ± 0.1
SPT2357-51	> 24.19	> 23.70	-	-	20 ± 0.3	19.6 ± 0.2

2.6.1 Redshift Distribution

One of the primary advantages of the source-selected SPT sample of gravitational lensing systems is that SMGs are detected independent of their redshift. We hypothesize that the redshift distribution of the corresponding lenses therefore provides a more comprehensive view of gravitational lenses as compared to those found in lens-selected surveys such as SLACS and BELLS, which have stringent limits on their lens redshifts ($0.063 < z < 0.513$ and $0.4 \lesssim z \lesssim 0.7$ respectively) due to selection effects.

Fig. 2.8 shows the spectroscopic redshift distribution for the SPT lenses in shaded red, the SLACS sample in purple, the BELLS sample in grey, and the *Herschel* sub-sample in green. While the SLACS and BELLS surveys have narrow, low-redshift distributions, the source-selected *Herschel* sub-sample spans a redshift range nearly identical to our own. The highest spectroscopic redshift for the SPT sample is 1.218 while *Herschel*'s highest redshift is 1.35. This gives credence to our hypothesis that source-selected surveys probe lenses independent of redshift constraints.

Unfortunately only a subset of the SPT lenses have spectra from which robust redshifts can be determined. The remainder either did not display strong enough features to accurately determine redshifts from, or were too faint to attempt spectroscopic observations as it would require long, costly integration times. As a consequence we determine single-band photometric redshifts using the $K - z$ relation. The empirical relation found by Willott et al. (2003) is a second order polynomial of $\log z$ and was derived from galaxies whose redshifts spanned as high as $z \sim 4$. We cannot justify applying the same fitting to our own lenses as they are at lower redshifts and occupy

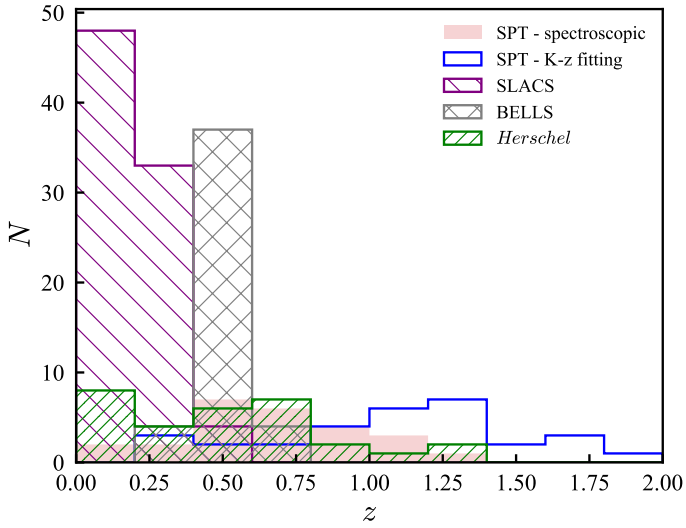

Figure 2.8: Lens redshift distribution. Spectroscopic redshifts for the SPT sample are in shaded red while the $K-z$ fitting redshifts are outlined in blue. Photometric redshifts from the $K-z$ fitting suggests a broader redshift distribution for the lenses as well as a higher median redshift.

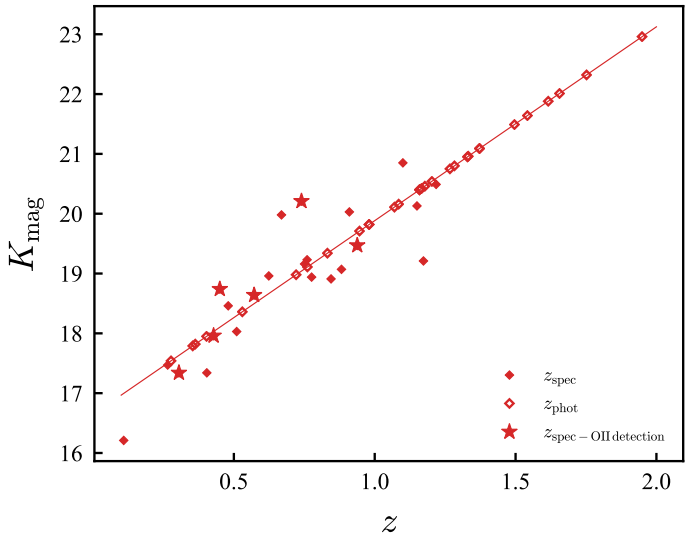

Figure 2.9: $K-$band magnitude as a function of redshift. A linear regression (solid red line) is applied to lenses with spectroscopic redshift (solid diamonds). $K-z$ redshifts (open diamonds) are calculated for lenses without spectroscopic redshifts. Lenses with significant [O II] detections are identified by star symbols.

a space in which a linear-correlation between the two parameters is better suited. We instead use the lenses for which we have spectroscopic redshifts and fit a simple linear regression to the $K-$band magnitude and the redshift, $K = 3.24z + 16.64$. We then apply the relation to all $K-$band magnitudes and calculate photometric redshifts. Fig. 2.9 plots the $K-$band magnitude as a function of redshift. Spectroscopic redshifts (of which there are 25) are shown as solid diamonds while photometric $K-z$ redshifts are shown as open diamonds. (The stars are used to identify lenses with strong [O II] detections and will be discussed in Sect. 2.6.2) In all future figures in this chapter the same redshift differentiation will apply to the SPT lenses - solid diamonds are used for lenses with spectroscopic redshifts while open diamonds are used to identify $K-z$ fitting photometric redshifts and stars highlight the lenses with strong [O II] detections.

In an effort to determine the credibility of the photometric redshifts we also calculated $z_{\rm phot}$ for lenses that had spectroscopic redshifts and compared the two. This comparison is shown in the left panel of Fig. 2.10. The red diamonds are photometric redshifts calculated from our $K-z$ relation while the blue diamonds are photometric redshifts determined from the multi-band SED fitting software EAZY. (EAZY fitting was conducted by Kedar Phadke, a graduate student at University of Illinois, using multi-band photometry provided from this work.) The dashed lines identify the root mean square (RMS) of the photometric redshifts to the one-to-one line (solid black). The RMS for the $K-z$ determined redshifts is noticeably smaller than that from the EAZY determined redshifts. This validates our decision to continue using single-band photometric redshifts ($K-z$ redshifts) as opposed to multi-band SED fitting redshifts (EAZY), which uses more data to attempt to determine a redshift, however, has very stringent requirements on photometry accuracy, introduces degeneracies, and in our case is therefore unjustified.

In the right panel of Fig. 2.10 we compare the ratio of the EAZY to $K-z$ redshifts. By segregating those lenses for which spectroscopic redshifts are known (solid diamonds) and for those where they are not (open diamonds) we find no marked agreement in photometric redshifts between the two sub-samples. The RMS, calculated with respect to the nominal ratio of $z_{\rm EAZY}/z_{K-z} = 1$, is high for both sub-samples.

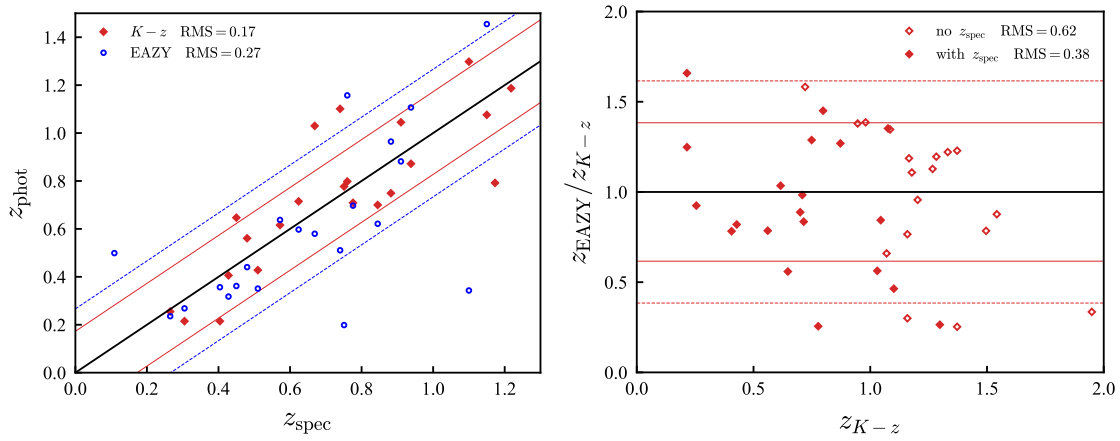

Figure 2.10: Redshift comparison between spectroscopic and photometric redshifts. *Left:* Photometric redshifts determined via two methods, $K-z$ fitting (red diamonds) and EAZY fitting (blue circles). The RMS for the scatter of both photometric redshift determinations is given. *Right:* EAZY photometric redshift as a function of $K-z$ photometric redshift. SPT lenses which have spectroscopic redshifts are shown as solid red diamonds, lenses with photometric redshifts are shown as open red diamonds.

The RMS is 0.38 and 0.62 for lenses with and without spectroscopic redshifts, respectively. The elevated RMS value for the sub-sample without spectroscopic redshifts is likely caused by the faint lenses it contains, the primary reason why spectroscopic redshifts could not be determined for them. The analysis of the two plots in Fig. 2.10 dictates that all further work rely on photometric redshifts determined from the $K-z$ relation calculated.

The earlier redshift distribution plot, Fig. 2.8, includes these photometric redshifts as well (blue outline). The photometric redshifts indicate that gravitational lenses can be found at higher redshifts than the spectroscopic data would suggest. This is quite possible as these high-$z_{\rm phot}$ values correspond to lenses with faint $K-$band magnitudes, which requires either that the lens is intrinsically not bright or it is at greater distances from us. This is a further reason in continuing to segregate spectroscopic and photometric redshifts (solid versus open symbols in plots). In our sample galaxies with spectroscopic redshifts not only have robust redshifts that provide confidence in continuing analysis, but they are generally brighter. They are therefore worth considering separately in more detail.

An additional diagnostic that we explored is the lensing geometry - we considered the difference in source and lens redshift as a function of lens redshift, see Fig.

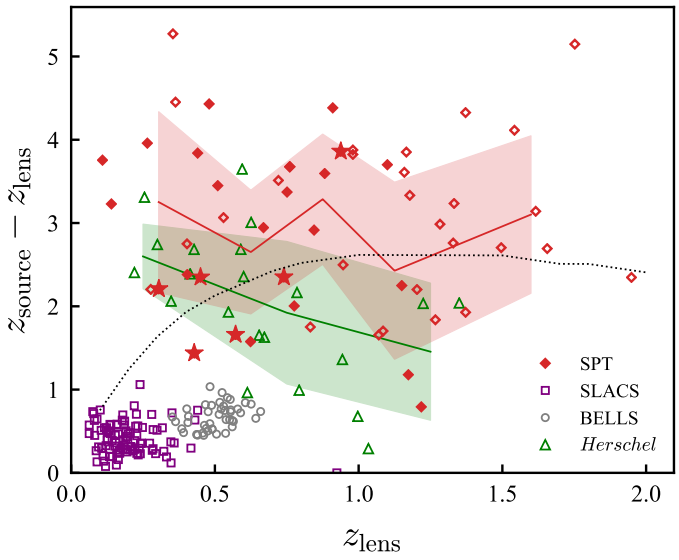

Figure 2.11: Gravitational lensing redshift geometry - difference in source and lens redshift as a function of lens redshift. Solid red and green lines are running averages for the SPT and *Herschel* samples, respectively, with the RMS drawn as a shaded region. Dotted black line represents a simplified "ideal" geometry. SPT lenses which have spectroscopic redshifts are shown as solid red diamonds, lenses with photometric redshifts are shown as open red diamonds.

2.11. The SLACS (purple squares) and BELLS (grey circles) sample occupy the low-z regime and individually do not present any strong trends. Both the *Herschel* sub-sample (green triangles) and our own SPT lensing systems (red diamonds) have significantly higher source redshifts than either SLACS or BELLS even in the same $z < 0.5$ range. It is important to note that the small number of lensing systems with $z_{\rm source} - z_{\rm lens} < 1$ in both the *Herschel* and SPT sample is expected. Both surveys identify lensing systems by conducting a blind search of SMGs in the sub-mm. However, the negative K-correction from which these observations benefit only takes affect past $z \sim 1$. Thus, a selection effect of sub-mm selected SMGs is high-z sources, we do not expect to detect many SMGs at low redshift. We conclude that lens-selected surveys only sample the closest (*i.e.* low-z) gravitational lensing systems whereas source-selected surveys extend that view into a higher redshift regime.

A running average (solid green and red lines) and the RMS (shaded regions) for the *Herschel* sub-sample and SPT lenses, respectively, are also drawn in Fig. 2.11. We find that, on average, the SPT lensing systems have a larger source-to-lens redshift difference at all redshifts compared to the *Herschel* systems. The difference

in source-to-lens redshift for the *Herschel* systems decreases slightly with increasing lens redshift, implying that the source redshifts are not increasing proportionally with the lens redshifts. This is due to their selection wavelengths ($250 - 500\,\mu$m), which preferentially selects sub-mm sources in the redshift range $1 < z_{\rm source} < 4$ (Bussmann et al. 2013; Negrello et al. 2017a), as opposed to our own SPT lensing systems in which the redshift distribution for the SMGs is $2 < z_{\rm source} < 6$ (Vieira et al. 2013). The difference in source-to-lens redshift for the SPT lensing systems appears to remain roughly constant as the lens redshift increases.

Lastly, we included a simple model (dotted black line in Fig. 2.11) for the preferred lensing geometry, in which the lensing amplification is maximized for a given geometry. In the case of on-axis geometry (refer to Eq. 2.5) and for a constant lens mass, the Einstein radius is at a maximum when the root of the distance ratio $\left(D_{\rm ls}/D_{\rm l}D_{\rm s}\right)^{1/2}$ is maximized. As we stepped through a range of lens redshifts, we determined the "ideal" source redshift. While the root of the distance ratio has no turn-over and therefore no explicit maximum, it does plateau. We defined our maximum to be 95 % of the plateau value. While we are presenting this trend as the preferred lensing geometry, it does not take a number of critical factors into account. These include the source and lens number densities as a function of redshift as well as variations in the lens mass. As mentioned earlier, the source number density is expected to fall with increasing redshift past $z \sim 4$. Conversely, the lens number density is expected to rise slightly, specifically, more massive lenses are expected at high-z whereas the intermediate mass lenses are found at lower-z (Cirasuolo et al. 2010). We do not delve further into these number densities. Lastly, the lens mass distribution is one of the astrophysical results we consider in more detail in Sect. 2.6.3.

2.6.2 Astrophysical Properties - Galaxy Type

In an effort to characterize the types of galaxies responsible for gravitational lensing we consider the colour of the galaxy (determined from magnitude differences) and the equivalent width (EW) of the [O II] emission line. The colour of a galaxy informs about the stellar population of said galaxy, which is indicative of galaxy type. The equivalent width is the ratio of the line flux to the continuum and is, as mentioned earlier, linked to star formation. The presence of the [O II] line is therefore suggestive

of an actively evolving galaxy (*i.e.* spiral galaxies or galaxies undergoing mergers) as opposed to passively evolving ellipticals. We also empirically analyze the galaxy morphology - visually classifying galaxies as ellipticals, disc-like spirals, or mergers. Appendix F contains a short description of all lenses.

From the visual inspection of spatial shape, we have identified three lenses as spiral galaxies due to clear visual signs of a central bulge and a disc (SPT0125-47, SPT0555-62, and SPT2101-60) as well as two further lenses as likely disc-like galaxies (SPT0345-47 and SPT2146-55) in which the evidence is less robust (only slightly visible in the *HST* imaging). We also identified two lenses (SPT0103-45 and SPT0243-49) with evidence of a tidal tail, indicative of an ongoing merger, and two with a possible companion galaxy (SPT2349-50, SPT2354-58) which can also result in star formation activity. These lenses are listed in Table 2.4 - a summary of those lenses which exhibit possible evidence for active star formation.

Colour-Magnitude Diagrams

The colour of a galaxy refers to the difference in magnitude (or equivalently the flux ratio) between two bands. We considered two colours, $J-K$ and $R-K$, in the left and right panels respectively of Fig. 2.12. Diamonds were used when the lens was detected in both bands. Triangles were used when the lens was not detected above the noise of the image, either because the lens was too faint in that band or because the image was not deep enough, *i.e.* the noise was too high. A lower limit of the magnitude was used instead. If the lens was not detected in the $K-$band then the colour is an upper limit in the colour-magnitude diagram. Conversely, if the lens was not detected in the $J-$ or $R-$band then the colour is a lower limit. The solid black curve represents the colour of a typical 5 Gyr. elliptical galaxy, determined from the SED template created by Polletta et al. (2007). The template models the effects of dust, stellar populations, age, metallicity, and other parameters on the spectral energy distribution of a typical elliptical galaxy. The model is calibrated using data of local ellipticals. For this work, we determine the colour by extracting the magnitude of the SED template at the two relevant bands. By redshifting the template from $z = 0-2$ and extracting the magnitudes in the same observed-frame bands, we identify how the colour changes with redshift. Any lenses whose colour falls above the template

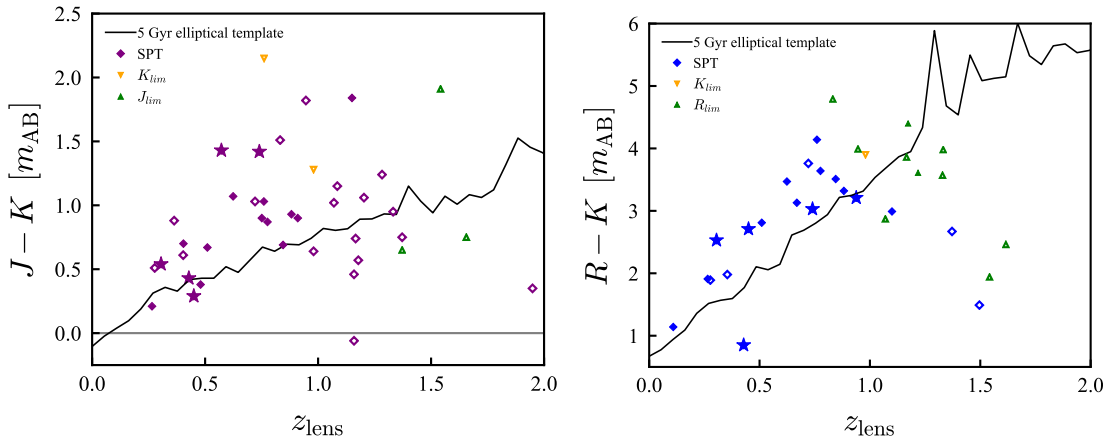

Figure 2.12: Colour-Magnitude Diagrams. Difference in $J-$ and $K-$band magnitude (*left*) and difference in $R-$ and $K-$band magnitude (*right*) as a function of redshift. Lenses which have spectroscopic redshifts are shown as solid symbols, lenses with photometric redshifts are shown as open symbols. Triangles indicate when the lens was not detected in a given band and a limit was used. Stars indicate lenses with significant [O II] detections. The solid black line represents the colour for the SED template of a typical 5 Gyr. elliptical galaxy created by Polletta et al. (2007).

curve are redder than a typical elliptical galaxy, *i.e.* the lens is brighter at longer, redder wavelengths. Conversely, lenses that fall below the template are bluer, *i.e.* the lens is brighter at shorter, bluer wavelengths than a typical elliptical galaxy.

In the left panel we find that while there are a number of lenses that are redder than the template (with differences between the template and lens $J-K$ colour greater than 0.5 magnitudes) and a couple that are bluer (by the same amount), predominantly the colour of the SPT lenses follow the slope of the template. We find that $\sim$ 74 % of all lenses lie within 0.5 magnitudes of the template, similarly ($\sim$ 76 %) if we only consider lenses with spectroscopic redshifts and robust detections in both bands. Lenses whose colour is a red upper limit (*i.e.* yellow triangles above the template) may not be as red as the limit would suggest and were excluded from these percentages. A redder lens can suggest an elliptical with an older stellar population or higher metallicity. Alternatively, it can also be suggestive of a dusty, star-forming galaxy in which the interstellar dust absorbs the shorter wavelength light. A bluer lens suggests a younger stellar population, implying ongoing star formation. Lenses that are redder and have additional evidence of star formation or are bluer than the template are listed in Table 2.4.

Table 2.4: Evidence for active star formation. Brackets in the visual morphology column indicates that the disc-like feature is only visible in HST imaging. Brackets in the colour column indicates that the colour is an upper limit red or a lower limit blue and therefore likely not as red or blue as suggested. Lenses with multiple results suggesting elevated star formation rates are identified in bold.

Lens	Visual Morphology	$J-K$ > 0.5 mag	$R-K$ > 1 mag	[O II] EW
SPT0103-45	tidal tail or spiral arm	red		detection
SPT0125-47	central bulge with disc		red	detection
SPT0243-49	tidal tail		blue	
SPT0345-47	(central bulge with disc)	blue		
SPT0346-52		(red)	(blue)	
SPT0403-58			blue	
SPT0459-59				detection
SPT0512-59		red		detection
SPT0555-62	central bulge with disc	red		
SPT0625-58			(blue)	
SPT2008-58		blue		
SPT2048-55			(blue)	
SPT2101-60	central bulge with disc			
SPT2146-55	(central bulge with disc)			
SPT2335-53			(blue)	
SPT2349-50	possible companion galaxy			detection
SPT2354-58	possible companion galaxy		blue	detection

In the right panel we once again find that for the majority of the lenses the slope of the $R-K$ colour matches that of the elliptical template. We find that ~ 75 % of all lenses lie within 1 magnitude of the template, which once again changes marginally (~ 80 %) if we only consider lenses with spectroscopic redshifts and robust detections in both bands. The accepted scatter was increased to 1 magnitude because higher variability is expected in $R-K$ colours compared to $J-K$. Lenses whose colour is a blue lower limit (*i.e.* green triangles below the template) may not be as blue as the limit would suggest and were excluded from these percentages. Once again, Table 2.4 lists those lenses whose colour is either red with additional evidence of star formation or blue.

It is important to note that different stellar populations and metallicities affect the $J-K$ and $R-K$ colours differently. Galaxies therefore may not appear blue (or red) in both colour-magnitude diagrams. From the visual morphology and the

colours of the galaxies, we conclude that there is some evidence of star formation in ~ 30 % of the lenses.

[O II] *Equivalent Widths*

The equivalent width of a spectral line is the ratio of its line flux to its continuum flux. It is the width of a rectangle whose height is that of the continuum and which has an equivalent area to the spectral line. For this work we focused on the forbidden-line doublet associated with singly-ionized oxygen [O II]. They have rest-wavelengths of 372.7 nm and 372.9 nm and have been suggested as an indicator for elevated star formation activities (Kennicutt 1998; Ly et al. 2012). Only stars more massive than ~ 20 $M_\odot$ (short-lived O & B type stars) will produce photons energetic enough to ionize metals in surrounding gas clouds (Calzetti 2012). Forbidden metal lines such as the [O II] doublet therefore trace the ionizing photons from young, hot stars and, consequently, the star formation rate.

In this work we treat the two lines as one because the resolution of our spectra is too low to resolve them. Appendix C shows the full spectrum on the left column and the spectrum centred on the [O II] line on the right for those lenses for which we have spectra. For each spectrum an attempt was made to fit a gaussian to the [O II] line. If the area of the gaussian exceeded 2.5×RMS, we considered the fit robust. The mean, standard deviation, area, EW, and FWHM of the gaussian as well as the RMS of the continuum are listed in the top left corner of the figures. Six of the spectra display strong [O II] lines - SPT0103-45, SPT0125-47, SPT0459-59, SPT0512-59, SPT2349-50, and SPT2354-58 with equivalent widths of (0.6 ± 0.2), (2.3 ± 0.3), (3.8 ± 0.5), (1.8 ± 0.7), (1.3 ± 0.2), (5.1 ± 2) Å respectively, where the error is the ratio of the RMS to the intensity of the continuum. These six lenses are labelled as having "some activity" in Fig. 2.13, which plots the equivalent width as a function of redshift. Lenses for which the gaussian fit was not robust are labelled as "dead ellipticals," *i.e.* they are not actively forming stars and are evolving passively. If a robust detection was not made, an upper limit is given, the ratio of the RMS to the continuum multiplied by the channel width.

The six lenses with clear [O II] detections are identified by a star symbol in previous figures. If we consider the colour-magnitude diagram once more, Fig. 2.12, a blue

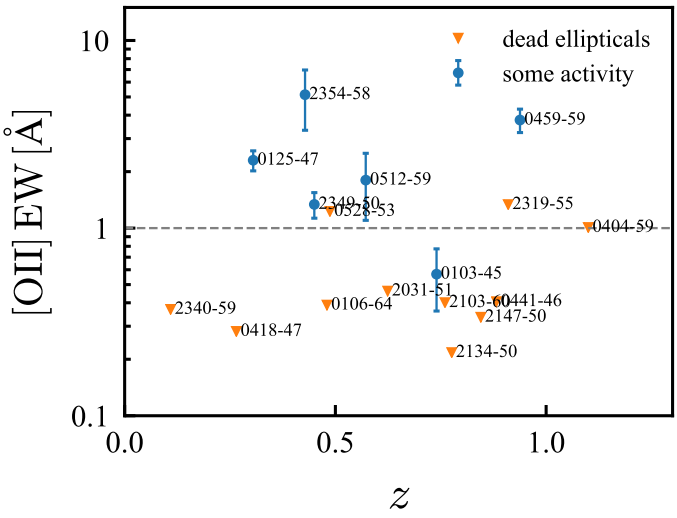

Figure 2.13: [O II] equivalent width determined from 1D spectra shown in Appendix C. [O II] detections above 2.5×RMS are categorized as having "some activity." Galaxies with no discernible [O II] feature are labelled "dead ellipticals." An upper limit on the equivalent width is determined from the RMS and channel width of the spectrum.

galaxy in the $R-K$ colour is indicative of a younger stellar population. Only one of the six lenses with clear [O II] detections, SPT2354-58, is identified as blue in the $R-K$ colour-magnitude diagram. However, SPT0125-47 was flagged for being redder than the typical elliptical galaxy when considering the $R-K$ colour and SPT0103-45 and SPT0512-59 are redder when considering the $J-K$ colour. This could suggest that they have a large dust reservoir which not only facilitates star formation but also absorbs blue light, leaving the galaxy to appear red. (Only five of the six [O II] lenses are in the colour-magnitude diagrams because SPT0459-59 does not have $J-$band imaging and SPT0512-59 does not have $R-$band imaging.) From our visual inspection, SPT0103-45 appeared to have either a tidal tail (indicating a possible ongoing merger) or a spiral arm along the southern edge and SPT0125-47 showed evidence of a central bulge with a disc suggesting an edge on view of a spiral galaxy. SPT2349-50, while not appearing redder or bluer than the template of a typical elliptical galaxy, and SPT2354-58 did show evidence of a possible companion galaxy in their imaging which would lead to star formation. SPT0459-59 and SPT0512-59 are the only lenses whose colour and morphology do not present any explanation for an [O II] detection. The star formation could be obscured by dust or a low level active nucleus could be present.

From the visual morphology and the colours of the galaxies, we concluded earlier that $\sim$ 30 % of the lenses displayed some evidence of active star formation. This does not change significantly when including [O II] detections (one additional lens is added). We find that only $\sim$ 16 % of the lenses in the SPT-SMG sample (highlighted in bold in Table 2.4) display evidence of active star formation (*i.e.* clear confirmation of a disc-like spiral structure in the morphology or from both the colour and an [O II] line detection). The vast majority, the remaining $\sim$ 84 %, are therefore passively evolving ellipticals or show inconclusive evidence of star formation.

2.6.3 Astrophysical Properties - Masses

Next we consider mass. The mass of a galaxy is a fundamental property and greatly affects its evolution. As discussed in the Chap. 1, while the mechanisms for the initial formation of a galaxy are still debated, consensus lies in a hierarchical growth model in which galaxies grow via major mergers and other galaxy interactions (*e.g.* Lacey and Cole 1993; Courteau et al. 2014). Predominantly the mass of a galaxy is contained in its dark matter halo which cannot be observed directly. Fortunately, techniques based on the galaxy's gravitational potential, *e.g.* the kinematics of stars or gravitational lensing, can be employed to determine the total mass (Zhu et al. 2010). Besides the dark matter content of a galaxy, the baryonic matter is also critical in dictating the galaxy's evolution. While external mechanisms such as major mergers lead to rapid growth, internal mechanisms such as the collapse of dense gas until nuclear fusion ignites and a star is formed also contributes a great deal to the growth of the galaxy. While star formation was most effective in the most massive galaxies early in our universe's evolution, with time the star formation has quenched (Courteau et al. 2014). Consequently the most massive galaxies today contain primarily an old stellar population while smaller galaxies have continued to form stars and consist of stellar populations of all ages.

We initially divide our analysis into two sections - stellar mass and Einstein mass, and conclude with a comparison of the two via the mass-to-light ratio.

Stellar Masses

The true stellar mass is the combination of the mass of "living" stars (*i.e.* nuclear fusion in the core is still ongoing) and of stellar remnants (*i.e.* the remains after the "death" of a star, either via a supernova event or the gradual collapse of the star after nuclear fusion has burned out) (Courteau et al. 2014). Unfortunately while stars radiate in the optical and near-IR, stellar remnants do not and therefore cannot be detected directly. In order to determine the true stellar mass of a galaxy astronomers model the evolution of stars over the age of the galaxy after having made an assumption about the initial mass function (IMF). The IMF is a function that defines the mass distribution of stars at the galaxy's conception. As the mechanism for the formation of a galaxy is still unknown, this function is based on empirical data. Two prevailing initial mass functions are the Salpeter IMF (Salpeter 1955) and the Chabrier IMF (Chabrier 2003). As an alternative to modelling the stellar evolution within a galaxy, a mass-to-light ratio (M/L) can be applied to the light emitted by the living stars to calculate an approximation of the true stellar mass. That is what we have done for this work. We determined an average mass-to-light ratio from the SLACS sample, for which the evolutionary modelling was done using both the Salpeter and Chabrier IMF. For consistency with the other comparison samples we use the SLACS Salpeter results ($M/L \sim 4.48$ $\mathrm{M}_\odot/\mathrm{L}_\odot$), noting that the difference between the Salpeter and Chabrier models is a scaling factor.

Determining the stellar mass of a galaxy therefore begins with measuring its luminosity and converting that into a mass. Differences in a star's age, mass, metallicity, *etc.* all contribute to its surface temperature and therefore the wavelength at which it radiates the strongest. The superposition of modified black-bodies from all stars in a galaxy results in the bump at optical and near-IR wavelengths in the galaxy's rest-frame spectral energy distribution (refer back to Fig. 1.4). The stellar luminosity of the galaxy can be determined by integrating across this bump in the SED. Once again this requires SED fitting that is not always justified and can lead to misleading results as discussed previously in Sect. 2.1.2. Fortunately, integrating across the entire optical and near-IR spectrum is often not necessary. While young, hot stars are more massive than the older and colder population they are short lived. The vast majority of the stellar mass in a galaxy therefore resides in low mass, old stars that

radiate most strongly in the near-IR (*e.g.* Zhu et al. 2010). It is therefore possible to focus on the light emitted in the near-IR and still approximate the stellar mass fairly well. This is especially true for ellipticals, which are passively evolving galaxies that formed their stellar mass early on and therefore consist almost exclusively of an older stellar population.

The luminosity (L_ν) is the power radiated at a given frequency and is a measure of the intrinsic brightness of the galaxy at that wavelength. It is a function of the luminosity distance of the object (D_L) and the flux density (S_ν, a measure of the apparent brightness of the galaxy at a given frequency) via the inverse square law,

$$L_\nu = 4\pi D_L^2 S_\nu \quad \text{where} \quad \nu S_\nu = \lambda S_\lambda. \tag{2.8}$$

The luminosity distance of a galaxy, given in units of parsec (pc), is defined by its apparent and absolute magnitudes (the absolute magnitude (M) of an astronomical object is defined such that it is equal to the apparent magnitude (m) if it were at a distance of 10 pc),

$$D_L = 10^{[(m-M)/5]+1}. \tag{2.9}$$

It can also be defined as the ratio of the intrinsic to apparent brightness of an object as in eq. 2.8, or it can be calculated from the redshift as redshift is simply another measure of astronomical distances. The conversion from z to D_L for this thesis assumes a flat cosmology (*i.e.* no curvature of space) with $H_\circ = 71$ km s^{-1} Mpc^{-1}, $\Omega_{\rm M} = 0.270$, and $\Omega_\Lambda = 0.730$. $H_\circ$ is the Hubble constant (the expansion rate of the universe), $\Omega_{\rm M}$ is the ratio of the baryonic matter density to the critical density, and Ω_Λ is the ratio of the dark energy density to the critical density. The critical density is the density of the universe that results in an expansion rate barely sufficient to prevent recollapse. Fortunately, while calculations of luminosity distances from redshifts require detailed knowledge of various cosmology parameters, the complexities are encoded in various python packages.

Finally, as we saw in Sect. 2.2.4, magnitudes are a logarithmic representation of the flux. Therefore, given that we measured the photometry of our lenses in

magnitudes, we can invert the relation and calculate the flux,

$$S_\nu = 10^{-(m_{AB}+48.60)/2.5} \qquad \text{where} \quad [S_\nu] = \frac{\text{erg}}{\text{s cm}^2 \text{ Hz}}. \tag{2.10}$$

Once the flux and luminosity distances are determined, the luminosity can be calculated using eq. 2.8. From here we apply the mass-to-light ratio determined from the SLACS sample to calculate the stellar mass.

The ideal wavelength at which to measure the luminosity so that the most accurate stellar mass can be calculated is the one in which the galaxy is most luminous. In the case of the SPT lenses this would either be in the $K-$band (at $2.16\,\mu$m) or in IRAC CH1 (at $3.6\,\mu$m), depending on the lens redshift. However, the only overlapping band of published magnitudes between our three comparison samples is the $i-$band. The top panel in Fig. 2.14 plots the observed $i-$band luminosity as a function of redshift. The right y-axis shows the corresponding stellar masses. Upon first glance it appears that our SPT lenses sample less luminous, and therefore less massive, galaxies. However, this is an observed-frame luminosity, which is expected to decrease with increasing redshift due to the slope in the SED. Referring back to Fig. 1.4 in the Introduction, as the SED for the elliptical galaxy is redshifted, *i.e.* moves to longer wavelengths, the $i-$band (rest-frame 0.7835 μm) samples shorter wavelengths on the SED and consequently fainter fluxes (the SED has a positive slope with increasing wavelength in this regime). This effect is shown by the dashed line in the top panel of Fig. 2.14, labelled "i template," normalized to the average SLACS luminosity.

For a true comparison between the samples, the effect of the shape of the SED on the luminosity needs to be removed. This effectively means we need to compare rest-frame luminosities, *i.e.* measure the luminosity of the lens in the band to which the $i-$band gets redshifted for that lens. For example, if the lens is at redshift $z = 1$ the rest-frame $i-$band wavelength gets redshifted to $0.7835 \times (1 + z) = 1.567$. This lens should therefore be observed at 1.567 μm. Unfortunately doing so exactly is impossible. Instead, for the three comparison samples, we can continue to use the observed $i-$band luminosities and adjust them by the ratio of the $i-$band template between the redshift at which the lens is at and $z = 0$ (rest-frame). Because we are using a M/L ratio determined from the SLACS sample we used the average SLACS redshift ($z \sim 0.204$) as our rest-frame instead of $z = 0$.

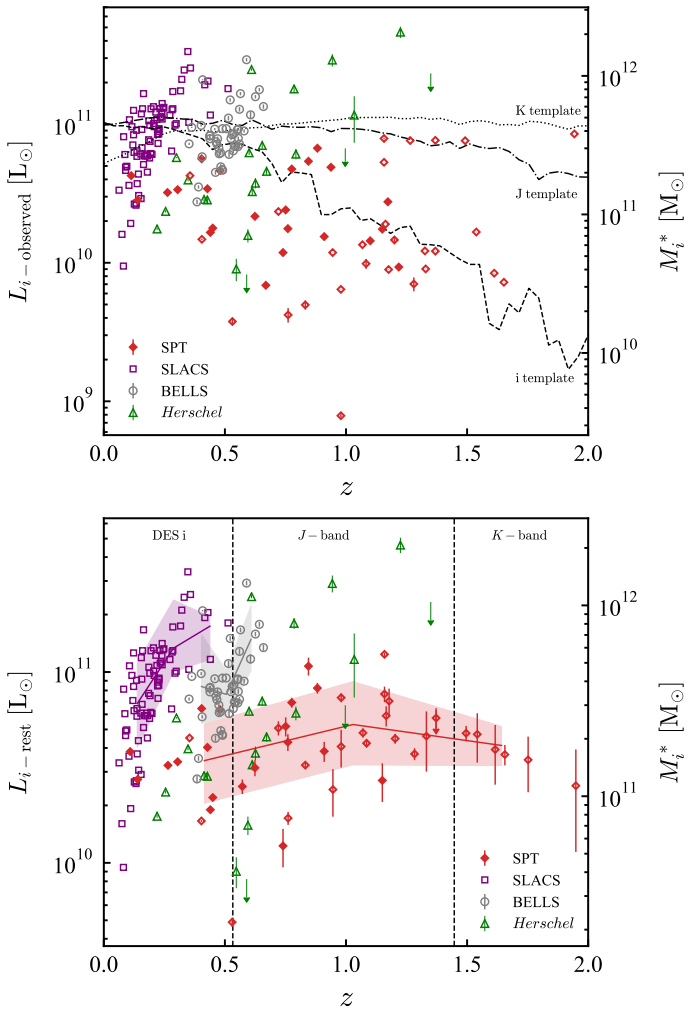

Figure 2.14: *Top:* Observed $i-$band luminosity as a function of redshift. The dashed (dash-dotted) [dotted] black line is the $i-$band ($J-$band) [$K-$band] luminosity determined from the 5 Gyr. elliptical galaxy SED template created by Polletta et al. (2007) as it is redshifted. *Bottom:* Rest-frame $i-$band luminosity as a function of redshift. The SLACS, BELLS, *Herschel*, and low-z SPT lenses are adjusted by the ratio in the $i-$band template at the lens redshift and at our chosen rest-frame redshift, the average redshift of the SLACS sample. For mid-z (high-z) SPT lenses as delineated by the vertical dashed lines, $J-$band ($K-$band) magnitudes were used instead of $i-$band and adjusted similarly using the $J-$band ($K-$band) template. Solid lines and the surrounding shaded regions are the running average and RMS for the relevant sample.

For our own SPT lenses we determined the rest-frame $i-$band luminosity by both using a more appropriate observing band and by applying necessary template corrections. First we found that for any lenses in the range $0.53 < z \leq 1.45$ the observed $J-$band is closer to the rest-frame $i-$band. Similarly for lenses past $z > 1.45$ the observed $K-$band is closer. So for lenses at $z < 0.53$ we continue to use the $i-$band magnitudes but for lenses at $0.53 < z \leq 1.45$ and at $z > 1.45$ we switch to using $J-$ and $K-$band magnitudes respectively to calculate luminosities. The dash-dotted line labelled "J template" and the dotted line labelled "K template" in Fig. 2.14 shows the $J-$ and $K-$band luminosities (rest frame 1.24 μm and 2.16 μm respectively) for the template elliptical as it is redshifted. The decrease in luminosity is markedly less for the $J-$band and barely perceptible, if at all, for the $K-$band. This is due to the relative flat top of the bump in the SED being considered. Regardless, for consistency we apply the ratio of the appropriate template between the lens redshift and our adopted rest-redshift to the luminosity so that we are comparing rest-frame $i-$band luminosities for all lenses. The resulting rest-frame luminosities and corresponding stellar masses as well as lens and source redshifts are listed in Table 2.5. Lens redshifts determined photometrically via the $K - z$ relation are identified with a " † " while photometric redshifts for the sources are identified by a trailing "p." Luminosities and masses in Table 2.5 are listed in solar units, where $\mathrm{L}_\odot = 3.846 \times 10^{26}$ W is the power radiated by the sun and $\mathrm{M}_\odot = 1.989 \times 10^{30}$ kg is the mass of the sun.

The rest-frame luminosities are plotted in the bottom panel of Fig. 2.14. We now no longer see a decrease in SPT luminosities with increasing redshift, with the slight exception in the $K-$band regime. This is due to the fact that these redshifts are all photometric redshifts determined from the $K - z$ relation and so fainter sources are extrapolated to be at higher redshift. A running average and the corresponding RMS were calculated and are shown as solid lines with surrounding shaded regions. For the SLACS and BELLS samples we see the luminosity is a sharply rising function of redshift, even over their short redshift ranges. This is a consequence of them being lens-selected samples. In order for higher-z lenses to be selected they must be intrinsically more luminous (more massive) than the lower-z lenses. As our SPT lenses do not suffer this selection effect, we are therefore able to probe the true mass range of lenses, finding a significant fraction of lower mass lenses in our sample. We

note that we do not identify any lenses as massive as the upper 30 % of the SLACS and BELLS lenses. This could be a result of our high source redshift bias ($z > 2$) from the SPT 1.4 mm selection effect.

Table 2.5: Redshifts and calculated astrophysical properties. † $K-z$ redshifts.

ID	$z_{\rm lens}$	$z_{\rm source}$	$L_{i-{\rm rest}}$ [10^{10} L$_\odot$]	M_i^* [10^{10} M$_\odot$]	$R_{\rm E}$ [$''$]	$M_{\rm E}$ [10^{10} M$_\odot$]
SPT0002-52	1.173	2.3513	-	-	-	-
SPT0020-51	0.751	4.1228	5.19 ± 0.6	23.2 ± 3	0.614 ± 0.007	10.9 ± 0.2
SPT0027-50	0.946†	3.4436	2.42 ± 0.7	10.8 ± 3	0.638 ± 0.007	15.2 ± 0.3
SPT0103-45	0.74	3.0917	1.23 ± 0.3	5.49 ± 1	0.88 ± 0.003	23.9 ± 0.2
SPT0106-64	0.48	4.91	6.35 ± 0.04	28.4 ± 0.2	-	-
SPT0109-47	0.669	3.6137	-	-	1.3 ± 0.03	46 ± 2
SPT0113-46	0.721†	4.2328	5.08 ± 0.4	22.8 ± 2	1.16 ± 0.01	37.3 ± 0.6
SPT0114-59	1.372†	3.3p	5.74 ± 0.7	25.7 ± 3	-	-
SPT0125-47	0.305	2.5148	3.39 ± 0.009	15.2 ± 0.04	1.01 ± 0.002	14.5 ± 0.06
SPT0125-50	0.51	3.959	-	-	0.984 ± 0.005	20.5 ± 0.2
SPT0147-64	0.98†	4.8036	7.34 ± 0.4	32.8 ± 2	-	-
SPT0150-59	1.085†	2.7881	4.23 ± 0.2	18.9 ± 0.9	-	-
SPT0155-62	1.656†	4.349	3.69 ± 0.5	16.5 ± 2	-	-
SPT0202-61	1.166†	5.018	5.9 ± 0.7	26.4 ± 3	0.758 ± 0.005	22.7 ± 0.3
SPT0243-49	1.372†	5.698	< 6.29	< 28.2	0.327 ± 0.003	4.61 ± 0.08
SPT0245-63	0.354†	5.626	4.51 ± 0.02	20.2 ± 0.07	-	-
SPT0300-46	0.53†	3.5954	0.489 ± 0.03	2.19 ± 0.1	0.337 ± 0.008	2.52 ± 0.1
SPT0311-58	1.752†	6.9	3.47 ± 1	15.5 ± 5	-	-
SPT0319-47	1.178†	4.51	7.04 ± 1	31.5 ± 5	0.283 ± 0.009	3.3 ± 0.2
SPT0345-47	1.949†	4.2957	2.53 ± 1	11.3 ± 6	0.306 ± 0.002	6.46 ± 0.08
SPT0346-52	1.542†	5.656	4.72 ± 1	21.1 ± 6	0.979 ± 0.007	45.3 ± 0.6
SPT0403-58	1.496†	4.2p	4.78 ± 0.4	21.4 ± 2	0.533 ± 0.05	15 ± 3
SPT0404-59	1.1	4.8p	-	-	0.549 ± 0.03	11.5 ± 1
SPT0418-47	0.265	4.224	3.24 ± 0.01	14.5 ± 0.05	1.25 ± 0.003	18.6 ± 0.09
SPT0441-46	0.882	4.477	8.23 ± 0.5	36.9 ± 2	0.678 ± 0.006	14.9 ± 0.3
SPT0452-50	1.218	2.0104	-	-	0.82 ± 0.1	52.3 ± 17
SPT0459-58	0.98†	4.857	4.07 ± 0.9	18.2 ± 4	0.468 ± 0.01	7.6 ± 0.5
SPT0459-59	0.938	4.7993	-	-	0.627 ± 0.02	13.2 ± 0.8
SPT0512-59	0.572	2.2331	2.51 ± 0.2	11.2 ± 1	-	-
SPT0516-59	1.203†	3.4045	4.48 ± 0.3	20 ± 1	-	-
SPT0529-54	0.14	3.369	2.74 ± 0.003	12.3 ± 0.01	1.36 ± 0.008	12.5 ± 0.1
SPT0532-50	1.15	3.399	2.7 ± 0.6	12.1 ± 3	0.556 ± 0.003	14 ± 0.2
SPT0538-50	0.404	2.7855	6.44 ± 0.02	28.8 ± 0.08	1.73 ± 0.004	54.2 ± 0.3
SPT0544-40	1.283†	4.2692	3.72 ± 0.3	16.7 ± 1	-	-
SPT0551-48	0.832†	2.5833	3.25 ± 0.1	14.6 ± 0.5	-	-
SPT0552-42	0.761†	4.437	1.72 ± 0.1	7.68 ± 0.6	-	-
SPT0555-62	0.363†	4.815	-	-	-	-
SPT0604-64	0.277†	2.48	-	-	-	-
SPT0625-58	1.07†	2.726	4.8 ± 0.3	21.5 ± 1	-	-

ID	$z_{\rm lens}$	$z_{\rm source}$	$L_{i-{\rm rest}}$ [10^{10} $L_\odot$]	M_i^* [10^{10} $M_\odot$]	$R_{\rm E}$ [$''$]	$M_{\rm E}$ [10^{10} $M_\odot$]
SPT2008-58	1.159†	-	12.4 ± 0.3	55.4 ± 1	-	-
SPT2031-51	0.624	2.2p	3.15 ± 0.3	14.1 ± 1	0.534 ± 0.005	8.34 ± 0.2
SPT2048-55	1.329†	4.089	-	-	0.361 ± 0.006	6.23 ± 0.2
SPT2101-60	0.403†	3.153	1.66 ± 0.02	7.42 ± 0.08	-	-
SPT2103-60	0.76	4.435	4.29 ± 0.4	19.2 ± 2	0.455 ± 0.009	5.97 ± 0.2
SPT2132-58	1.159†	4.768	7.67 ± 0.7	34.3 ± 3	0.335 ± 0.006	4.48 ± 0.2
SPT2134-50	0.776	2.78	6.92 ± 0.4	31 ± 2	0.518 ± 0.002	8.98 ± 0.07
SPT2146-55	1.332†	4.567	4.61 ± 2	20.7 ± 7	0.858 ± 0.004	33.6 ± 0.3
SPT2147-50	0.845	3.7602	10.7 ± 1	48.1 ± 5	1.2 ± 0.006	46.9 ± 0.5
SPT2307-50	1.267†	3.105	-	-	-	-
SPT2311-54	0.44	4.2795	1.9 ± 0.02	8.5 ± 0.1	0.209 ± 0.007	0.807 ± 0.05
SPT2319-55	0.91	5.2929	3.85 ± 0.5	17.2 ± 2	0.43 ± 0.003	5.94 ± 0.08
SPT2335-53	1.616†	4.757	3.92 ± 1	17.6 ± 6	-	-
SPT2340-59	0.109	3.864	3.83 ± 0.004	17.1 ± 0.02	1.58 ± 0.02	13.3 ± 0.3
SPT2349-50	0.45	2.8p	2.2 ± 0.02	9.85 ± 0.1	0.244 ± 0.005	1.19 ± 0.05
SPT2354-58	0.428	1.867	4.03 ± 0.05	18 ± 0.2	0.321 ± 0.003	2.15 ± 0.04
SPT2357-51	-	3.0703	-	-	0.215 ± 0.003	-

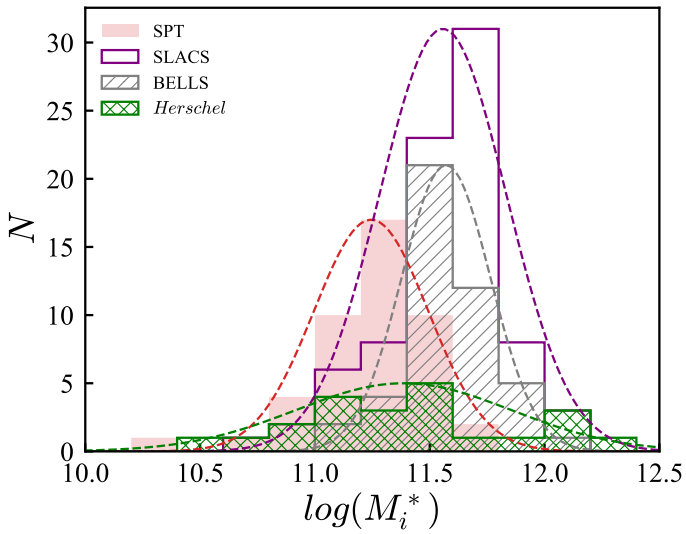

Figure 2.15: Stellar mass distribution. Rest-frame $i-$band luminosities are converted to rest-frame stellar masses using a M/L ratio. Gaussian distribution: SPT = $(17.56\pm 10.06)\times 10^{10}$ $M_\odot$; SLACS = $(36.08\pm 23.01)\times 10^{10}$ $M_\odot$; BELLS = $(37.24\pm 16.61)\times 10^{10}$ $M_\odot$; *Herschel* = $(24.30 \pm 26.24) \times 10^{10}$ $M_\odot$.

Another way of comparing the stellar masses is through the stellar mass distribution for each survey as in Fig. 2.15. A gaussian was fit to each distribution, the mean and standard deviation of which are: SPT = $(17.56 \pm 10.06) \times 10^{10}$ $M_\odot$; SLACS = $(36.08 \pm 23.01) \times 10^{10}$ $M_\odot$; BELLS = $(37.24 \pm 16.61) \times 10^{10}$ $M_\odot$; *Herschel* = $(24.30 \pm 26.24) \times 10^{10}$ $M_\odot$. Here we see more clearly that the SLACS and BELLS

samples occupy a higher stellar mass regime than the SPT sample. The *Herschel* distribution is broadly consistent with our own SPT distribution with the addition of four high-mass lenses ($M_i^* > 10^{12}$ $M_\odot$). Two possible explanations for this are *Herschel*'s selection wavelength (lower redshift galaxies are typically brighter and therefore more massive) or randomness.

Einstein Masses

The Einstein mass, $M_{\rm E}$, is a measure of the total mass of the galaxy, light and dark matter combined, within the Einstein radius. If the Einstein radius is known as well as both the lens and source redshift, then Eq. 2.5 can be inverted to solve for the Einstein mass,

$$M_{\rm E} = \left[\frac{D_{\rm l} D_{\rm s}}{D_{\rm ls}} \frac{c^2}{4G}\right] \theta_{\rm E}^2. \tag{2.11}$$

In this analysis we treat the mass of the lens as a point mass, ignoring mass density distributions within the lens that could cause asymmetric lensing. The Einstein radii (in units of arcseconds) for the SPT sample were determined via lens modelling done by Spilker et al. (2016). They, along with the Einstein masses we calculated, can be found in Table 2.5.

The Einstein radii and the Einstein masses as a function of redshift for our own lenses as well as the three comparison samples are plotted in Fig. 2.16. As expected from the $M_{\rm E}$-$\theta_{\rm E}$ relation, the two plots are very similar. We find that both lens-selected (SLACS and BELLS) as well as source-selected (*Herschel* and SPT) surveys probe a very similar range in Einstein masses. Neither method seems to be biased towards either low or high masses, however, the SPT and *Herschel* samples fill out the low-mass tail. This can be seen well in the Einstein mass distribution plot in Fig. 2.17. Once again we fit a gaussian to the distribution, the mean and standard deviations of which are: SPT $= (11.11 \pm 11.48) \times 10^{10}$ $M_\odot$; SLACS $= (18.06 \pm 12.09) \times 10^{10}$ $M_\odot$; BELLS $= (23.91 \pm 18.01) \times 10^{10}$ $M_\odot$; *Herschel* $= (13.84 \pm 20.69) \times 10^{10}$ $M_\odot$. All of the gaussians fall within one standard deviation of each other. With the exception of one *Herschel* sources, there seems to be an upper limit to the Einstein radius of ~ 13 kpc (or $\sim 2''$). Conversely only one *Herschel* source lies below a seeming lower limit to

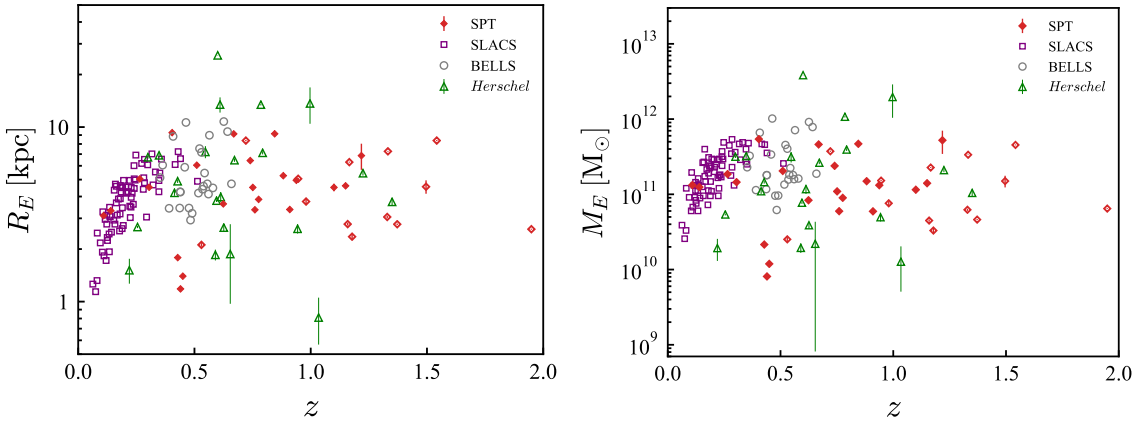

Figure 2.16: *Left:* Einstein radius as a function of redshift. *Right:* Einstein mass as a function of redshift. SPT lenses which have spectroscopic redshifts are shown as solid red diamonds, lenses with photometric redshifts are shown as open red diamonds.

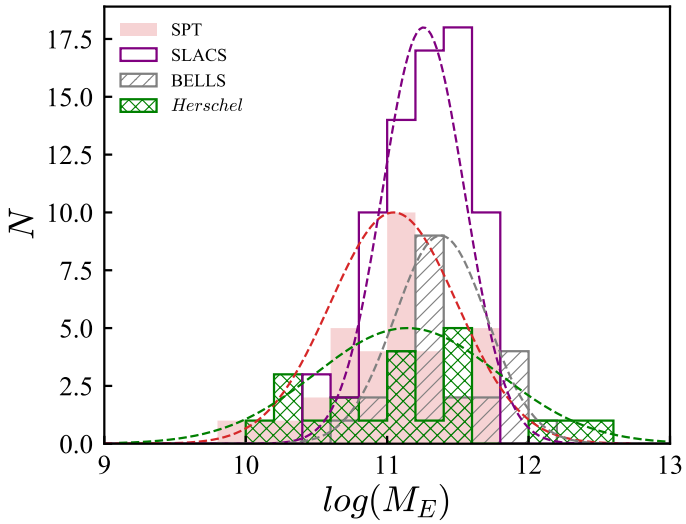

Figure 2.17: Total (Einstein) mass distribution. Gaussian distribution: SPT = $(11.11 \pm 11.48) \times 10^{10}$ $M_\odot$; SLACS = $(18.06 \pm 12.09) \times 10^{10}$ $M_\odot$; BELLS = $(23.91 \pm 18.01) \times 10^{10}$ $M_\odot$; *Herschel* = $(13.84 \pm 20.69) \times 10^{10}$ $M_\odot$.

the Einstein radius of ~ 1 kpc (or $\sim 0.2''$). This results in Einstein masses spanning, but remaining within, about two orders of magnitude, 10^{10} $M_\odot < M_E < 10^{12}$ $M_\odot$. While the SPT and *Herschel* Einstein masses appear to be independent of redshift, the SLACS lenses in particular have a strong correlation between Einstein mass and redshift - as the lens moves to higher redshift, the Einstein mass must be greater for the survey to detect the lens. This bias was seen in the stellar masses as well.

Lastly we can compare the stellar mass component to the Einstein mass. This

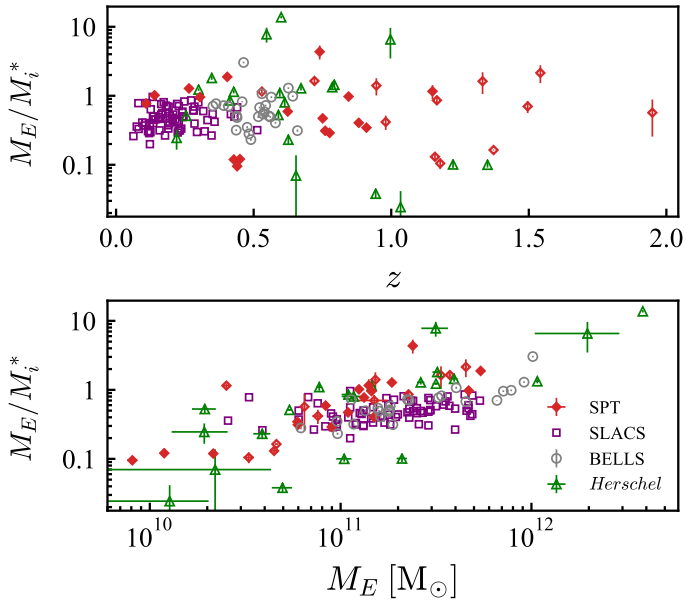

Figure 2.18: Einstein mass to stellar mass ratio, *i.e.* total mass to light mass ratio. Rest-frame $i-$band luminosities are scaled into rest-frame stellar masses. *Top*: Ratio vs redshift. *Bottom*: Ratio vs Einstein Mass. SPT lenses which have spectroscopic redshifts are shown as solid red diamonds, lenses with photometric redshifts are shown as open red diamonds.

ratio is plotted in Fig. 2.18 as a function of redshift on the top panel and as a function of the Einstein mass on the bottom panel. It is important to note that a large number of lenses have a ratio below $M_{\rm E}/M_i^* < 1$, *i.e.* the stellar mass component is bigger than the Einstein mass. This is possible because while the Einstein mass is the cumulative mass of light and dark matter, it is only the mass contained within the Einstein radius. In the case of a larger stellar field, we find more stellar mass residing outside of the Einstein radius. This can certainly be true for ellipticals whose stars are not densely populated near the centre of the galaxy. Furthermore, stellar mass calculations notoriously have high uncertainties due to the adoption of an initial mass function (Courteau et al. 2014). In the bottom panel of Fig. 2.18 we find that the $M_{\rm E}/M_i^*$ ratio for the SPT lenses is consistently larger than that of SLACS and BELLS. This is possibly another manifestation of source-selection versus lens-selection. Lens-selected surveys preferentially detect lenses with larger, more extended stellar envelopes relative to their $\theta_{\rm E}$, therefore resulting in a lower $M_{\rm E}/M_i^*$ ratio.

2.7 Conclusion

We make these final conclusions:

1. Applying a $K - z$ fitting to elliptical lenses produces reliable photometric redshifts. Single-band $K - z$ redshifts have an RMS of 0.17 around the ideal one-to-one relation with spectroscopic redshifts, while the multi-band SED fitting procedure results in a slightly larger RMS of 0.27. Thus, we determine the single-band $K - z$ redshifts to be more accurate and choose to use them in further analysis. Furthermore, we deem the $K - z$ relation to be an attractive alternative method to estimating redshifts for a population of faint, dust-free galaxies for which spectroscopic or multi-band photometric approaches are costly, time-consuming, and in some cases unjustified.
2. Source-selected surveys span a larger lens redshift range (both SPT and *Herschel* have $\langle z \rangle \sim 0.7 \pm 0.3$, where the error is the standard deviation to the mean) as compared to lens-selected surveys (SLACS: 0.20 ± 0.09 and BELLS: 0.50 ± 0.07, both of which have significantly smaller standard deviations in addition to lower mean redshifts). This is especially true if we include our $K - z$ redshifts, which further expands the SPT range to $\langle z \rangle \sim 0.9 \pm 0.9$. This needs to be confirmed spectroscopically. The implication, however, is a sub-sample of gravitational lenses discovered by the SPT survey that exist at a higher-redshift than previously thought.
3. Lens-selected surveys probe geometrically small gravitational lensing systems while source-selected surveys appear not to be constrained in a similar manner. This is in large part due to the selection effects of SLACS and BELLS which require a spectroscopic detection of both the lens and source in the SDSS database. As the database is compiled from a shallow but large-sky survey in the optical and near-IR, only the brightest and consequently low-z sources are detected. Conversely, source-selected surveys benefit from negative K-correction and so for a given lens redshift, the corresponding source can lie over a large redshift range. Alternatively, source-selected surveys compile a sample of gravitational lenses without constraints on their redshift distribution.
4. We find the majority of the SPT lenses to be passively evolving elliptical galaxies

($\sim 84\%$) with indications from blue colours on the colour-magnitude diagrams and robust [O II] detections for elevated star formation activity in the remaining lenses. This is supported by the imaging, three of the lenses ($\sim 5\%$) are very clearly spiral galaxies, with a few more showing evidence for interactions with neighbouring galaxies.

5. We determine rest-frame $i-$band luminosities and convert them to stellar masses, finding that the SPT sample discovers a low-mass tail to the stellar mass range, undetected by either the SLACS or BELLS samples. Furthermore we find that the median stellar mass for source-selected surveys (SPT = $(17.56\pm10.06)\times10^{10}$ $M_\odot$ and *Herschel* = $(24.30 \pm 26.24) \times 10^{10}$ $M_\odot$) is smaller than that of lens-selected surveys (SLACS = $(36.08 \pm 23.01) \times 10^{10}$ $M_\odot$ and BELLS = $(37.24 \pm 16.61) \times 10^{10}$ $M_\odot$). Importantly, we also note a strong correlation between redshift and stellar mass for the lens-selected surveys, which is notably absent for the source-selected surveys. Source-selected surveys therefore provide an unconstrained mass distribution.

6. Lastly we calculate Einstein masses from Einstein radii and conclude that the SPT sample discovers a similar low-mass tail to the Einstein mass range. Once again the median Einstein mass is lower for the source-selected surveys (SPT = $(11.11 \pm 11.48) \times 10^{10}$ $M_\odot$ and *Herschel* = $(13.84 \pm 20.69) \times 10^{10}$ $M_\odot$) as compared to the lens-selected surveys (SLACS = $(18.06 \pm 12.09) \times 10^{10}$ $M_\odot$ and BELLS = $(23.91 \pm 18.01) \times 10^{10}$ $M_\odot$). The deviations for the Einstein mass though, are not as great as those for the stellar mass. Only $\sim 12\%$ of the SPT lenses have Einstein masses below the bulk of the SLACS and BELLS masses. Of these, just under half are also part of the low-stellar mass tail. A low Einstein mass does not necessarily result in a low stellar mass. We conclude that gravitational lensing is most effective when the Einstein mass of the lens falls within $10^{10} - 10^{12}$ $M_\odot$ (corresponding to Einstein radii of $\sim 0.2 - 2''$), as is evident from both source- and lens-selected surveys.

These are critical findings for building a statistical representation of gravitational lenses. A detailed understanding of the lenses, especially redshift and mass, is crucial for lens models, which aim to model gravitational lensing systems in an effort to de-lens the SMGs.

Chapter 3

A Characterization of the Galaxies in the SPT2349 Proto-cluster at $z = 4.3$

3.1 Introduction

The $2,500$ deg^2 sub-mm South Pole Telescope (SPT) survey detected $\gtrsim$ 80 sub-millimetre galaxies (SMGs) that had previously been obscured from view due to their high dust content (Vieira et al. 2010; Mocanu et al. 2013). The vast majority ($\gtrsim 90\%$) of these SMGs have been shown to be part of gravitational lensing systems in which the light from the SMGs is magnified and distorted (*e.g.* Hezaveh et al. 2013; Spilker et al. 2016). The lenses of these systems were discussed in the previous Chapter. A small sub-sample ($\lesssim 10\%$) of the SMGs, however, display no evidence of gravitational lensing, both by not exhibiting Einstein rings or arcs in the sub-mm imaging and through the lack of a detection of a possible foreground lens in the optical through mid-IR range. While a lot can be learned from the greater population of lensed, high-z SMGs, requiring a detailed understanding of the gravitational lenses themselves (as discussed in Chap. 2), the candidate unlensed SMGs are incredibly rare with implied intrinsic luminosities that are much larger than the lensed examples of the SPT survey (Spilker et al. 2016). One such candidate was SPT2349-56.

3.1.1 SPT2349-56

SPT2349-56 (SPT2349 from here on) was initially discovered in the SPT survey as a point source (SPT's resolution is $\sim 1'$). At 1.4 mm, one of the three SPT bands, it has a flux density of $S_{1.4\,\mathrm{mm}} = 23.3 \pm 3.7$ mJy, similar to the median lensed flux of the SPT sample at 24 mJy (Vieira et al. 2010; Mocanu et al. 2013). SPT2349 is therefore intrinsically brighter than a majority of the SPT-SMGs when considering their de-lensed fluxes. As with many of the SPT-SMGs, follow-up observations were initially conducted at 870 μm with the Large APEX BOlometer CAmera (LABOCA)

on the Atacama Pathfinder EXperiment (APEX) telescope in order to obtain a more precise location in the sky. Despite LABOCA being a low-resolution camera, $\sim 19''$ (Siringo et al. 2009), SPT2349 was resolved into two elongated sources, in contrast to the majority of the sample which continue to appear as a single unresolved source at this resolution. The bright southern source was found to have a flux density of $S_{870\,\mu\mathrm{m}} \sim 77$ mJy while the northern source is a bit dimmer at $S_{870\,\mu\mathrm{m}} \sim 25$ mJy. The two are connected via a bridge with $S_{870\,\mu\mathrm{m}} \sim 7$ mJy (Miller et al. 2018). The elongated nature of SPT2349 suggests a large structure both in physical extent and in mass. Fig. 3.1 (taken from Miller et al. 2018) shows the two LABOCA lobes (in green contours) overlaid on a near-IR (3.6 μm) grey-scale image. High-resolution ($< 4.7''$) Atacama Large Millimeter/submillimeter Array (ALMA) observations at 3 mm further divided the southern source in two (Vieira et al. 2013). The CO(4-3) transition (discussed in Sect. 1.2.3), observed with ALMA, identified the redshift of both southern components to be 4.300 ± 0.002 (Strandet et al. 2016). The number density, three bright SMGs in a circle with $\sim 1'$ diameter (SPT's resolution), two of which unambiguously are at the same redshift, solidified SPT2349 as a very interesting source and prompted significant higher-resolution follow-up observations, the initial results of which were published by Miller et al. (2018).

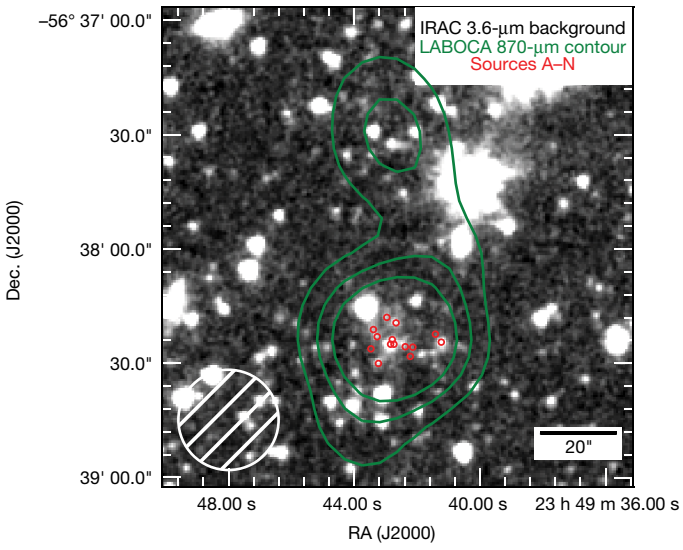

Figure 3.1: SPT2349 proto-cluster core. LABOCA lobes (green contours) overlaid on the IRAC CH1 grey-scale image. The 14 sources are identified by red circles. The LABOCA beam size ($26''$) is shown in white. Image taken from Miller et al. (2018).

Upon further spectral observations with ALMA at 1.1 mm, Miller et al. (2018) detected a total of 14 sources in the southern lobe of SPT2349 emitting [C II] lines (also discussed in Sect. 1.2.3) that robustly identify all 14 redshifts at ~ 4.31. They are identified by red circles in Fig. 3.1. Eight of the sources also have strong CO(4-3) line detections in their spectra. All 14 sources are detected in high-resolution ($\lesssim 1''$) 1.1 mm ALMA continuum imaging. The over-density of SMGs at very similar redshifts and the large implied dark matter halo mass lead Miller et al. (2018) to classify SPT2349 as a proto-cluster, possibly one more massive and at a much more advanced stage of evolution than other high-redshift proto-cluster candidates. At $z \sim 4.31$, the SPT2349 proto-cluster is being observed only ~ 1.35 billion years after the Big Bang, one tenth of the current age of the universe, yet it has already accumulated a significant mass.

3.1.2 Dark Matter Halos & Proto-clusters

Numerous galaxies that are gravitationally bound are called either "galaxy groups" or "galaxy clusters." While the transition between the two is smooth, the characteristics of galaxies in the system change past some mass threshold, which generally occurs around ~ 50 member galaxies. As a consequence, galaxy clusters are the most massive gravitationally bound structures in the universe with masses upwards of $M \gtrsim 10^{14}$ $M_\odot$ (Schneider 2006). While the galaxies themselves are frequently some of the most massive ellipticals in the universe, a significant fraction of the cluster mass is attributed to a substantial dark matter (DM) halo surrounding the galaxies (Schneider 2006).

Proto-clusters are the high-redshift progenitors to galaxy clusters. The distinction between proto-clusters and clusters is not strictly defined. Generally though, clusters are massive virialized (*i.e.* stable, gravitationally bound, and relaxed) structures whereas proto-clusters are over-densities of both massive galaxies as well as dark matter that will eventually become a cluster (Overzier 2016). It is expected that the massive galaxies in proto-clusters are luminous starbursts, *i.e.* bright SMGs (Miley and De Breuck 2008). Similarly to SMGs in the field (field galaxies are those that are not gravitationally bound to a large-scale structure such as (proto-)clusters), they are thought to be the product of major-merger events. This is in large part

because simulations of secular origins, in which the primary growth mechanism is smooth accretion of gas from the intergalactic medium, have failed to produce the star formation rates observed in SMGs. Furthermore, the dense environments of proto-clusters easily lend themselves to significantly elevated galaxy interactions as compared to the field. While the starburst phase is short-lived, it is critical as the vast majority of the stellar mass build-up of a SMG occurs during this time. Studying proto-clusters can therefore help shed light on an early era of immense stellar mass growth of the universe previously undetected. Due to the density of proto-clusters and thus the high merger rates, it is likely that proto-clusters are sites that contain a significant percentage of the star forming activity at their redshift. Furthermore, the violent nature of major-mergers leads to the expulsion of gas and dust clouds likely enriched with metals from explosive supernova events of massive stars. The enriched intra-cluster medium will consequently affect the formation of new galaxies. Star formation processes at high-redshift may also vary as compared to at low-redshift, due to potentially different compositions of the interstellar medium (ISM). This could lead to a different initial mass function, a function that defines the mass distribution of stars at the galaxy's conception, between high-z galaxies in over-densities and low-z galaxies. All of these questions are still debated. Studying the elusive high-z proto-clusters will undoubtably help answer some of them.

The evolutionary consequence of proto-clusters containing bright SMGs is that once a galaxy cluster has fully formed and stabilized, the highly active SMGs undergoing major-mergers will have depleted their gas reservoir and evolved into old, massive ellipticals. This is borne out in observations of local galaxy clusters, which show that the member galaxies are massive ellipticals that are remarkably homogeneous and contain primarily an old stellar population implying the stars formed early in their evolutionary sequence. It is also believed that all ellipticals host a supermassive black hole at their centre. As outlined in the introduction (Sect. 1.1.1), if a black hole was not previously present, the major-merger between two galaxies would trigger the formation of one. The growth of the black hole, through the accretion of matter from the galaxy or the collision of two black holes, is yet another interesting phenomenon. Studies have shown that the size of the supermassive black hole is likely linked to the size of its host galaxy. The high merger rate within the densest

of proto-clusters, such as SPT2349, therefore means that the resulting ellipticals may host some of the most massive supermassive black holes.

Searching for Proto-clusters

Searches for proto-clusters thus far have relied on identifying over-densities of optically luminous galaxies using the Lyman break technique (Steidel et al. 1998). This makes use of the dramatic drop-off observed in a galaxy's spectral energy distribution (SED) at $\lambda_{\rm rest} = 91.2$ nm due to the abundance of intervening neutral hydrogen and its ionization energy of 13.6 eV (as discussed in Sect. 1.2). In an effort to observe the Lyman break, large-area surveys are conducted across multiple wavelength bands. By identifying sources that consistently are observed at longer wavelengths but "drop-out," *i.e.* disappear, in shorter wavelength bands, a rough redshift range can be determined for that source. Over-densities of similar redshift sources suggests the detection of a proto-cluster. Targeted follow-up spectroscopy of proto-cluster candidates can then be done. This method has been successfully replicated over many optical and near-IR bands and has lead to the discovery of many confirmed proto-clusters, including out to $z \sim 6$ (Toshikawa et al. 2012).

Despite the incredible success of the optical searches for proto-cluster candidates, high-z proto-clusters still remain relatively rare. For example, in the 121 deg^2 survey conducted by Subaru (an 8.2 m optical and IR telescope located on the summit of Mauna Kea, Hawaii) 179 proto-cluster candidates at $z \sim 4$ were identified (Toshikawa et al. 2018). Upon spectroscopic follow-up, however, only a fraction of the candidates were confirmed as proto-clusters. As of 2016, Overzier (2016) compiled a comprehensive list of ~ 40 confirmed proto-clusters from a literature search.

The Lyman break method relies on the optical output of the galaxies, which, if they are starburts, or dusty, star-forming galaxies (DSFGs), are highly dust-obscured and difficult to observe at optical wavelengths. It is therefore likely that the Lyman break technique misses large numbers of highly active proto-clusters that have high dust content and are therefore possibly at earlier stages of their proto-cluster evolution. The detection of SPT2349 provides a new method in which high-z proto-clusters can be identified: 1) Identify an unlensed SMG which does not have an optical or near-IR counterpart that could suggest gravitational lensing. 2) Confirm the source is

extended, possibly with multiple components, at 870 μm using LABOCA. 3) Follow-up observations with ALMA, which may identify multiple sources at the same redshift, while also presenting a missing flux compared to the LABOCA observations, suggesting the presence of further un-detected galaxies. This new method relies on the over-density of luminous (sub-)mm galaxies, which are observed via their thermal dust radiation instead of the obscured optical light. In this way, the SPT survey will identify only the most active proto-cluster cores at high-z, such as SPT2349. Furthermore, the over-densities identified via optical methods are significantly less concentrated than SPT2349. For example, the 8 galaxies discovered by Toshikawa et al. (2012) at $z = 6.01 \pm 0.05$ using the Lyman break technique are within a region covering $196,000,000$ kpc^2, unlike the 14 SMGs in the core of SPT2349 within the incredibly small area of $13,300$ kpc^2.

3.1.3 Motivation

Identifying differences between field SMGs and those growing in over-densities, such as in proto-clusters and cluster cores, can help elucidate aspects of galaxy evolution that lead to the vastly different properties of galaxies in clusters and in the field in the present epoch. SMGs are sites of intense star formation often long before the height of galaxy assembly (*e.g.* Casey et al. 2014), and so observing massive SMGs at high redshifts is crucial in understanding the evolution of galaxy structures. Field SMGs are found predominantly at $z > 2$ (Chapman et al. 2003a, 2005), host rapid star formation at rates sometimes exceeding $1,000$ M$_\odot$ yr^{-1} (Swinbank et al. 2013), and have stellar masses on the order of 10^{11} M$_\odot$ (Michałowski et al. 2012). Their rapid evolution early in cosmic time stresses the importance of understanding SMGs at high redshift, with current models still struggling to match their detailed properties (*e.g.* Cowley et al. 2017). SMGs growing in the dense environments of proto-clusters are expected to have formed earlier, be more massive, and undergo major-mergers more frequently than their field galaxy counterparts (Overzier 2016).

Furthermore, the enormous build up of mass in galaxy clusters makes them critical when investigating large-scale structures in the universe and can help constrain cosmological parameters (*e.g.* Wen and Han 2011). Understanding their origins, *i.e.*

proto-clusters, is likewise important. Galaxy (proto-)clusters are additionally interesting laboratories in which the mass budget of galaxies in dense environments as well as that of the cluster itself can be studied.

In this chapter we study the high-redshift proto-cluster SPT2349. SPT2349 is the most spectacular object of its kind in the SPT sample, and, arguably, in the universe. Its number density, 14 SMGs in a $\sim 1'$ diameter circle, far exceeds that of any other proto-cluster observed to date. Our analysis expands on the foundation set by Miller et al. (2018). In Sect. 3.2 we will describe the ALMA continuum imaging and spectral analysis conducted. In Sect. 3.3 we present the results of modelling the far-IR emission as a modified black-body, various star formation rate tracers, estimates of masses, and a mass fraction analysis. A discussion of the findings and the final conclusions are made in Sect. 3.4 and 3.5.

3.2 ALMA Data

Miller et al. (2018) outline the multitude of follow-up observations that were conducted for SPT2349 and we briefly mentioned some of them in Sect. 3.1.1. Additional imaging from the Infrared Array Camera (IRAC) mounted on *Spitzer* and from the Spectral and Photometric Imaging Receiver (SPIRE) mounted on *Herschel* as well as spectroscopy from the Australia Telescope Compact Array (ATCA) were studied in Miller et al. (2018). The follow-up observations are summarized in Table 3.1. Each of the 14 sources in the core of SPT2349 has a secure spectroscopic redshift determined from the CO(4-3) line or, if CO(4-3) was not detected, from the [C II] line.

The fainter sources of SPT2349 were not detected in all observations, so deeper

Table 3.1: Summary of follow-up observations published by Miller et al. (2018)

Telescope-Camera	Continuum/Line	Wavelength/Rest Freq.
APEX-LABOCA	continuum	$\lambda = 870\,\mu$m
ALMA	continuum	$\lambda = 1.1\,$mm & 3 mm
Spitzer-IRAC CH1 & CH2	continuum	$\lambda = 3.6\,\&\,4.5\,\mu$m
Herschel-SPIRE	continuum	$\lambda = 250,\ 350,\ 500\,\mu$m
ALMA cycle 3 band 3	CO(4-3)	$\nu_{\rm rest} = 461.041$ GHz
ALMA cycle 4 band 7	[C II]	$\nu_{\rm rest} = 1900.5$ GHz
ATCA	CO(2-1)	$\nu_{\rm rest} = 230.5380$ GHz

ALMA observations were proposed and granted. These are the observations this work focuses on. Band 7, targeting [C II] ($\nu_{\rm rest}$ = 1900.5 GHz) and [N II] ($\nu_{\rm rest}$ = 1461.134 GHz) in two different tunings, was observed on 2018-08-25 (PI: S.C. Chapman). Band 4 containing the H_2O line ($\nu_{\rm rest}$ = 752.051 GHz) was originally observed on 2016-03-20 (PI: K. Lacaille) and then later followed-up with observations on 2018-10-03 (PI: S.C. Chapman).

ALMA, an interferometer, observes the sky in the u, v-plane (Fourier domain) and records the so-called "visibilities" - the Fourier transform of the true brightness of the sky (in the x, y-plane) convolved with the point spread function. The ALMA data cube is a series of visibilities observed over a range of frequencies. The incomplete sampling in the u, v-plane (due to a finite number of antennae, *i.e.* ALMA dishes) results in sidelobes of the point spread function which leads to structure in the "dirty image" in the x, y-plane that needs to be removed. The Common Astronomy Software Applications package (CASA, McMullin et al. 2007) version 5.1.1 and older was used to reduce our ALMA data using the standard ALMA reduction pipeline. This consists of 1) calibrating the observed visibilities (Fourier domain observations). Some of the calibrations applied are bandpass calibrations (frequency-dependent gain variations), gain calibrations (time-dependent variations in antenna gain), dealing with the effects of the atmosphere, and general delays in the electronics and offsets in the antenna positions. 2) Computing the Fourier transform to create a "dirty image" - a map of point spread functions with sidelobes in the x, y-plane. 3) Iteratively cleaning the image. Step 3 consists of 3i) initializing a "model image" as a map of point sources, delta functions or gaussians, whose intensity is a fraction of that of the brightest pixel in each region of the dirty image, 3ii) convolving the model image with the "dirty beam" - the point spread function, 3iii) subtracting the convolved model image from the dirty image, 3iv) identifying new locations of peak brightness in the residual map and adding fractions of their intensity to the model image, 3v) repeating steps ii-iv, replacing the dirty image with the residuals from the previous iteration until the noise level of the residual map meets a desired threshold, and finally 3vi) convolving the resulting model image with the "clean beam" - an elliptical gaussian whose central region fits that of the dirty beam, and adding the final residual map to produce the "clean image." 4) The cleaned image is scaled to correct for the radial dependence

in the sensitivity of the image caused by the "primary beam" - a gaussian whose full width at half max (FWHM) is $\theta = 1.13\lambda/D$, where λ is the wavelength and D is the effective diameter of the interferometer. Lastly, 5) the data cube of primary beam corrected images is collapsed into a single continuum image - a linear (median) combination of each pixel along the spectral axis.

The reference wavelength of the three continuum images created are 851 μm, 1.06 mm, and 2.02 mm respectively. A summary including the final beam size and image RMS can be found in Table 3.2. Fig. 3.2 shows the three continuum images in grey-scale on the left. The band 7 continuum is drawn as green contours and band 7 centred on the [C II] emission is drawn as purple contours to identify the 14 sources in SPT2349. They are labelled A-N in descending order of their SPT 1.1 mm flux. A false-colour composite using the three continuum colours is shown on the far right.

Table 3.2: ALMA continuum imaging

Band	Reference Wavelength	Targeted Line	Beam Size RA, DEC [″]	RMS [mJy/beam]	Date
B7	851 μm	[C II]	0.55, 0.48	0.036	2018-08-25
B7	1.06 mm	[N II]	0.59, 0.55	0.017	2018-08-25
B4	2.02 mm	H_2O	0.29, 0.25	0.013	2016-03-20 & 2018-10-03

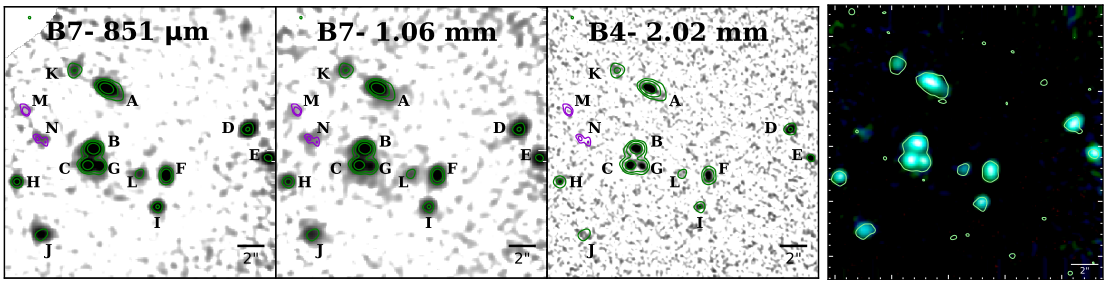

Figure 3.2: *From Left to Right*: ALMA B7 851 μm, ALMA B7 1.06 mm, and ALMA B4 2.02 mm images of SPT2349, and ALMA false-colour composite of the three previous images on a log-scale. The green contours are drawn at 4σ, 10σ, and 30σ of the ALMA B7 continuum. The purple contours are drawn at 3σ and 4σ of the ALMA B7 image centred on the [C II] emission.

3.2.1 Continuum Fluxes

Continuum fluxes at 851 μm, 1.06 mm, and 2.02 mm were determined for each of the 14 sources in SPT2349 using the new, deep imaging. The optimal aperture size is one which is large enough to encompass the total flux while remaining small enough so that the signal-to-noise ratio (SNR) is not artificially inflated. For each source in each band, an aperture was manually drawn around the peak near the 1σ level such that an increased aperture size would result in a variation in the flux of less than ~ 5 % for the brightest sources and ~ 10 % for the intermediately bright sources. In this way the total flux of resolved sources is captured. For the faintest, unresolved sources where a peak flux was used, the flux is not affected by aperture size. In band 4, the aperture size has a greater affect on the extracted flux, ~ 15 % and ~ 30 % for the brightest and intermediately bright sources, respectively. This is likely due to negative structures from the point spread function directly around bright objects introduced during CASA's CLEAN procedure.

The flux was extracted using CASA's IMSTAT function. The continuum images were created by collapsing the data cubes and therefore contain both the pure continuum as well as emissions from any spectral features that fall within the wavelength range of the data cube. The integrated line fluxes of the appropriate emission feature therefore need to be subtracted from the continuum. The [C II] line fluxes, which we adopt from Hill (in prep.), were subtracted from the continuum of band 7 centred on 851 μm, yielding a pure $S_{851\,\mu\mathrm{m}}$. Detections of the [N II] line in band 7 centred on 1.06 mm are weak with low SNR. We therefore do not adjust $S_{1.06\,\mathrm{mm}}$. Band 4 contains both H_2O and C I, neutral carbon ($\nu_{\mathrm{rest}} = 809$ GHz). The H_2O line is discussed in more detail in Section 3.3.2. We adopt the C I line fluxes from Hill (in prep.). We subtract both the H_2O and the C I line fluxes from the band 4 continuum yielding a pure $S_{2.02\,\mathrm{mm}}$. Source ID, redshifts adopted from Miller et al. (2018), and continuum fluxes for the 14 sources are presented in columns $1-5$ of Table 3.3. The errors listed are the RMS of the source and of the image added in quadrature. The RMS of the source is dependent on the size of the source and the RMS of "blank" space in the immediate surroundings, while the RMS of the image is determined by the previously mentioned IMSTAT function.

Many of the sources, especially the brighter ones, are resolved in our deep imaging,

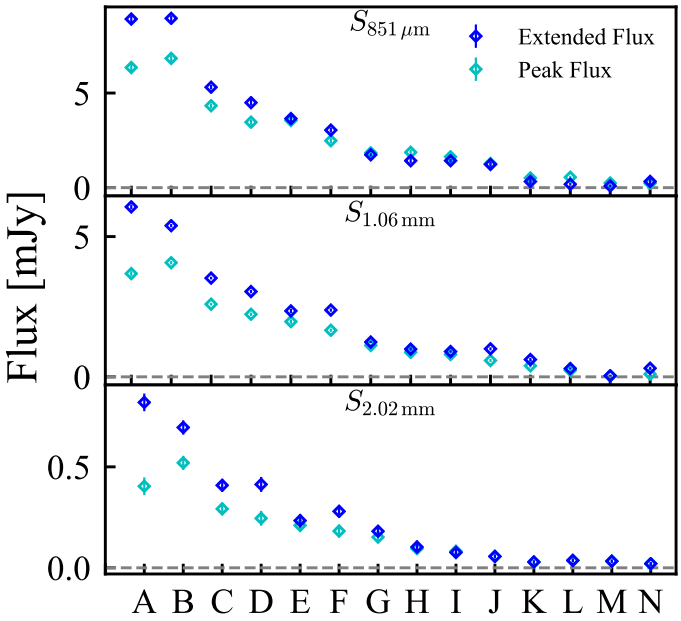

Figure 3.3: Flux comparison between line subtracted continuum fluxes in blue and peak fluxes in cyan for the 14 sources. *Top*: 851 μm, *Middle*: 1.06 mm, and *Bottom*: 2.02 mm. For the extended source, if SNR < 3 we revert to using peak fluxes.

i.e. are larger than the beam size. They appear as extended sources as opposed to point sources. Fig. 3.3 compares the line subtracted extended fluxes (blue) and peak fluxes (cyan) of each source across all three bands. This comparison clearly highlights those sources that are resolved (sources A, B, C, D, and F), *i.e.* where the extended and peak flux differ from each other, and distinguishes them from the fainter sources that still appear as point sources, *i.e.* extended and peak fluxes are virtually identical. If the SNR < 3 for the extended flux we revert to using peak fluxes. This is only done for sources J-N in the band 4 colour and for source M in all colours. With deeper data available to us, these new continuum fluxes supersede the Miller et al. (2018) fluxes, which generally were fainter. However, the slight increase in flux we observe mainly affects the brighter sources as the fainter sources remain predominantly unresolved.

3.2.2 Spectral Analysis

CO(4-3) and [C II] spectra were presented in Miller et al. (2018). Here we focus on the water line. Line fluxes for H_2O are determined via the same method as in Miller et al. (2018) wherein one-dimensional spectra are extracted at the centroid of

Table 3.3: Continuum and line fluxes for the 14 sources in SPT2349.

Source	z [a]	$S_{851\,\mu\mathrm{m}}$ [b] [mJy]	$S_{1.06\,\mathrm{mm}}$ [b] [mJy]	$S_{2.02\,\mathrm{mm}}$ [b] [mJy]	$H_2O \int S\mathrm{dv}$ [c] [Jy km s^{-1}]	CI $\int S\mathrm{dv}$ [c] [Jy km s^{-1}]	[CII] $\int S\mathrm{dv}$ [c] [Jy km s^{-1}]
A	4.3024	8.91 ± 0.19	6.06 ± 0.08	0.819 ± 0.04	0.219 ± 0.027	0.27 ± 0.27	16.86 ± 0.2
B	4.3018	8.95 ± 0.15	5.39 ± 0.06	0.695 ± 0.03	0.235 ± 0.011	0.49 ± 0.13	7.89 ± 0.12
C	4.3147	5.31 ± 0.12	3.52 ± 0.05	0.409 ± 0.03	0.361 ± 0.025	0.5 ± 0.08	6.08 ± 0.11
D	4.3034	4.49 ± 0.14	3.04 ± 0.06	0.413 ± 0.04	0.0156 ± 0.0039	0.42 ± 0.22	5.93 ± 0.15
E	4.3055	3.65 ± 0.18	2.35 ± 0.08	0.234 ± 0.03	0.062 ± 0.011	0.42 ± 0.15	3.68 ± 0.12
F	4.3110	3.04 ± 0.13	2.38 ± 0.06	0.280 ± 0.03	0.036 ± 0.007	0.26 ± 0.12	5.19 ± 0.15
G	4.2986†	1.74 ± 0.08	1.24 ± 0.04	0.181 ± 0.02	< 0.026	-	1.83 ± 0.08
H	4.2913†	1.42 ± 0.14	0.99 ± 0.06	0.103 ± 0.03	< 0.025	0.17 ± 0.08	2.95 ± 0.1
I	4.3095	1.43 ± 0.10	0.90 ± 0.04	0.076 ± 0.02	< 0.028	0.14 ± 0.09	3.35 ± 0.11
J	4.2955	1.23 ± 0.13	1.00 ± 0.05	0.056 ± 0.01	< 0.02	-	8.82 ± 0.13
K	4.3152†	0.32 ± 0.16	0.62 ± 0.06	0.029 ± 0.01	< 0.021	-	3.76 ± 0.09
L	4.2973†	0.18 ± 0.07	0.30 ± 0.04	0.036 ± 0.01	< 0.022	-	2.7 ± 0.11
M	4.3046†	0.09 ± 0.08	0.04 ± 0.02	0.033 ± 0.01	< 0.069	-	0.89 ± 0.08
N	4.3056†	0.33 ± 0.15	0.31 ± 0.05	0.020 ± 0.01	< 0.081	-	1.7 ± 0.08
Sum	4.30	41.1 ± 0.5	28.1 ± 0.2	3.38 ± 0.10	0.929 ± 0.041	2.67 ± 0.443	71.63 ± 0.45

[a] Redshifts were determined from CO(4-3) or, if not detected in CO(4-3), from [C II]. Redshifts determined from [C II] are identified with a †. Adopted from Miller et al. (2018).

[b] 851 μm, 1.06 mm, and 2.02 mm fluxes are line-subtracted continuum fluxes.

[c] H_2O, C I, and [C II] fluxes are integrated line fluxes. C I and [C II] line fluxes are adopted from Hill (in prep.).

each source. The channel widths from the CASA reduction pipeline are ~ 32 km s^{-1}. The emissions are further binned such that the SNR is maximized. Source A and C are binned into channel widths of 64 km s^{-1} and sources M and N are binned into channel widths of 96 km s^{-1} while the remaining sources are not binned past their initial extraction channel widths. The background continuum levels are determined by fitting a linear regression to the flux, excluding the region which contains the H_2O line. The background continuum is then subtracted from the spectrum. Single- or double-gaussians, where appropriate, are fit and integrated over 3 standard deviations of the gaussian to either side of the mean. Errors to the integrated line fluxes ($\sigma_{\rm line}$) are given by the RMS of the line free spectra ($\sigma_{\rm channel}$) multiplied by the channel width (Δv) and the square root of the number of channels ($\sqrt{N_{\rm channel}}$), $\sigma_{\rm line} = \sigma_{\rm channel}\Delta v\sqrt{N_{\rm channel}}$. In the case of a non-detection, this line error is used as an upper limit to the flux. The H_2O spectra are presented in Fig. 3.4 (yellow), alongside CO(4-3) (grey) and [C II] (purple), which are scaled down by factors of 20 and 2 respectively for ease of viewing. The H_2O line is only detected in sources A-F. For all but source D the detection is strong with SNR > 5. Source D is detected at a more moderate SNR > 4. Source B has the most robust detection with SNR > 21. Integrated line fluxes are presented in column 6 in Table 3.3.

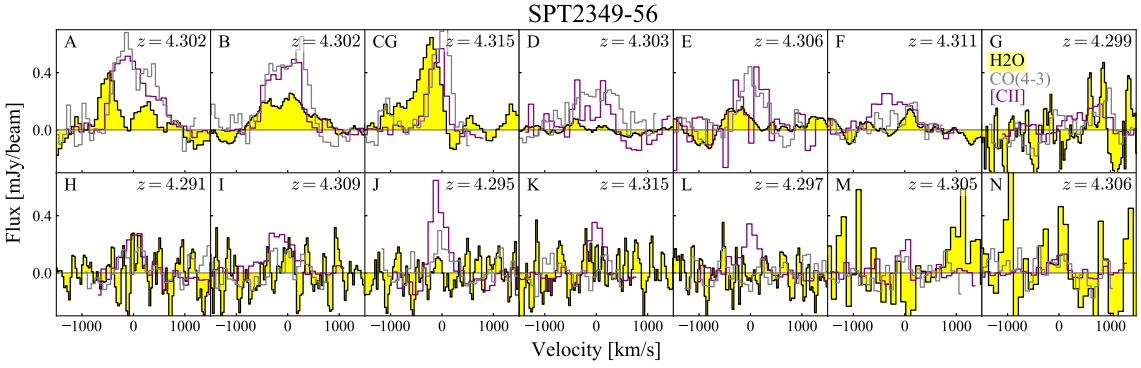

Figure 3.4: H_2O in SPT2349. Spectra are binned to maximize the SNR. CO(4-3) and [C II] lines are scaled down by factors of 20 and 2 respectively for ease of viewing.

3.3 Results - Astrophysical Properties

3.3.1 Modified Black-Body Fitting

As discussed in the Introduction (Sect. 1.2.1), the thermal dust emission of a galaxy in the far-IR is commonly modelled as a modified black-body (MBB) and can help ascertain various properties including dust temperature, $T_{\rm dust}$, and infrared luminosities, $L_{\rm IR}$. The two parameters of the modified black-body in our analysis are $T_{\rm dust}$ and the spectral dust emissivity index, β. $T_{\rm dust}$ primarily affects the peak of the MBB while β predominantly affects the slope of the Rayleigh-Jeans tail.

The difference between the effects of the two parameters $T_{\rm dust}$ and β can be seen in Fig. 3.5. The left panel keeps $\beta = 2$ constant while adjusting $T_{\rm dust}$ over a range of values, $\sim 25 - 55$ K (blue-red colour scale). This temperature range was chosen as Greve et al. (2012) found the median dust temperature of unlensed SMGs in the SPT sample to be ~ 34 K, while Strandet et al. (2016) found a marginally warmer $T_{\rm dust}$ at $\sim 39 \pm 10$ K for the sub-sample they considered. In the figure we see that as temperature increases, the MBB peak shifts towards shorter wavelengths. This highlights the well-known degeneracy between $T_{\rm dust}$ and $(1 + z)$ (*e.g.* Blain et al. 2002; Greve et al. 2012), which shifts the SED of a galaxy in accordance with $\lambda_{\rm obs} = \lambda_{\rm rest}(1 + z)$. For the right panel $T_{\rm dust} = 46.7$ K is kept constant (as found previously for SPT2349 by Strandet et al. 2016) while β is allowed to range from $\sim 1 - 2.5$ (blue-red colour scale). As β increases, so does the steepness of the Rayleigh-Jeans tail, while the wavelength of the peak remains largely unchanged.

The fluxes in Fig. 3.5 at 851 μm, 1.06 and 2.02 mm (orange diamonds) are a summation of the 14 SMGs in the core of SPT2349. SPIRE fluxes at 250, 350, and 500 μm (green arrows) from Miller et al. (2018) are also included. The resolution of SPIRE is too low ($\sim 18''$, $24''$, and $35''$ for the three bands respectively) to resolve the individual sources. Furthermore the SPIRE flux is confused with a neighbouring source at $z \sim 1$ peaking at $\sim 250\,\mu$m. The 250, 350, and 500 μm fluxes are therefore upper limits and are a summation of the 14 SPT2349 sources. Despite this, they were included in an attempt to help constrain the MBB fitting. The SEDs are normalized to the summed 1.06 mm flux. In both plots, a simple error-weighted least squares minimization of the three ALMA fluxes and the SPIRE 350 and 500 μm flux is applied

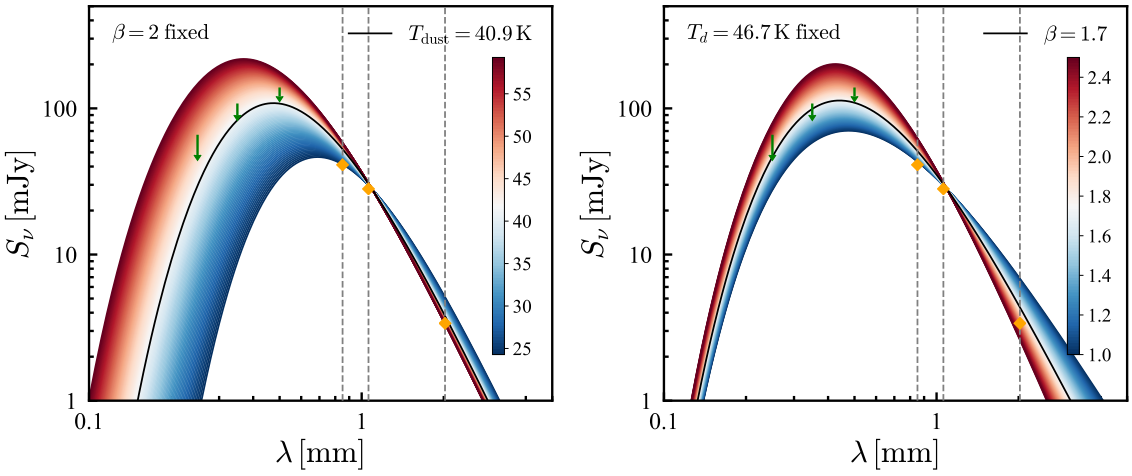

Figure 3.5: *Left*: Modified blackbodies ranging over $T_{\rm dust} \sim 25 - 55$ K while keeping $\beta = 2$ constant. *Right*: Modified blackbodies ranging over $\beta \sim 1 - 2.5$ while keeping $T_{\rm dust} = 46.7$ K constant (Strandet et al. 2016). The greybodies are redshifted to $z = 4.3$ and normalized to $S_{1.06\,\rm mm}$. ALMA 851 μm, 1.06 mm, and 2.02 mm fluxes (orange diamonds) are summed over all 14 sources. The SPIRE 250, 350, and 500 μm fluxes (green arrows) are identified as upper limits as discussed in the text. An error-weighted least squares analysis identifies the MBB with $T_{\rm dust} = 40.9$ K to be the best fit in the *left* panel and $\beta = 1.7$ in the *right* panel.

to determine the MBB which best fits the data, drawn in bold black. The SPIRE 250 μm was omitted from the least squares minimization due to the neighbouring low-z source peaking at this wavelength. When keeping $\beta = 2$ constant we find an upper limit of $T_{\rm dust} \leq 40.9$ K, which is colder compared to the old value of 46.7 K for SPT2349 but matches the median value of 39 ± 10 K (Strandet et al. 2016). Conversely if we fix $T_{\rm dust} = 46.7$ K we find that $\beta \leq 1.7$ best matches the data, but if we fix $T_{\rm dust}$ to the new 40.9 K we find that $\beta \leq 1.9$ best matches the data.

If we want to fit a MBB to the 14 sources individually, we are left with just the ALMA fluxes as the SPIRE fluxes cannot be resolved and separated. Unfortunately, the ALMA wavelengths lie along the Rayleigh-Jeans tail. $T_{\rm dust}$ is therefore unconstrained and any fitting attempts without additional resolved, shorter wavelength data can produce somewhat random results. Conversely, fitting while allowing β to vary can yield meaningful results as it is the slope of the Rayleigh-Jeans tail that affects β. We set $T_{\rm dust}$= 40.9 K and find the median and standard deviation to be 1.7 ± 0.4, unchanged from the upper limit determined when including the SPIRE

fluxes.

As an initial diagnostic of the variations across the 14 sources, a colour-colour diagram can be considered, see Fig. 3.6. The ratio between $S_{851\,\mu\mathrm{m}}$ and $S_{2.02\,\mathrm{mm}}$ is plotted as a function of $S_{1.06\,\mathrm{mm}}$. We chose this ratio, instead of one including $S_{1.06\,\mathrm{mm}}$, because it highlights any deviations from the mean to a greater extent due to the large difference in wavelength. The mean flux ratio is shown as a green horizontal line. The shaded region represents 1 standard deviation of the mean when all 14 sources are considered, 11.5 ± 5.3 (unit-less). We find that sources with $S_{1.06\,\mathrm{mm}} \gtrsim 1$ mJy, within error, exhibit the same colour, 11.5 ± 1.7 (unit-less). Colour is directly correlated to T_{dust}, the majority of the SPT2349 sources should therefore have very similar dust temperatures. The large flux ratio error for sources with $S_{1.06\,\mathrm{mm}} \lesssim 1$ mJy further confirms that our constraints on T_{dust} are poor and individual MBB fitting is ill-advised.

Besides T_{dust}, the other property that can be ascertained from MBB fitting is the IR luminosity. L_{IR} is the integrated luminosity from $8 - 1,100\,\mu$m and therefore measures the luminosity of the thermal dust emission. Unfortunately, any uncertainty in our spectral shape due to an unconstrained T_{dust} will carry forward into

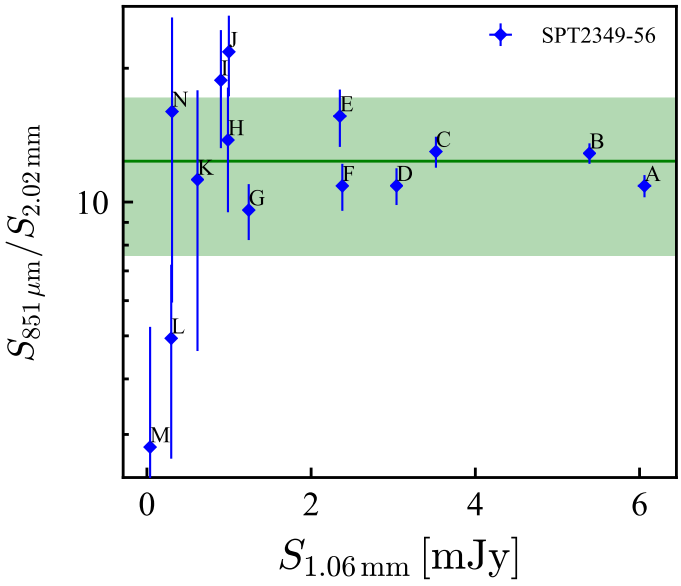

Figure 3.6: Colour-colour diagram for the 14 SPT2349 sources. The mean flux ratio is shown as a green horizontal solid line. The shaded region represents 1 std. dev. of the mean. Sources with $S_{1.06\,\mathrm{mm}} \gtrsim 1$ mJy, within error, have the same colour.

$L_{\rm IR}$ calculations. We therefore choose to adopt a spectral shape for an average $T_{\rm dust}$ appropriate to SMGs. Specifically, the SMG population discussed by Swinbank et al. (2013) display a correlation between $L_{870\,\mu{\rm m}}$ and $L_{\rm IR}$. We determine a conversion using the Swinbank et al. (2013) sample and apply it to our own $L_{851\,\mu{\rm m}}$ (calculated from $S_{851\,\mu{\rm m}}$ using the inverse square law),

$$\log\left(L_{\rm IR}/{\rm L}_\odot\right) = 0.964\log\left(L_{851\,\mu{\rm m}}/{\rm L}_\odot\right) + 1.58, \tag{3.1}$$

where $L_{\rm IR}$ and $L_{851\,\mu{\rm m}}$ are given in $\rm L_\odot$. We find the cumulative IR luminosity for SPT2349 to be $L_{\rm IR} = (1.024 \pm 0.013) \times 10^{14}$ $\rm L_\odot$. $L_{851\,\mu{\rm m}}$ and $L_{\rm IR}$ for our 14 sources are presented in Appendix G Table G.1.

3.3.2 Star Formation Rates

The star formation rate (SFR) is defined by the cumulative mass (measured in $\rm M_\odot$) of new stars that formed over the span of a year. Starbursts frequently have SFRs upwards of 100 $\rm M_\odot\ yr^{-1}$. The 14 sources of SPT2349 are expected to form stars at even higher rates than their $z \sim 2$ counterparts because they are evolving in a dense environment and are likely undergoing major-mergers which trigger star formation. A variety of methods have been used in the past to estimate SFRs, a number of which are discussed by Kennicutt (1998). Unfortunately, as SMGs are heavily dust-obscured, a direct measure of its stellar light across the UV and optical is not possible. Other methods have therefore been sought, we explore a few of them, all of which simplify to a correlation between the star formation rate and varying luminosities.

We have shown in the last chapter that luminosities and fluxes are related via the relation $L_\nu = 4\pi D_L^2 S_\nu$. Thus far we have calculated luminosities from continuum fluxes. For the following analysis, we also deal with line luminosities stemming from spectral emission features and their integrated line fluxes. Solomon et al. (1997) show that line luminosities can be calculated using a modified inverse-square law:

$$L_{\rm line} = 1.04 \times 10^{-3} S_{\rm line} \frac{\nu_{\rm rest}}{(1+z)} D_L^2, \tag{3.2}$$

where $L_{\rm line}$ is the line luminosity in $\rm L_\odot$, the factor 1.04×10^{-3} includes the typical 4π term as well as unit conversions, $S_{\rm line}$ is the integrated line flux in Jy km $\rm s^{-1}$,

$\nu_{\rm rest}/(1+z)$ is the rest frequency in GHz of the spectral line redshifted to the observed frequency, and D_L is the luminosity distance in Mpc. Line luminosities for both the H_2O and [C II] lines for our 14 sources are presented in Appendix G Table G.1. In some instances it is preferable to express the line luminosity as a so-called brightness temperature, which scales as $D_L^2/(1+z)^3$ as opposed to simply D_L^2 (Solomon et al. 1997, & references therein),

$$L'_{\rm line} = \frac{c^2}{2k} S_{\rm line} \frac{D_L^2}{\nu_{\rm rest}^2 (1+z)}, \tag{3.3}$$

where $L'_{\rm line}$ is the line luminosity expressed as a brightness temperature and has units K km s^{-1} pc^2, c is the speed of light, and $k = 1,380$ Jy m^2 K^{-1} (a unit conversion factor). Of the two line luminosity representations, our analysis will rely on the "regular" line luminosity in units of $L_\odot$ (eq. 3.2) except when explicitly stated when determining brightness ratios between lines, in which case we will use the brightness temperature line luminosity (eq. 3.3).

SFR-$L_{\rm IR}$ Correlation

One of the most commonly used approaches to determine the star formation rate of a SMG is to take advantage of the correlation between $L_{\rm IR}$ and SFR. The absorption cross-section of interstellar dust is strongly peaked in the UV, the thermal dust re-emission in the IR is therefore a tracer of the UV radiation field dominated by young, hot stars (Kennicutt 1998). Under the assumption of high dust opacity, thus primarily a method reserved for starbursts, and the adoption of a stellar age ($\sim 10-100$ Myrs), the IR luminosity can be converted into a SFR. The original calibration done by Kennicutt (1998) was later updated by Buat et al. (2010) and adopted by, among others, Sargsyan et al. (2012). It takes the form,

$$\log\left({\rm SFR_{IR}}/{\rm M_\odot\,yr^{-1}}\right) = \log\left(L_{\rm IR}/{\rm L_\odot}\right) - 9.76. \tag{3.4}$$

As discovered by Blain and Longair (1993) and later applied by Barger et al. (2014), this SFR-$L_{\rm IR}$ relation is essentially redshift-independent for $z > 1.5$. Furthermore, by applying a spectral shape similar to Arp 220 (a starburst undergoing a major-merger), Barger et al. (2014) found that the SFR can be estimated from just the 850 μm flux.

This has the advantage of no longer needing to integrate across the entire IR spectrum. While Barger et al. (2014) found a mean conversion factor of 200 for high-z galaxies, we adopt (as was done by Miller et al. 2018) the more modest conversion factor of 150 found by Cowley et al. (2017) for high-z starbursts: $\mathrm{SFR}_{851\,\mu\mathrm{m}} = 150 \times S_{851\,\mu\mathrm{m}}$, where $S_{851\,\mu\mathrm{m}}$ is in mJy. We find $\mathrm{SFR}_{851\,\mu\mathrm{m}}$ to range between $\sim 14 - 1,300$ $\mathrm{M}_\odot$ yr^{-1} for the 14 SPT2349 sources, with a cumulative $\mathrm{SFR}_{851\,\mu\mathrm{m}}$ of $6,163 \pm 76$ $\mathrm{M}_\odot$ yr^{-1}.

It is important to note that while the luminosity of the IR spectrum is dominated by the thermal dust emission, other sources such as an active galactic nucleus (AGN) can contribute to it, thereby artificially inflating $\mathrm{SFR}_{\mathrm{IR}}$. However, our conversion uses $\mathrm{SFR}_{851\,\mu\mathrm{m}}$ as a proxy, not the entire integrated IR spectrum. Furthermore, in our previous analysis we found T_{dust} to be cold at < 40.9 K. $S_{851\,\mu\mathrm{m}}$ and all properties derived from it, *i.e.* $L_{851\,\mu\mathrm{m}}$, L_{IR}, and $\mathrm{SFR}_{851\,\mu\mathrm{m}}$, therefore sample the cold dust component which is only marginally heated by a possible AGN. Both L_{IR} and $\mathrm{SFR}_{851\,\mu\mathrm{m}}$ in our analysis are therefore not artificially inflated even though an AGN may be present.

The [C II] *Line as a Tracer of SFR*

Another method is to use the [C II] line as a tracer of SFR. Sargsyan et al. (2012) demonstrate empirically that [C II] is associated with photodissociation regions surrounding starburst activity and is therefore an excellent diagnostic of the SFR, especially for high-z galaxies in which [C II] is a strong emission line in the IR. Photoionization and photoelectric heating models for [C II] (Stacey et al. 1991; Hollenbach and Tielens 1999; Malhotra et al. 2001; Abel et al. 2009) have demonstrated the same. Importantly, Sargsyan et al. (2012) determine that the [C II] flux is independent of an AGN presence. While the integrated IR luminosity is therefore a combination of both AGN and star formation contributions, the [C II] line luminosity, $L_{[\mathrm{C\,II}]}$, measures the starburst luminosity only and is a direct probe of the SFR, unaffected by AGN presence. This is a critical finding as starbursts frequently host AGN and their SFRs determined from L_{IR} may be artificially inflated if not treated properly. By comparing $L_{[\mathrm{C\,II}]}$ to L_{IR} of starbursts, Sargsyan et al. (2012) determine a calibration

that can be incorporated into the earlier SFR-$L_{\rm IR}$ relation,

$$\log\left(\mathrm{SFR}_{[\mathrm{C\,II}]}/\mathrm{M}_\odot\,\mathrm{yr}^{-1}\right) = \log\left(L_{[\mathrm{C\,II}]}/\mathrm{L}_\odot\right) - 7.08 \pm 0.3. \tag{3.5}$$

The error in the relation is the 1σ dispersion among starbursts. Despite having been derived from starbursts without AGN components, this relation holds for sources containing AGN as well. Furthermore, Sargsyan et al. (2012) find that the largest SFRs arise from starbursts despite not having the brightest $L_{\rm IR}$, *i.e.* the presence of an AGN may be boosting $L_{\rm IR}$ while the SFR remains unchanged. Adopting this relation for the SPT2349 sources we find $\mathrm{SFR}_{[\mathrm{C\,II}]}$ to range from $\sim 40-830$ $\mathrm{M}_\odot$ yr^{-1} (a narrower range than that found from $S_{851\,\mu\mathrm{m}}$), with a cumulative $\mathrm{SFR}_{[\mathrm{C\,II}]}$ of $3,526\pm22$ $\mathrm{M}_\odot$ yr^{-1}.

The top panel in Fig. 3.7 compares the $L_{[\mathrm{C\,II}]}$-to-$L_{\rm IR}$ ratio of the 14 SPT2349 sources to other high-z SMGs (Gullberg et al. (2015) as well as a few additional individual high-z sources compiled by Gullberg et al. 2015). The Gullberg et al. (2015) sample consists of SMGs discovered by SPT. We find the SPT2349 sources to track well with the other SMGs. Sargsyan et al. (2012) make a point of highlighting the "[C II] deficit," in which $L_{[\mathrm{C\,II}]}$ is weak compared to $L_{\rm IR}$. They state that while the explanation for this deficit remains an ongoing question for the general population of starbursts, for their sample they found the most IR luminous sources to be powered by AGN (thereby increasing $L_{\rm IR}$) but lacking in photodissociation regions (therefore presenting diminished $L_{[\mathrm{C\,II}]}$). They stress that only the most luminous AGN present a [C II] deficit, so while a [C II] deficit indicates the presence of a strong AGN, the presence of an AGN does not necessarily result in a [C II] deficit. However, virtually all their sources with $L_{\rm IR} > 10^{12}$ $\mathrm{L}_\odot$ have a [C II] deficit. This is also true for SMGs independent of AGN presence. Sources A-I with $L_{\rm IR} > 10^{12}$ $\mathrm{L}_\odot$ all present the [C II] deficit compared to the less luminous sources K-N. Source J is the only $L_{\rm IR} > 10^{12}$ $\mathrm{L}_\odot$ source which does not present the [C II] deficit.

The H_2O Line as a Tracer of SFR

The water line is another emission feature that has been used as a tracer of SFRs. Omont et al. (2013) studied numerous $\mathrm{H_2O}$ lines in high-z ultra-luminous IR galaxies.

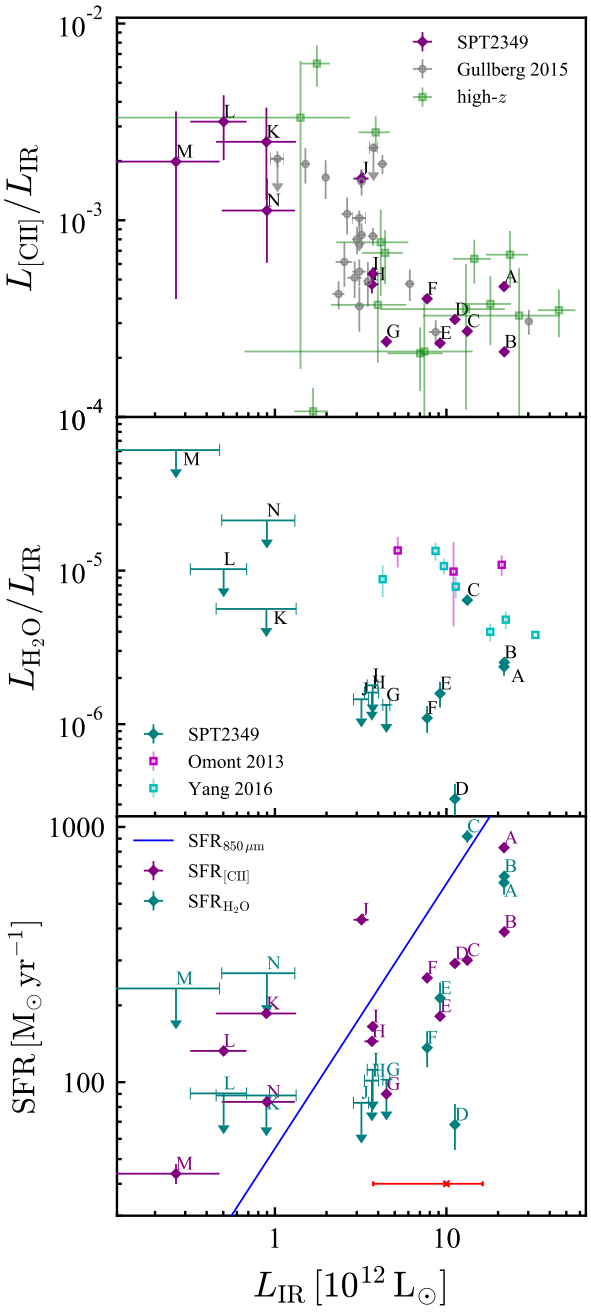

Figure 3.7: *Top*: Luminosity ratio of the [C II] line with $L_{\rm IR}$ highlighting the [C II] deficit at $L_{\rm IR} > 10^{12}$ L$_\odot$. SPT2349 are shown as purple diamonds, Gullberg et al. (2015) SMGs are grey circles, and other high-z sources are shown as green squares. *Middle*: Luminosity ratio of the H_2O line with $L_{\rm IR}$. SPT2349 (teal diamonds) is compared to samples presented by Omont et al. (2013) (magenta squares) and Yang et al. (2016) (cyan squares). *Bottom*: Comparison of SFRs estimated from $S_{851\,\mu\rm m}$ (blue line), the [C II] line luminosities (purple diamonds), and the H_2O line luminosities (teal diamonds) as a function of $L_{\rm IR}$. The red error bar represents the average $L_{\rm IR}$ error for the 14 SPT2349 sources.

They found that the H_2O lines are some of the strongest molecular lines in starbursts. Yang et al. (2013) found the H_2O line luminosity, L_{H_2O}, and L_{IR} to be tight correlated,

$$\log\left(L_{H_2O}/L_\odot\right) = \alpha \log\left(L_{IR}/L_\odot\right) + \beta, \tag{3.6}$$

where $\alpha = 1.21 \pm 0.04$ and $\beta = -7.72 \pm 0.49$ for the $\nu_{rest} = 752$ GHz water line. Similar to the [C II] line this can be incorporated in the SFR-L_{IR} relation for an H_2O calibration,

$$\log\left(SFR_{H_2O}/M_\odot\,yr^{-1}\right) = \frac{1}{1.21 \pm 0.04} \log\left(L_{H_2O}/L_\odot\right) - 3.59 \pm 0.4. \tag{3.7}$$

We find SFR_{H_2O} to range from $\sim 70 - 920$ $M_\odot$ yr^{-1} for the 14 SPT2349 sources (similar to the $SFR_{[C\,II]}$ range), with a cumulative SFR_{H_2O} of $2,583 \pm 94$ $M_\odot$ yr^{-1} for the six detections. This is in comparison to the cumulative $SFR_{[C\,II]}$ for the same six sources of $2,247 \pm 17$ $M_\odot$ yr^{-1}. The middle panel in Fig. 3.7 plots the L_{H_2O}-to-L_{IR} ratio for SPT2349, the Omont et al. (2013) sample, and the Yang et al. (2016) sample. We use the same SFR-L_{IR} relation for both our own H_2O lines as well as those published by Omont et al. (2013) and Yang et al. (2016). The H_2O line was not detected for sources G-N and appear as upper limits in the figure. For the sources with H_2O detections, only the three brightest (sources A, B, and C) have L_{H_2O}-to-L_{IR} ratios that match the comparison samples. The remaining three (sources D, E, and F) have significantly fainter H_2O luminosities. We therefore determine that the H_2O line is not a robust tracer of SFR, especially if only a single, low-J H_2O line is used. Omont et al. (2013) and Yang et al. (2016) used numerous H_2O lines, importantly including higher-J transitions, and are therefore able to produce more reliable SFRs.

SFR Comparisons

The bottom panel in Fig. 3.7 compares the three methods of estimating SFRs discussed. $SFR_{851\,\mu m}$ and L_{IR} are both scalings from $S_{851\,\mu m}$ and so their relation is linear, shown as the blue line in the figure. SFR_{CII} (purple diamonds) has a slightly less steep slope than $SFR_{851\,\mu m}$. We find the brightest sources to have a decreased SFR_{CII} as compared to $SFR_{851\,\mu m}$, while on the fainter end SFR_{CII} is larger than $SFR_{851\,\mu m}$. SFR_{H_2O} (teal diamonds) has a similar trend to that of SFR_{CII}.

If we compare $\mathrm{SFR}_{\mathrm{H_2O}}$ and $\mathrm{SFR}_{\mathrm{CII}}$ to each other, we find a median ratio of 0.7 with sources C, M, and N having ratios > 2.5. The H_2O line was not detected in sources M and N and so their $\mathrm{SFR}_{\mathrm{H_2O}}$ is an upper limit. Their true $\mathrm{SFR}_{\mathrm{H_2O}}$-to-$\mathrm{SFR}_{\mathrm{CII}}$ ratio is therefore likely smaller. That leaves source C with an elevated ratio, due to its strong H_2O line detection. Yang et al. (2016) state that previous work would suggest stronger high-J H_2O lines in the presence of an AGN. However, in their own work they find a diminished $L_{\mathrm{H_2O}}/L_{\mathrm{IR}}$ ratio when the galaxy is host to an AGN because the AGN boosts the L_{IR} more so than it does $L_{\mathrm{H_2O}}$. In contrast, we find an elevated $L_{\mathrm{H_2O}}/L_{\mathrm{IR}}$ ratio for source C implying a strong H_2O detection, suggestive of an AGN.

3.3.3 Masses

We now turn to determining the masses of the SPT2349 sources. The three mass types that we will focus on are stellar mass, gas mass, and dynamical mass. As the names would suggest, the stellar mass is a measure of all the stars in a galaxy while the gas mass measures the mass of the hydrogen and helium gas in the interstellar medium. The dynamical mass, determined by assuming a dynamical structure for the galaxy, measures the gravitating mass of the galaxy within a certain radius, including the dark matter whose mass can only be ascertained indirectly, in this work by subtracting the stellar mass and gas mass from the dynamical mass. All mass estimates are tabulated in Appendix G Table G.1.

Stellar Mass

The stellar mass, M^*, of a galaxy is the cumulative mass of young and old stars in a galaxy. Ideally multi-band photometry fully sampling the UV, optical, near- and mid-IR (depending on the redshift) is used in SED fitting in an effort to constrain the stellar mass. Fortunately, the vast majority of the stellar mass manifests itself as a rest-frame near-IR bump in the SED of an SMG and is predominantly attributed to the old stellar population, whose emission peaks at 1.6 μm. Young, hot stars radiating at shorter wavelengths are comparatively short-lived and contribute negligibly to the cumulative stellar mass. As an effective alternative to SED fitting, the rest-frame 1.6 μm luminosity is therefore frequently used in a mass-to-light conversion - using a scaling relation to convert the 1.6 μm luminosity to estimate the stellar mass.

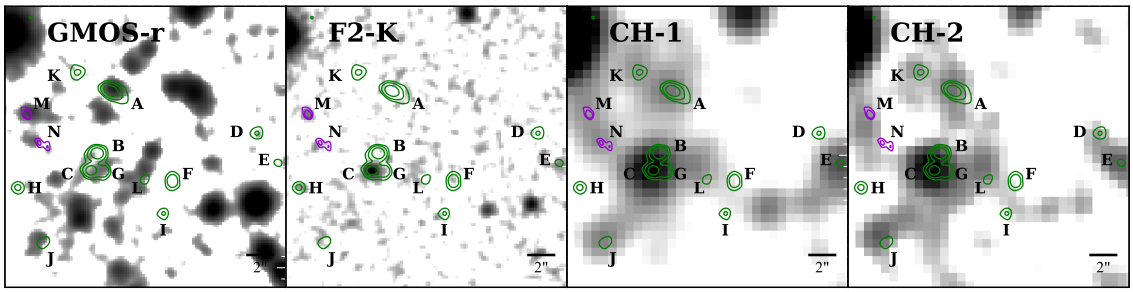

Figure 3.8: Optical and Near-IR imaging. *From left tot right*: Gemini-S GMOS i-band (0.8 μm), Gemini-S F2 K-band (2.16 μm), *Spitzer* IRAC CH1 (3.6 μm), and *Spitzer* IRAC CH2 (4.5 μm). The green contours are drawn at 4σ, 10σ, and 30σ of the ALMA B7 continuum. The purple contours are drawn at 3σ and 4σ of the ALMA B7 image centred on the [C II] emission.

For SPT2349 at $\langle z \rangle \sim 4.3$, the peak in stellar light is redshifted to $\sim 8.5\,\mu$m, in the mid-IR. We obtained deep Gemini Multi-Object Spectrographs (GMOS) R-band and FLAMINGOS-2 (F2) K-band imaging of SPT2349, both on Gemini-S. We include *Spitzer* IRAC CH1 & CH2 imaging (published in Miller et al. 2018). Thumbnails of each band are shown in Fig. 3.8. Only 7 of the 14 sources are detected in K-band imaging. In R-band we do slightly better and detect 8 of the 14 sources. While IRAC's CH1 does detect all 14 sources, CH2 only detects 9. The multi-band photometry can be found in Appendix G Table G.2.

With such sparse photometry points any SED fitting procedure will produce poorly constrained results. Furthermore, the longest-wavelength imaging we have are IRAC CH1 & CH2 bands at 3.6 and 4.5 μm, respectively. We are therefore not sampling the peak of the emission of the old stellar population (at $\sim 8.5\,\mu$m), we are only catching the shortward tail of it. We therefore choose to adopt a simple scaling relation from the CH1 luminosity to estimate a stellar mass. (The shorter-wavelength CH1 was chosen over CH2 because all 14 SMGs are detected in CH1 unlike in CH2.)

Hainline et al. (2011) studied the stellar mass content of SMGs by scaling from their rest-frame $H-$band ($\lambda = 1.63\,\mu$m) luminosity derived from multi-band photometry SED fitting. We determine a mass-to-light ratio from the Hainline et al. (2011) SMGs ($M/L_H \sim 0.107$ $M_\odot/L_\odot$) and apply it to our SPT2349 sources. Importantly, the mass-to-light ratio determined from the Hainline et al. (2011) SMGs applies to a rest-frame $H-$band luminosities sampling the stellar peak in the SED, see where the

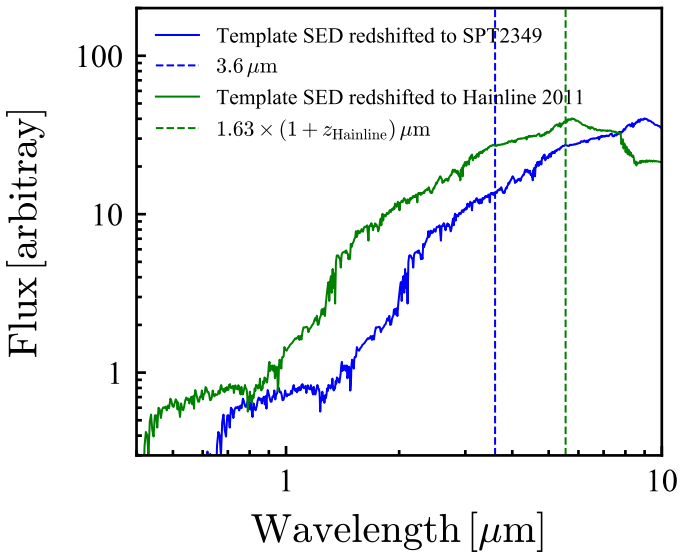

Figure 3.9: Template SED created by Polletta et al. (2007) for SMGs redshifted by $z = 4.3$ (SPT2349, blue) and $z = 2.4$ (average Hainline et al. (2011), green). The 1.6 μm peak of the stellar bump is selected by the Hainline et al. (2011) H-band (dashed green line). For SPT2349 (dashed blue line) the observed CH1 (3.6 μm) samples shortward of the rest-frame 1.6 μm peak.

dashed green line intersects with the green SED template in Fig. 3.9. The observed CH1 (3.6 μm) luminosities for SPT2349 are shortward of the $z = 4.3$ redshifted peak, see where the dashed blue line intersects with the blue SED template in Fig. 3.9. We must therefore first apply a flux ratio to the CH1 flux to correct for the shortward sampling of the 1.6 μm peak so that the $H-$band mass-to-light ratio from Hainline et al. (2011) is applicable. We determine this flux ratio from a rest-frame template SED between 1.63 μm ($H-$band) and the rest-frame CH1 flux $3.6/(1+4.3) = 0.68\,\mu$m. We find $[S_{1.63\,\mu\mathrm{m}}/S_{0.68\,\mu\mathrm{m}}]_{\mathrm{template}} \sim 2.86$.

We determine the stellar mass to lie in the $(1.5 - 25) \times 10^{10}$ $\mathrm{M}_\odot$ range with a median M^* of $(4.7 \pm 1.7) \times 10^{10}$ $\mathrm{M}_\odot$. This is on the lower end of the stellar mass range observed by Michałowski et al. (2010), who through SED fitting found M^* to lie between $10^{11} - 10^{12}$ $\mathrm{M}_\odot$ with a median M^* of 4.4×10^{11} $\mathrm{M}_\odot$ for high-redshift $\langle z \rangle \sim 2.1$ SMGs. Hainline et al. (2011) on the other hand find a median stellar mass for their $z > 1.5$ SMGs to be $(7.2 \pm 1.2) \times 10^{10}$ $\mathrm{M}_\odot$, similar to our own. The cumulative stellar mass for SPT2349 is $(8.4 \pm 0.6) \times 10^{11}$ $\mathrm{M}_\odot$.

Once again source C stands out, this time with an elevated $M^* \sim (2.5 \pm 0.5) \times 10^{11}$,

roughly a factor of 5 larger than the median for SPT2349 sources. This finding is in keeping with the earlier suggestion that source C might contain an AGN, as the probability of a galaxy containing an AGN rises strongly with stellar mass (Overzier 2016, & references therein), *i.e.* such an anomalously high M^* is unlikely unless some of the light can be attributed to an AGN. Overzier (2016) notes that several studies have found proto-clusters to contain elevated AGN fractions, likely due to the over-dense nature of the proto-cluster. Furthermore, at lower redshift $\langle z \rangle \sim 2.1$ Michałowski et al. (2010) found a significant fraction of SMGs to contain AGN.

Source C stands out as significantly brighter than the other sources as well in the K-band, CH1, and CH2 imaging both from a visual inspection, refer back to Fig. 3.8, and from the extracted photometry. In the R-band it is too faint to detect. Elevated near-IR emission compared to the optical has been found to indicate a significant amount of warm dust, likely heated by the presence of an AGN in SMGs (Casey et al. 2014, & references therein), further suggesting source C in particular to be host to an AGN.

Having estimated the stellar masses, we can assess whether or not a correlation exists between SFR and M^* for SPT2349. For a given redshift, the majority of star-forming field galaxies are observed to exhibit such a correlation (Noeske et al. 2007; Santini et al. 2017). Santini et al. (2017) suggest that the tightness of the correlation, defined as the main sequence (MS), is due to similarities in the gas accretion histories. For galaxies along the MS, it is expected that the dominant mechanism for growth is via a smooth accretion of gas from the intra-galactic medium over long timescales. Merging starbursts in the field like SMGs are often found to lie significantly above these correlations (*e.g.* Hainline et al. 2011; Michałowski et al. 2012). The empirically defined MS is typically parameterized as a power law,

$$\log\left(\mathrm{SFR}/\mathrm{M}_\odot\,\mathrm{yr}^{-1}\right) = \alpha \log\left(M^*/\mathrm{M}_\odot\right) + \gamma, \tag{3.8}$$

where α is the slope of the $\log \mathrm{SFR} - \log M^*$ relation, and γ is the MS normalization. While the normalization is clearly observed to increase with redshift, the slope is still debated. Generally it is believed that the slope is predominantly unevolving, approximately linear, and near unity. Santini et al. (2017) separated their sample of star-forming field galaxies into five redshift bins and fit a power law for each.

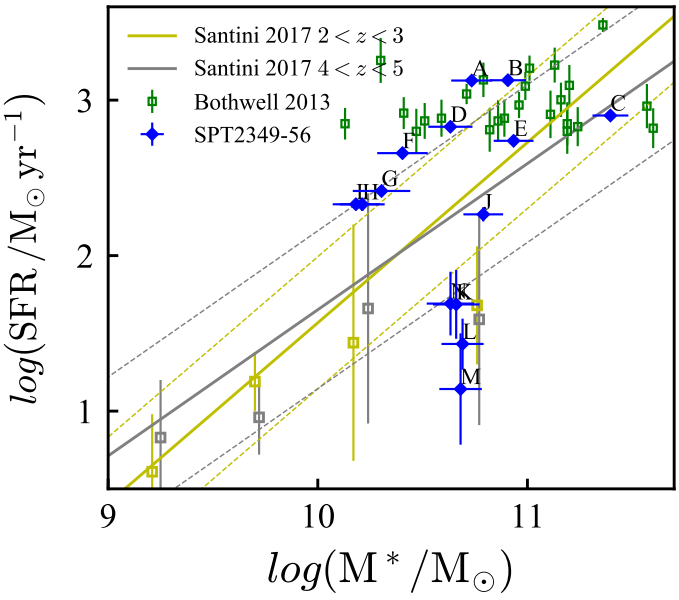

Figure 3.10: Assessing the SPT2349-56 sources (blue diamonds) relative to the main sequence of star-forming galaxies. The power law for the $4 \leq z < 5$ range (grey line) along with the 1σ envelope (grey dashed lines) and the 2σ-clipped average values (grey squares) are included, the $2 \leq z < 3$ range is in gold (Santini et al. 2017). The Bothwell et al. (2013) SMG sources with $\langle z \rangle \sim 2.2$ are the green squares.

For $4 \leq z < 5$, the range in which SPT2349 falls, they find $\alpha = 0.94 \pm 0.06$ and $\gamma = 1.37 \pm 0.05$. They perform a 2σ-clipping procedure in which they reject all points outside 2σ from their best-fit and calculate the average SFR for various stellar masses.

Fig. 3.10 shows the relation between SFR and M^*. The grey line is the MS power law for $4 \leq z < 5$ regime as determined by Santini et al. (2017). The grey squares are the associated 2σ-clipped average values. The dashed grey lines are the 1σ envelope determined from the 2σ clipped average values, highlighting those sources in SPT2349 that are clear outliers to the MS. We find three regimes for the SPT2349 sources (labelled blue diamonds): the faintest four sources (K-N) well below the MS, source C, E, and J which lie along the MS, and those whose SFR is well above the MS, strongly suggesting they are undergoing major-mergers.

We include the Bothwell et al. (2013) sample of sub-mm galaxies, which adopts M^* from Hainline et al. (2011), as a comparison to other starburst galaxies. We convert their $S_{850\,\mu\mathrm{m}}$ into a SFR using the same scaling as for our own sources and use their M^* values. It is important to note, that not only are their SMGs field galaxies compared to our sources in the dense environment of a proto-cluster, their

sample has a median redshift of $\langle z \rangle \sim 2.4$, compared to our own $\langle z \rangle \sim 4.3$. We therefore include the Santini et al. (2017) determined power law for the $2 \leq z < 3$ regime, along with 1σ envelope and the associated 2σ-clipped average values in gold in Fig. 3.10. The Bothwell et al. (2013) SMGs display a similar trend to the SPT2349 sources - the majority lie above or align themselves with the MS, confirming that the SPT2349 sources are starbursts triggered by major-mergers. However, the SFR of field galaxies (Bothwell et al. 2013) is relatively constant across the stellar mass range $10 < \log(M^*/\mathrm{M}_\odot) < 12$. This is due to the selection effect of the Bothwell et al. (2013) sources ($S_{850\,\mu\mathrm{m}} = 4 - 20$ mJy) which puts stringent limits on the SFR. This is in contrast to the proto-cluster sources (A-L) whose SFR increases with M^*. Consequently, the SPT2349 sources allow us to observe the relation between SFR and M^* without constraints on the full range of either property. SPT2349 sources K-N are clear outliers both in comparison to the other SPT2349 sources as well as to field galaxies. While the stellar masses are within range, the corresponding star formation rates are anomalously low. This suggests either a period between star formation bursts or a depletion of the interstellar gas.

Gas Mass

The gas mass, M_{gas}, of a galaxy provides information about the reservoir from which new stars can be formed. The combination of gas and stellar mass is an important diagnostic when extrapolating to the final, total mass of a galaxy once the starburst phase has completed and the galaxy is no longer evolving actively (Bothwell et al. 2013). The gas mass reservoir is comprised predominantly of H and He. As discussed earlier H is challenging to observe directly. The CO(1-0) line luminosity, as a tracer of H_2, is therefore used instead by adopting a conversion factor, α, which has units $\mathrm{M}_\odot$ (K km s^{-1} pc^2)$^{-1}$. The H_2 gas mass is then, $M(\mathrm{H}_2) = \alpha L'_{\mathrm{CO}(1-0)}$, where $L'_{\mathrm{CO}(1-0)}$ is represented in units of brightness temperature, as discussed in Sect. 3.3.2, specifically Eq. 3.3. The exact value of α is still being debated both via observational and theoretical work and is dependent on galaxy type and dynamics. The value determined by Downes and Solomon (1998) for ultra-luminous IR starbursts, $\alpha = 0.8$ $\mathrm{M}_\odot$ (K km s^{-1} pc^2)$^{-1}$, is still frequently adopted. Bothwell et al. (2013) note that this conversion factor underestimates the true H_2 gas mass by about < 10 %. We

will continue to use it here for a conservative estimate of $M_{\rm gas}$, as was done by Miller et al. (2018). For a total gas mass He needs to be included as well. A correction can be applied to the H_2 gas mass, $M_{\rm gas} = 1.36 \times M(H_2)$ (Bothwell et al. 2013).

Lastly, if the CO(1-0) line was not observed but a higher J transition of CO was, a brightness temperature ratio, *i.e.* $L'_{\rm CO(1-0)}/L'_{\rm CO(4-3)}$, needs to be applied to convert to the CO(1-0) line luminosity. For their sample of SMGs, Bothwell et al. (2013) determined the brightness temperature ratios for a number of higher J transitions. They found $r_{43/10} = 0.41 \pm 0.7$ to be the brightness ratio between the $J = 4 \rightarrow 3$ and the $J = 1 \rightarrow 0$ CO transitions. Finally a gas mass can be calculated from our CO(4-3) line luminosities:

$$M_{\rm gas} = 1.36\alpha \frac{L'_{\rm CO(4-3)}}{r_{43/10}}, \tag{3.9}$$

where $M_{\rm gas}$ is in $M_\odot$. In the instances where CO(4-3) was not detected, we use [C II] instead. For these calculations a further conversion is needed - we determine the brightness temperature ratio between our CO(4-3) and [C II] detections and include it in the gas mass calculations when using [C II] instead of CO(4-3). We find $r_{43/[\rm C\,II]} = 1.4 \pm 0.7$, where the error is 1 standard deviation from the mean. Using CO(4-3) line detections when possible and [C II] when not, we calculate $M_{\rm gas}$ to be in the $\sim (0.8 - 12) \times 10^{10}$ $M_\odot$ range, similar to M^*, with a cumulative $M_{\rm gas} = (6.4 \pm 0.4) \times 10^{11}$ $M_\odot$.

Dynamical Mass

The dynamical mass, $M_{\rm dyn}$, is defined as the total mass (stellar mass, gas mass, and dark matter) within a chosen radius and can be estimated from the kinematics of the galaxy, which manifest themselves in the FWHM of its spectral features, *i.e.* in the CO(4-3) and [C II] linewidths. The benefit of deriving dynamical masses from molecular gas linewidths is that they are free from uncertainties that plague derivations stemming from optical and near-IR observations, such as dust extinction effects (Bothwell et al. 2013). Instead, dynamical mass estimates stemming from the kinematics of the galaxy require a few key assumptions about the dynamical structure - the two extremes are a fully virialized body and a rotating disc. For

a stable, virialized body, the kinetic energy of the random motion of the stars is balanced by half of the gravitational potential energy of the object, thus keeping it from collapsing. The random motion of stars manifests itself in a broadening of the spectral lines, the velocity dispersion. In contrast, for an ordered rotating disc, the centrifugal force, a function of the rotational velocity, is balanced by the gravitational force. Bothwell et al. (2013) argue that the full SMG population is likely a mix of virialized systems and disc-like structures. They notice though that at lower luminosities SMGs are predominantly disc-like while at higher luminosities SMGs are dominated by major-merger events, in which case the virialized mass estimator is more appropriate. Furthermore, individual SMGs are likely to exhibit some combination of the two extremes. Even ongoing mergers, turbulent events, can quickly re-establish gas in rotating discs. Here, as a reference, we present dynamical masses estimated using the virialized approximation,

$$M_{\rm dyn} = 1.56 \times 10^6 \sigma^2 R, \tag{3.10}$$

where $M_{\rm dyn}$ is given in $M_\odot$, the velocity dispersion σ has units of km s^{-1}, and the radius R is in kpc. We adopt the [C II] velocity dispersions found by Miller et al. (2018) and the radii determined by Perry (2018). We find the dynamical mass to lie in the $\sim (1-70)\times10^{10}$ $M_\odot$ range with a cumulative mass of $M_{\rm dyn} = (3.3\pm0.4)\times10^{12}$ $M_\odot$. It is important to note that the SPT2349 sources may not be fully virialized and therefore these mass estimates are upper limits.

In Fig. 3.11 we plot the SFR (determined from $S_{851\,\mu\rm m}$) in relation to the dynamical mass. As comparisons we also plot the Bothwell et al. (2013) SMGs (in green) and the star-forming field galaxies presented by Tacconi et al. (2006) that are part of the main sequence (in purple). For each comparison sample we include a least-squares fit to help guide the eye. We find that the SPT2349 sources once again appear to separate into three SFR bins: the brightest sources (A-F) at ~ 800 $M_\odot$ yr^{-1} aligning with other SMGs, the intermediately bright sources (G-J) at ~ 200 $M_\odot$ yr^{-1} at the high end of the MS, and the dimmest sources (K-N) at $\lesssim 50$ $M_\odot$ yr^{-1} at the low end of the MS. While the dimmest SPT2349 sources occupy the lower end of the dynamical mass range, the other sources do not appear to have a correlation between the $S_{851\,\mu\rm m}$ and $M_{\rm dyn}$, *i.e.* brighter sources are not necessarily more massive. We conclude

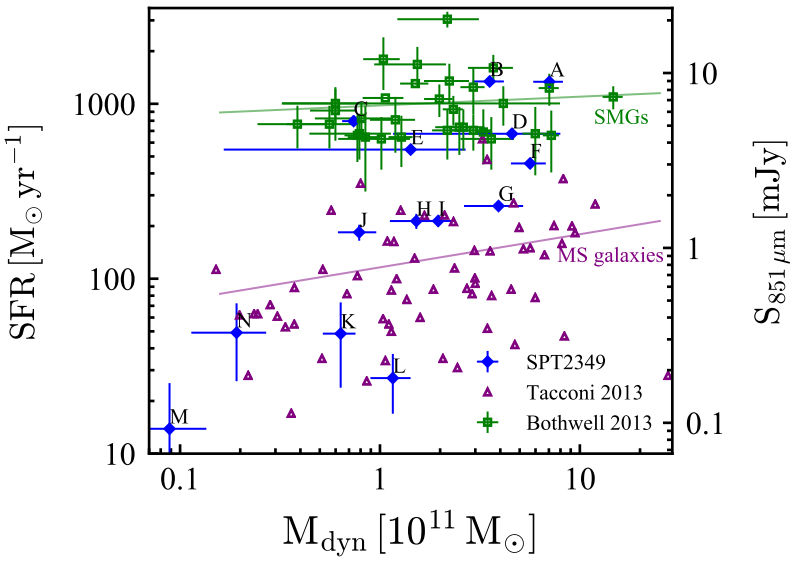

Figure 3.11: SFR (determined from $S_{851\,\mu\mathrm{m}}$, blue diamonds) as a function of dynamical mass estimated from the velocity dispersion assuming a virialized system. SMGs from the Bothwell et al. (2013) sample (green squares) and MS star-forming galaxies from the Tacconi et al. (2006) sample (purple triangles) are included for comparison.

from this that we could be observing the SMGs during any stage of the merger. The SFR is often stochastic with cycles of intense bursts followed by slower star formation rates. This is due to the turbulent nature and chaotic environments of major-mergers, among other physical factors. The 14 sources within SPT2349 may therefore be at varying stages of mergers, consequently resulting in uncorrelated SFRs.

3.3.4 Mass Fraction Analysis

Fig. 3.12 compares the baryon mass fraction $(M_{\mathrm{gas}} + M^*)/M_{\mathrm{dyn}}$ for the 14 SPT2349 sources (blue diamonds) with other SMGs (Bothwell et al. 2013, green squares). As discussed, the virial mass estimator for M_{dyn} is an upper limit and so the mass fractions for SPT2349 are lower limits. The horizontal grey dashed line identifies when the baryonic matter equals the total mass, $(M_{\mathrm{gas}} + M^*) = M_{\mathrm{dyn}}$, *i.e.* there is no dark matter. A baryon mass fraction > 1, as seen in sources C, E, J, K, M, and N, is technically unphysical, it implies that the mass associated with stars and gas alone is greater than the total mass. However, while M_{dyn} and M_{gas} estimates are coupled via the gas tracers used (CO(4-3) and [C II] depending on detection) and therefore represent masses within the same region, M^* is not similarly limited. Furthermore

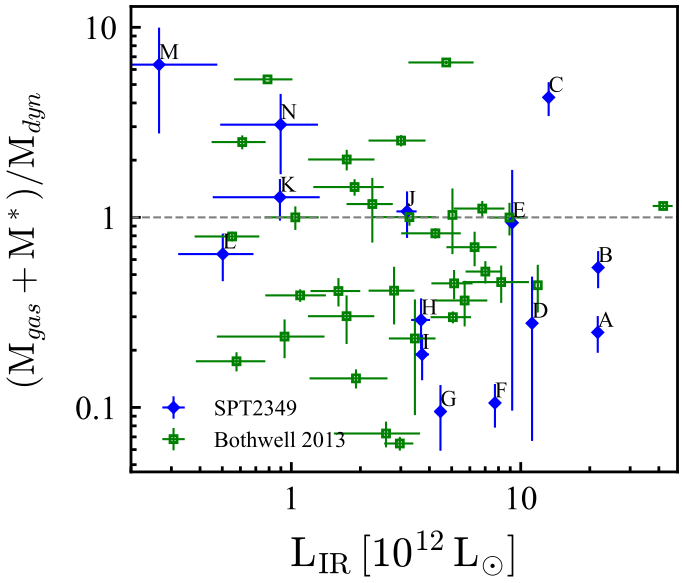

Figure 3.12: Baryon mass fraction of SPT2349 sources. The dynamical mass is estimated from velocity dispersion and is an upper limit, therefore the mass fraction is a lower limit. SPT2349 displays similar mass fractions to other SMGs (Bothwell et al. (2013), green squares).

M^* uncertainties are notoriously large as AGN activity could be contributing to the light radiated. It is therefore quite feasible that estimates of these three masses lead to a mass fraction greater than 1. As pointed out earlier, Bothwell et al. (2013) argue that it is unlikely that all SMGs can be modelled as either fully virialized or completely disc-like, but are rather a combination of the two. They also strongly suggest that the value of α is a potential large source of error in $M_{\rm gas}$ calculations.

Lastly, we analyze the mass budget of the 14 SPT2349 sources, both as individual galaxies and as galaxies within a proto-cluster. In the left panel of Fig. 3.13 the cumulative gas mass, stellar mass, and dark matter content are displayed as fractions of the combined dynamical mass. The horizontal dashed grey line is the fractional error of the cumulative dynamical mass. We find that the gas and stellar mass make up ~ 45 % of the cumulative mass and the 14 sources are therefore dark matter dominant at ~ 55 % of the total mass. This is quite surprising as Bothwell et al. (2013) argue that while SMGs are commonly found to reside in large dark matter halos, they themselves typically do not have a large dark matter content. This discrepancy is possibly due to the dense proto-cluster environment of these 14 sources. Importantly, a cumulative chart such as Fig. 3.13 looses information about the individual sources.

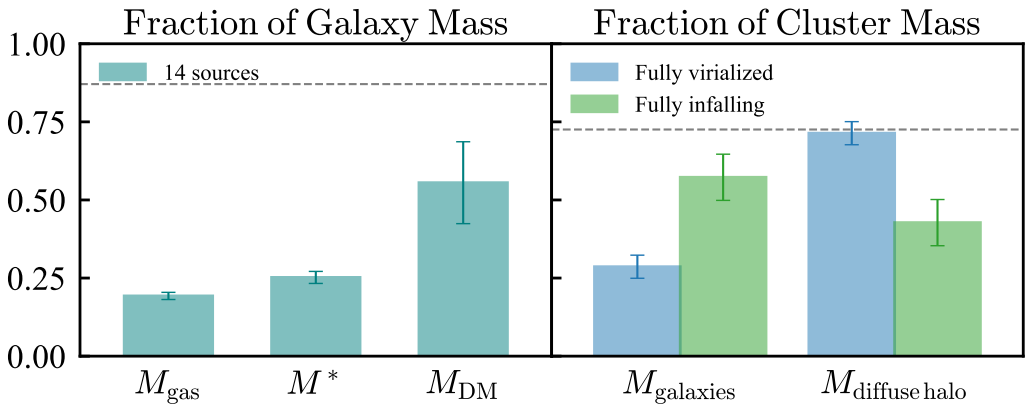

Figure 3.13: Mass budgets for the SPT2349-56 proto-cluster. *Left*: Sum of mass components as a fraction of the dynamical mass of all 14 observed galaxies. The dynamical mass is an upper limit and therefore so too is the DM mass fraction. *Right*: Mass components as a fraction of the dynamical mass of the cluster. $\mathrm{M_{galaxies}}$ is the cumulative dynamical mass of the 14 SPT2349 sources. $\mathrm{M_{diffuse\,halo}}$ represents contributions including dark matter and intracluster gas as well as other low mass galaxies too faint to detect.

While on average the sources may therefore be dark matter dominated, referring back to 3.12 we find a $L_{\rm IR}$ correlation with the dark matter content. For example, sources F and G are near 90 % dark matter.

In the right panel of Fig. 3.13 the mass budget of the 14 sources is placed into context with the greater proto-cluster mass. Miller et al. (2018) determine the velocity dispersion of the 14 sources and, approximating SPT2349 to be fully virialized, estimate the dynamical mass of the proto-cluster to be $M_{\rm dyn} = (1.16 \pm 0.70) \times 10^{13}$ $\mathrm{M_\odot}$. Using the virial dynamical mass estimator was justified via analysis in which the velocity offsets from the mean for the 14 sources were determined, finding 12 to be bound even with the most conservative total mass estimates, *i.e.* the velocity offsets were less than the escape velocity. The dashed grey line in the figure is once again the fractional error of the total proto-cluster mass. We determine the fraction of the proto-cluster mass that is the cumulative dynamical mass of the 14 sources, ~ 30 % (labelled $M_{\rm galaxies}$). The remaining fraction of the proto-cluster mass includes the proto-cluster dark matter halo as well as hot and cold intracluster gas (labelled $M_{\rm diffuse\,halo}$). $M_{\rm diffuse\,halo}$ is an upper limit in this plot as there is the potential that less massive galaxies too dim to detect in the current data set exist. We further differentiate between a fully virialized system and an infalling structure. Simulations

have found that in an infalling structure the gravitational collapse boosts the velocity dispersion of member galaxies and using the virialized estimator yields a dynamical mass $\sim 2\times$ larger than the corresponding infalling structure (Behroozi et al. 2013). Consequently, by setting the total mass for the infalling structure to be half that of the virialized system, we find the fractional cumulative galaxy mass to be doubled.

3.4 Discussion

SPT2349 is a unique proto-cluster at high-z with overdensities (the number of DSFGs within a given region), star formation rates, and gas reservoirs significantly higher than other proto-cluster candidates. One such proto-cluster candidate, more similar to STP2349 than others, was discovered by Oteo et al. (2018), nicknamed the Distant Red Core, and consists of 10 DSFGs within a (260×310) kpc^2 region spectroscopically confirmed to lie at $z = 4.002$. This is in comparison to the 14 DSFGs in SPT2349 within a circle whose diameter is 130 kpc (Miller et al. 2018), an area ($13,300$ kpc^2) roughly $6\times$ smaller than that of the Distant Red Core ($80,600$ kpc^2).

In their low-resolution, unresolved LABOCA imaging at 870 μm Oteo et al. (2018) found the cumulative flux of the Distant Red Core to be $S_{870\,\mu\mathrm{m}} = 64\pm11$ mJy, slightly less than that of SPT2349 at $S_{870\,\mu\mathrm{m}} \sim 77$ mJy. If we scale the 870 μm flux to estimate the SFR, as we have done in this work, the Distant Red Core has a SFR of $9,600 \pm 1,650$ M$_\odot$ yr^{-1} whereas SPT2349 has a SFR of $\sim 11,550$ M$_\odot$ yr^{-1}. The 870 μm LABOCA imaging show both the Distant Red Core and SPT2349 to be surrounded by other 870 μm bright sources. The Distant Red Core is surrounded by potentially six additional DSFGs, the cumulative flux being ~ 106 mJy, if all DSFGs are confirmed to be at the same redshift. The cumulative flux of the northern and southern LABOCA sources of SPT2349 with the connecting bridge is also ~ 107 mJy, suggesting that the SFR for the entire system for both proto-clusters could be as extreme as $\sim 16,000$ M$_\odot$ yr^{-1}. In both cases, the majority of the star formation occurs in the central core of the proto-cluster - the Distant Red Core at ~ 60 % and SPT2349 to an even higher degree at ~ 72 %. With deeper, higher-resolution ALMA imaging at 851 μm, however, we resolved SPT2349 into 14 individual sources whose cumulative flux is $S_{851\,\mu\mathrm{m}} = 41.1\pm0.5$ mJy, substantially lower than the ~ 77 mJy suggested by LABOCA. The "confirmed" cumulative SFR of SPT2349 is therefore $6,163 \pm 76$

$M_\odot$ yr^{-1}. Oteo et al. (2018) scale their 2 mm ALMA fluxes (in which the LABOCA object was resolved into 10 sources) to SFRs and found the cumulative $SFR_{2\,mm}$ to be $\sim 6,538$ $M_\odot$ yr^{-1}. These SFRs are tabulated in Table 3.4. It is interesting to note that while the unresolved LABOCA SFRs vary significantly between SPT2349 and the Distant Red Core, the SFRs in the core (determined from resolved ALMA imaging) are very similar. This might be suggestive of an upper limit to star formation rates in dense proto-cluster cores.

Table 3.4: Comparative Star Formation Rates for SPT2349 and the Distant Red Core

Proto-cluster	Cumulative SFR of DSFGs $\sum SFR_{ALMA}$ [$M_\odot$ yr^{-1}]	Core SFR $SFR_{870\,\mu m}$ [$M_\odot$ yr^{-1}]	System SFR $SFR_{870\,\mu m}$ [$M_\odot$ yr^{-1}]
SPT2349	6,163	11,550	16,050
Distant Red Core	6,538	9,600	15,900

We can also compare the molecular gas reservoir between the two proto-clusters. Oteo et al. (2018) find a cumulative molecular hydrogen reservoir of $M_{H_2} \sim 6.6 \times 10^{11}$ $M_\odot$. If we include the correction factor for He, as we have done in the analysis for SPT2349, the molecular gas reservoir for the Distant Red Core is $M_{gas} \sim 9 \times 10^{11}$ $M_\odot$. This is on par with that of SPT2349, $M_{gas} = (6.4 \pm 0.4) \times 10^{11}$ $M_\odot$. We find remarkable agreement between the cumulative SFRs of the individual DSFGs within the cores of the Distant Red Core and SPT2349 as well as in the molecular gas mass. These similarities suggest that the two proto-cluster cores will evolve into similarly massive cluster cores.

Lastly, we consider the total mass of the proto-cluster. Using velocity dispersions, Oteo et al. (2018) estimate the total virialized mass to be $\sim 9.3 \times 10^{13}$ $M_\odot$, a factor of 8 larger than our own $(1.16 \pm 0.70) \times 10^{13}$ $M_\odot$. Oteo et al. (2018) argue that such an estimation for the total mass of the entire system is highly uncertain due to the assumption that the system is virialized and that only the velocity dispersions of the sources in the core are used, the most violent region of the system with extreme SFRs. They therefore calculate a new total mass assuming a spherical distribution and find $M_{total} \sim 3.2 \times 10^{13}$ $M_\odot$. The large discrepancy between the two results further suggests that the Distant Red Core is not virialized and that these mass estimates are upper limits. The total mass of the core is likely closer to, or less than, that

of SPT2349. Furthermore, it is unlikely that the greater proto-cluster mass is much larger than that for SPT2349 considering the similarities between the gas mass and the cumulative SFR in the core.

3.5 Conclusion

We make the following conclusions:

1. We present high-resolution 851 μm, 1.06 mm, and 2.02 mm line subtracted continuum fluxes for 14 SMGs in the dense proto-cluster core of SPT2349 lying at $z = 4.3$ with the goal of constraining $L_{\rm IR}$ and thus determining SFRs. Modified black-body fitting only produces reliable results when including the lower-wavelength SPIRE data so that both sides of the peak are sampled. Due to the poor resolution of SPIRE we cannot resolve the 14 sources. We therefore constrain the average dust parameters $T_{\rm dust} \leq 40.9$ K and $\beta \leq 1.9$ for the proto-cluster as a whole, not for the individual sources within it.

2. We determine a SFR for each of the 14 sources using a scaling from $S_{851\,\mu{\rm m}}$. We find ${\rm SFR}_{851\,\mu{\rm m}}$ to range between $\sim 13 - 1,300$ M$_\odot$ yr^{-1} for the 14 SPT2349 sources, with a cumulative ${\rm SFR}_{851\,\mu{\rm m}}$ of $6,163 \pm 76$ M$_\odot$ yr^{-1}.

3. As alternative SFR estimators we explore using the H_2O and [C II] line. We present resolved ALMA observations of the H_2O line with robust detections in six of the 14 sources. We adopt the [C II] line fluxes from Hill (in prep.). For the two line methods we find the SFR range to be substantially smaller than that determined from a $S_{851\,\mu{\rm m}}$-scaling but consistent between the two; ${\rm SFR}_{[{\rm C\,II}]}$ ranges from $\sim 40 - 830$ M$_\odot$ yr^{-1} and ${\rm SFR}_{\rm H_2O}$ ranges from $\sim 70 - 920$ M$_\odot$ yr^{-1}. However, only the three brightest H_2O detections have $L_{\rm H_2O}$-to-$L_{\rm IR}$ ratios that are similar to other high-z ultra-luminous infrared galaxies. We conclude that a single, low-J transition of H_2O is an unreliable SFR indicator, especially in the dense environments of proto-cluster cores. For the [C II] line we observe the "[C II] deficit" in all but one source with $L_{\rm IR} > 10^{12}$ L$_\odot$ (sources A-I), resulting in low SFR estimates. Conversely, for the less luminous sources, the ${\rm SFR}_{[{\rm C\,II}]}$ estimates are high in comparison to ${\rm SFR}_{851\,\mu{\rm m}}$. The cumulative SFR for the [C II] line is $3,526 \pm 22$ M$_\odot$ yr^{-1}, barely ~ 60 % of the ${\rm SFR}_{851\,\mu{\rm m}}$ estimation.

We determine that the [C II] line is a poor SFR estimator as it is sensitive to AGN contamination, exhibited by the "[C II] deficit." We conclude that the $S_{851\,\mu\mathrm{m}}$ scaling approach provides a more accurate estimate of the SFR than either the H_2O or [C II] line.

4. We estimate the stellar mass via a mass-to-light conversion determined from similar SMGs. We find the stellar mass to lie in the $\sim (1.5 - 25) \times 10^{10}$ $M_\odot$ range with a median of $(4.7 \pm 1.7) \times 10^{10}$ $M_\odot$. This is on the lower end, but still within the range, for other SMGs around $z \sim 2$. It therefore suggests that the 14 sources within SPT2349 are at an advanced stage of evolution. The cumulative stellar mass for SPT2349 is $(8.4 \pm 0.6) \times 10^{11}$ $M_\odot$.

5. We convert $L'_{\mathrm{CO(4-3)}}$ into a gas mass when CO(4-3) was detected, otherwise we use [C II] detections and included an additional conversion factor. We calculate M_{gas} to be in the $\sim (0.8 - 12) \times 10^{10}$ $M_\odot$ range, with a cumulative $M_{\mathrm{gas}} = (6.4 \pm 0.4) \times 10^{11}$ $M_\odot$, similar but slightly below that for M^*. We conclude that the stellar mass is likely to increase by at least a factor of two due to the presence of these massive gas reservoirs alone. If the gas reservoirs of the 14 sources are replenished by the intra-cluster medium or through major-mergers with other, less massive SMGs in the proto-cluster, the stellar mass may increase substantially more than just by a factor of 2.

6. Lastly, we make the assumption that the 14 individual sources are virialized and calculate dynamical masses. We find the dynamical mass to lie in the $\sim (0.9 - 70) \times 10^{10}$ $M_\odot$ range with a cumulative mass of $M_{\mathrm{dyn}} = (3.3 \pm 0.4) \times 10^{12}$ $M_\odot$. In the case that the sources are not individually fully virialized, the dynamical mass estimate would decrease by a factor of a few, but likely remain within a similar range. Furthermore, any gaseous discs present during major-mergers will be highly turbulent and short-lived. A virial dynamical mass estimator is generally therefore still the appropriate choice.

Chapter 4

Design, Fabrication, and Testing of Planar Lithographed Superconducting LC Resonators

4.1 Introduction

A critical consequence of an inflationary period early in the universe's history is the effect on the gravitational metric, *i.e.* the mathematical formalism for the gravitational potential of space-time. Small quantum fluctuations result in perturbations of the gravitational metric that expand to all size scales through inflation and are imprinted on the cosmic microwave background (CMB) at $z \sim 1,100$, around $400,000$ years after the Big Bang. The temperature anisotropies observed in the CMB are a consequence of such perturbations. Two types of perturbations are important. Scalar perturbations are density, and hence temperature, fluctuations of matter. In contrast, fluctuations in the gravitational field itself resulting from "primordial" gravitational waves, the compression and rarefaction of space, are a type of tensor perturbation. Scalar and tensor perturbations affect the temperature as well as the polarization of the CMB in different ways.

4.1.1 Polarization of the Cosmic Microwave Background

To measure the polarization of the CMB the Stokes parameters are measured. The four Stokes parameters (I, Q, U, and V) are a formalism that describe the nature of polarized electromagnetic radiation. I is the total intensity, Q is the linear polarization along the $x-$ and $y-$axis, U is the linear polarization at 45° to the $x-$ and $y-$axis, and V is circularly polarized light. For the CMB, I is the temperature anisotropy and $V = 0$ because the CMB does not contain circularly polarized light. The two Stokes parameters Q and U are measured via two antenna, one rotated by 45°, from which the vector field of the linearly polarized light of the CMB can be created. The polarization vector is defined by its amplitude, $P = \sqrt{Q^2 + U^2}$, and

the angle clockwise from north, $\alpha = \frac{1}{2}\tan^{-1}(U/Q)$ (*e.g.* Hu and White 1997). The Stokes parameters Q and U are dependent on the choice of reference frame. Alternatively, the polarization field can be decomposed into E-mode and B-mode polarization patterns, scalar fields that are invariant under rotation. E-modes are defined as the gradient-like component of the CMB polarization, the component of the polarization vector that creates patterns without handedness, while B-modes are the curl-like component with handedness, as depicted by the coloured headless vectors in Fig. 4.1(a). Specifically, E-modes are comprised of the component of the polarization vector that are either perpendicular or parallel to the wavevector $\vec{k}$ representing the bulk flow of photons from effective hot to cold regions. The effective temperature is a combination of the temperature anisotropy and the gravitational potential gradient of the CMB (Hu and White 1997). Conversely, B-modes are those whose polarization vectors are at 45° to the wavevector. The orientation of the E- and B-mode components with

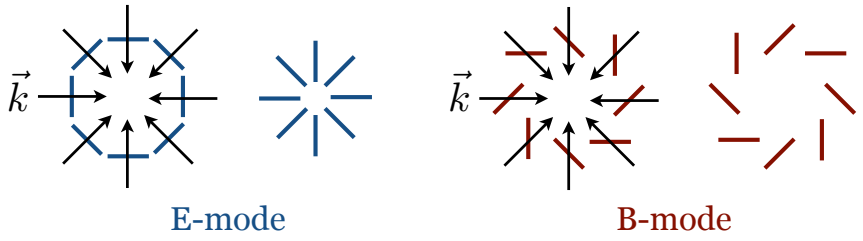

(a) Polarization patterns - E-modes: no handedness, B-modes: handedness.

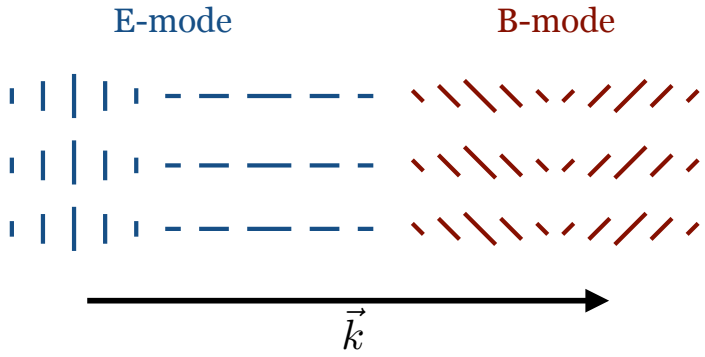

(b) Polarization vector orientations with respect to the wavevector $\vec{k}$ pointing towards a cold spot.

Figure 4.1: Cartoon of E-mode and B-mode polarization.

respect to the wavevector are shown in Fig. 4.1(b). Importantly, the polarization vectors in Fig. 4.1 (decomposed into the pure E- and B-mode components) in the $x-y$ plane stem from CMB photons scattering off of free electrons and are, as always, perpendicular to the outgoing scattered wavevector propagating along $\hat{z}$ (discussed in further detail shortly). This scattered wavevector is not the same as the wavevector depicted in Fig. 4.1. Thus, the angle between the headless polarization vectors and the wavevector in Fig. 4.1 are not constrained to be perpendicular to one another.

E- and B-modes can be distinguished from each other by the patterns that the headless polarization vectors make around a hot or cold spot in the E- and B-mode maps of the CMB. Fig. 4.2 is an image of the E-mode (*top*) and B-mode (*bottom*) polarization of the CMB observed by the second generation Background Imaging of Cosmic Extragalactic Polarization (BICEP2) collaboration and the Keck Array team. The colour scale shows the sign and strength of the E- or B-mode signal and

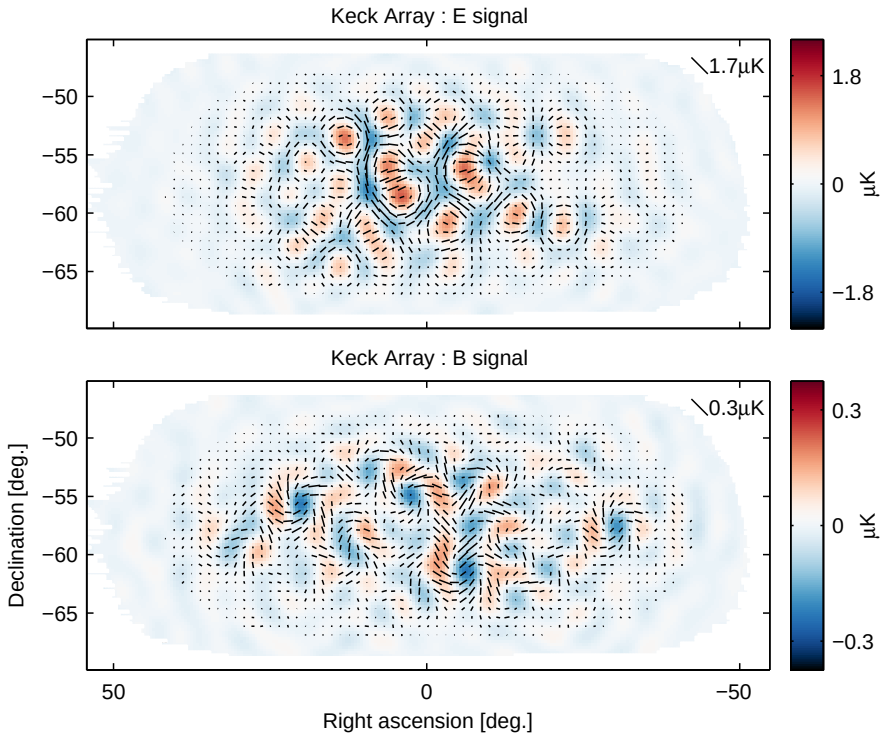

Figure 4.2: E-mode (*top*) and B-mode (*bottom*) polarization pattern (black headless vectors) of the CMB as measured by the BICEP2/Keck Array Collaboration. The length of the vectors is proportional to the polarization strength. The colour scale shows the sign and strength of the E- or B-mode signal. The E- and B-mode maps use different colour and length scales. Image credit: BICEP2/Keck Array Collaboration.

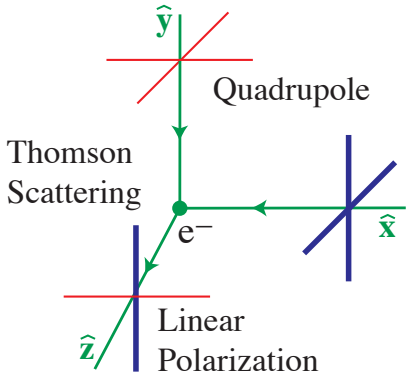

Figure 4.3: Thomson scattering of CMB photons with a quadrupole anisotropy, *i.e.* two incoming photons at 90° to each other with different temperatures, off of an electron generates linearly polarized light. Figure taken from Hu and Dodelson (2002).

the black headless vectors superimposed show the orientation and strength (length) of the decomposed linear polarization. The E- and B-mode maps use different colour and length scales. The radial symmetry of the E-modes is visible in contrast to the characteristic swirling pattern (*i.e.* handedness) of B-modes.

Both E- and B-modes arise from a couple of different sources. One source of E-modes is Thomson scattering. When photons scatter off electrons via Thomson scattering at 90°, the outgoing radiation is linearly polarized perpendicular to the incoming photon. Averaging over all photons of the same temperature from all directions leads to a net-zero polarization. If, however, the temperature of two perpendicularly incoming photons varies due to scalar (density) perturbations, a quadrupole anisotropy exists and a net linear polarization results (Hu and Dodelson 2002). This is depicted in Fig. 4.3 taken from Hu and Dodelson (2002), where the outgoing scattered photon propagates along $\hat{z}$ and the linear polarization is in the $x - y$ plane, perpendicular to the scattered photon's wavevector. The polarization from Thomson scattering and the temperature anisotropy are therefore correlated. This polarization can only ever be tangential or radial around a hot or cold spot in the effective temperature map (Hu and White 1997). Consequently, the polarization is perpendicular or parallel to the wavevector $\vec{k}$ pointing towards a cold spot and therefore results in E-mode polarization of the CMB.

One way in which to create B-mode polarization is through the weak gravitational lensing of the CMB by the entirety of the matter column between it and the observer.

In this way, the original E-modes get distorted into B-modes. These lensing B-modes can therefore convey important information about the the neutrino mass and number of the universe, an ongoing debate in the community (*e.g.* Schneider 2006; Abazajian et al. 2016). B-modes can also be created by primordial gravitational waves, which compress and rarefact space in the plane perpendicular to its wavevector. The wavevector of the gravitational wave, however, is not constrained to the $\hat{z}$ direction, unlike Thomson scattering. The resulting polarization can therefore take on any orientation projected onto the $x - y$ plane, contributing to both E- and B-modes. Gravitational waves are a consequence of inflation. Measuring the resulting B-modes is therefore direct evidence of inflationary theory. Furthermore, the strength of these B-modes informs on the energy density of the universe, a critical parameter that affects the expansion rate of the universe.

The strength, *i.e.* the amplitude, of the various sources of polarization are commonly plotted as a function of angular size, this is known as the angular power spectrum, C_ℓ. Fig. 4.4 shows the theoretical relative strength of various components of the CMB. The multipole number, ℓ, (bottom x-axis) is inversely proportional to angular size (top x-axis), so larger multipole numbers correspond to smaller angular sizes. The black curve is the power spectrum of the temperature anisotropy. The E-modes are shown in red, they are correlated to the temperature anisotropy but are at least two orders of magnitude weaker, depending on the angular scale of interest. In green are the B-modes caused by the gravitational lensing of E-modes, which occurs primarily at small angular scales. These are another two orders of magnitude weaker - only a fraction of the E-modes get distorted into B-modes. The power spectra for gravitational wave B-modes are in blue (labelled "GW" in the figure). The two GW B-mode curves represent two different tensor-to-scalar ratios, $r = 0.05$ and $r = 0.001$. The tensor-to-scalar ratio is the ratio between the angular power of tensor and scalar perturbations of the CMB, $\mathrm{r} = C_\ell^{\mathrm{T}}/C_\ell^{\mathrm{S}}$. The relative strength of tensor perturbations (GW B-modes) with respect to scalar perturbations (E-modes from quadrupole temperature anisotropies) can help constrain inflationary models. As is evident in the figure, the temperature anisotropy, E-modes, and B-modes are easily distinguishable from each other by their relative strengths. Fortunately, the two types of B-modes can be differentiated as well by the angular scale at which the effect is expected to

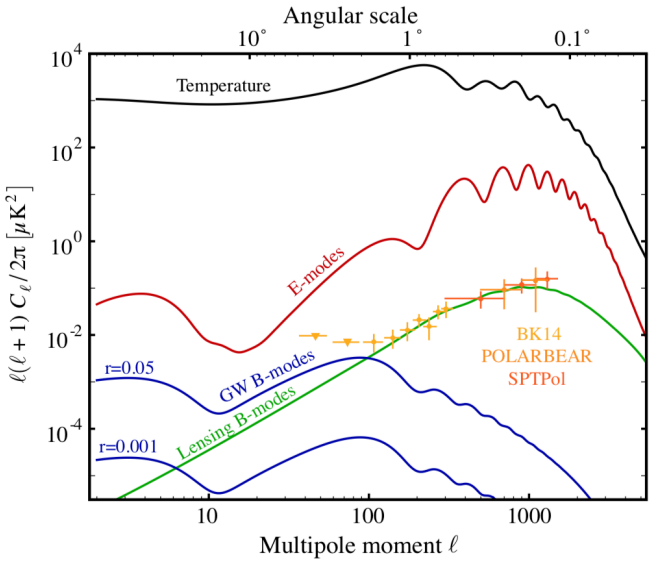

Figure 4.4: Theoretical angular power spectrum of the temperature anisotropies and E- and B-mode polarization of the CMB. Figure taken from Abazajian et al. (2016)

peak, B-modes caused by gravitational waves dominate at large angular scale while those created via gravitational lensing dominate at small angular scales.

All but the gravitational wave B-modes of the CMB have been detected. The temperature anisotropies were first measured by the COsmic Background Explorer (COBE) satellite in 1994. In 2002 the E-mode polarization was detected by the Degree Angular Scale Interferometer (DASI), located at the Amundsen-Scott South Pole Research Station, with high confidence at $\geq 4.9\sigma$ (Kovac et al. 2002). A decade later in 2013, the first B-modes from gravitational lensing were detected by the polarization-sensitive receivers on the South Pole Telescope (SPTpol) with a confidence of 7.7σ (Hanson et al. 2013), in 2014 by the the CMB polarimetry experiment POLARBEAR located in the Atacama Desert of Chile at a statistical significance of 4.0σ (Ade et al. 2014), and in 2015 by the polarization-sensitive receivers on the Atacama Cosmology Telescope (ACTpol) at a statistical significance of 4.5σ (van Engelen et al. 2015).

The search for primordial B-mode polarization, B-modes imprinted directly onto the CMB by gravitational waves, is still ongoing. Observations of these B-modes would provide definitive proof for inflationary theory. Additionally, determining an accurate tensor-to-scalar ratio will constrain the energy density of the universe as well as other cosmological parameters. While primordial B-modes have not yet been

observed, many experiments and their successors (SPT-3G, AdvACT, and POLARBEAR-2) have placed upper limits on their strength. In order to observe such an incredibly faint signal, the sensitivity of these various experiments need to increase dramatically.

4.1.2 POLARBEAR

In this chapter we will focus on the efforts put forth by the POLARBEAR team. The original POLARBEAR receiver was mounted on the Huan Tran Telescope (HTT) on the Cerro Toco site in the Atacama Desert in Chile at 5.2 km altitude. The site location was chosen for its low atmospheric water vapour content. Water lines are some of the most dominant in the frequency range at which POLARBEAR operates, 150 GHz. This frequency band was chosen for its proximity to the peak radiation of the CMB ($\sim$ 160 GHz) while also minimizing the polarization effects of foreground sources including our own galaxy. These foreground polarizations are primarily caused by synchrotron radiation of charged particles accelerating in a magnetic field (a decreasing function with frequency) and from thermal dust emission also an effect caused by a magnetic field, this time with the spin alignment of interstellar dust grains (an increasing function with frequency) (discussed in Suzuki 2013).

For the POLARBEAR receiver, the signal from the CMB is incident on an antenna sensitive to two orthogonal linear polarizations, passes through a bandpass filter that selects a small range centred on the observing frequency, and then gets detected by transition edge sensor (TES) bolometers. Bolometers measure incoming radiation by exploiting the temperature-dependent electrical resistance of a metal. TES bolometers further capitalize on the phase transition between the superconducting and regular state - in the superconducting state a current will experience zero resistance. When the power from a photon hits the superconducting metal of the bolometer it raises its temperature. Even a slight increase in temperature will result in a dramatic change in resistance if the metal is held near its superconducting transition temperature. The $1,274$ TES bolometers of POLARBEAR are cooled to 0.25 K, just below the transition temperature of the bolometers at $\sim$ 0.5 K. By voltage biasing the bolometer with electrical power, *i.e.* maintaining a constant voltage drop

across them, a slight change in the optical power, *i.e.* an incoming photon, is countered by a decrease in the electrical power. In this way, the operating temperature of the bolometers is locked onto the steep transition between its superconducting and regular state via negative feedback (Dobbs et al. 2012). This is referred to as reverse biasing of the bolometers. Consequently, a change in resistance results in a change in current. The optical power of the CMB photon has thus been converted into an electrical current.

TES detector technology is at such an advanced stage in the mm regime that they are photon-noise limited. This means that their sensitivity is limited by the statistical noise inherent to the incoming radiation, *i.e.* fluctuations in the arrival rate of photons (Dobbs et al. 2012). Therefore, in order to increase the sensitivity of the instrument, more detectors are required. However, more detectors leads to increased thermal loading of the sub-Kelvin stage due to the additional wiring required, as well as raises the cost of the readout components, increases the power consumption, and complicates the wiring (Arnold 2010). Bundling the signal from multiple detectors mitigates all of these issues to great effect. The cold readout of TES bolometers thus makes use of frequency-domain multiplexing (FDM), in which bolometers are placed in series with inductors and capacitors that define a carrier frequency so that the response from multiple bolometers can be readout simultaneously through one wire, thereby minimizing the thermal loading on the sub-Kelvin bolometers. For POLARBEAR the multiplexing factor was 8, *i.e.* 8 bolometers were read out at once. Subsequently, the multiplexed electrical current generated by the TES bolometers gets passed through a superconducting quantum interference device (SQUID) (held at 4 K), which effectively pre-amplifies the signal from the bolometers before being read-out by further warm-electronics (held at ~ 300 K).

SQUIDs are devices that measure with incredible precision the magnetic flux created by superconducting current flowing through a coil. The so-called "direct current SQUID" consists of a superconducting ring which is interrupted by two thin insulators creating two symmetric, parallel Josephson junctions across which cooper pairs, superconducting electron pairs that experience zero resistance, can tunnel. The phase difference of the wave functions between the upper and lower half of the superconducting ring (separated by the two Josephson junctions) can only take on integer

multiples of 2π, which results in a quantization of the flux. A coil (an inductor), through which the current from the bolometers passes, is placed above the SQUID. As the current through the coil changes, a magnetic flux is generated that passes through both the coil and the SQUID. Consequently a superconducting current is induced in the SQUID loop. If the SQUID is current biased, *i.e.* a constant current is maintained across the SQUID, then the presence of the induced current from the external magnetic field requires a decrease in the bias current. This consequently results in a change in the voltage drop across the SQUID, which can be measured. Due to the quantization of flux, the voltage response to an increasing external magnetic flux is sinusoidal in nature. To measure changes in magnetic flux smaller than one quantum of flux, the dynamic range of the SQUIDs must be reduced to operate in the linear-response regime, *i.e.* where the voltage response to the flux has a maximum slope. This is done via a shunt-feedback loop, in which the measured voltage is converted to a current (via a resistor) and then a flux (via an inductor) and fed back into the SQUID, effectively nulling the original input flux and locking the SQUID response to a constant flux. The inverted response of the bolometers is now contained in the nulling signal.

POLARBEAR-2 is the next generation polarimetry experiment to POLARBEAR. The number of TES bolometers was increased to $7,588$ each with the capability to observed the sky in two bands simultaneously, 95 GHz and 150 GHz. A summary of the readout parameters for POLARBEAR and POLARBEAR-2 can be found in Table 4.1, including a number of parameters discussed in the following sections. The increased number of bolometers requires an increased multiplexing factor. While there are many benefits to multiplexing the readout, there are a number challenges that need to be overcome. The inductor-capacitor resonators that define the carrier frequencies, the increased multiplexing factors and the associated challenges will be discussed in detail.

4.1.3 Cold Readout

In the FDM readout system, each TES bolometer with resistance $R_{\rm bolo} = 1\,\Omega$ is placed in series with an inductor (L) and capacitor (C), thus forming a series-resonant circuit, all at 0.25 K. In the case of POLARBEAR, the so-called "carrier comb" consists

Table 4.1: Summary of POLARBEAR readout parameters

Readout Parameter	POLARBEAR	POLARBEAR-2
Band	150 GHz	95 & 150 GHz
TES bolometers	1,274	7,588
Multiplexing factor	8	40
Frequency range	$400 - 900$ kHz	$1.6 - 4.2$ MHz
Inductor	$16\,\mu$H	$60\,\mu$H
Capacitor	$\approx 10 - 2$ nF	$\approx 165 - 24$ pF

of 8 parallel $\mathrm{LCR_{bolo}}$ resonators. If we keep the inductance constant ($L = 16\,\mu$H for POLARBEAR) across all resonance channels the electrical bandwidth remains constant as well, $R_{\mathrm{bolo}}/(2\pi L)$ (Dobbs et al. 2012). The resonance frequency (f) is therefore defined by the capacitor alone, $f = 1/(2\pi\sqrt{LC})$. This is important as the relative frequencies between channels, *i.e.* the channel spacing (Δf), is significantly more important to the cross talk (CT) than the absolute channel frequencies, $\mathrm{CT} = [R/(4\pi\Delta f L)]^2$. Cross talk arises when external sources to the resonator attempt to change the carrier signal. There are two main sources of cross talk within the $\mathrm{LCR_{bolo}}$ resonators that need to be contended with: 1) leakage of the carrier signal into neighbouring channels and 2) cross-coupling between inductors.

To mitigate leakage of the carrier signal the channel spacing can simply be increased. This can either take the form of reducing the electrical bandwidth of the channels or by increasing the total bandwidth of the FDM system. For POLARBEAR the total bandwidth for each multiplexed readout chain was limited to 1 MHz (Dobbs et al. 2012). This was due to the shunt-feedback loop that was employed. To reduce the dynamic range requirements on the SQUIDs (to ensure that they continue to operate in their linear-response regime), a "nulling comb," which is an inverted version of the carrier comb, was injected at the input of the SQUID to cancel out the carrier signal (Dobbs et al. 2012). This feedback loop contained an operational amplifier at room temperature, that was limited in bandwidth to 1 MHz and additionally introduced a phase delay between the 4 K SQUIDs and its 300 K wiring. To accommodate the increased number of bolometers for POLARBEAR-2 the multiplexing factor had to increase. To do so both the electrical bandwidth of the channels was decreased by increasing the inductance ($L = 60\,\mu$H) and the total bandwidth was widened. To

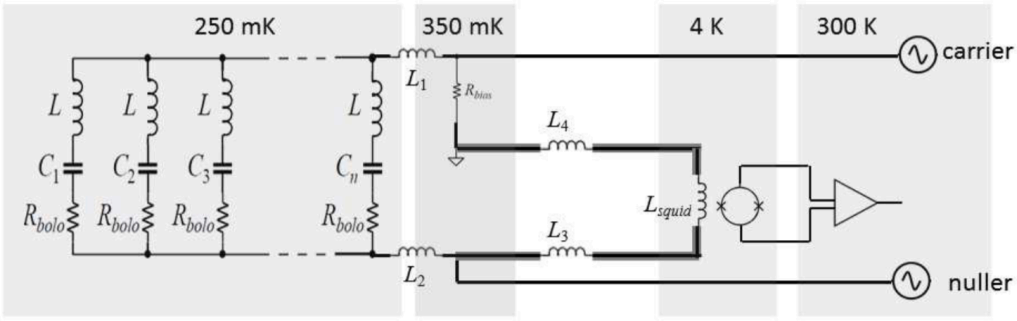

Figure 4.5: Frequency-domain multiplexed readout circuit diagram incorporating digital active nulling. Figure taken from Hattori et al. (2013)

overcome the limitations set by the shunt-feedback loop an alternative technique was implemented - digital active nulling (DAN) (*e.g.* Hattori et al. 2013). DAN works by applying the feedback, *i.e.* the nulling comb, across the narrow bandwidth of each resonator individually instead of across the SQUID as a whole. Furthermore the nulling comb is no longer connected to the room temperature operational amplifier. DAN digitally calculates the necessary feedback and actively removes the phase delay. Fig. 4.5, taken from Hattori et al. (2013), is the circuit diagram for one $\mathrm{LCR_{bolo}}$ resonator carrier comb of the cold readout for POLARBEAR-2 incorporating the DAN technique. The SQUID acts to pre-amplify the carrier signal so that the nulling comb injected via DAN is as precise as possible. While DAN allows for higher carrier frequencies, it does introduce new hurdles, discussed later in this section.

While leakage of the carrier signal affects neighbouring channels in frequency-space, cross-coupling of inductors is an issue that arises due to physical proximity. When a current flows through inductor i, a voltage is induced in its physical neighbour inductor j, $|V_j| = 2\pi f_i M_{i,j} I_i$, due to the mutual inductance between them, $M_{i,j} = k_{i,j} L_i L_j$ (Dobbs et al. 2012). In an FDM system, the coupling coefficient $k_{i,j}$ is the parameter dependent on the physical proximity of the two inductors. This is a source of cross talk that needs to be mitigated, which can be done by placing neighbouring inductors in frequency-space far apart physically. For the FDM system in POLARBEAR the coupling coefficient was measured to be $k = 0.010 \pm 0.002$ (Dobbs et al. 2012, & references therein). For POLARBEAR-2 we require the mutual inductance of the resonators to be less than that from external parasitic inductance, L_s, introduced by stray impedance from wiring between the sub-Kelvin and the 4 K stages and from

the wiring of the SQUIDs. For POLARBEAR-2 the parasitic inductance was estimated to be 50 nH (Hattori et al. 2014). With inductors at 60 μH, the coupling coefficient for the parasitic inductance is then $k_s = L_s/L = 8.3 \times 10^{-4}$. Ideally, the coupling coefficient for the $\mathrm{LCR_{bolo}}$ resonators should be less than this to minimize cross talk. However, because the cross talk follows $\mathrm{CT} \propto (\Delta f)^{-2}$, if we require the frequency spacing between physical neighbours to be $10\times$ larger than Δf, then the requirement on k can be relaxed by a factor of 100, *i.e.* the coupling coefficient must be smaller than 8.3×10^{-2} (Hattori et al. 2014). We are therefore reducing the cross talk between frequency channels by maximizing the physical spacing between neighbours in frequency space.

Another critical aspect of the readout is maintaining the aforementioned voltage bias across the bolometers. Any stray impedances that may spoil it need to be minimized. One such potential source is the so-called equivalent series resistance (ESR) associated with the $\mathrm{LCR_{bolo}}$ resonators themselves. The series resistance, the primary contributor to ESR, is in part a function of the loss tangent ($\tan\delta$) of the dielectric material of the capacitor, $R_{\mathrm{ESR}} = 2\pi L f \tan\delta$ (Hattori et al. 2013). Low-loss materials are therefore preferable. R_{ESR} is also an increasing function with both inductance and frequency. While a higher inductance is therefore beneficial as it decreases the bandwidth of the resonators allowing for tighter channel spacing, it increases the ESR. Higher carrier frequencies, now allowed by the application of DAN, also increases the ESR. A balance needs to be met. Fig. 4.6 taken from Hattori et al. (2013) shows the measured ESR with increasing frequency for the $\mathrm{LCR_{bolo}}$ resonators used by POLARBEAR. Ideally, to minimize the possibility of spoiling the voltage bias, the ESR should remain below 0.1 Ω (10 % of R_{bolo}) (Hattori et al. 2013). This was approximately true for frequencies < 1 MHz, however, decidedly not for the higher frequency regime.

For POLARBEAR, the $\mathrm{LCR_{bolo}}$ resonators consisted of planar lithographed inductors ($L = 16\,\mu$H) from the National Institute for Standards and Technology (NIST) and commercially available ceramic capacitors. The inductors, being sufficiently uniform, allowed for stable channel bandwidths. The channel spacing was chosen to be 75 kHz, exceeding the minimum requirement set by the channel bandwidth in an attempt to minimize cross talk. The capacitors, which were stacked in parallel to obtain

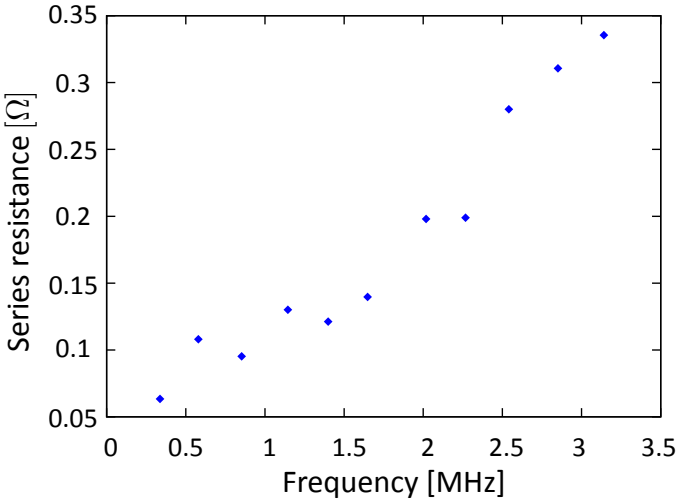

Figure 4.6: Series resistance at high-frequencies for commercial ceramic capacitors cooled to 4 K. Figure taken from Hattori et al. (2013)

the desired capacitance, introduced a significant error as their capacitance changed by several percent when cooled to sub-Kelvin temperatures (Hattori et al. 2013). In addition, the ESR was found to significantly exceed the desired 0.1 Ω threshold at high-frequencies, see Fig. 4.6. As discussed previously, the channel spacing, not the absolute frequency, is the critical parameter setting the cross talk. Lithographed inductors will shift identically for all channels and the spacing between channels is unaffected. The same is not true for multiple ceramic capacitors stacked in parallel.

4.2 A Novel Cold Readout System

For POLARBEAR-2 the decision was made to switch to a fully lithographed "LC chip" containing both lithographed capacitors and inductors. The LC chip is superconducting at 0.25 K, the LC resonators therefore do not introduce any loss to the signal being measured by the bolometers. A fully lithographed LC chip has the added benefit of 1) being able to design precise capacitance values instead of stacking commercially available capacitors, and 2) fabricating capacitors and inductors on a single device which has immense implications for scalability - decreasing both assembly time and the physical space required at sub-Kelvin temperatures. Furthermore, the capacitors can be fabricated with a low-loss dielectric in order to reduce the ESR. The design (taking the concepts of the previous section into account), fabrication, and testing of

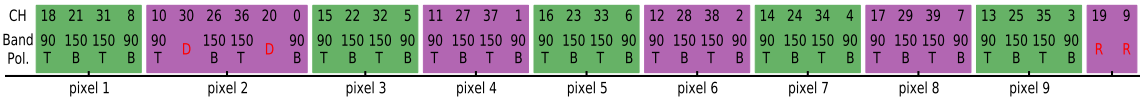

Figure 4.7: Pixel scheduling for the 40 channels. Each resonator is assigned a channel number. The band, polarization it reads out, and the pixel it belongs to are identified.

these LC chips are the focus of the research presented in this chapter.

4.2.1 Resonator Design Considerations

A number of design considerations were taken into account regarding frequency scheduling, physical proximity, as well as limitations set by the fabrication process. They are briefly mentioned in Rotermund et al. (2016) (attached in Appendix H), here we will elaborate on those considered.

1. The POLARBEAR-2 pixels, developed by Suzuki (2013), consist of an antenna sensitive to two orthogonal linear polarizations (labelled Top and Bottom), a bandpass filter that splits the signal into two bands (95 & 150 GHz), and four bolometers that each detect one of the combinations of band and linear polarization (95B, 95T, 150B, and 150T). Each band and polarization are separated by a calibration channel in the frequency scheduling. Two dark bolometers (D) and two resistors (R) make up the calibration channels. Dark bolometers are not sensitive to the sky and are therefore not affected by temperature leakage from neighbouring channels, which results in cross talk. For POLARBEAR-2, the multiplexing factor was increased to 36, so a total of 40 frequency channels are required. See Fig. 4.7 for a schematic identifying the channels assigned to a pixel, each consisting of four bolometers sensitive to either 95B, 95T, 150B, and 150T. Pixel 2 contains the two dark bolometers (channels 20 and 30). The two calibration resistors (channels 9 and 19) are not associated with a pixel as they replace the bolometer in the LCR resonator. Channel pairs 0 and 10, 1 and 11, 2 and 12, *etc.* were placed in the same pixel to maximize frequency spacing in order to mitigate cross talk.

2. The physical scheduling was set to maximize the difference in frequency between physically neighbouring channels. See Fig. 4.8 for the physical layout of the

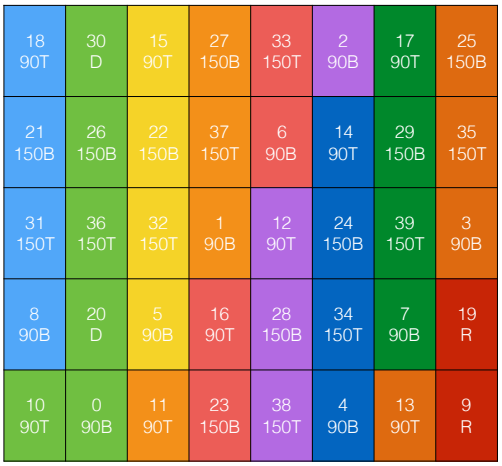

Figure 4.8: LC chip layout. Each box represents an LC pair, identified by its channel number and the band and polarization it reads out. Four LC pairs make up one pixel, identified by different colours. Pixel 2 contains two dark bolometers (D). The calibration resistors (R) are not associated with a pixel.

channels on the LC chip. Each box represents an LC pair, identified by its channel number and the band and polarization it reads out. Four LC pairs make up one pixel, identified by different colours.

3. The LC chips were fabricated in the Berkeley Marvell Nanofabrication Laboratory (NanoLab) on 150 mm high-resistivity silicon wafers using a one-to-one photolithography and subsequent lift-off process, discussed in more detail in Rotermund et al. (2016). The achievable uniformity of metal traces the fabrication procedure is capable of set a limitation on the minimum width - reliable results were found for widths as small as $4\,\mu$m. This, along with the maximum dimensions allowed for the LC chip, the multiplexing factor, and an inductance of $60\,\mu$H, set the maximum capacitance (161.440 pF) thereby setting the minimum frequency (1.617 MHz).

4. The electrical bandwidth of each channel is a mere 2.65 kHz. Assuming a generous maximum 10 kHz shift of any given channel either up or down the frequency spectrum, the minimum channel spacing was set to 40 kHz. A logarithmic frequency spacing was chosen, $\Delta f/f = \text{constant}$, so that the cross talk remains constant between all carrier frequencies. This sets the full frequency scheduling with a maximum frequency of 4.194 MHz, from which the required

capacitance values can be determined (minimum capacitance of 24.004 pF). At the high-frequency (low-capacitance) end, the channel spacing grew to 102 kHz - a further benefit from logarithmic spacing in which the smallest capacitors have a greater allowance for relative shifts in capacitance. See Fig. 4.9 for the full frequency scheduling including the separation of the band and polarization resonator sets.

5. The fabricated inductors are planar, spiral inductors, see Fig. 4.10 for a cartoon drawing, with 4 μm wide traces separated by a 4 μm gap. The inductance is a function of the outer diameter of the spiral as well as the number of coils in the spirals. So-called "bonding pads" are placed at the centre of the spiral inductor and at either the top or bottom so that a wire-bond can be used to connect the two bond pads to complete the circuit post-fabrication.
6. The fabricated capacitors are interdigitated capacitors, a cartoon of which can also be found in Fig. 4.10. Interdigitated capacitors consist of two parallel plates from which traces extend from alternating sides, effectively increasing the length of the parallel plates. The capacitance is a function of the length of the protruding traces as well as the number of interdigitated pairs.
7. The inductors and capacitors are placed in a checkerboard design to maximize the spacing between inductors in an effort to minimize the mutual coupling between them, see Fig. 4.10 for a truncated layout.

4.2.2 Fabrication Process

As stated, the LC chips were fabricated in the Berkeley NanoLab on 150 mm diameter, high-resistivity (30 Ω·cm) silicon wafers. As outlined in Rotermund et al. (2016), the fabrication process consists of 1) spin coating the wafer with photoresist, 2) patterning the photoresist using one-to-one projection lithography, 3) developing the exposed

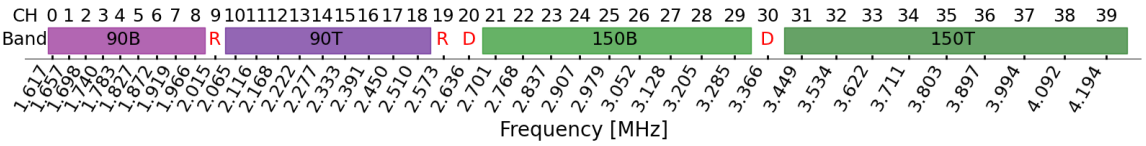

Figure 4.9: Frequency scheduling for the 40 channels. Each frequency is assigned a channel number. The band and polarization that channel reads out are identified.

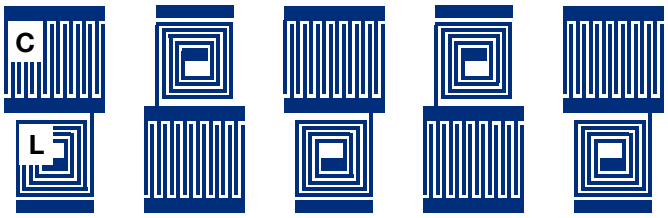

Figure 4.10: Cartoon drawings of planar, spiral inductor (L) and planar, interdigitated capacitors (C) in a checkerboard design.

photoresist, 4) depositing a 100 Å titanium adhesion layer followed by a 1,400 Å film of aluminum (Al) on both the front and back side of the wafer using e-beam evaporation, and finally 5) lifting off the Al from the photoresist covered areas using an ultrasonic acetone bath. Lastly, we dice the wafer.

The Lift-off Technique

The lift-off process was employed due to the observed non-uniformity when using the more traditional plasma etching technique. In plasma etching the metal is deposited first. The wafer is then spin coated with photoresist, patterned and developed before being plasma etched. See Fig. 4.11 for a schematic identifying the difference between the two techniques. In the case of plasma etching, the metal deposited was niobium (Nb). Plasma etching begins from the centre of the wafer and continues to the edge, introducing a radial non-uniformity in the degree to which the wafer is etched. Fig. 4.12(a) is a photograph of the thin film rings visible due to the non-uniform radial plasma etching. While the photoresist was burned for this wafer due to an error in the helium flow and proper plasma etching does not result in such thin film rings, the photograph does clearly show the radial non-uniformity that results from plasma etching. This results in varying trace thickness across the device, which greatly impacts the capacitance and inductance values. Furthermore, plasma etching has poor end-point detection between the metal and the Si substrate. Over-etching into the low-dielectric loss Si wafer once again introduces scatter in the capacitance values. Over-etching could be mitigated by including an oxide boundary layer between the Si wafer and the metal. Unfortunately, radial non-uniformity concerns would remain. Instead, a lift-off process was opted for and Nb was replaced with Al. The switch

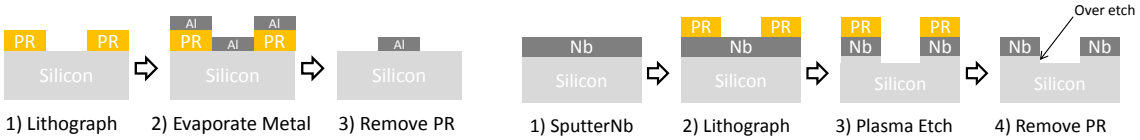

Figure 4.11: Fabrication techniques. *Left:* Lift-off. *Right:* Plasma etching.

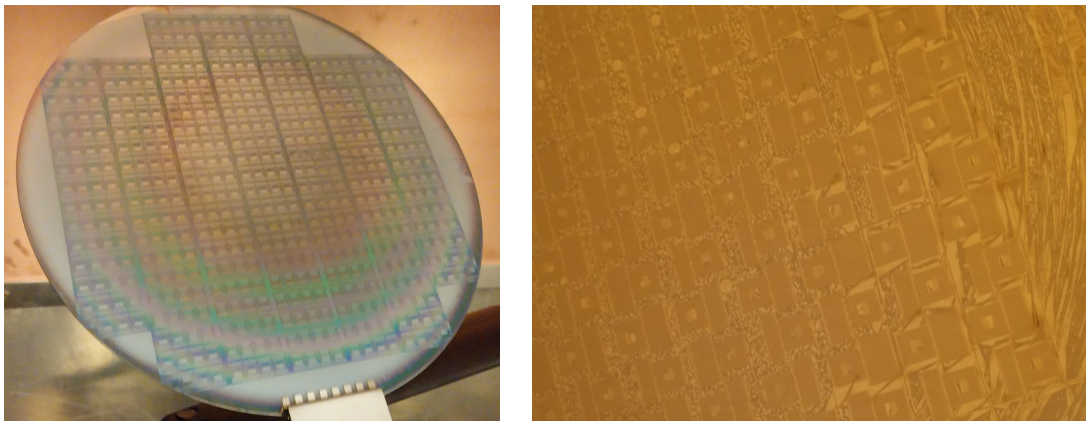

(a) Burnt photoresist resulting in thin film rings visible due to radial plasma etching.

(b) Melted photoresist and poor adhesion during niobium e-beam evaporation.

Figure 4.12: Photographs of the wafer after a failed fabrication step.

in metal was a consequence of the change in fabrication process and the subsequent adjustment of tools used and their capabilities. E-beam Nb evaporation requires significantly higher temperatures than Al evaporation which results in the melting, boiling, and/or burning of the patterned and developed photoresist as well as poor adhesion of the Nb metal to the wafer. Fig. 4.12(b) is a photograph of the wafer when Nb evaporation was attempted.

Defects

Two types of defects can occur in photolithography - open and shorted traces. These occur due to dust contamination on either the mask used to pattern the photoresist or due to some form of residue (dust, metal, *etc.*) on the wafer itself. For the lift-off technique, dust on the mask results in open traces, which for inductors breaks the coil and is fatal, *i.e.* current cannot be conducted. For capacitors an open trace simply disconnects an interdigitated finger from the parallel plate resulting in a minimal

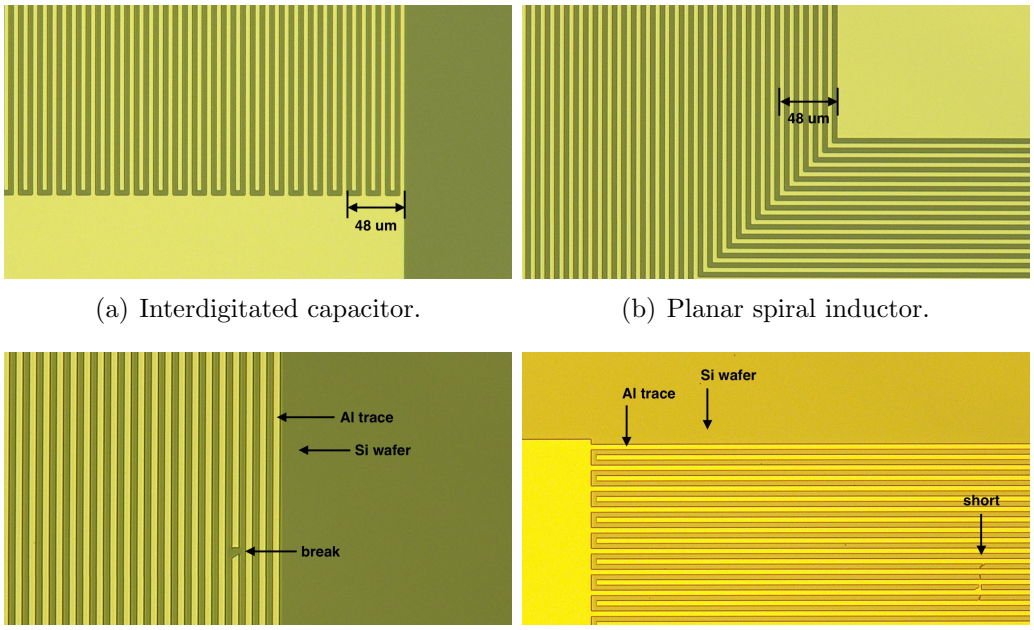

(a) Interdigitated capacitor.

(b) Planar spiral inductor.

(c) Break in trace.

(d) Short in trace.

Figure 4.13: Microscope photographs zoomed in on traces and defects.

effect. Conversely, shorted traces, potentially due to incomplete lift-off or due to dust or metal residue, are less common and have the opposite effect to open traces. Shorted traces are fatal to capacitors as the two parallel plates are now connected, while inductors simply loose a couple of coils, reducing the inductance. Throughout the fabrication process a clean environment is therefore required to minimize potential fatal defects. Each step is carefully inspected and defects occur seldom. Fig. 4.13 is a microscope photograph zoomed in on (a) the interdigitated capacitor and (b) the planar spiral inductor. In Fig. 4.13 (c) and (d) we highlight a break and a short in the trace respectively.

After having switched to the lift-off technique, we conducted scanning electron microscope (SEM) measurements near the centre and the edge of the wafer. This allowed us to measure the trace and gap widths, ensuring that they are close to the nominal $4\,\mu$m width and, importantly, consistent across the wafer. Fig. 4.14(a) shows two example SEM images measuring the trace and gap widths. While the trace widths were larger than the gap widths, the deviations were consistent and therefore not considered problematic. Furthermore, we inspected the profile of the traces, shown in Fig. 4.14(b), confirming that the lift-off technique is capable of

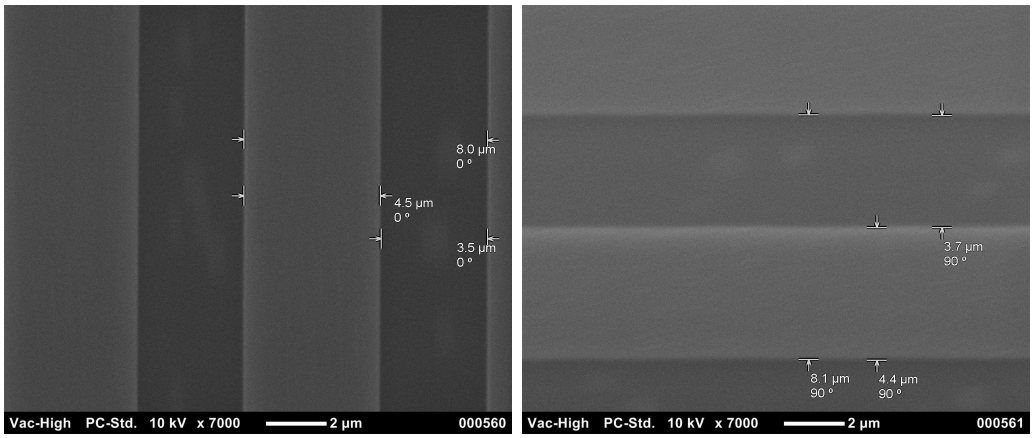

(a) SEM images measuring trace and gap widths near the centre and edge of the wafer

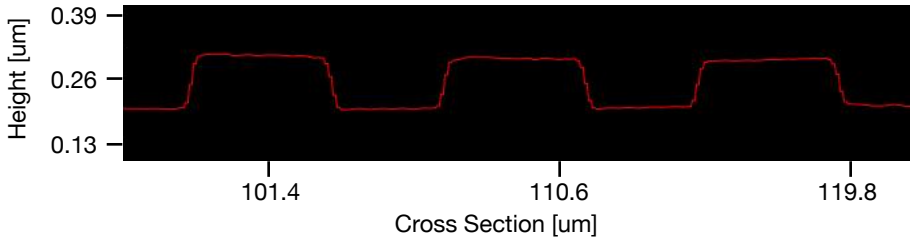

(b) Profile measurement of traces with a laser microscope

Figure 4.14: SEM images and laser microscope images of traces.

producing relatively vertical walls without defects or abnormalities at the edges.

The Ground Plane

Before mounting the finished LC chip on an "LC board" (discussed in the following section), a metal layer is placed between the two to minimize eddy current losses in the board. For POLARBEAR a thin Nb sheet was glued onto the board followed by the LC chip. Coupling between the LC devices and the so-called "ground plane" (*i.e.* the Nb sheet), see Fig. 4.15 for a schematic, results in a decrease in the inductance. Non-uniformities in glue thickness and potential creases in the metal film introduce scatter in said decrease, yielding a range of inductances. For POLARBEAR-2 the decision was therefore made to deposit an Al film onto the backside of the LC chip, removing deviations caused by non-uniformities, effectively stabilizing the inductors. The inductances were found to decrease by a factor of ~ 25 %. The inductors were therefore fabricated to be $80\,\mu$H inductors so that they behave as $60\,\mu$H inductors in the presence of the ground plane.

Figure 4.15: Cartoon drawing of capacitive coupling to the ground plane.

4.2.3 Device Assembly

Finally, the LC chip is mounted on the LC board - a printed circuit board which contains 1) 40 bond pads on either side of where the LC chip gets mounted, 2) traces that lead to a 90 pin ZIF connector which connects the LC pairs in series with the bolometers, and 3) traces that lead from the other end of the LC chip along the backside of the circuit board to a summing point to create the full carrier comb. See Fig. 4.16 for a picture of the LC chip mounted on the LC board. Lastly an "Al shield" is placed over LC chip on the LC board, see Fig. 4.17 (a). This has two benefits - to protect the LC chip and the wire bonds physically from damages, as well as to shield the LC chip from external magnetic fields similar to the Al film deposited on the backside of the wafer. Two such LC boards and their Al shields are attached back-to-back, creating an "LC cartridge," which are then mounted on the backing plate, the front of which holds the bolometer array. Fig. 4.17 (b) shows the empty backing plate (copper plate) and Fig. 4.17 (c) shows five LC cartridges mounted on it. Each backing plate holds three sets of five cartridges, yielding a total of $1,080$ LC resonators that connect to the bolometers for readout. The antennae-coupled bolometer array is mounted on the front side of the copper backing plate, see Fig. 4.17 (d) (taken from Suzuki (2013)). POLARBEAR-2's focal plane consists of 7 of these bolometer arrays. Fig. 4.17 (e) is a CAD drawing of the focal plane (taken from Suzuki (2013)), all of which is cooled to 250 mK.

4.3 Testing

While switching to the lift-off technique has many advantages, including simplifying the fabrication process, it does make testing the devices more challenging. Niobium has a superconducting transition temperature of 9.3 K, which means that the LC devices can be tested via a "dunk test" - submerging the device into liquid nitrogen

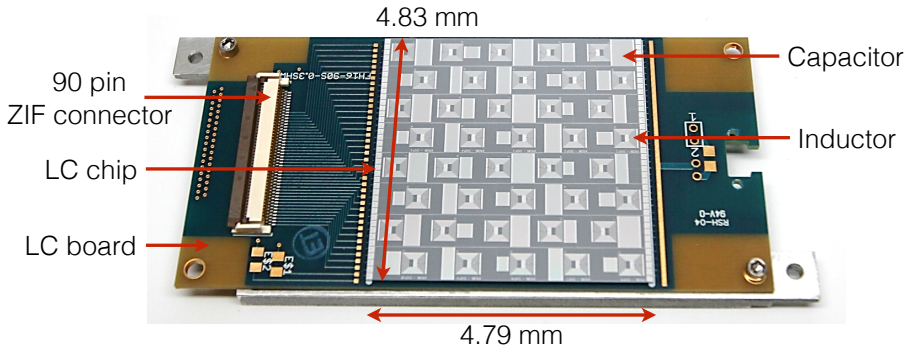

Figure 4.16: Photograph of the 40× LC chip mounted on the LC board.

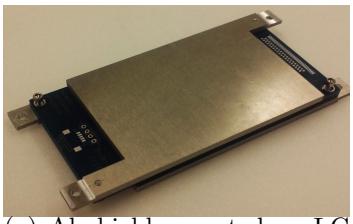

(a) Al shield mounted on LC board

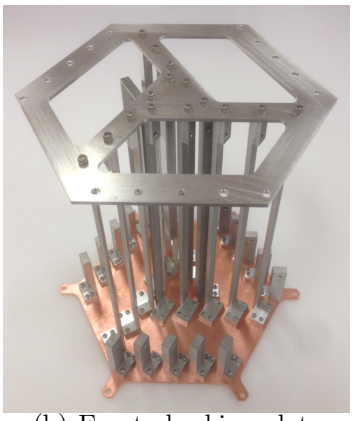

(b) Empty backing plate

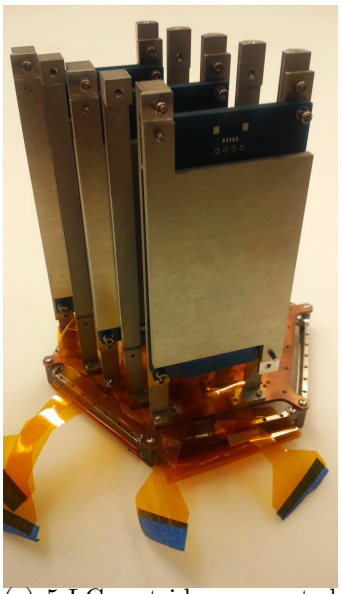

(c) 5 LC cartridges mounted on backing plate. Dummy flexible cables attached at base.

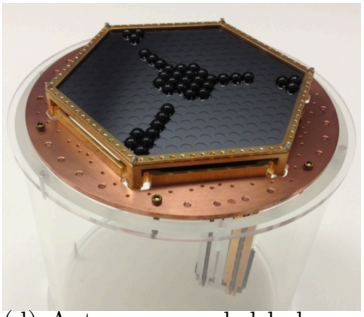

(d) Antennae-coupled bolometer array partially populated with lenslets. Wafer size (side-to-side) 119.5 mm.

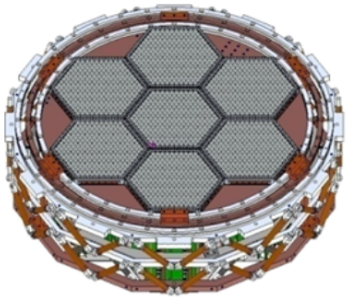

(e) CAD drawing of POLARBEAR-2 focal plane, diameter 365 mm.

Figure 4.17: Photographs displaying components of the cold read-out for POLARBEAR-2. Figures (d) and (e) taken from Suzuki (2013).

at $\sim$ 77 K and subsequently into liquid helium at $\sim$ 4 K. Aluminum, however, has a superconducting transition temperature of 1.2 K. Liquid helium is therefore not cold enough to bring the devices into their superconducting state. A more rigorous testing system had to be employed in which the LC devices were placed inside a wet dewar and were cooled to $\sim$ 600 mK via a Helium-3 sorption fridge. As in the POLARBEAR-2 deployment, the LC filters are read out via current-biased SQUIDs. This is done by frequency-sweeping a small-amplitude bias carrier across the full range of carrier frequencies of the LC filters (Dobbs et al. 2012). When the bias carrier frequency matches the resonance frequency of one of the LC filters the series impedance is at a minimum and the current passes through unimpeded. This is contrary to off-resonance frequencies where the current is unable to pass through the LC filter. SQUIDs are then used to amplify and measure the current. In this way a "network analysis," an amplitude versus frequency plot, can be created. Fig. 4.18 shows an example network analysis for a 40$\times$ LC filter. While the amplitude of the resonance peaks is in arbitrary units, the peaks can be fit and analyzed. The two gaps between 2.5 and 3 MHz indicates that either the capacitor, inductor, or the wire bond failed here.

Initial testing in the wet dewar resulted in poor yield, a surprising result considering visual inspections of the LC devices suggested a lithographic yield of $\gtrsim$ 95 %.

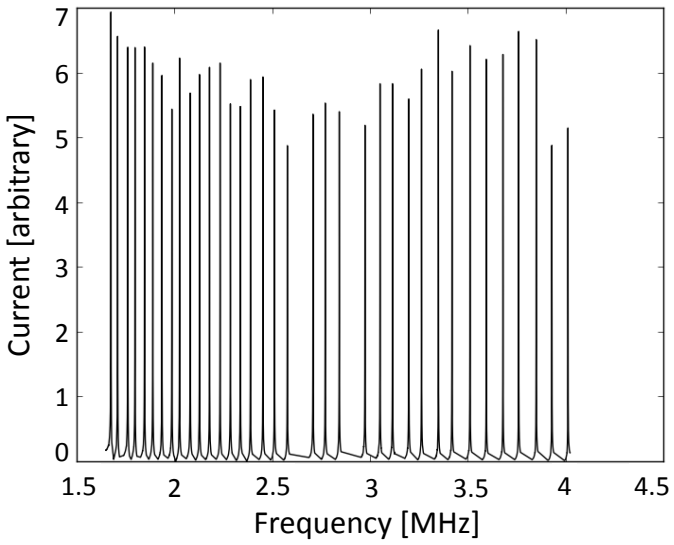

Figure 4.18: Network Analysis of a 40$\times$ LC filter. Channels 20 and 24 are missing.

Through further testing we concluded that the low yield was a consequence of poor wire bonds. The original bond pads (during the plasma etching process) were made of niobium, a robust metal to which wire bonds adhered to well. When switching to aluminum, the wire bond settings (power, time, force, *etc.*) had to be adjusted for the more delicate Al pads. Importantly we determined that the wire bonds were likely "punching through" the bond pads - creating micro-fractures in the bond pad and therefore resulting in poor electrical conductivity. In an attempt to mitigate this problem the wire bond settings were adjusted and the Al layer in the fabrication process was increased. Increasing the Al layer thickness too much makes the lift-off step more difficult. Furthermore the thickness is limited to that of the spin-coated photoresists. A thickness of $1,400$ Å was settled on. Thicker pond pads as well as finely tuned wire bond settings increased the yield of the LC devices dramatically.

A number of key results from the testing of the LC filters are stated in Rotermund et al. (2016): "Typical yield of the individual LC devices is upwards of 90 %. Cleanliness during the fabrication process and consistency of wire bonding should increase the yield further. We found the frequency scatter of channels to be less than 0.3 %, inductances to be incredibly stable at $60.0 \pm 0.1\,\mu$H, and the mutual coupling coefficients k to be negligibly low. Fitting experimental data resulted in $k = 0.0014$ for nearest neighbours, while $k = 0.0002$ for next-to-nearest neighbours. The capacitive coupling term of inductors to the ground plane is negligibly small compared to parallel capacitances of further cold-readout components."

As we saw earlier, the series resistance is a steeply rising function of frequency for ceramic capacitors, reaching $\sim 0.35\,\Omega$ by 3.5 MHz. The goal in switching to interdigitated capacitors fabricated on a low-loss silicon substrate was to maintain a small series resistance even at higher frequencies. In Fig. 4.19 the series resistance of the LC channels is plotted with respect to their frequency. Three sets of LC resonators are tested per plot, each fabricated on a high-resistivity (30 Ω·cm) Si substrate. We find that with the exception of one 40× LC filter, the series resistance remains low and constant over the full range of resonant frequencies, at $\lesssim 0.2\,\Omega$. We further probed the effects of an aluminum shield (*left* plot) and the effects of the aluminum thickness (*right* plot). We find that the Al shield has a stabilizing effect on the series resistance - the only 40× LC filter where the series resistance increased with frequency was when

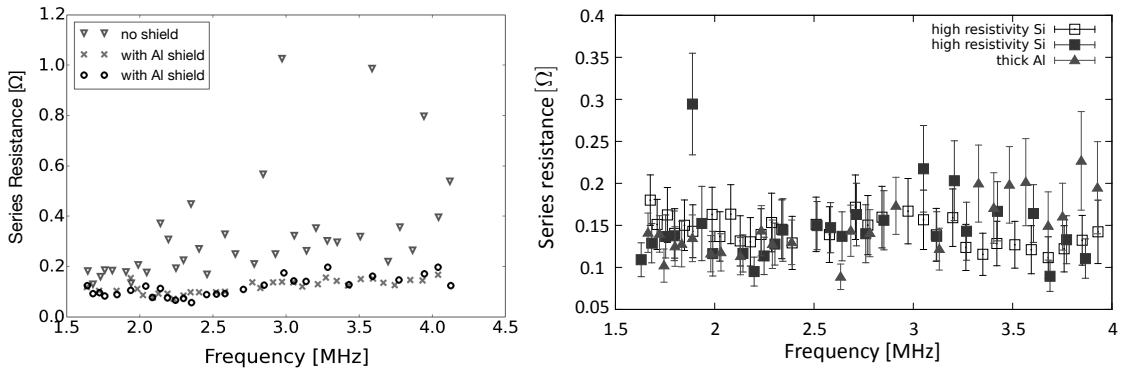

Figure 4.19: Series resistance as a function of frequency for LC filters using interdigitated capacitors fabricated on a 30 Ω·cm resistivity Si substrate. *Left:* The effects of the Al shield are probed - open triangle: no Al shield, cross and open circle: with Al shield. *Right*: The effects of Al thickness are investigated - solid and empty square: 1,000 Å Al layer, solid triangle: 3,000 Å Al layer.

an Al shield was not used (open triangles in *left* plot). For all further testing, the Al shield was therefore used, including in the measurements for the *right* plot. Here we find that the thickness of the Al layer, 1,000 Å for the solid and empty squares and 3,000 Å for the solid triangles, does not affect the series resistance in any appreciable way. At the high frequency end the thicker Al layer may show signs of having a slightly elevated series resistance to the thinner Al layer, however, the measurement differences are within error of each other. Performance of the LC resonators within the full cold-readout system has shown that this is acceptable compared to the desired 10 % of the bolometer resistance ($R_{\rm bolo} = 1\Omega$)

4.4 Conclusion

We have designed and developed an LC chip used in the deployment of POLARBEAR-2 as well as in other CMB polarimetry experiments such as SPT-3G. In doing so we have

1. increased the multiplexing factor from 8 (for POLARBEAR) to 40

2. increased the full carrier frequency range past 1 MHz, made feasible by the implementation of DAN instead of a shunt feedback loop in the cold-readout electronics

3. increased the inductance from 16 μH (for POLARBEAR) to 60 μH in an effort to decrease the electrical bandwidth of each resonator

4. switched to using interdigitated capacitors instead of commercially available ceramic capacitors in an effort to decrease the series resistance of each resonator

5. developed a frequency scheduling for the cold-readout of the TES bolometers such that neighbouring channels in frequency are not also physical neighbours

6. placed the inductors and capacitors in a checkerboard design in order to decrease the mutual coupling between inductors

7. deposited a ground plane on the backside of the chip to stabilize the inductors, and

8. switched to using a lift-off technique to ensure uniformity, reducing frequency scatter.

All of these design and fabrication decisions has lead to an LC chip with high yield, negligibly small mutual inductance, and low series resistance. Critically, the fabrication process is easily scalable for mass production and assembly time is a fraction of what it once was for POLARBEAR.

Chapter 5

Conclusion

5.1 Three research projects

This thesis focused on three topics all aimed broadly at better understanding galaxy growth and evolution in the early universe. In Chapter 2 we presented a survey of 56 gravitational lenses in the redshift range $0.1 < z < 2$. A detailed catalogue of multi-band photometry as well as key astrophysical properties for the lenses was created. We found the lenses to predominantly be massive, passively evolving elliptical galaxies, a population for which the $K - z$ relation holds and provides an attractive alternative method to determining photometric redshifts compared to the costly and time-consuming spectroscopic or multi-band photometric approaches. The $K - z$ method will be especially useful for large sample sizes from next-generation surveys that conduct deeper searchers, *i.e.* can observe fainter objects, and will no longer be observing just the brightest sources. We have found that the identification of gravitational lensing systems via their high-redshift sub-millimetre galaxy (SMG) source results in a sample of lenses whose redshifts are unconstrained and whose masses are redshift independent. This is a critical finding for building a statistical representation of gravitational lenses. Furthermore, a detailed understanding of the lenses, especially redshift and mass, is critical for lens models, which aim to model gravitational lensing systems in an effort to de-lens the SMGs whose light has been magnified as well as distorted by the presence of the lens in the foreground. The vast majority of the SMGs discovered by the South Pole Telescope (SPT) are gravitationally lensed and require lens modelling for further analysis. The redshifts and masses of the lenses in this work specifically help the lens modelling of the SPT-SMG sample.

One of the rare, unlensed, high-redshift objects identified by the SPT-SMG sample is SPT2349-56, a proto-cluster with 14 sources in its core. It was the focus of Chapter 3. SPT2349-56 is unique in its incredible overdensity of SMGs in its core, the 14 core

galaxies within a physical extent $\sim 6\times$ smaller than the only other proto-cluster comparable in compactness, over-density, and star formation rate, the Distant Red Core. This suggests SPT2349 will evolve to be one of, if not the, most massive structures in the local universe. The cumulative stellar mass is likely to grow by at least a factor of two due to the immense gas reservoirs alone. From the analysis of the larger cluster mass we hypothesize that faint, as of yet, undetected galaxies are likely to exist in the core as well. Further galaxy interactions are therefore probable, increasing the stellar mass even more. Understanding the effects of such dense environments on galaxy evolution is immensely interesting. Specifically, we have found that the star formation rate and the stellar mass are not correlated, unlike field SMGs. We are therefore observing the 14 galaxies in the core at various stages of their major-mergers.

Lastly, in an effort to increase measurement sensitivities such that the incredibly faint B-mode polarization of the cosmic microwave background (CMB) caused by gravitational waves can be detected, we delved into a critical instrumentation component. Chapter 4 presented the development of the improved cold-readout electronics, specifically superconducting capacitor-inductor resonator pairs, for transition edge sensor (TES) bolometer arrays. The advances made in developing a fully lithographed LC chip are a critical component of the cold-readout of instruments with detector numbers $O(10,000)$ and higher. The LC chips allow for precise designs of inductance and capacitance values, dramatically lower the thermal loading on the sub-Kelvin stage, as well as decrease device assembly time. They were initially designed and fabricated for POLARBEAR-2 (Rotermund et al. 2016), however, have since been implemented in SPT-3G as well. These two telescopes observing the CMB are making direct use of the work done in this thesis.

5.2 Future outlook of the South Pole Telescope

SPT has hosted three instruments since first light in 2007 - SPT-SZ, SPTpol, and SPT-3G. While all three instruments first and foremost are designed to make high-resolution maps of the CMB, the science objectives vary slightly. With each SPT instrument generation, the sensitivity gets pushed deeper via an increase in detector numbers and the ancillary science goals, such as detecting SMGs and their lenses

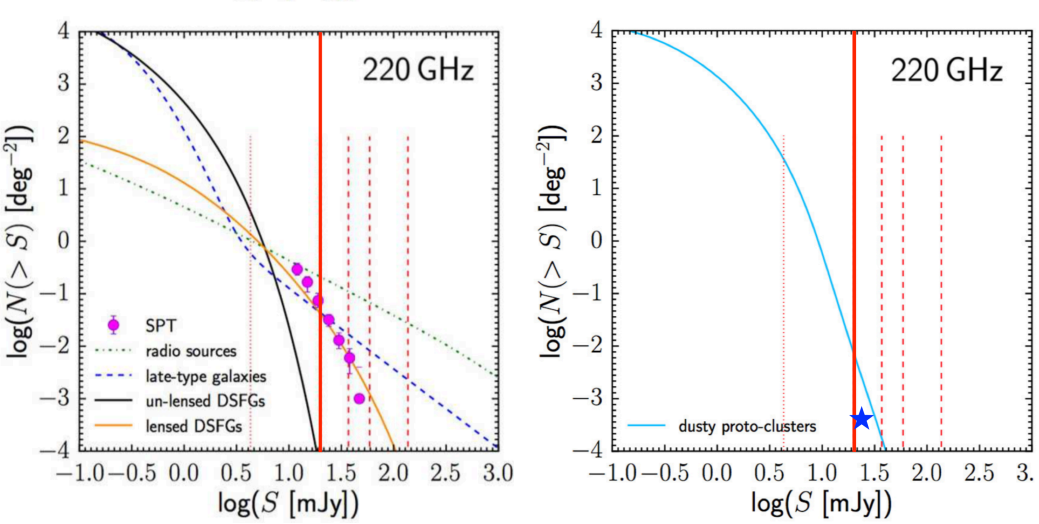

(a) Strongly lensed and unlensed DSFGs. (b) Proto-clusters.

Figure 5.1: Integral number counts at 220 GHz (1.4 mm). (a) Comparison of strongly lensed DSFGs (magenta circles, SPT Vieira et al. 2010) with predicted counts for lensed (orange curve) and unlensed DSFGs (black curve) as determined by Cai et al. (2013) (b) Integral number counts for proto-clusters as predicted by Negrello et al. (2017b) (light blue curve). The blue star (added for comparison purposes) represents the SPT2349 proto-cluster. In both figures, the bold red vertical line shows the SPT completeness limit as determined by Mocanu et al. (2013), the 50 % completeness level is 17.6 mJy at 220 GHz. Figures taken from De Zotti et al. (2019).

as well as searching for high-redshift proto-clusters and galaxy clusters, benefit immensely. As the sensitivity increases, observations of fainter objects can be made. This is exemplified in the two plots in Fig. 5.1, taken from De Zotti et al. (2019). The figures show the integral number counts at 220 GHz (1.4 mm) of 5.1(a) dusty, star-forming galaxies (DSFGs) and 5.1(b) proto-clusters. In Fig. 5.1(a) the number counts for the strongly lensed DSFGs detected in the SPT survey (magenta circles, Vieira et al. 2010) are compared to models done by Cai et al. (2013) of lensed (orange curve) and unlensed DSFGs (black curve). In Fig. 5.1(b) the number counts for proto-clusters as predicted by Negrello et al. (2017b) are shown (light blue curve). The blue star (added for comparison purposes) represents SPT2349-56, with $S_{1.4\,\mathrm{mm}} = 23.3 \pm 3.7$ mJy. In both figures, the bold red vertical line shows the SPT completeness limit as determined by Mocanu et al. (2013), the 50 % completeness level is 17.6 mJy at 220 GHz. This means that detections below 17.6 mJy are rare and likely have low signal-to-noise ratios.

As the model curves suggest for lensed and unlensed DSFGs as well as for proto-clusters, it is expected that the number densities will increase as we are able to probe deeper and sample less bright objects, *i.e.* as we are able to observe objects to the left of the bold red line. In the case of DSFGs, it is likely that a population of high-z, unlensed yet bright DSFGs get observed, possibly with number densities even higher than those for lensed DSFGs. The original detection threshold of SPT-SZ at $S_{1.4\,\mathrm{mm}} > 20$ mJy has since improved in SPT-3G to $S_{1.4\,\mathrm{mm}} > 15$ mJy, a remarkable achievement already, due to the increased number of TES bolometers used made possible by the implementation of the lithographed LC chip. In the search for other proto-clusters, measurements with higher sensitivities will likely lead to the detection of less massive proto-clusters as well as push detections to higher redshift. The location of the SPT2349-56 blue star in Fig. 5.1(b) below the model curve suggests that other similarly bright proto-clusters must exist. In fact, in the $2,500$ deg^2 SPT survey nine additional proto-cluster candidates have been identified. It is possible that one or more will be confirmed.

The power of SPT-3G lies in the large sky coverage, long observing wavelengths, and sensitivities that are continuously improving, allowing for the observations of previously undetected objects out to higher redshifts at unprecedented rates.

Bibliography

Abazajian, K. N., Adshead, P., Ahmed, Z., et al.: 2016, *arXiv e-prints* p. arXiv:1610.02743

Abel, N. P., Dudley, C., Fischer, J., Satyapal, S., and van Hoof, P. A. M.: 2009, *ApJ* **701(2)**, 1147

Abgrall, H., Le Bourlot, J., Pineau Des Forets, G., et al.: 1992, *A&A* **253**, 525

Ade, P. A. R., Akiba, Y., Anthony, A. E., et al.: 2014, *Phys Rev Lett* **112(13)**, 131302

Arnold, K.: 2010, *Ph.D. thesis*, University of California, Berkeley

Auger, M. W., Treu, T., Bolton, A. S., et al.: 2009, *ApJ* **705(2)**, 1099

Barger, A. J., Cowie, L. L., Chen, C. C., et al.: 2014, *ApJ* **784(1)**, 9

Bartelmann, M. and Maturi, M.: 2017, *Scholarpedia* **12(1)**, 32440

Baum, W. A.: 1962, in *Problems of Extra-Galactic Research.*, International Astronomical Union and Symposium 15, p. 390, New York, Macmillan, New York

Behroozi, P. S., Wechsler, R. H., and Conroy, C.: 2013, *ApJ* **770(1)**, 57

Bertin, E. and Arnouts, S.: 1996, *A&AS* **117**, 393

Bertin, E., Mellier, Y., Radovich, M., et al.: 2002, in D. A. Bohlender, D. Durand, and T. H. Handley (eds.), *ADASS XI*, Vol. 281 of *ASPCS*, p. 228

Bertoldi, F., Carilli, C. L., Menten, K. M., et al.: 2000, *A&A* **360**, 92

Bettoni, D., Falomo, R., Fasano, G., et al.: 2001, *A&A* **380(2)**, 471

Blain, A. W.: 1996, *MNRAS* **283(4)**, 1340

Blain, A. W. and Longair, M. S.: 1993, *MNRAS* **264**, 509

Blain, A. W., Smail, I., Ivison, R., Kneib, J.-P., and Frayer, D. T.: 2002, *Phys. Rep.* **369(2)**, 111

Blain, A. W., Smail, I., Ivison, R. J., and Kneib, J.-P.: 1999, *MNRAS* **302**, 632

Bolton, A. S., Burles, S., Koopmans, L. V. E., et al.: 2008, *ApJ* **682(2)**, 964

Bolton, A. S., Burles, S., Koopmans, L. V. E., Treu, T., and Moustakas, L. A.: 2006, *ApJ* **638**, 703

Bolzonella, M., Miralles, J.-M., and Pelló, R.: 2000, *A&A* **363**, 476

Borys, C., Smail, I., Chapman, S. C., et al.: 2005, *ApJ* **635(2)**, 853

Bothwell, M. S., Smail, I., Chapman, S. C., et al.: 2013, *MNRAS* **429(4)**, 3047

Brammer, G. B., van Dokkum, P. G., and Coppi, P.: 2008, *ApJ* **686(2)**, 1503

Brownstein, J. R., Bolton, A. S., Schlegel, D. J., et al.: 2011, *ApJ* **744(1)**, 41

Buat, V., Giovannoli, E., Burgarella, D., et al.: 2010, *MNRAS* **409(1)**, L1

Bussmann, R. S., Pérez-Fournon, I., Amber, S., et al.: 2013, *ApJ* **779(1)**, 25

Cai, Z.-Y., Lapi, A., Xia, J.-Q., et al.: 2013, *ApJ* **768(1)**, 21

Calzetti, D.: 2012, *Star Formation Rate Indicators*, p. 419, Cambridge University Press

Carlstrom, J. E., Ade, P. A. R., Aird, K. A., et al.: 2011, *PASP* **123(903)**, 568

Casey, C. M., Narayanan, D., and Cooray, A.: 2014, *Phys. Rep.* **541(2)**, 45

Chabrier, G.: 2003, *PASP* **115**, 763

Chapman, S. C., Blain, A. W., Ivison, R. J., and Smail, I. R.: 2003a, *Nat* **422(6933)**, 695

Chapman, S. C., Blain, A. W., Smail, I., and Ivison, R. J.: 2005, *ApJ* **622**, 772

Chapman, S. C., Windhorst, R., Odewahn, S., Yan, H., and Conselice, C.: 2003b, *ApJ* **599(1)**, 92

Cirasuolo, M., McLure, R. J., Dunlop, J. S., et al.: 2010, *MNRAS* **401(2)**, 1166

Conroy, C.: 2013, *ARAA* **51(1)**, 393

Conselice, C. J., Chapman, S. C., and Windhorst, R. A.: 2003, *ApJ* **596(1)**, L5

Courteau, S., Cappellari, M., de Jong, R. S., et al.: 2014, *Rev Mod Phys* **86**, 47

Cowley, W. I., Béthermin, M., Lagos, C. d. P., et al.: 2017, *MNRAS* **467(1)**, 1231

da Cunha, E., Groves, B., Walter, F., et al.: 2013, *ApJ* **766(1)**, 13

Dalgarno, A. and Stephens, T. L.: 1970, *ApJ* **160**, L107

De Breuck, C., van Breugel, W., Stanford, S. A., et al.: 2002, *AJ* **123(2)**, 637

De Zotti, G., Bonato, M., Negrello, M., et al.: 2019, *Frontiers in Astronomy and Space Sciences* **6**, 53

Decarli, R., Walter, F., Carilli, C., et al.: 2014, *ApJ* **782(2)**, L17

Dobbs, M. A., Lueker, M., Aird, K. A., et al.: 2012, *Rev Sci Instrum* **83(7)**, 073113

Dole, H., Lagache, G., Puget, J. L., et al.: 2006, *A&A* **451(2)**, 417

Downes, D. and Solomon, P. M.: 1998, *ApJ* **507(2)**, 615

Dye, S., Eales, S. A., Aretxaga, I., et al.: 2008, *MNRAS* **386(2)**, 1107

Eisenstein, D. J., Weinberg, D. H., Agol, E., et al.: 2011, *AJ* **142(3)**, 72

Ferrière, K. M.: 2001, *Rev Mod Phys* **73(4)**, 1031

Galliano, F.: 2004, *Ph.D. thesis*, Service d'Astrophysique, CEA/Saclay, L'Orme des Merisiers

González-Alfonso, E., Fischer, J., Isaak, K., et al.: 2010, *A&A* **518**, L43

Greve, T. R., Bertoldi, F., Smail, I., et al.: 2005, *MNRAS* **359**, 1165

Greve, T. R., Vieira, J. D., Weiß, A., et al.: 2012, *ApJ* **756(1)**, 101

Gullberg, B., De Breuck, C., Vieira, J. D., et al.: 2015, *MNRAS* **449(3)**, 2883

Habart, E., Walmsley, M., Verstraete, L., et al.: 2005, *Space Sci Rev* **119(1)**, 71

Hainline, L. J., Blain, A. W., Smail, I., et al.: 2011, *ApJ* **740(2)**, 96

Han, Z., Podsiadlowski, P., and Lynas-Gray, A. E.: 2007, *MNRAS* **380(3)**, 1098

Hanson, D., Hoover, S., Crites, A., et al.: 2013, *Phys Rev Lett* **111(14)**, 141301

Hattori, K., Akiba, Y., Arnold, K., et al.: 2014, in W. S. Holland and J. Zmuidzinas (eds.), *Millimeter, Submillimeter, and Far-Infrared Detectors and Instrumentation for Astronomy VII*, Vol. 9153, pp 445 – 453, International Society for Optics and Photonics, SPIE

Hattori, K., Arnold, K., Barron, D., et al.: 2013, *Nucl Instrum Meth A* **732**, 299 , Vienna Conference on Instrumentation 2013

Hauser, M. G., Arendt, R. G., Kelsall, T., et al.: 1998, *ApJ* **508**, 25

Hezaveh, Y. D. and Holder, G. P.: 2011, *ApJ* **734**, 52

Hezaveh, Y. D., Marrone, D. P., Fassnacht, C. D., et al.: 2013, *ApJ* **767**, 132

Hollenbach, D. J. and Tielens, A. G. G. M.: 1999, *Rev Mod Phys* **71**, 173

Hu, W. and Dodelson, S.: 2002, *ARAA* **40**, 171

Hu, W. and White, M.: 1997, *New Astron.* **2(4)**, 323

Ivison, R. J., Greve, T. R., Smail, I., et al.: 2002, *MNRAS* **337**, 1

John, T. L.: 1988, *A&A* **193**, 189

Kennicutt, R. C.: 1998, *ARA&A* **36(1)**, 189

King, L. J. and Browne, I. W. A.: 1996, *MNRAS* **282**, 67

Kovac, J. M., Leitch, E. M., Pryke, C., et al.: 2002, *Nature* **420(6917)**, 772

Lacey, C. and Cole, S.: 1993, *MNRAS* **262**, 627

Lagache, G., Puget, J.-L., and Dole, H.: 2005, *ARA&A* **43(1)**, 727

Lilly, S. J., Eales, S. A., Gear, W. K. P., et al.: 1999, *ApJ* **518(2)**, 641

Lilly, S. J. and Longair, M. S.: 1984, *MNRAS* **211(4)**, 833

Ly, C., Malkan, M. A., Kashikawa, N., et al.: 2012, *ApJ* **757(1)**, 63

Maiolino, R., Cox, P., Caselli, P., et al.: 2005, *A&A* **440(2)**, L51

Malhotra, S., Kaufman, M. J., Hollenbach, D., et al.: 2001, *ApJ* **561(2)**, 766

Mather, J. C., Cheng, E. S., Cottingham, D. A., et al.: 1994, *ApJ* **420**, 439

McMullin, J. P., Waters, B., Schiebel, D., Young, W., and Golap, K.: 2007, in R. A. Shaw, F. Hill, and D. J. Bell (eds.), *ADASS XVI*, Vol. 376 of *ASPCS*, p. 127

Michałowski, M., Hjorth, J., and Watson, D.: 2010, *A&A* **514**, A67

Michałowski, M. J., Dunlop, J. S., Cirasuolo, M., et al.: 2012, *A&A* **541**, A85

Miley, G. and De Breuck, C.: 2008, *A&AR* **15(2)**, 67

Miller, T. B., Chapman, S. C., Aravena, M., et al.: 2018, *Nat* **556(7702)**, 469

Mocanu, L. M., Crawford, T. M., Vieira, J. D., et al.: 2013, *ApJ* **779(1)**, 61

Myers, S. T., Jackson, N. J., Browne, I. W. A., et al.: 2003, *MNRAS* **341(1)**, 1

Nagao, T., Maiolino, R., De Breuck, C., et al.: 2012, *A&A* **542**, L34

Narayan, R. and Bartelmann, M.: 1996, *arXiv e-prints* pp astro–ph/9606001

Negrello, M., Amber, S., Amvrosiadis, A., et al.: 2017a, *MNRAS* **465(3)**, 3558

Negrello, M., Gonzalez-Nuevo, J., De Zotti, G., et al.: 2017b, *MNRAS* **470(2)**, 2253

Negrello, M., Perrotta, F., González, J. G.-N., et al.: 2007, *MNRAS* **377(4)**, 1557

Noeske, K. G., Weiner, B. J., Faber, S. M., et al.: 2007, *ApJ* **660**, L43

Noll, S., Burgarella, D., Giovannoli, E., et al.: 2009, *A&A* **507(3)**, 1793

Omont, A., Yang, C., Cox, P., et al.: 2013, *A&A* **551**, A115

Oteo, I., Ivison, R. J., Dunne, L., et al.: 2018, *ApJ* **856(1)**, 72

Overzier, R. A.: 2016, *A&AR* **24(1)**, 14

Pak, S., Yu, Y., Lee, D.-H., Min, K.-W., and Dishoeck, E.: 2003, *J Korean Phys Soc* 42

Pavesi, R., Riechers, D. A., Capak, P. L., et al.: 2016, *ApJ* **832(2)**, 151

Perry, R.: 2018, *Master's thesis*, Dalhousie University

Polletta, M., Tajer, M., Maraschi, L., et al.: 2007, *ApJ* **663**, 81

Pope, A., Scott, D., Borys, C., et al.: 2005, in R. de Grijs and R. M. González Delgado (eds.), *Starbursts: From 30 Doradus to Lyman Break Galaxies*, Vol. 329 of *Astrophysics and Space Science Library*, p. P63

Puget, J.-L., Abergel, A., Bernard, J.-P., et al.: 1996, *A&A* **308**, L5

Puget, J. L. and Léger, A.: 1989, *ARA&A* **27(1)**, 161

Rotermund, K., Barch, B., Chapman, S., et al.: 2016, *JLTP* **184(1)**, 486

Salpeter, E. E.: 1955, *ApJ* **121**, 161

Sanders, D. B. and Mirabel, I. F.: 1996, *ARA&A* **34(1)**, 749

Sanders, D. B., Soifer, B. T., Elias, J. H., et al.: 1988, *ApJ* **325**, 74

Sandstrom, K. M., Leroy, A. K., Walter, F., et al.: 2013, *ApJ* **777**, 5

Santini, P., Fontana, A., Castellano, M., et al.: 2017, *ApJ* **847(1)**, 76

Sargsyan, L., Lebouteiller, V., Weedman, D., et al.: 2012, *ApJ* **755(2)**, 171

Schmidt, S. J., Connolly, A. J., and Hopkins, A. M.: 2006, *ApJ* **649**, 63

Schneider, P.: 2006, *Extragalactic Astronomy and Cosmology*, Springer-Verlag Berlin Heidelberg

Siringo, G., Kreysa, E., Kovács, A., et al.: 2009, *A&A* **497(3)**, 945

Smail, I., Ivison, R. J., and Blain, A. W.: 1997, *ApJ* **490**, L5

Solomon, P. M., Downes, D., Radford, S. J. E., and Barrett, J. W.: 1997, *ApJ* **478**, 144

Spilker, J. S., Marrone, D. P., Aravena, M., et al.: 2016, *ApJ* **826(2)**, 112

Stacey, G. J., Geis, N., Genzel, R., et al.: 1991, *ApJ* **373**, 423

Stacey, G. J., Hailey-Dunsheath, S., Ferkinhoff, C., et al.: 2010, *ApJ* **724(2)**, 957

Steidel, C. C., Adelberger, K. L., Dickinson, M., et al.: 1998, *ApJ* **492(2)**, 428

Strandet, M. L., Weiss, A., Vieira, J. D., et al.: 2016, *ApJ* **822(2)**, 80

Suzuki, A.: 2013, *Ph.D. thesis*, University of California, Berkeley

Swinbank, A. M., Chapman, S. C., Smail, I., et al.: 2006, *MNRAS* **371(1)**, 465

Swinbank, A. M., Simpson, J. M., Smail, I., et al.: 2013, *MNRAS* **438(2)**, 1267

Swinbank, A. M., Smail, I., Chapman, S. C., et al.: 2004, *ApJ* **617(1)**, 64

Tacconi, L. J., Neri, R., Chapman, S. C., et al.: 2006, *ApJ* **640(1)**, 228

Toshikawa, J., Kashikawa, N., Ota, K., et al.: 2012, *ApJ* **750(2)**, 137

Toshikawa, J., Uchiyama, H., Kashikawa, N., et al.: 2018, *PASJ* **70**, S12

van Engelen, A., Sherwin, B. D., Sehgal, N., et al.: 2015, *ApJ* **808(1)**, 7

Vernet, J., Dekker, H., D'Odorico, S., et al.: 2011, *A&A* **536**, A105

Vieira, J. D., Crawford, T. M., Switzer, E. R., et al.: 2010, *ApJ* **719(1)**, 763

Vieira, J. D., Marrone, D. P., Chapman, S. C., et al.: 2013, *Nat* **495**, 344 EP

Walsh, D., Carswell, R. F., and Weymann, R. J.: 1979, *Nat* **279(5712)**, 381

Weiß, A., Breuck, C. D., Marrone, D. P., et al.: 2013, *ApJ* **767(1)**, 88

Wen, Z. L. and Han, J. L.: 2011, *ApJ* **734**, 68

Willott, C. J., Rawlings, S., Jarvis, M. J., and Blundell, K. M.: 2003, *MNRAS* **339(1)**, 173

Yang, C., Gao, Y., Omont, A., et al.: 2013, *ApJ* **771(2)**, L24

Yang, C., Omont, A., Beelen, A., et al.: 2016, *A&A* **595**, A80

Yang, M.: 2007, *Ph.D. thesis*, California Institute of Technology

Zhu, Y.-N., Wu, H., Li, H.-N., and Cao, C.: 2010, *Res Astron Astrophys* **10(4)**, 329

Appendix A

SWarp Configuration File

```
# Configuration file for SWarp 2.38.0
# EB 2016-02-15

#--- Output -------------------------------------------------
IMAGEOUT_NAME    coadd.fits  # Output filename
WEIGHTOUT_NAME   coadd.weight.fits  # Output weight-map filename
HEADER_ONLY      N      # Only a header as an output file (Y/N)?
HEADER_SUFFIX    .head  # Filename extension for additional headers

#--- Input Weights ------------------------------------------
WEIGHT_TYPE      NONE # BACKGROUND,MAP_RMS,MAP_VARIANCE or MAP_WEIGHT
WEIGHT_SUFFIX    .weight.fits  # Suffix to use for weight-maps
WEIGHT_IMAGE     cov.fits  # Weightmap filename if suffix not used

#--- Co-addition --------------------------------------------
COMBINE          N        # Combine resampled images (Y/N)?
COMBINE_TYPE     MEDIAN   # MEDIAN,AVERAGE,MIN,MAX,WEIGHTED,CLIPPED,
                            CHI-OLD,CHI-MODE,CHI-MEAN,SUM,
                            WEIGHTED_WEIGHT,MEDIAN_WEIGHT,AND,NAND,
                            OR or NOR

#--- Astrometry ---------------------------------------------
CELESTIAL_TYPE   EQUATORIAL  # NATIVE,PIXEL,EQUATORIAL,GALACTIC,
                               ECLIPTIC, or SUPERGALACTIC
PROJECTION_TYPE  TAN      # Any WCS projection code or NONE
PROJECTION_ERR   0.001  # Maximum projection error (in output pixels)
```

```
CENTER_TYPE      MANUAL   # MANUAL, ALL or MOST
CENTER     00:00:00.00, +00:00:00.0  # Coordinates of the image center
PIXELSCALE_TYPE  MANUAL   # MANUAL,FIT,MIN,MAX or MEDIAN
PIXEL_SCALE      0        # Pixel scale
IMAGE_SIZE       300,300  # Image size

#--- Resampling ------------------------------------------------
RESAMPLE         Y        # Resample input images (Y/N)?
RESAMPLE_DIR     .        # Directory path for resampled images
RESAMPLE_SUFFIX  .resamp.fits  # filename extension for
                                 resampled images

RESAMPLING_TYPE  LANCZOS3  # NEAREST,BILINEAR,LANCZOS2,LANCZOS3,
                             LANCZOS4, or FLAGS
OVERSAMPLING     0        # Oversampling in each dimension
                           (0 = automatic)
INTERPOLATE      N        # Interpolate bad input pixels (Y/N)?

FSCALASTRO_TYPE  FIXED    # NONE,FIXED, or VARIABLE
FSCALE_KEYWORD   FLXSCALE # FITS keyword for the multiplicative
                           factor applied to each input image
FSCALE_DEFAULT   1.0      # Default FSCALE value if not in header

GAIN_KEYWORD    GAIN     # FITS keyword for effect. gain (e-/ADU)
GAIN_DEFAULT     1.0      # Default gain if no FITS keyword found

#--- Background subtraction ------------------------------------
SUBTRACT_BACK    Y        # Subtraction sky background (Y/N)?
BACK_TYPE        AUTO     # AUTO or MANUAL
BACK_DEFAULT     0.0      # Default background value in MANUAL
BACK_SIZE        512      # Background mesh size (pixels)
BACK_FILTERSIZE  3        # Background map filter range (meshes)
```

```
#--- Memory management ----------------------------------------
VMEM_DIR         .        # Directory path for swap files
VMEM_MAX         2047     # Maximum amount of virtual memory (MB)
MEM_MAX          256      # Maximum amount of usable RAM (MB)
COMBINE_BUFSIZE  256      # RAM dedicated to co-addition(MB)

#--- Miscellaneous --------------------------------------------
DELETE_TMPFILES  Y # Delete temporary resampled FITS files (Y/N)?
COPY_KEYWORDS    OBJECT   # List of FITS keywords to propagate
                          from the input to the output headers
WRITE_FILEINFO   N        # Write information about each input
                          file in the output image header?
WRITE_XML        Y        # Write XML file (Y/N)?
XML_NAME         swarp.xml  # Filename for XML output
VERBOSE_TYPE     NORMAL   # QUIET,LOG,NORMAL, or FULL
NTHREADS         0        # Number of simultaneous threads for
                          the SMP version of SWarp (0 = automatic)
```

Appendix B

SExtractor Configuration File

```
# Default configuration file for SExtractor 2.3b2
# EB 2003-02-07

#--- Catalog ------------------------------------------------
CATALOG_NAME    K.cat  # name of the output catalog
CATALOG_TYPE    ASCII_HEAD
PARAMETERS_NAME newiracparams.param  # name of the file
                                     containing catalog contents

#--- Extraction ---------------------------------------------
DETECT_TYPE     CCD  # "CCD" or "PHOTO"
FLAG_IMAGE      flag.fits  # filename for an input FLAG-image
DETECT_MINAREA  4    # minimum number of pixels above threshold
DETECT_THRESH   1.1  # <sigmas>
ANALYSIS_THRESH 1.1  # <sigmas>

FILTER          Y    # apply filter for detection ("Y" or "N")?
FILTER_NAME     gauss_5.0_9x9.conv  # name of the file containing
                                      the filter

DEBLEND_NTHRESH 64   # Number of deblending sub-thresholds
DEBLEND_MINCONT 0.0001 # Minimum contrast parameter for deblending

CLEAN           Y    # Clean spurious detections? (Y or N)?
CLEAN_PARAM     1.0  # Cleaning efficiency
```

```
MASK_TYPE       CORRECT  # type of detection MASKing

#--- Photometry ------------------------------------------------
PHOT_AUTOPARAMS 2.5, 3.5  # MAG_AUTO parameters:
                            <Kron_fact>,<min_radius>
SATUR_LEVEL       500.0  # level (in ADUs) at which arises saturation
MAG_ZEROPOINT   0    # magnitude zero-point
MAG_GAMMA       4.0  # gamma of emulsion (for photographic scans)
GAIN            0    # detector gain in e-/ADU
PIXEL_SCALE     0.148  # size of pixel in arcsec

#--- Star/Galaxy Separation -------------------------------------
SEEING_FWHM     1.1  # stellar FWHM in arcsec
STARNNW_NAME    default.nnw  # Neural-Network_Weight table filename

#--- Background ------------------------------------------------
BACK_SIZE       128  # Background mesh: <size>
BACK_FILTERSIZE 3    # Background filter: <size>
BACK_TYPE       AUTO  # Background being subtracted
BACKPHOTO_TYPE  GLOBAL  # can be "GLOBAL" or "LOCAL"

#--- Check Image -----------------------------------------------
CHECKIMAGE_TYPE BACKGROUND,OBJECTS,APERTURES
CHECKIMAGE_NAME K_check_bg.fits,K_check_obj.fits,K_check_aper.fits
                     # Filename for the check-image

#--- Memory (change with caution!) -----------------------------
MEMORY_OBJSTACK 8000  # number of objects in stack
MEMORY_PIXSTACK 1600000  # number of pixels in stack
MEMORY_BUFSIZE  2048  # number of lines in buffer

#--- Miscellaneous ---------------------------------------------
```

```
VERBOSE_TYPE    NORMAL  # can be "QUIET", "NORMAL" or "FULL"
```

Table B.1

Band	Seeing FWHM [arcsec]	Gaussian Filter
DES grizY	1.24, 1.03, 0.96, 1.12, 1.33	3.65-5.06
G & R	$\sim$ 0.5-1.0 (median $\sim$ 0.8)	3.9-7.9
F110 & F140 & F160	0.130 & 0.141 & 0.151	1.0 or 0.1
J & K	$\sim$ 0.7-1.6 (median $\sim$ 1.1)	4.7-10.8
CH1 & CH2 (cold)	1.66 & 1.72	2.77 & 2.87
CH1 & CH2 (warm)	1.95 & 2.02	3.25 & 3.37

Appendix C

Spectra for a Sub-sample of the SPT Lenses

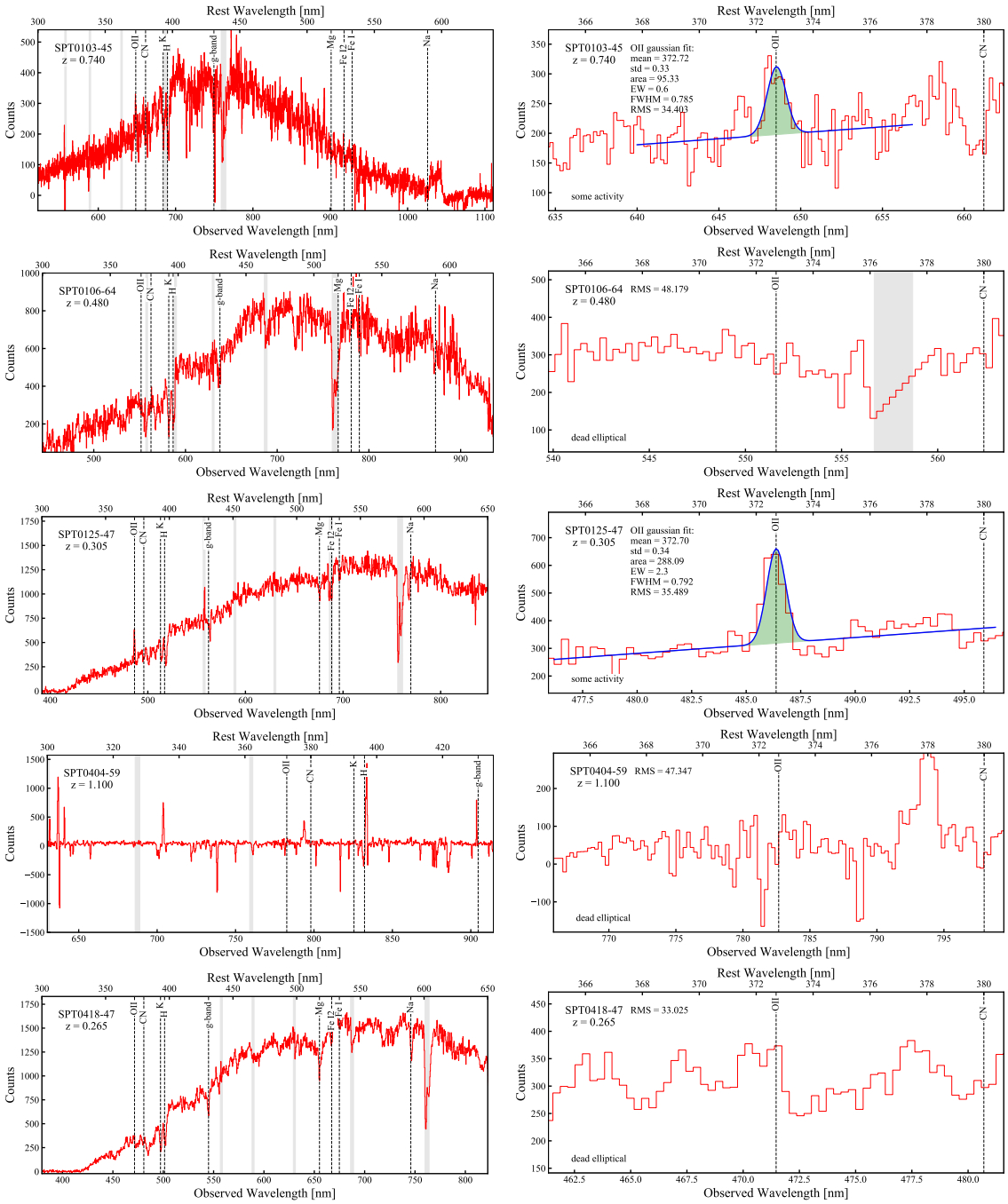

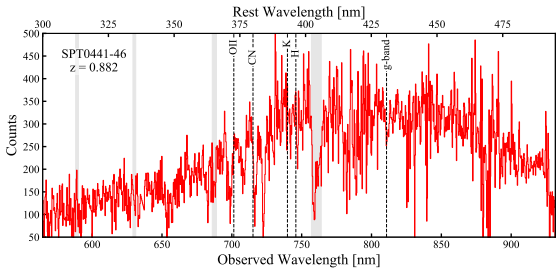
Rest Wavelength [nm]
SPT0441-46
z = 0.882
OII
CN
K
H
g-band
Counts
Observed Wavelength [nm]

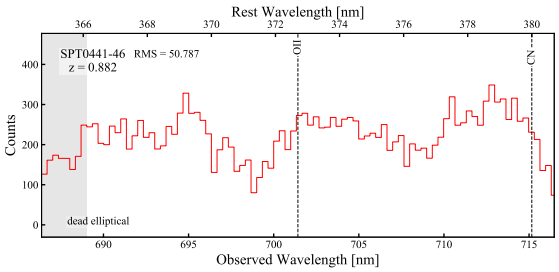
Rest Wavelength [nm]
SPT0441-46 RMS = 50.787
z = 0.882
OII
CN
dead elliptical
Counts
Observed Wavelength [nm]

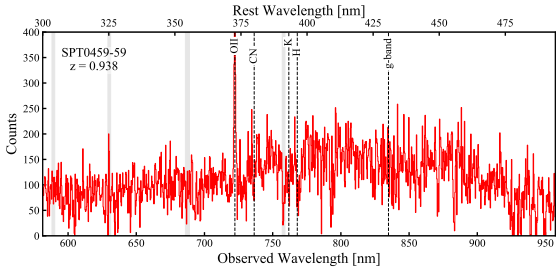
Rest Wavelength [nm]
SPT0459-59
z = 0.938
OII
CN
K
H
g-band
Counts
Observed Wavelength [nm]

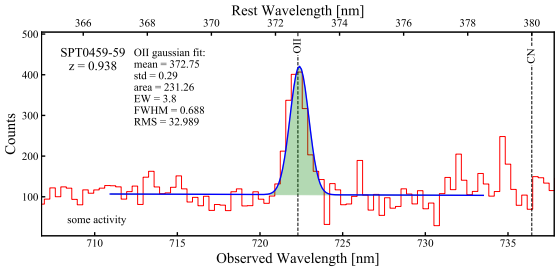
Rest Wavelength [nm]
SPT0459-59 OII gaussian fit:
z = 0.938 mean = 372.75
std = 0.29
area = 231.26
EW = 3.8
FWHM = 0.688
RMS = 32.989
OII
CN
some activity
Counts
Observed Wavelength [nm]

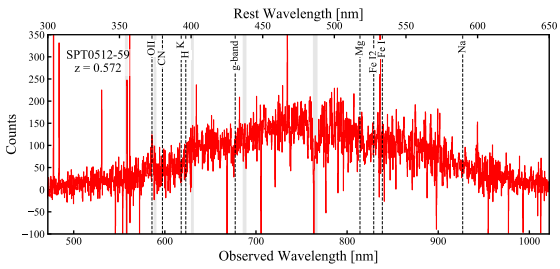
Rest Wavelength [nm]
SPT0512-59
z = 0.572
OII
CN
K
H
g-band
Mg
Fe I2
Fe I1
Na
Counts
Observed Wavelength [nm]

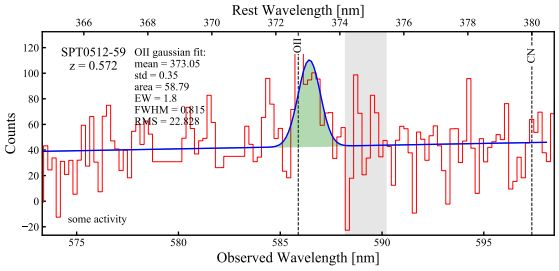
Rest Wavelength [nm]
SPT0512-59 OII gaussian fit:
z = 0.572 mean = 373.05
std = 0.35
area = 58.79
EW = 1.8
FWHM = 0.815
RMS = 22.828
OII
CN
some activity
Counts
Observed Wavelength [nm]

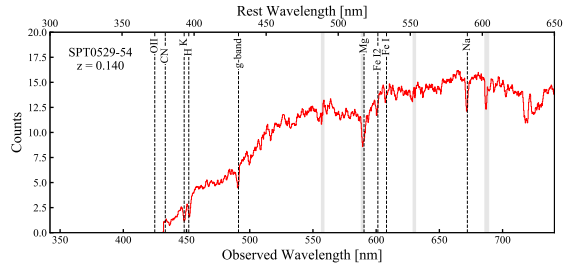
Rest Wavelength [nm]
SPT0529-54
z = 0.140
OII
CN
K
H
g-band
Mg
Fe I2
Fe I1
Na
Counts
Observed Wavelength [nm]

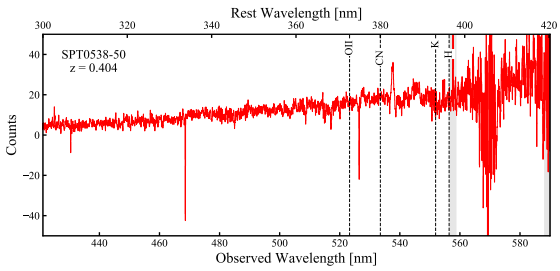
Rest Wavelength [nm]
SPT0538-50
z = 0.404
OII
CN
K
H
Counts
Observed Wavelength [nm]

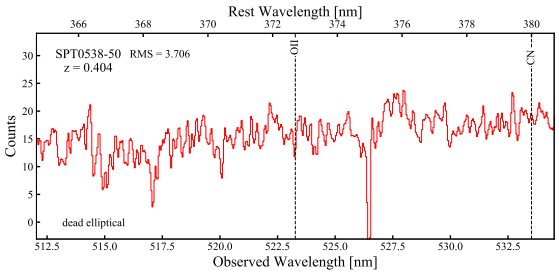
Rest Wavelength [nm]
SPT0538-50 RMS = 3.706
z = 0.404
OII
CN
dead elliptical
Counts
Observed Wavelength [nm]

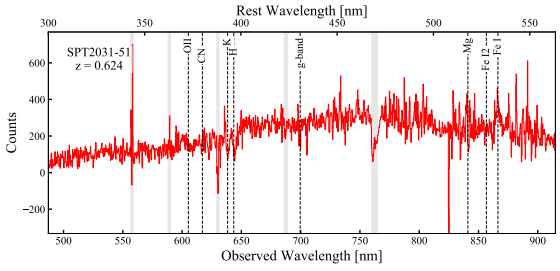
Rest Wavelength [nm]
SPT2031-51
z = 0.624
OII
CN
K
H
g-band
Mg
Fe I2
Fe I1
Counts
Observed Wavelength [nm]

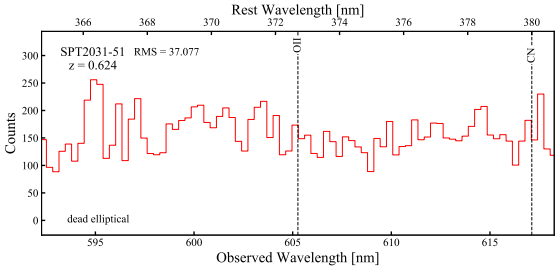
Rest Wavelength [nm]
SPT2031-51 RMS = 37.077
z = 0.624
OII
CN
dead elliptical
Counts
Observed Wavelength [nm]

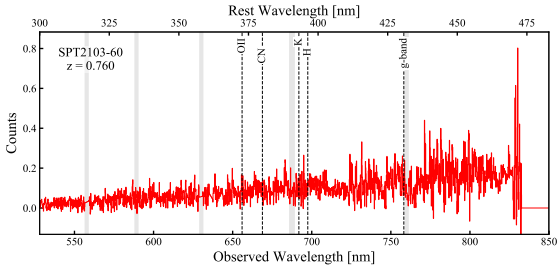
Rest Wavelength [nm]
SPT2103-60
z = 0.760
OII
CN
K
H
g-band
Counts
Observed Wavelength [nm]

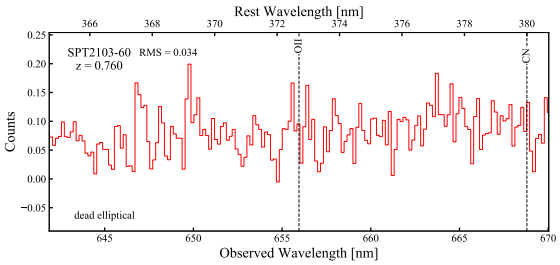
Rest Wavelength [nm]
SPT2103-60 RMS = 0.034
z = 0.760
OII
CN
dead elliptical
Counts
Observed Wavelength [nm]

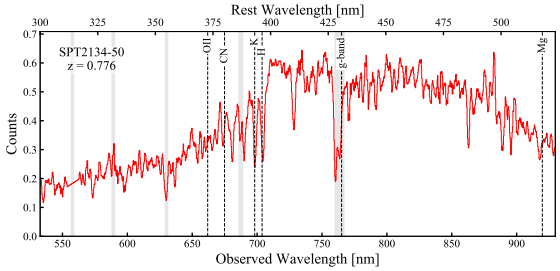
Rest Wavelength [nm]
SPT2134-50
z = 0.776
OII
CN
H
K
g-band
Mg
Counts
Observed Wavelength [nm]

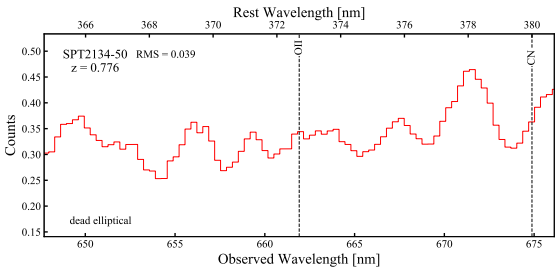
Rest Wavelength [nm]
SPT2134-50 RMS = 0.039
z = 0.776
OII
CN
dead elliptical
Counts
Observed Wavelength [nm]

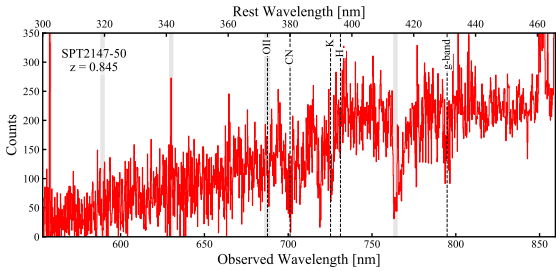
Rest Wavelength [nm]
SPT2147-50
z = 0.845
OII
CN
K
H
g-band
Counts
Observed Wavelength [nm]

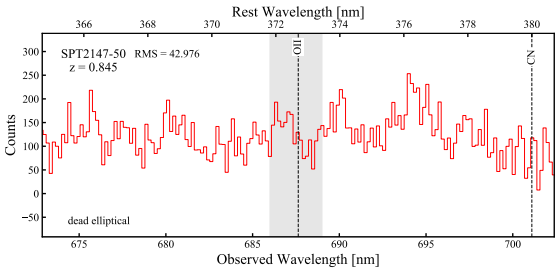
Rest Wavelength [nm]
SPT2147-50 RMS = 42.976
z = 0.845
OII
CN
dead elliptical
Counts
Observed Wavelength [nm]

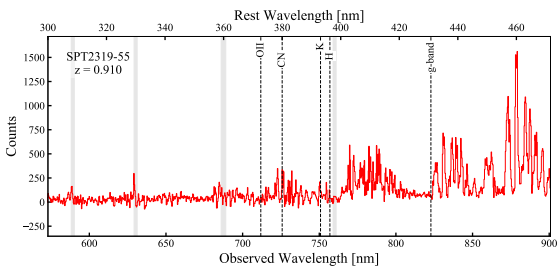
Rest Wavelength [nm]
SPT2319-55
z = 0.910
OII
CN
K
H
g-band
Counts
Observed Wavelength [nm]

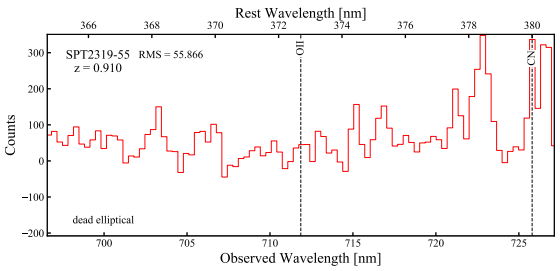
Rest Wavelength [nm]
SPT2319-55 RMS = 55.866
z = 0.910
OII
CN
dead elliptical
Counts
Observed Wavelength [nm]

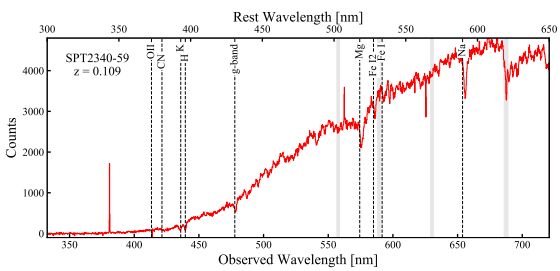
Rest Wavelength [nm]
SPT2340-59
z = 0.109
OII
CN
H
K
g-band
Mg
Fe I2
Fe I1
Na
Counts
Observed Wavelength [nm]

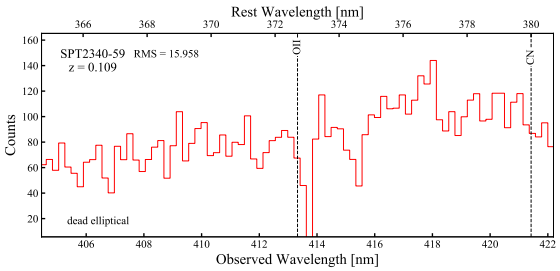
Rest Wavelength [nm]
SPT2340-59 RMS = 15.958
z = 0.109
OII
CN
dead elliptical
Counts
Observed Wavelength [nm]

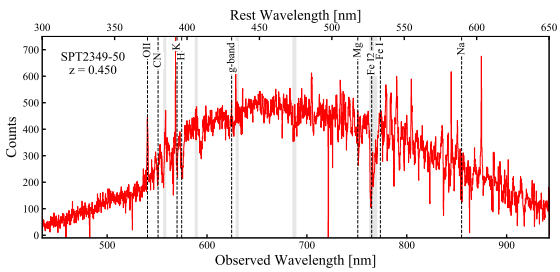
Rest Wavelength [nm]
SPT2349-50
z = 0.450
OII
CN
H
K
g-band
Mg
Fe I2
Fe I1
Na
Counts
Observed Wavelength [nm]

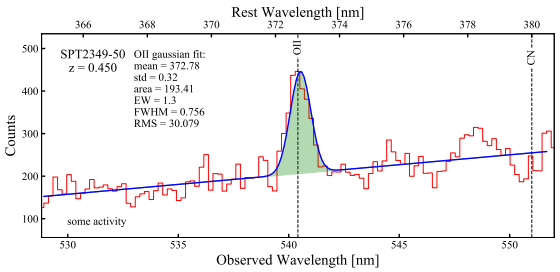
Rest Wavelength [nm]
SPT2349-50
z = 0.450
OII gaussian fit:
mean = 372.78
std = 0.32
area = 193.41
EW = 1.3
FWHM = 0.756
RMS = 30.079
OII
CN
some activity
Counts
Observed Wavelength [nm]

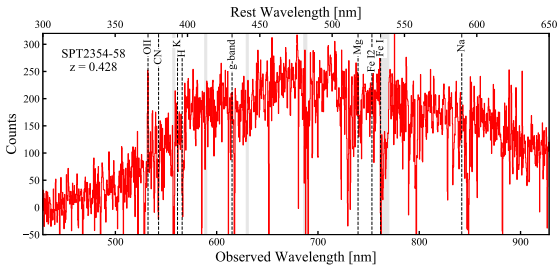
Rest Wavelength [nm]
SPT2354-58
z = 0.428
OII
CN
K
H
g-band
Mg
Fe 12
Fe 1
Na
Counts
Observed Wavelength [nm]

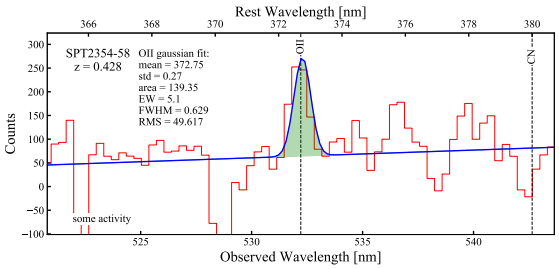
Rest Wavelength [nm]
SPT2354-58
z = 0.428
OII gaussian fit:
mean = 372.75
std = 0.27
area = 139.35
EW = 5.1
FWHM = 0.629
RMS = 49.617
OII
CN
some activity
Counts
Observed Wavelength [nm]

Appendix D

Thumbnails for the SPT Lenses

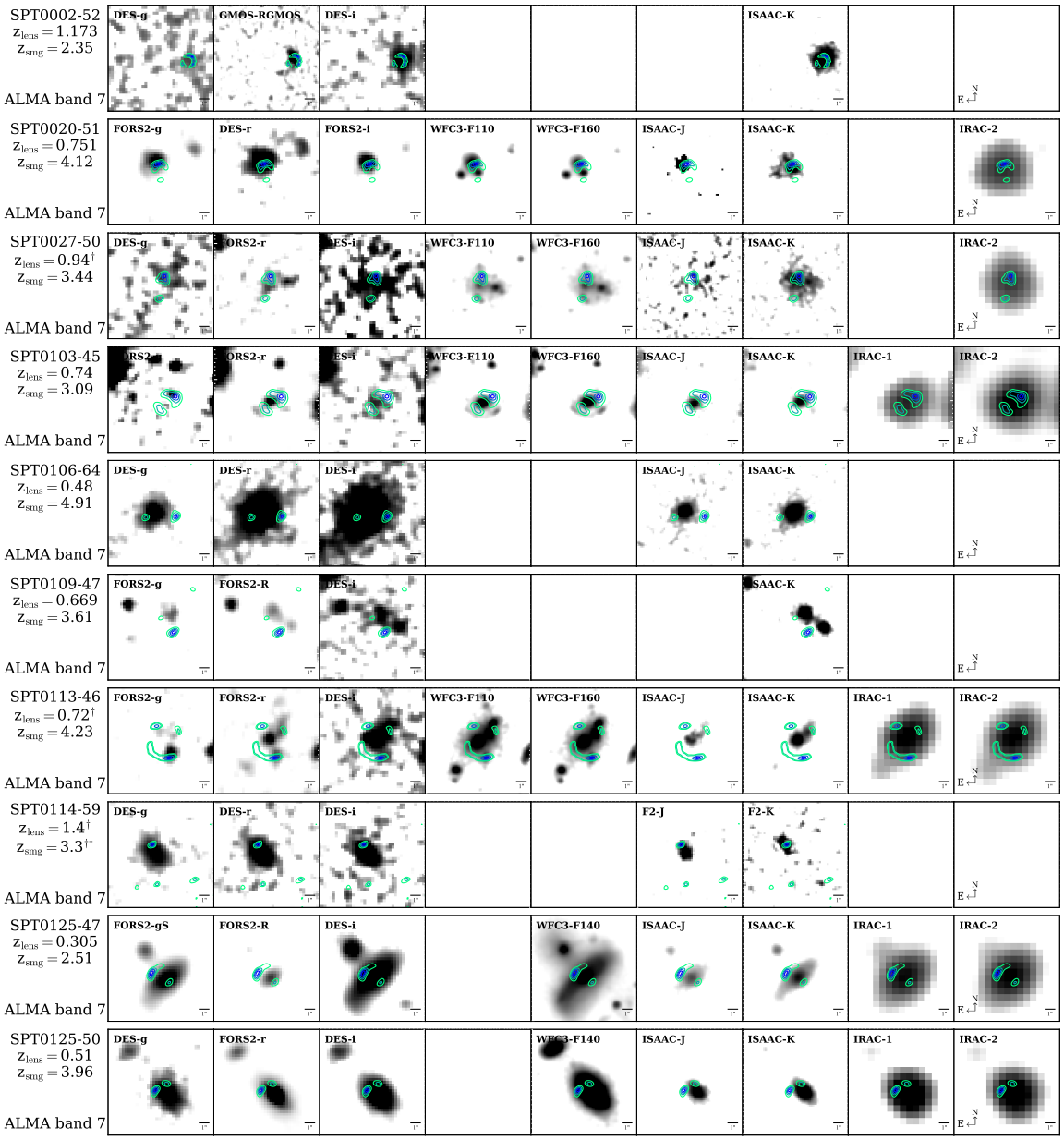

† Lens $K-z$ redshift

†† SMG multi-band photometric redshift

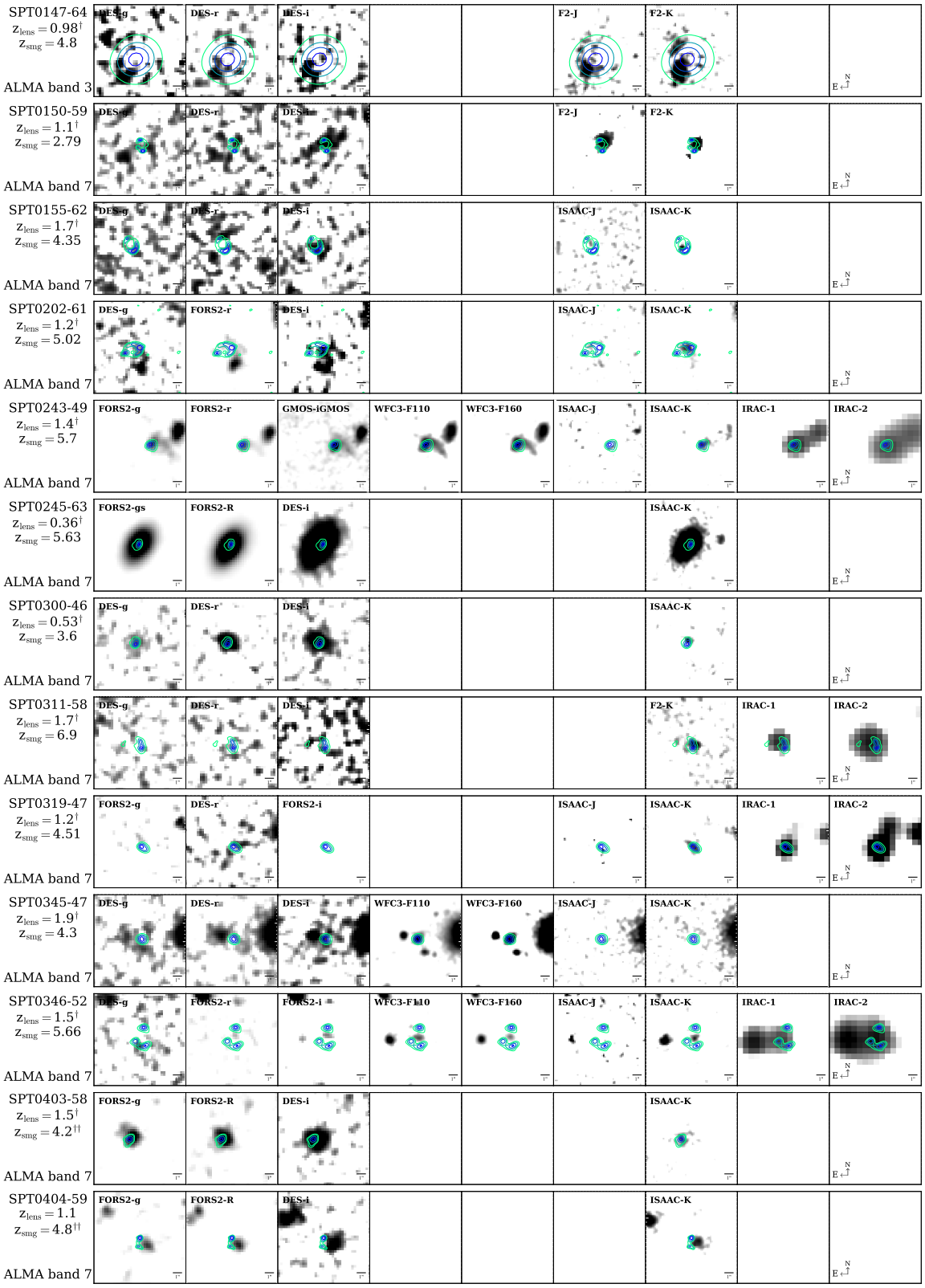
SPT0147-64
$z_{lens} = 0.98^{\dagger}$
$z_{smg} = 4.8$
ALMA band 3
DES-g
DES-r
DES-i
F2-J
F2-K
SPT0150-59
$z_{lens} = 1.1^{\dagger}$
$z_{smg} = 2.79$
ALMA band 7
DES-g
DES-r
DES-i
F2-J
F2-K
SPT0155-62
$z_{lens} = 1.7^{\dagger}$
$z_{smg} = 4.35$
ALMA band 7
DES-g
DES-r
DES-i
ISAAC-J
ISAAC-K
SPT0202-61
$z_{lens} = 1.2^{\dagger}$
$z_{smg} = 5.02$
ALMA band 7
DES-g
FORS2-r
DES-i
ISAAC-J
ISAAC-K
SPT0243-49
$z_{lens} = 1.4^{\dagger}$
$z_{smg} = 5.7$
ALMA band 7
FORS2-g
FORS2-r
GMOS-iGMOS
WFC3-F110
WFC3-F160
ISAAC-J
ISAAC-K
IRAC-1
IRAC-2
SPT0245-63
$z_{lens} = 0.36^{\dagger}$
$z_{smg} = 5.63$
ALMA band 7
FORS2-gs
FORS2-R
DES-i
ISAAC-K
SPT0300-46
$z_{lens} = 0.53^{\dagger}$
$z_{smg} = 3.6$
ALMA band 7
DES-g
DES-r
DES-i
ISAAC-K
SPT0311-58
$z_{lens} = 1.7^{\dagger}$
$z_{smg} = 6.9$
ALMA band 7
DES-g
DES-r
DES-i
F2-K
IRAC-1
IRAC-2
SPT0319-47
$z_{lens} = 1.2^{\dagger}$
$z_{smg} = 4.51$
ALMA band 7
FORS2-g
DES-r
FORS2-i
ISAAC-J
ISAAC-K
IRAC-1
IRAC-2
SPT0345-47
$z_{lens} = 1.9^{\dagger}$
$z_{smg} = 4.3$
ALMA band 7
DES-g
DES-r
DES-i
WFC3-F110
WFC3-F160
ISAAC-J
ISAAC-K
SPT0346-52
$z_{lens} = 1.5^{\dagger}$
$z_{smg} = 5.66$
ALMA band 7
DES-g
FORS2-r
FORS2-i
WFC3-F110
WFC3-F160
ISAAC-J
ISAAC-K
IRAC-1
IRAC-2
SPT0403-58
$z_{lens} = 1.5^{\dagger}$
$z_{smg} = 4.2^{\dagger\dagger}$
ALMA band 7
FORS2-g
FORS2-R
DES-i
ISAAC-K
SPT0404-59
$z_{lens} = 1.1$
$z_{smg} = 4.8^{\dagger\dagger}$
ALMA band 7
FORS2-g
FORS2-R
DES-i
ISAAC-K

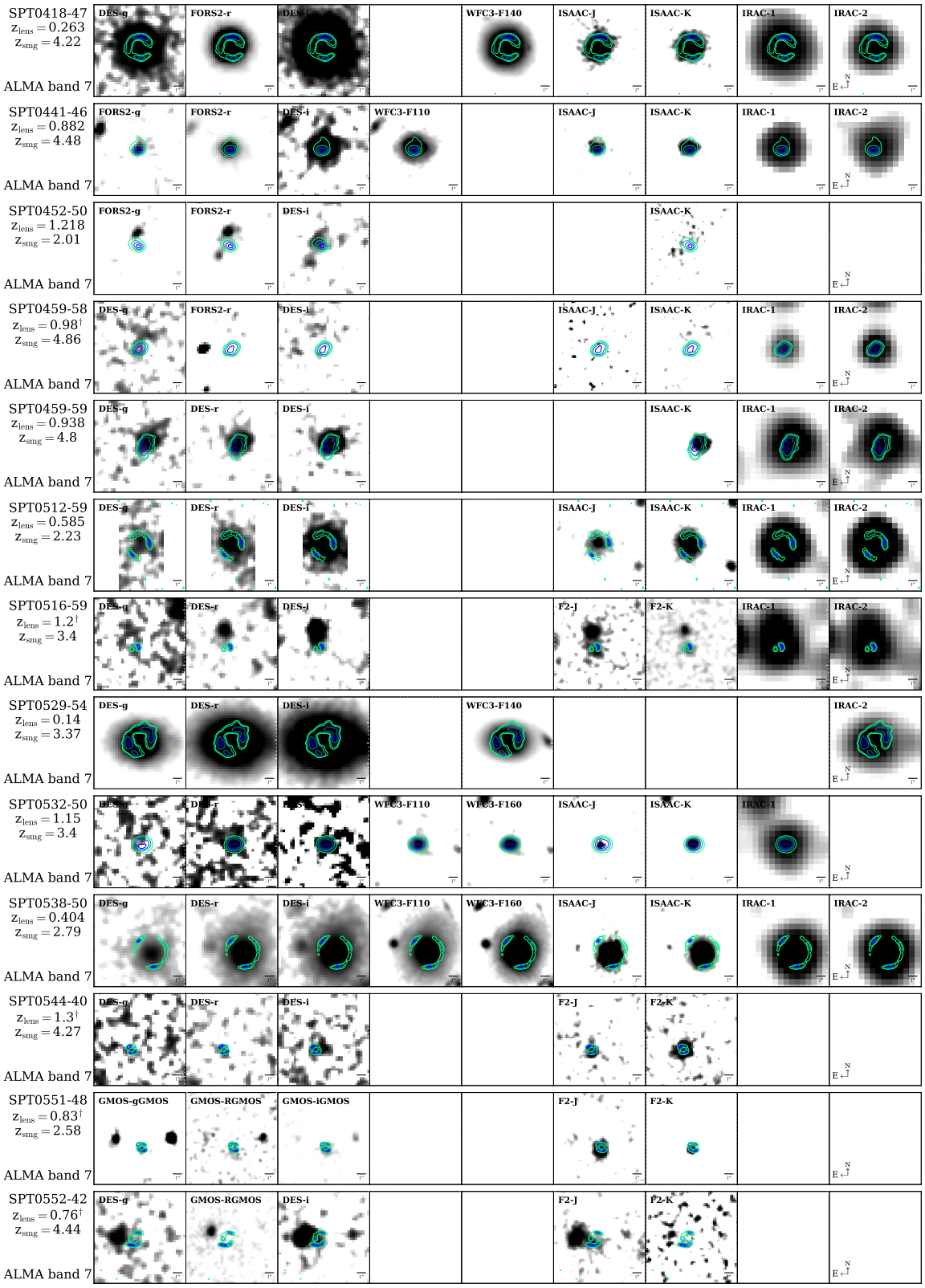
SPT0418-47
$z_{lens} = 0.263$
$z_{smg} = 4.22$
ALMA band 7
DES-g
FORS2-r
DES-i
WFC3-F140
ISAAC-J
ISAAC-K
IRAC-1
IRAC-2
SPT0441-46
$z_{lens} = 0.882$
$z_{smg} = 4.48$
ALMA band 7
FORS2-g
FORS2-r
DES-i
WFC3-F110
ISAAC-J
ISAAC-K
IRAC-1
IRAC-2
SPT0452-50
$z_{lens} = 1.218$
$z_{smg} = 2.01$
ALMA band 7
FORS2-g
FORS2-r
DES-i
ISAAC-K
SPT0459-58
$z_{lens} = 0.98^{\dagger}$
$z_{smg} = 4.86$
ALMA band 7
DES-g
FORS2-r
DES-i
ISAAC-J
ISAAC-K
IRAC-1
IRAC-2
SPT0459-59
$z_{lens} = 0.938$
$z_{smg} = 4.8$
ALMA band 7
DES-g
DES-r
DES-i
ISAAC-K
IRAC-1
IRAC-2
SPT0512-59
$z_{lens} = 0.585$
$z_{smg} = 2.23$
ALMA band 7
DES-g
DES-r
DES-i
ISAAC-J
ISAAC-K
IRAC-1
IRAC-2
SPT0516-59
$z_{lens} = 1.2^{\dagger}$
$z_{smg} = 3.4$
ALMA band 7
DES-g
DES-r
DES-i
F2-J
F2-K
IRAC-1
IRAC-2
SPT0529-54
$z_{lens} = 0.14$
$z_{smg} = 3.37$
ALMA band 7
DES-g
DES-r
DES-i
WFC3-F140
IRAC-2
SPT0532-50
$z_{lens} = 1.15$
$z_{smg} = 3.4$
ALMA band 7
WFC3-F110
WFC3-F160
ISAAC-J
ISAAC-K
IRAC-1
SPT0538-50
$z_{lens} = 0.404$
$z_{smg} = 2.79$
ALMA band 7
DES-g
DES-r
DES-i
WFC3-F110
WFC3-F160
ISAAC-J
ISAAC-K
IRAC-1
IRAC-2
SPT0544-40
$z_{lens} = 1.3^{\dagger}$
$z_{smg} = 4.27$
ALMA band 7
DES-r
DES-i
F2-J
F2-K
SPT0551-48
$z_{lens} = 0.83^{\dagger}$
$z_{smg} = 2.58$
ALMA band 7
GMOS-gGMOS
GMOS-RGMOS
GMOS-iGMOS
F2-J
F2-K
SPT0552-42
$z_{lens} = 0.76^{\dagger}$
$z_{smg} = 4.44$
ALMA band 7
DES-g
GMOS-RGMOS
DES-i
F2-J
F2-K

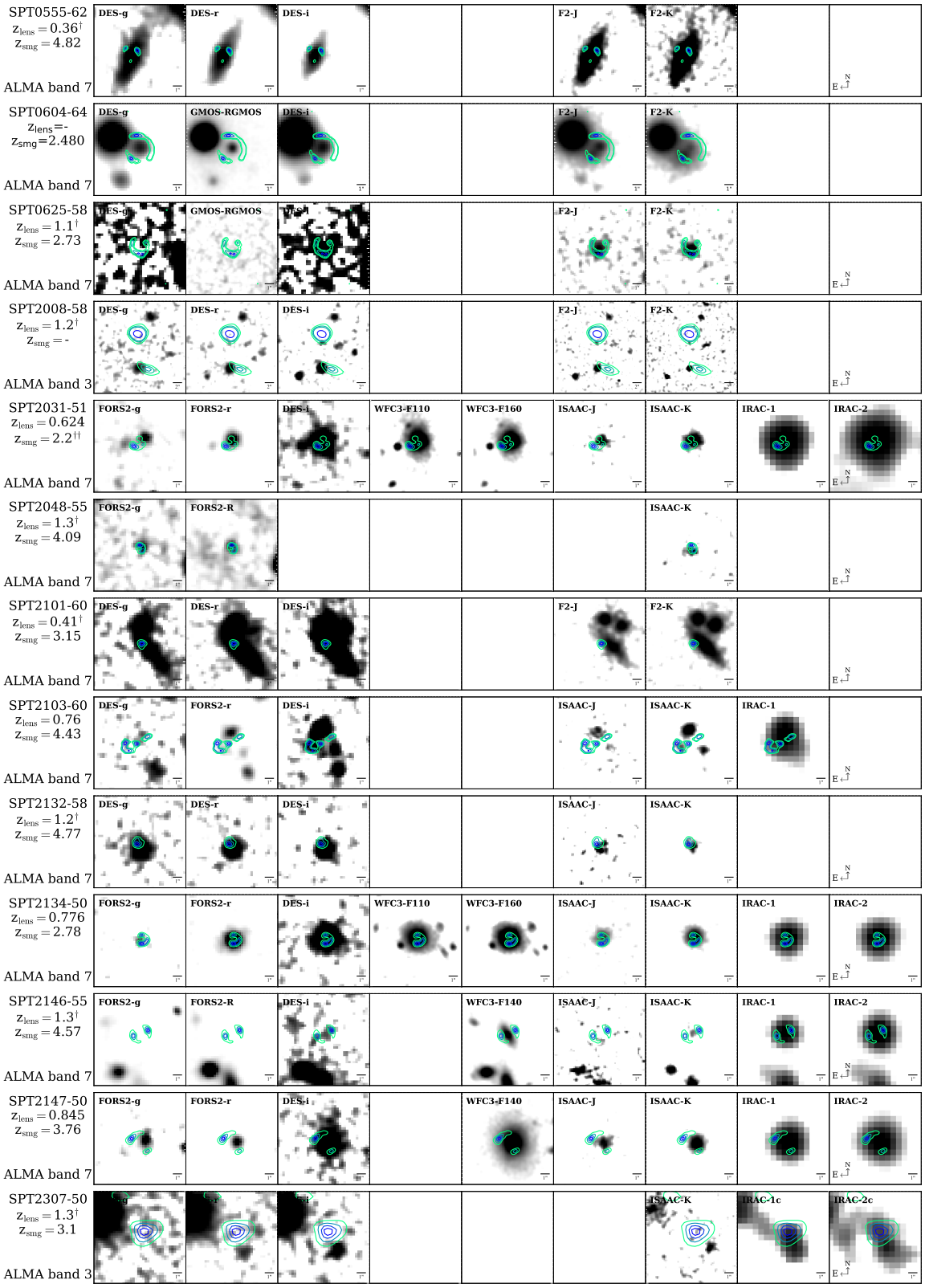
SPT0555-62
z_lens = 0.36†
z_smg = 4.82
ALMA band 7
DES-g
DES-r
DES-i
F2-J
F2-K
SPT0604-64
z_lens=-
z_smg=2.480
ALMA band 7
DES-g
GMOS-RGMOS
DES-i
F2-J
F2-K
SPT0625-58
z_lens = 1.1†
z_smg = 2.73
ALMA band 7
GMOS-RGMOS
F2-J
F2-K
SPT2008-58
z_lens = 1.2†
z_smg = -
ALMA band 3
DES-g
DES-r
DES-i
F2-J
F2-K
SPT2031-51
z_lens = 0.624
z_smg = 2.2††
ALMA band 7
FORS2-g
FORS2-r
DES-i
WFC3-F110
WFC3-F160
ISAAC-J
ISAAC-K
IRAC-1
IRAC-2
SPT2048-55
z_lens = 1.3†
z_smg = 4.09
ALMA band 7
FORS2-g
FORS2-R
ISAAC-K
SPT2101-60
z_lens = 0.41†
z_smg = 3.15
ALMA band 7
DES-g
DES-r
DES-i
F2-J
F2-K
SPT2103-60
z_lens = 0.76
z_smg = 4.43
ALMA band 7
DES-g
FORS2-r
DES-i
ISAAC-J
ISAAC-K
IRAC-1
SPT2132-58
z_lens = 1.2†
z_smg = 4.77
ALMA band 7
DES-g
DES-r
DES-i
ISAAC-J
ISAAC-K
SPT2134-50
z_lens = 0.776
z_smg = 2.78
ALMA band 7
FORS2-g
FORS2-r
DES-i
WFC3-F110
WFC3-F160
ISAAC-J
ISAAC-K
IRAC-1
IRAC-2
SPT2146-55
z_lens = 1.3†
z_smg = 4.57
ALMA band 7
FORS2-g
FORS2-R
DES-i
WFC3-F140
ISAAC-J
ISAAC-K
IRAC-1
IRAC-2
SPT2147-50
z_lens = 0.845
z_smg = 3.76
ALMA band 7
FORS2-g
FORS2-r
DES-i
WFC3-F140
ISAAC-J
ISAAC-K
IRAC-1
IRAC-2
SPT2307-50
z_lens = 1.3†
z_smg = 3.1
ALMA band 3
ISAAC-K
IRAC-1c
IRAC-2c

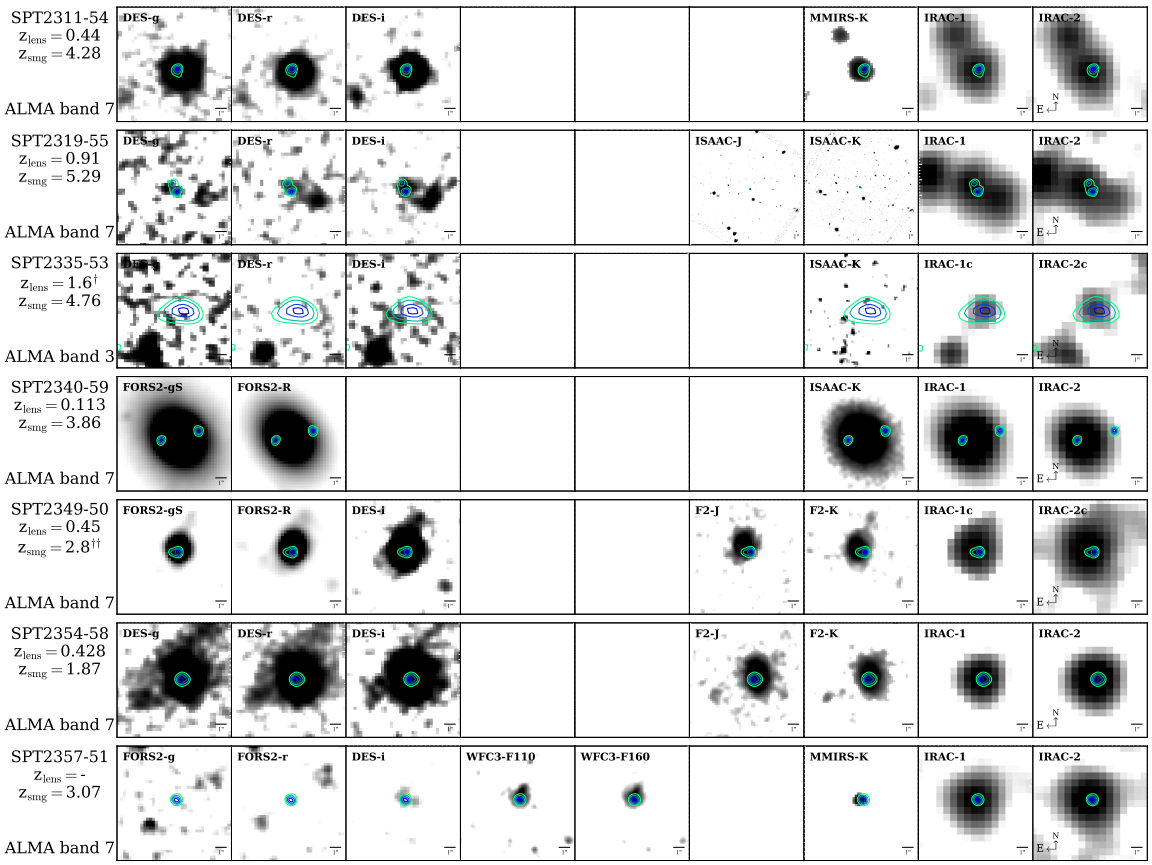
SPT2311-54
$z_{lens} = 0.44$
$z_{smg} = 4.28$
ALMA band 7
DES-g
DES-r
DES-i
MMIRS-K
IRAC-1
IRAC-2
SPT2319-55
$z_{lens} = 0.91$
$z_{smg} = 5.29$
ALMA band 7
DES-g
DES-r
DES-i
ISAAC-J
ISAAC-K
IRAC-1
IRAC-2
SPT2335-53
$z_{lens} = 1.6^{\dagger}$
$z_{smg} = 4.76$
ALMA band 3
DES-r
DES-i
ISAAC-K
IRAC-1c
IRAC-2c
SPT2340-59
$z_{lens} = 0.113$
$z_{smg} = 3.86$
ALMA band 7
FORS2-gS
FORS2-R
ISAAC-K
IRAC-1
IRAC-2
SPT2349-50
$z_{lens} = 0.45$
$z_{smg} = 2.8^{\dagger\dagger}$
ALMA band 7
FORS2-gS
FORS2-R
DES-i
F2-J
F2-K
IRAC-1c
IRAC-2c
SPT2354-58
$z_{lens} = 0.428$
$z_{smg} = 1.87$
ALMA band 7
DES-g
DES-r
DES-i
F2-J
F2-K
IRAC-1
IRAC-2
SPT2357-51
$z_{lens} = -$
$z_{smg} = 3.07$
ALMA band 7
FORS2-g
FORS2-r
DES-i
WFC3-F110
WFC3-F160
MMIRS-K
IRAC-1
IRAC-2

Appendix E

DES Photometry for SPT Lenses

Table E.1: DES photometry for the SPT Lenses

ID	DES-g	DES-r	DES-i
SPT0002-52	25 ± 0.2	23.6 ± 0.07	22.6 ± 0.05
SPT0020-51	22.6 ± 0.06	21.9 ± 0.04	21.5 ± 0.04
SPT0027-50	23.7 ± 0.1	23.4 ± 0.2	22.9 ± 0.2
SPT0103-45	24 ± 0.2	23.1 ± 0.2	22.2 ± 0.1
SPT0106-64	22.1 ± 0.03	20.3 ± 0.008	19.6 ± 0.007
SPT0109-47	24.3 ± 0.1	24.5 ± 0.3	22.6 ± 0.07
SPT0113-46	23.8 ± 0.2	22.4 ± 0.08	21.4 ± 0.05
SPT0114-59	22.6 ± 0.03	21.9 ± 0.02	21.9 ± 0.03
SPT0125-47	20.6 ± 0.008	19.3 ± 0.004	18.8 ± 0.003
SPT0125-50	-	-	-
SPT0147-64	23.9 ± 0.3	23.8 ± 0.2	23.6 ± 0.4
SPT0150-59	25.8 ± 0.3	25.9 ± 0.4	23.5 ± 0.09
SPT0155-62	26.7 ± 0.5	28.6 ± 4	24.9 ± 0.2
SPT0202-61	24.1 ± 0.1	23.8 ± 0.1	22.9 ± 0.1
SPT0243-49	23.5 ± 0.07	23.1 ± 0.08	23.9 ± 0.3
SPT0245-63	20.2 ± 0.006	19.3 ± 0.004	18.9 ± 0.004
SPT0300-46	25.1 ± 0.2	24 ± 0.1	22.6 ± 0.06
SPT0311-58	-	-	-
SPT0319-47	-	25 ± 0.6	23.8 ± 0.4
SPT0345-47	24.7 ± 0.1	23.7 ± 0.08	22.7 ± 0.07
SPT0346-52	26.8 ± 2	-	23.8 ± 0.5
SPT0403-58	22.9 ± 0.03	22.7 ± 0.03	22.1 ± 0.03
SPT0404-59	24.6 ± 0.2	23.3 ± 0.07	23.1 ± 0.09
SPT0418-47	20.4 ± 0.009	19 ± 0.003	18.5 ± 0.004
SPT0441-46	23.8 ± 0.09	22.1 ± 0.03	20.8 ± 0.02
SPT0452-50	24.3 ± 0.1	24.1 ± 0.1	23.8 ± 0.2
SPT0459-58	24.4 ± 0.3	23.9 ± 0.3	25.9 ± 3
SPT0459-59	23.3 ± 0.08	22.4 ± 0.05	21.3 ± 0.03
SPT0512-59	-	-	-
SPT0516-59	26.2 ± 0.4	24.7 ± 0.1	23.3 ± 0.07
SPT0529-54	18.6 ± 0.002	17.5 ± 0.001	17.1 ± 0.001
SPT0532-50	26.6 ± 0.6	24.4 ± 0.1	23.7 ± 0.1
SPT0538-50	21.3 ± 0.01	19.6 ± 0.004	18.9 ± 0.003
SPT0544-40	-	26.3 ± 0.5	24.3 ± 0.1
SPT0551-48	25.6 ± 0.2	24.7 ± 0.1	23.5 ± 0.08
SPT0552-42	25.3 ± 0.3	24.5 ± 0.2	23.4 ± 0.1
SPT0555-62	-	-	-
SPT0604-64	-	-	-
SPT0625-58	27.6 ± 3	23.8 ± 0.1	23.1 ± 0.09
SPT2008-58	23.9 ± 0.04	22.6 ± 0.02	21.4 ± 0.01
SPT2031-51	24.1 ± 0.1	22.2 ± 0.03	21.1 ± 0.02
SPT2048-55	26.3 ± 0.3	24.9 ± 0.1	23.8 ± 0.1
SPT2101-60	22.3 ± 0.03	20.9 ± 0.01	20.4 ± 0.01
SPT2103-60	26.3 ± 0.7	23 ± 0.04	21.9 ± 0.03
SPT2132-58	22.7 ± 0.03	22 ± 0.03	21.8 ± 0.04
SPT2134-50	24.1 ± 0.2	22 ± 0.03	20.9 ± 0.02
SPT2146-55	-	-	24.1 ± 0.3
SPT2147-50	23.8 ± 0.2	22 ± 0.05	20.9 ± 0.04
SPT2307-50	22.4 ± 0.03	21.9 ± 0.03	21.7 ± 0.04
SPT2311-54	21.4 ± 0.01	20.6 ± 0.009	20.5 ± 0.01
SPT2319-55	-	24.7 ± 0.3	22.5 ± 0.1
SPT2335-53	-	-	24.7 ± 0.4
SPT2340-59	17.5 ± 0.002	16.5 ± 0.001	16.1 ± 0.001
SPT2349-50	21.9 ± 0.02	20.8 ± 0.009	20.5 ± 0.01
SPT2354-58	20.9 ± 0.02	20 ± 0.01	19.6 ± 0.01
SPT2357-51	-	-	-

Appendix F

Descriptions of Individual Lenses from the SPT sample

SPT0002-52 - This is a high-redshift lens ($z_{\rm lens} = 1.173$) while the corresponding SMG was found to have a redshift on the low end of the SPT-SMG distribution. Atacama Large Millimeter/submillimeter Array (ALMA) imaging was conducted in band 3 and did not resolve the SMG into Einstein rings or even counter-images and so an Einstein radius and mass were not calculated for the lens. The lens was clearly detected in Infrared Spectrometer And Array Camera (ISAAC)'s $K-$band, with poor detections in the shorter wavelengths. No Infrared Array Camera (IRAC) imaging was conducted.

SPT0020-51 - This lens appears to be comprised of a group of three galaxies. Spilker et al. (2016), however, find the northern-most and brightest galaxy to have little effect on the lens model and hypothesize it to be at a different redshift than the remaining galaxies. The ALMA band 7 imaging resolves the SMG into a compact bright image and a faint counter-image centred on the south-west galaxy, suggesting the other galaxies detected in the near-IR are only influencing the lensing in a minor way. The south-west galaxy is undetected in the optical bands and IRAC fails to resolve the three galaxies. Furthermore SExtractor fails to resolve the three galaxies as well. The multi-band photometry therefore is a summation of all three galaxies.

SPT0027-50 - This lens is a complex group lens. Spilker et al. (2016) find the most reasonable model to contain three galaxies. SExtractor once again fails to resolve the three galaxies and the multi-band photometry therefore is a summation of all three galaxies. With the assumption that they all have the same redshift, a $K-z$ redshift was determined. ALMA band 7 imaging clearly resolves the SMG into two images.

SPT0103-45 - This lens consists of a bright central core and an arced feature to the south, visible most clearly in the Spectral and Photometric Imaging Receiver (SPIRE)

imaging. ALMA band 7 resolves the SMG into two images, seemingly unaffected by the southern arcs. Spilker et al. (2016) hypothesize the arcs of the lens to be either a tidal system or spiral arms. This lens is a candidate spiral lens.

SPT0106-64 - The physical extent of this lens, especially observed in the optical bands, is significantly larger compared to the other lenses in the sample. The same is not true in the near-IR. While the old stellar population therefore is fairly compact and central, the young stellar population spans a much larger halo. ALMA band 7 imaging resolves the SMG into two counter-images that reflect the physical size of the lens. Lens modelling for this system were not published by Spilker et al. (2016).

SPT0109-47 - This lens is a complex group lens, as indicated by a third counter-image of the SMG, imaged by ALMA band 7, that is further away from the central bright image than typical. Near-IR and optical imaging suggest the presence of two lensing galaxies, however, Spilker et al. (2016) required three in their lens model and were still not entirely able to reproduce the flux ratios between the three counter images. Photometry measurements were done on the north-east galaxy alone, while the spectroscopic redshift is for the south-west galaxy.

SPT0113-46 - This lens is modelled as a three galaxy system by Spilker et al. (2016). ALMA band 7 imaging resolves the SMG into a long arc with two counter images all centred on the bright, core galaxy of the lens with its companion lens galaxies located to the south-west and north-west of the central galaxy. SExtractor fails to resolve the three galaxies and the multi-band photometry therefore is a summation of all three galaxies, under the assumption that they all have the same redshift. A $K - z$ redshift was determined for the lens.

SPT0114-59 - While near-IR and optical imaging present a rather ordinary single galaxy lens, the ALMA band 7 resolved imaging depicts a central image with three counter images along a straight line to the south of the main image, suggesting a more complex lens. A $K - z$ redshift was determined for the lens and a photometric redshift is used for the SMG as well as no spectroscopic data was taken for this source. Consequently no lens modelling was conducted either.

SPT0125-47 - This lens is highly elongated along the south-east to north-west axis with a bright central bulge and is therefore likely a spiral galaxy viewed nearly perfectly edge-on. ALMA band 7 resolves the SMG into two images centred on the

central bulge. Lens modelling done by Spilker et al. (2016) contains $\sim 6\sigma$ residuals which they discuss is likely due to an imperfect representation of the lens mass profile within their model.

SPT0125-50 - This lens is elongated along the north-east to south-west axis, however, no clear evidence of a disc-like feature is visible, so the lens is likely an elliptical galaxy with a high eccentricity. The two ALMA band 7 counter images are curved around the north-east corner of the lens indicating a large offset of the SMG from the optical line-of-sight axis.

SPT0147-64 - This lens is poorly detected across the optical and near-IR bands. The south-east component seen in $K-$band is used for photometry purposes. A $K-z$ redshifts was determined for this lens. ALMA imaging was done in band 3 and so the SMG was not resolved into individual components, consequently Spilker et al. (2016) did not conduct lens modelling.

SPT0150-59 - The physical extent of this lens is small, under $2''$ in diameter and the ALMA band 7 imaging resolves the SMG into a near perfect, compact Einstein ring. Lens modelling was not conducted for this lensing system. A $K-z$ redshifts was determined for this lens.

SPT0155-62 - This lens is only detected well in the $K-$band. It's physical extent is small, $\sim 1''$ in diameter. A $K-z$ redshifts was determined for this lens. ALMA band 7 imaging resolves the SMG once again into a near perfect, compact Einstein ring. Lens modelling was not conducted for this lensing system either.

SPT0202-61 - The primary lens, brightest in the $K-$band, appears to be loosely linked via a bridge to a secondary component to the south, which is not detected in the near-IR, however, is observed in the optical. A $K-z$ redshifts was determined for this lens. The Einstein rings of the SMG observed in ALMA's band 7 are centred on the northern component and do not appear to be affected by the southern one. Furthermore Spilker et al. (2016) make no mention of using a multi-component lens in their modelling. SExtractor cannot resolve the two components and so a summation of the two is used in multi-band photometry.

SPT0243-49 - This SMG is one of the highest redshift ($z_{\rm source} = 5.698$) sources of the SPT sample. It's high-resolution imaging is unable to resolve the source into multiple images even in ALMA's band 7. The lens contains an elongated, possibly

tidal tail westward of the bright centre. A $K-z$ redshifts was determined for this lens.

SPT0245-63 - This lens is highly elongated along the south-east to north-west axis. No clear evidence of a disc-like feature is visible, so the lens is likely an elliptical galaxy with a high eccentricity. A $K-z$ redshifts was determined for this lens. ALMA's band 7 is unable to resolve the SMG into multiple imaging. Spilker et al. (2016) hypothesize that the ALMA imaging is of a massive foreground object, possibly the lens itself, as lens modelling results in a lens mass much too small given the brightness of the lens in the near-IR. The SMG is one of the highest redshift sources in the SPT sample at $z_{\rm source} = 5.626$.

SPT0300-46 - This lens is poorly detected in the $K-$band, however, it is quite evident in the optical. A $K-z$ redshifts was determined for this lens. While ALMA's band 7 does not resolve the SMG into multiple images, Spilker et al. (2016)'s modelling find a two source model best represents the system, which is born out by the two velocity components found in the CO(4-3) line by Gullberg et al. (2015).

SPT0311-58 - This SMG is the highest redshift ($z_{\rm source} = 6.9$) source of the SPT sample. The ALMA band 7 imaging resolves into a bright, main component and a faint counter image centred on the lens visible only in the near- and mid-IR. A $K-z$ redshifts was determined for this lens.

SPT0319-47 - This lens is best detected in the mid-IR, with poor-to-no detection in most of the optical bands. A $K-z$ redshifts was determined for this lens. ALMA band 7 is unable resolve the SMG into counter-images.

SPT0345-47 - This lens is best modelled by Spilker et al. (2016) by a single galaxy. In the near-IR SPIRE images slight extensions to the south-east and north-west can be seen possibly indicating the edge-on view of a spiral galaxy. This is hard to confirm visually because of the faintness of the lens in the other near-IR and optical imaging. A $K-z$ redshifts was determined for this lens.

SPT0346-52 - This SMG is one of the highest redshift ($z_{\rm source} = 5.656$) sources of the SPT sample. It's high-resolution imaging in ALMA's band 7 resolves the source into three components of similar flux, centred on a single galaxy as the lens. The results found by Spilker et al. (2016) largely confirm those found previously by Hezaveh et al. (2013). A $K-z$ redshifts was determined for this lens.

SPT0403-58 - This lens is identified as a blue lens as it's optical flux is significantly brighter than its near-IR flux. A $K-z$ redshifts was determined for this lens. Spectroscopic data was not taken for this SMG either, so a photometric redshift is used. ALMA band 7 does not resolve the SMG. Spilker et al. (2016) only find faint magnifications factors for the source.

SPT0404-59 - The single lens is detected in both optical and near-IR imaging. ALMA's band 7 resolves this SMG into two counter-images that are curved around the north-east corner of the lens indicating a large offset of the SMG from the optical line-of-sight axis. Spectroscopic analysis was not performed on the SMG and so a photometric redshift is used.

SPT0418-47 - The physical extent of the lens is one of the largest for a single galaxy lens in this sample and is detected robustly across all optical, mid- and near-IR bands. ALMA band 7 data shows the SMG to be a near perfect Einstein ring. Spilker et al. (2016) find this source to be one of the highest magnified SMGs of the SPT sample ($\mu_{870\,\mu\mathrm{m}} = 32$), an increase in magnification factor from that found by Hezaveh et al. (2013) which only had lower-resolution imaging of the source available to them.

SPT0441-46 - This lensing system is modelled by Spilker et al. (2016) by a single galaxy lens and a single component source, as is born out by optical and near-IR imaging of the lens, and the ALMA band 7 data which does not resolve the source into multiple images.

SPT0452-50 - This lens has the highest spectroscopic redshift of the SPT sample. Spilker et al. (2016) find only the southern object, visible in the optical, to be mildly lensing the SMG observed in ALMA band 7. The northern object seen in the optical imaging does not contribute to the lensing.

SPT0459-58 - This lens is only robustly detected in the mid-IR. A $K-z$ redshifts was determined for this lens using a lower limit $K-$band magnitude. This suggests the lens redshift is higher than the one used in this work.

SPT0459-59 - This lens is robustly detected across all bands observations were conducted in. Spilker et al. (2016) found there to be two components of the source being lensed with different magnification factors, one strongly lensed component and one fainter, barely lensed component.

SPT0512-59 - This lens is exceptionally bright across all optical, near-, and mid-IR bands. ALMA band 7 imaging resolves the SMG into well defined Einstein arcs with a large radius. Unfortunately a lens model has not yet been conducted for this lensing system.

SPT0516-59 - ALMA band 7 imaging suggests the southern, fainter object of the two observed in optical and near-IR imaging is the lens. Lens modelling, thus far not conducted, could confirm this. A $K - z$ redshift is determined for this lens.

SPT0529-54 - This lens is bright across all optical, near-, and mid-IR bands. The lens is slightly elongated along the east-west axis with a companion galaxy visible in the near-IR due west of the lens. Photometry measurements exclude the companion galaxy. Spectroscopic analysis shows this lens to be the lowest redshift lens of the SPT sample. ALMA band 7 high-resolution imaging resolves the SMG into a near-perfect Einstein ring centred on the main lens. Spilker et al. (2016) find large discrepancies with their model compared to Hezaveh et al. (2013) but found the differences to be accounted for completely by their use of ellipticity in the background source whereas Hezaveh et al. (2013) used circular symmetry.

SPT0532-50 - This lens is most clearly detected in the near-IR. ALMA band 7 imaging does not resolve the SMG into multiple images. Spilker et al. (2016) found a strong magnification factor of 10.

SPT0538-50 - This lens was observed across all optical, near- and mid-IR bands and is robustly detected in all. ALMA band 7 resolves the SMG into a near-perfect Einstein ring. Spilker et al. (2016) confirmed the need for two source-components in their modelling. They attributed this to the two velocity components found in CO(1-0) and CO(3-2) observations of the source. This lensing system was also discussed by Bothwell et al. (2013) and Hezaveh et al. (2013).

SPT0544-40 - ALMA band 7 imaging shows a near-perfect Einstein ring with a sub-arcsec radius, implying a very low mass lens. Lens modelling has not yet been performed. A $K - z$ redshift was determined for this lens.

SPT0551-48 - This single galaxy lens results in a near-perfect Einstein ring imaging of the SMG with a sub-arcsec radius observed in ALMA band 7. Lens modelling has not yet been performed. A $K - z$ redshift was determined for this lens.

SPT0552-42 - The high-resolution ALMA band 7 imaging is a unique, asymmetric Einstein ring, centred on the western, fainter galaxy observed in the optical and near-IR. Due to the asymmetry of the SMG image, it is likely that the brighter galaxy to the east of the main lens is also contributing to the lensing. This can be confirmed by lens modelling, which has not yet been done. Photometry measurements were performed on the western lens. A $K - z$ redshift was determined for the lens.

SPT0555-62 - This lens is highly elongated along the south-east to north-west axis. In the optical a central bulge with fainter wings is visible. It is therefore likely a spiral galaxy viewed edge-on. A $K - z$ redshift was determined for this lens. ALMA band 7 resolves the SMG into three counter images centred on the central bulge of the lensing galaxy. Lens modelling has not yet been done for this lensing system.

SPT0604-64 - This lens produces near-perfect Einstein rings in the ALMA band 7 imaging of the SMG. The Einstein radius is larger than the physical extent of the lens, unlike the majority of observations in the SPT sample. This suggests a larger dark matter halo compared to most lenses. While in the optical bands the lens appears to be a single galaxy with the ALMA counters centred on it, in the near-IR the lens appears to either be elongated or have a companion to the south-east. The symmetry of the ALMA contours would suggest this second object in the near-IR does not contribute significantly to the lensing, which could be confirmed through lens modelling not yet conducted. A $K - z$ redshift was determined for the combined objects as SExtractor could not resolve the two.

SPT0625-58 - ALMA band 7 images the SMG in a "U-"shape centred on the lens. A $K - z$ redshift was determined for this lens. Lens modelling has not yet been conducted for this lensing system.

SPT2008-58 - The ALMA band 3 imaging of the SMG shows two counter-images, however, they are not centred on a galaxy in the optical or near-IR. This lens is therefore likely comprised of a group of galaxies. Photometry presented in this work corresponds to the galaxy at the eastern tip of the southern image, the brightest object nearby. A $K - z$ redshift was determined for this lens. Neither spectroscopic data for a redshift determination of the SMG or lens modelling for the system has been done.

SPT2031-51 - This is a single galaxy lens, as determined via lens modelling performed by Spilker et al. (2016). ALMA band 7 shows the SMG image as a tight arc with a counter image. Spectroscopic analysis was not performed on the SMG and so a photometric redshift was determined.

SPT2048-55 - This lens is a single low mass galaxy as suggested from the ALMA band 7 imaging of the SMG which has a small, sub-arcsec Einstein radius and is centred on the lens. Lens modelling done by Spilker et al. (2016) confirms this. A $K - z$ redshift was determined for this lens.

SPT2101-60 - This lens is highly elongated and appears to have a central bulge with thinner wings, suggesting it is a spiral galaxy viewed edge-on. Only the southern object, not the two northerly potential companions, was used in photometry measurements. A $K - z$ redshift was determined for this lens. A lensing model has not yet been done for this system.

SPT2103-60 - This lens is comprised of a group of galaxies. Spilker et al. (2016) find three foregrounds galaxies to be doing the lensing. The bright, northern most lensing galaxy was centred on during spectroscopic measurements for a redshift determination. Subsequently it was also used for photometry measurements. ALMA band 7 shows a unique shape to the images of the SMG, a typical lensing arc with two counter images that extend in a tail like fashion north-west ward.

SPT2132-58 - This lens is a single galaxy lens. A $K - z$ redshift was determined for this lens. The ALMA band 7 imaging barely resolves the SMG, which appears slightly off-centre from the lens. Spilker et al. (2016) predict a faint counter image in their best fit lens model.

SPT2134-50 - This lens is a single galaxy lens. ALMA band 7 resolves the SMG into a tight arc with a counter image centred on the lens. Lens modelling of Spilker et al. (2016) find the SMG to have a large magnification factor at 21.

SPT2146-55 - This lens is only detected in the near- and mid-IR. In SPIRE imaging it appears to be elongated with a central bulge, possibly indicating a spiral galaxy viewed edge on. The faint detections in ISAAC and the poor resolution of IRAC cannot confirm this though. A high $K - z$ redshift was determined for this lens, as suggested by the lack of detection in the optical. The SMG in resolved into two similarly bright counter images by ALMA band 7 imaging and is modelled by

Spilker et al. (2016) as a single galaxy lens.

SPT2147-50 - This lens is a single galaxy lens. The ALMA band 7 resolved imaging is slightly off-centre of the foreground lens. Spilker et al. (2016) find a simple single object lensing system to best fit the data.

SPT2307-50 - This lens is difficult to define. ALMA band 3 displays a central bright image of the SMG as well as a faint counter image. The lens may either be the bright object to the north-east of the ALMA contours, the much smaller object to the south-west, or a combination of the two, potentially successively instead of simultaneously. Lens modelling, which has not yet been performed, will verify which object is the lens. Here we present photometry for the south-west lensing candidate. A $K - z$ redshift was determined for this lens. The bright object to the north-east has been confirmed via spectroscopy to be at $z = 0.1$, which is likely too low to be an effective primary lens.

SPT2311-54 - This is a single galaxy lens. ALMA band 7 only marginally resolves this SMG. Spilker et al. (2016) find their model to represent the data well.

SPT2319-55 - Lens modelling performed by Spilker et al. (2016) confirms this to be a single galaxy lens, the south-west object not contributing to the lensing. ALMA band 7 resolves the SMG into two counter images separated by $\sim 1''$.

SPT2335-53 - Spectroscopy identifies the galaxy south-west of the ALMA band 3 image to be at a redshift of 0.0375 and is therefore unlikely to be the lens of the SMG. The significantly fainter object primarily detected in IRAC imaging centred on the ALMA contours was considered the lens instead. Photometry measurements and a $K - z$ redshift were determined for this galaxy. A lensing model has not yet been conducted for this lensing system.

SPT2340-59 - The two similarly bright images observed in the ALMA band 7 imaging of the SMG are centred on a lens with large physical extent. Despite the standard double-imaging of the SMG, Spilker et al. (2016) discuss the possibility that the two images are in fact two unlensed SMGs and not a single lensed SMG. They model both scenarios. In this work we assume a single SMG is being lensed.

SPT2349-50 - This is a single galaxy lens with a possible tidal feature extending to the north. Spilker et al. (2016) resolve the ALMA band 7 imaging into two components. No spectroscopic data was taken for this SMG so a photometric redshift is

used instead.

SPT2354-58 - This single galaxy lens is observed well throughout the bands observed in. ALMA band 7 only slightly resolves the SMG. Spilker et al. (2016) are able to model the system well. The SMG has the lowest redshift of the SPT sample.

SPT2357-51 - This is a single galaxy lens clearly visible in the near- and mid-IR, less robustly detected in the optical. A $K - z$ redshift was determined for the the lens. The presence of the foreground lens suggests a lensing system despite the ALMA band 7 not resolving the SMG at all, as discussed in Spilker et al. (2016) who model the system and find a low magnification factor of ~ 2.9.

Table G.1: Astrophysical properties

Source	L_{H_2O} [a] $[10^6\,L_\odot]$	$L_{[CII]}$ [a] $[10^7\,L_\odot]$	$L_{851\,\mu m}$ [b] $[10^{10}\,L_\odot]$	L_{IR} [b] $[10^{11}\,L_\odot]$	M^* [c] $[10^{10}\,M_\odot]$	M_{gas} [d] $[10^{10}\,M_\odot]$	$M_{dyn,\,disp}$ [e] $[10^{10}\,M_\odot]$
A	51.2 ± 6.4	997.3 ± 11.8	155.0 ± 3.3	216.6 ± 4.4	5.42 ± 1.22	12.05 ± 2.1	70.38 ± 11.9
B	54.9 ± 2.5	466.6 ± 7.1	155.6 ± 2.6	217.5 ± 3.5	8.07 ± 1.60	11.19 ± 1.9	35.38 ± 6.3
C	85.0 ± 5.8	361.3 ± 6.5	92.9 ± 2.1	132.3 ± 2.9	24.89 ± 4.91	6.72 ± 1.2	7.39 ± 0.9
D	3.7 ± 0.9	350.9 ± 8.9	78.2 ± 2.4	112.0 ± 3.3	4.29 ± 1.04	8.40 ± 1.5	45.76 ± 34.1
E	14.5 ± 2.7	217.9 ± 7.1	63.6 ± 3.1	91.8 ± 4.4	8.59 ± 1.88	4.75 ± 0.8	14.24 ± 12.6
F	8.5 ± 1.6	308.0 ± 8.9	53.1 ± 2.3	77.2 ± 3.2	2.53 ± 0.70	3.42 ± 0.7	56.37 ± 11.2
G	< 6.0	108.1 ± 4.7	30.1 ± 1.5	44.7 ± 2.1	2.01 ± 0.64	1.72 ± 0.3	39.18 ± 12.8
H	< 5.9	173.8 ± 5.9	24.6 ± 2.4	36.8 ± 3.5	1.63 ± 0.40	2.76 ± 0.5	15.21 ± 4.0
I	< 6.7	198.7 ± 6.5	24.9 ± 1.8	37.2 ± 2.6	1.52 ± 0.39	2.20 ± 0.5	19.55 ± 4.0
J	< 4.6	520.4 ± 7.7	21.3 ± 2.2	31.9 ± 3.2	6.16 ± 1.34	2.31 ± 0.5	7.87 ± 1.7
K	< 5.0	223.5 ± 5.3	5.7 ± 2.9	8.9 ± 4.4	4.57 ± 1.17	3.55 ± 0.6	6.36 ± 1.2
L	< 5.1	159.4 ± 6.5	3.1 ± 1.2	5.0 ± 1.8	4.90 ± 1.14	2.53 ± 0.4	11.60 ± 2.6
M	< 16.1	52.7 ± 4.7	1.6 ± 1.3	2.7 ± 2.1	4.80 ± 1.12	0.84 ± 0.2	0.89 ± 0.5
N	< 19.1	100.7 ± 4.7	5.7 ± 2.7	9.0 ± 4.1	4.30 ± 1.12	1.60 ± 0.3	1.92 ± 0.8
Sum	217.8 ± 9.5	4239 ± 27	715.4 ± 8.8	1024 ± 13	83.7 ± 6.4	64.0 ± 3.8	332 ± 43

[a] Line luminosities determined from the integrated line flux.

[b] Continuum luminosities determined from the 851 μm flux.

[c] Stellar masses are calculated from the IRAC CH1 flux and a mass-to-light ratio determined from the Hainline et al. (2011) SMGs.

[d] Molecular gas masses are calculated from the the CO(4-3) line luminosity (or [C II] if CO(4-3) was not detected) using a conversion factor α

[e] Dynamical masses are calculated using the velocity dispersions estimator, dispersions determined from the [C II] line.

Table G.2: Optical and near-IR photometry ($m_{\rm AB}$) for the 14 SMGs in SPT2349.

Source	$R-$band	$K-$band	CH1	CH2
A	31.58 ± 0.03	-	22.32 ± 0.1	22.05 ± 0.1
B	-	-	21.88 ± 0.05	-
C	-	22.8 ± 0.1	20.67 ± 0.04	20.76 ± 0.05
D	34.97 ± 0.24	-	22.57 ± 0.2	22.2 ± 0.1
E	33.55 ± 0.14	24.7 ± 0.4	21.82 ± 0.1	21.77 ± 0.1
F	-	26.1 ± 0.4	23.15 ± 0.2	-
G	32.31 ± 0.08	-	23.39 ± 0.3	-
H	-	26.0 ± 0.4	23.62 ± 0.2	-
I	-	26.0 ± 0.6	23.7 ± 0.2	-
J	32.43 ± 0.07	25.1 ± 0.4	22.17 ± 0.1	21.8 ± 0.08
K	-	-	22.51 ± 0.2	22.11 ± 0.1
L	32.27 ± 0.05	-	22.42 ± 0.1	22.07 ± 0.1
M	31.87 ± 0.05	-	22.45 ± 0.1	22.13 ± 0.1
N	33.17 ± 0.11	25.8 ± 0.4	22.57 ± 0.2	22.24 ± 0.1

Appendix H

Rotermund, K., Barch, B., Chapman, S., et al.: 2016, *Journal of Low Temperature Physics* **184(1)**, 486.

SPRINGER NATURE LICENSE
TERMS AND CONDITIONS

Apr 13, 2020

This Agreement between Ms. Kaja Rotermund ("You") and Springer Nature ("Springer Nature") consists of your license details and the terms and conditions provided by Springer Nature and Copyright Clearance Center.

License Number	4807131089090
License date	Apr 13, 2020
Licensed Content Publisher	Springer Nature
Licensed Content Publication	Journal of Low Temperature Physics
Licensed Content Title	Planar Lithographed Superconducting LC Resonators for Frequency-Domain Multiplexed Readout Systems
Licensed Content Author	K. Rotermund et al
Licensed Content Date	Mar 1, 2016
Type of Use	Thesis/Dissertation
Requestor type	academic/university or research institute
Format	electronic

Portion	full article/chapter
Will you be translating?	no
Circulation/distribution	100 - 199
Author of this Springer Nature content	yes
Title	Exploring Infrared-Bright Sources Detected by the South Pole Telescope - Lensing Galaxies and the Most Massive Structures in the Universe
Institution name	Dalhousie University
Expected presentation date	Apr 2020
Requestor Location	Ms. Kaja Rotermund 151 Haleginia Landin Lower East Chezzetcook, NS B0J1N0 Canada Attn: Ms. Kaja Rotermund
Total	0.00 CAD

Terms and Conditions

Springer Nature Customer Service Centre GmbH
Terms and Conditions

This agreement sets out the terms and conditions of the licence (the **Licence**) between you

and **Springer Nature Customer Service Centre GmbH** (the **Licensor**). By clicking 'accept' and completing the transaction for the material (**Licensed Material**), you also confirm your acceptance of these terms and conditions.

1. Grant of License

1. 1. The Licensor grants you a personal, non-exclusive, non-transferable, world-wide licence to reproduce the Licensed Material for the purpose specified in your order only. Licences are granted for the specific use requested in the order and for no other use, subject to the conditions below.

1. 2. The Licensor warrants that it has, to the best of its knowledge, the rights to license reuse of the Licensed Material. However, you should ensure that the material you are requesting is original to the Licensor and does not carry the copyright of another entity (as credited in the published version).

1. 3. If the credit line on any part of the material you have requested indicates that it was reprinted or adapted with permission from another source, then you should also seek permission from that source to reuse the material.

2. Scope of Licence

2. 1. You may only use the Licensed Content in the manner and to the extent permitted by these Ts&Cs and any applicable laws.

2. 2. A separate licence may be required for any additional use of the Licensed Material, e.g. where a licence has been purchased for print only use, separate permission must be obtained for electronic re-use. Similarly, a licence is only valid in the language selected and does not apply for editions in other languages unless additional translation rights have been granted separately in the licence. Any content owned by third parties are expressly excluded from the licence.

2. 3. Similarly, rights for additional components such as custom editions and derivatives require additional permission and may be subject to an additional fee. Please apply to Journalpermissions@springernature.com/bookpermissions@springernature.com for these rights.

2. 4. Where permission has been granted **free of charge** for material in print, permission may also be granted for any electronic version of that work, provided that the material is incidental to your work as a whole and that the electronic version is essentially equivalent to, or substitutes for, the print version.

2. 5. An alternative scope of licence may apply to signatories of the STM Permissions Guidelines, as amended from time to time.

3. Duration of Licence

3. 1. A licence for is valid from the date of purchase ('Licence Date') at the end of the relevant period in the below table:

Scope of Licence	Duration of Licence
Post on a website	12 months
Presentations	12 months
Books and journals	Lifetime of the edition in the language purchased

4. Acknowledgement

4. 1. The Licensor's permission must be acknowledged next to the Licenced Material in print. In electronic form, this acknowledgement must be visible at the same time as the figures/tables/illustrations or abstract, and must be hyperlinked to the journal/book's homepage. Our required acknowledgement format is in the Appendix below.

5. Restrictions on use

5. 1. Use of the Licensed Material may be permitted for incidental promotional use and minor editing privileges e.g. minor adaptations of single figures, changes of format, colour and/or style where the adaptation is credited as set out in Appendix 1 below. Any other changes including but not limited to, cropping, adapting, omitting material that affect the meaning, intention or moral rights of the author are strictly prohibited.

5. 2. You must not use any Licensed Material as part of any design or trademark.

5. 3. Licensed Material may be used in Open Access Publications (OAP) before publication by Springer Nature, but any Licensed Material must be removed from OAP sites prior to final publication.

6. Ownership of Rights

6. 1. Licensed Material remains the property of either Licensor or the relevant third party and any rights not explicitly granted herein are expressly reserved.

7. Warranty

IN NO EVENT SHALL LICENSOR BE LIABLE TO YOU OR ANY OTHER PARTY OR ANY OTHER PERSON OR FOR ANY SPECIAL, CONSEQUENTIAL, INCIDENTAL OR INDIRECT DAMAGES, HOWEVER CAUSED, ARISING OUT OF OR IN CONNECTION WITH THE DOWNLOADING, VIEWING OR USE OF THE MATERIALS REGARDLESS OF THE FORM OF ACTION, WHETHER FOR BREACH OF CONTRACT, BREACH OF WARRANTY, TORT, NEGLIGENCE, INFRINGEMENT OR OTHERWISE (INCLUDING, WITHOUT LIMITATION, DAMAGES BASED ON LOSS OF PROFITS, DATA, FILES, USE, BUSINESS OPPORTUNITY OR CLAIMS OF THIRD PARTIES), AND
WHETHER OR NOT THE PARTY HAS BEEN ADVISED OF THE POSSIBILITY OF SUCH DAMAGES. THIS LIMITATION SHALL APPLY NOTWITHSTANDING ANY FAILURE OF ESSENTIAL PURPOSE OF ANY LIMITED REMEDY PROVIDED HEREIN.

8. Limitations

8. 1. ***BOOKS ONLY:*** Where **'reuse in a dissertation/thesis'** has been selected the following terms apply: Print rights of the final author's accepted manuscript (for clarity, NOT the published version) for up to 100 copies, electronic rights for use only on a personal website or institutional repository as defined by the Sherpa guideline (www.sherpa.ac.uk/romeo/).

9. Termination and Cancellation

9. 1. Licences will expire after the period shown in Clause 3 (above).

9. 2. Licensee reserves the right to terminate the Licence in the event that payment is not received in full or if there has been a breach of this agreement by you.

Appendix 1 — Acknowledgements:

For Journal Content:
Reprinted by permission from [**the Licensor**]: [**Journal Publisher** (e.g. Nature/Springer/Palgrave)] [**JOURNAL NAME**] [**REFERENCE CITATION** (Article name, Author(s) Name), [**COPYRIGHT**] (year of publication)

For **Advance Online Publication papers:**
Reprinted by permission from [**the Licensor**]: [**Journal Publisher** (e.g. Nature/Springer/Palgrave)] [**JOURNAL NAME**] [**REFERENCE CITATION** (Article name, Author(s) Name), [**COPYRIGHT**] (year of publication), advance online publication, day month year (doi: 10.1038/sj.[JOURNAL ACRONYM].)

For Adaptations/Translations:
Adapted/Translated by permission from [**the Licensor**]: [**Journal Publisher** (e.g. Nature/Springer/Palgrave)] [**JOURNAL NAME**] [**REFERENCE CITATION** (Article name, Author(s) Name), [**COPYRIGHT**] (year of publication)

Note: For any republication from the British Journal of Cancer, the following credit line style applies:

Reprinted/adapted/translated by permission from [**the Licensor**]: on behalf of Cancer Research UK: : [**Journal Publisher** (e.g. Nature/Springer/Palgrave)] [**JOURNAL NAME**] [**REFERENCE CITATION** (Article name, Author(s) Name), [**COPYRIGHT]** (year of publication)

For **Advance Online Publication** papers:
Reprinted by permission from The [**the Licensor**]: on behalf of Cancer Research UK: [**Journal Publisher** (e.g. Nature/Springer/Palgrave)] [**JOURNAL NAME**] [**REFERENCE CITATION** (Article name, Author(s) Name), [**COPYRIGHT**] (year of publication), advance online publication, day month year (doi: 10.1038/sj. [JOURNAL ACRONYM])

For Book content:
Reprinted/adapted by permission from [**the Licensor**]: [**Book Publisher** (e.g. Palgrave Macmillan, Springer etc) [**Book Title**] by [**Book author**(s)] [**COPYRIGHT**] (year of publication)

Other Conditions:

Version 1.2

Questions? customercare@copyright.com or +1-855-239-3415 (toll free in the US) or +1-978-646-2777.

J Low Temp Phys (2016) 184:486–491
DOI 10.1007/s10909-016-1554-4

Planar Lithographed Superconducting LC Resonators for Frequency-Domain Multiplexed Readout Systems

K. Rotermund[1] · B. Barch[2] · S. Chapman[1] · K. Hattori[4] · A. Lee[2] · N. Palaio[3] · I. Shirley[2] · A. Suzuki[2] · C. Tran[3]

Received: 30 September 2015 / Accepted: 12 February 2016 / Published online: 1 March 2016

Abstract Cosmic microwave background (CMB) polarization experiments are increasing the number of transition edge sensor (TES) bolometers to increase sensitivity. In order to maintain low thermal loading of the sub-Kelvin stage, the frequency-domain multiplexing (FDM) factor has to increase accordingly. FDM is achieved by placing TES bolometers in series with inductor–capacitor (LC) resonators, which select the readout frequency. The multiplexing factor can be raised with a large total readout bandwidth and small frequency spacing between channels. The inductance is kept constant to maintain a uniform readout bandwidth across detectors, while the maximum acceptable value is determined by bolometer stability. Current technology relies on commercially available ceramic chip capacitors. These have high scatter in their capacitance thereby requiring large frequency spacing. Furthermore, they have high equivalent series resistance (ESR) at higher frequencies and are time consuming and tedious to hand assemble via soldering. A solution lies in lithographed, planar spiral inductors (currently in use by some experiments) combined with interdigitated capacitors on a silicon (Si) substrate. To maintain reasonable device dimensions, we have reduced trace and gap widths of the LCs to 4 μm. We increased the inductance from 16 to 60 μH to achieve a higher packing density, a requirement for FDM systems with large multiplexing factors. Additionally, the Si substrate yields low ESR

✉ K. Rotermund
kaja@dal.ca

1 Department of Physics and Atmospheric Science, Dalhousie University, Halifax, NS B3H 4R2, Canada

2 Department of Physics, University of California, Berkeley, CA 94720-7300, USA

3 Department of Physics, Lawrence Berkeley National Laboratory, Berkeley, CA 94720, USA

4 Kavli Institute for the Physics and Mathematics of the Universe, The University of Tokyo, Kashiwa 277-8583, Japan

values across the entire frequency range and lithography makes mass production of LC pairs possible. We reduced mutual inductance between inductors by placing them in a checkerboard pattern with the capacitors, thereby increasing physical distances between adjacent inductors. We also reduce magnetic coupling of inductors with external sources by evaporating a superconducting ground plane onto the backside of the substrate. We report on the development of lithographed LCs in the 1–5 MHz range for use with FDM systems. These resonators will be used by CMB polarization experiments such as POLARBEAR-2, Simons Array, and SPT-3G. Existing FDM systems have multiplexing factors up to 16×. We report the extension to 40×, i.e., POLARBEAR-2, and 68×, i.e., SPT-3G. We present the design criteria of POLARBEAR-2's LC circuits, the fabrication techniques, and the testing. Concerns such as yield, accuracy in frequency, loss, and mutual inductance between spatially neighboring channels will be discussed.

Keywords Cosmic microwave background · Multiplexing · Fabrication technique · Lithography · Superconducting resonators

1 Introduction

The Cosmic microwave background (CMB) contains even parity, E-mode, and odd parity, B-mode, polarization. While density fluctuations of the CMB produce E-modes, B-modes can be a result of either gravitational lensing distorting the intrinsic E-modes, or due to inflated primordial gravitational waves compressing and rarefacting space. It is the latter of these two that are a signature of inflation theory. CMB polarimetry experiments, such as POLARBEAR-2, SPT-3G, and AdvACTPOL, aim to detect them [1–4]. These experiments exploit the dramatic effects of transition edge sensor (TES) bolometers when tuned to their superconducting transition temperature. Current TES bolometers, which operate at ∼250 mK, are photon-noise limited [5]. In order to achieve the required sensitivity to detect primordial B-modes, the number of TES bolometers needs to increase. POLARBEAR-2 plans to increase the number of bolometers from 1274 to 7588 [1,2,6]. The frequency-domain multiplexing (FDM) factor needs to increase accordingly, from 8 to 40 for POLARBEAR-2, so that thermal loading of the cold plate does not exceed acceptable levels [2,5]. This in turn requires a larger carrier frequency range. Concurrently to increasing detector count, the equivalent series resistance (ESR) of the capacitors (C) and inductors (L), which set the carrier frequency, in series with the bolometers also needs to be reduced. Commercial ceramic chip capacitors have ESR values that increase with frequency. ESRs that are comparable to the bolometer resistance (∼1 Ω) hurt the voltage bias across them, thereby destabilizing them. A low-dielectric loss capacitor is needed. Additional motivation for finding a suitable replacement for the ceramic capacitors lies in scalability, both for mass fabrication and in assembly.

A solution lies in superconducting lithographed interdigitated capacitors and planar inductors. The devices must be superconducting so that only minimal amounts of stray impedance are introduced into the system. The benefit of using lithography to fabricate them is twofold: (1) We are no longer constrained to capacitance values that

are achieved by combining commercially available ceramic capacitors. We therefore have more freedom in the frequency scheduling. (2) Capacitors and inductors can be fabricated on a single chip, i.e., LC chip. Scalability of fabrication is thus more feasible and assembly time is reduced. Superconducting LC resonators in FDM systems have become popular in many research fields, the SAFARI instrument developed by SRON being a notable example outside of the CMB field [7].

2 Design Considerations

Determining the appropriate frequency scheduling is crucial. A primary concern is to keep the cross talk (CT) between neighboring channels low and constant. CT is proportional to the channel's resistance R and inversely proportional to the frequency spacing between the two channels Δf and the inductance L: CT=$[R/(4\pi\Delta f L)]^2$. Maintaining a uniform readout bandwidth across the detectors requires that L remains constant. We therefore vary C in order to set the frequency for each channel: $f = 1/[2\pi\sqrt{LC}]$. Furthermore, we chose a logarithmic frequency scheduling, $\Delta f/f =$ constant. In this way, CT remains constant for all carrier frequencies. Logarithmic spacing has the added benefit of allowing for larger relative capacitive shifts for smaller capacitors. A minimum spacing of 40 kHz between the two lowest frequency channels mitigates potential CT between them, assuming a maximum shift of ∼10 kHz of either channel. In addition to minimize CT between neighboring channels in frequency space, potential CT between the TES bolometer's bands and polarizations also needs to be low. TES bolometers for POLARBEAR-2 are dual band, operating at 95 and 150 GHz, and are dual polarization sensitive [1,2]. The combination of two bands and polarizations are labeled 95T, 95B, 150T, and 150B. Each of these has designated ranges in the frequency schedule and is separated by a calibration resistor and/or a dark bolometer. See Fig. 1 for a schematic of the frequency scheduling described.

Additional modifications made to the original scheduling used in the POLARBEAR experiment are as follows: (1) The inductance was increased from 16 to 60 μH [2]. The operating resistance of the TES bolometers is 1 Ω with a time constant τ_{TES} of 10 ms, which needs to exceed the electrical time constant τ_{e} for bolometer stability purposes, $\tau_{\mathrm{TES}} > 5.8\tau_e$. This results in a maximum allowable inductance of 86 μH [8]. Larger inductance decreases resonant peak widths, thereby enabling tighter channel packing. This allows the total carrier frequency range to remain small. (2) The maximum capacitance is constrained by the physical size allotted to each capacitor. This sets the lower limit on the carrier frequency range to 1.617 MHz. Given a minimum spacing of 40 kHz, an FDM factor of 40, and logarithmic spacing, the upper carrier frequency

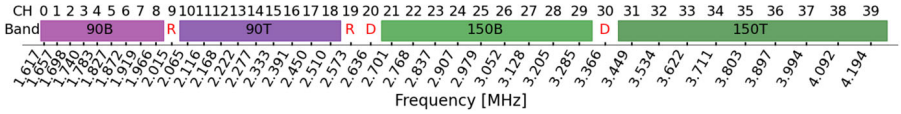

Fig. 1 A schematic of the logarithmic frequency scheduling. Band and polarization combinations, 90B, 90T, 150B, and 150T, are separated by either a calibration resistor (R) or a dark bolometer (D) (Color figure online)

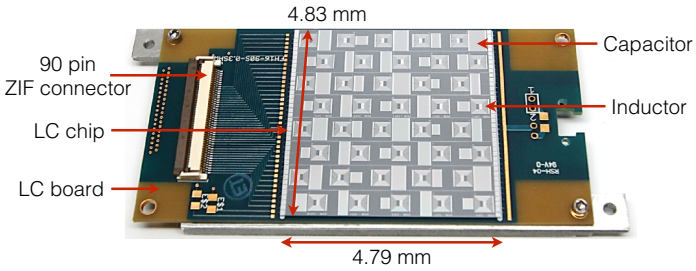

Fig. 2 Photograph of the 40× LC chip mounted on the LC board. The checkerboard design of the LCs is clearly visible (Color figure online)

is thus 4.194 MHz. And (3) finger and gap widths are set to 4 μm. Narrow traces result in capacitors and inductors that are physically small, hence reducing capacitive coupling to the ground plane, which will be discussed in more detail in Sect. 3. However, given the capabilities of the Berkeley Marvell Nanofabrication Laboratory and the Lawrence Berkeley National Laboratory, choosing traces that are too narrow can lead to non-uniformity. 4 μm was tested to produce reliable uniformity.

An important modification made to the earlier LC chips was to place the LC devices in a checkerboard design. See Fig. 2 for a photograph. In this way, the physical spacing between adjacent inductors is maximized, thereby reducing the mutual coupling between them.

3 Fabrication Process

We use 150 mm silicon (Si) wafers, whose resistivity is 30 Ω·cm, to fabricate the LC chips. The process includes (1) spin coating the wafer with photoresist (PR), (2) patterning the PR using one-to-one projection lithography, (3) developing the exposed PR, (4) depositing a 100 Å titanium adhesion layer followed by a 1400 Å film of aluminum (Al) on both the front and back side of the wafer using e-beam evaporation, and finally (5) lifting off the Al from the PR covered areas using an ultrasonic acetone bath. Lastly, we dice the wafer.

Choosing to deposit Al on the backside of the substrate has many consequences. The presence of a metal film between the LC devices and the mounting board mitigates eddy current losses in said board. This has the added benefit of stabilizing the inductors. However, it does decrease the inductance by ∼25 %. We therefore design the inductors as 80 μH inductors, so that they behave as 60 μH inductors in the presence of the ground plane. On the converse, the ground plane does introduce a capacitive coupling term: the ground plane and the LC devices sandwich the Si substrate, producing a parallel plate capacitor. Evaporating the ground plane onto the backside of the wafer is a huge improvement over the original method in which niobium foil was glued between the mounting board and the LC chips. Uncontrollable factors such as glue thickness and wrinkles in the foil produced non-uniform effects.

A lift-off process, as opposed to a plasma etching process, solved many hurdles encountered during fabrication. Plasma etching introduces a radial non-uniformity,

as wafers are etched from the center to the edge. Varying trace thicknesses across the wafer leads to scatter in the capacitance and inductance values. Etching also has poor end-point detection between the metal and the Si substrate in the absence of additional oxide layers between them. It is therefore easy to over-etch into the Si. Si has low-dielectric loss and over-etching with radially varying amounts results in large scatter in capacitance. Both of these issues, radial non-uniformity in trace thickness and over-etching, are negated by using a lift-off process. A wet-etch process was opted against because of the unpredictability of potential lateral etching, which would cause non-uniformity in trace thickness. It is important to note that an overall shift in the frequency due to a common change in trace widths is inconsequential as compared to relative shifts in frequencies.

The lift-off technique is more likely to produce traces that are open rather than shorted, due to potential dust contamination of the mask during photolithography. While open traces are fatal for inductors, their effect on capacitors is minimal. On the other hand, a shorted trace, a less common occurrence, is fatal for capacitors and affects inductances. Each step of the fabrication process is inspected and defects in the traces occur seldom, ensuring that the capacitance yield remains high.

4 Results

Testing was done in a wet dewar with a He-3 sorption fridge. The superconducting transition temperature of Al is 1.2 K and measurements were taken $\sim$ 600 mK. The LC filters were read out via current-biased SQUIDS [1,2]. Testing of the 40x LC chips has produced very encouraging results. Typical yield of the individual LC devices is upwards of 90 %. Cleanliness during the fabrication process and consistency of wire bonding should increase the yield further. We found the frequency scatter of channels to be less than 0.3 %, inductances to be incredibly stable at 60.0 ± 0.1 μH, and the mutual coupling coefficients k to be negligibly low. Fitting experimental data resulted in $k = 0.0014$ for nearest neighbors, while $k = 0.0002$ for next-to-nearest neighbors. The capacitive coupling term of inductors to the ground plane is negligibly small compared to parallel capacitances of further cold-readout components.

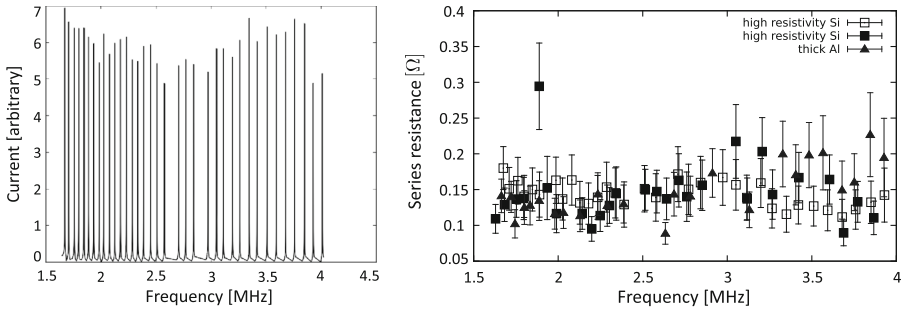

Fig. 3 *Left* Network analysis of a 40× LC filter. *Right* Plot of series resistance versus frequency for interdigitated capacitors. Three measurements are displayed using a 30 Ω·cm resistivity Si substrate. *Solid and empty square* 1000 Å Al layer. *Solid Triangle* 3000 Å Al layer

The *left* plot of Fig. 3 shows the network analysis for a 40× LC filter. The two gaps between 2.5 and 3 MHz correspond to the calibration resistor channels. In the *right* graph, we plotted the series resistance of the LC channels with respect to their frequency. For ceramic capacitors, the resistance is a steeply rising function of frequency, reaching 0.35 Ω by 3.5 MHz. Within error, the resistance for our LCs remains constant and low at $\lesssim 0.2$ Ω. Performance of the LC resonators within the full cold-readout system has shown that this is acceptable compared to the desired 10 % of the bolometer resistance ($R_{bolo} = 1\,\Omega$) [8].

We developed a frequency scheduling for LC pairs used in POLARBEAR-2's cold-readout of TES bolometers as well as a fabrication process that is easily scalable for mass production and assembly. The lift-off process ensures uniformity, reducing frequency scatter. A ground plane stabilizes the inductors and a checkerboard design decreases the mutual inductance. The series resistance was reduced by a factor of ∼2 at high frequencies and is constant across the readout range.

Acknowledgments We acknowledge support from the MEXT Kakenhi Grant 21111002, National Science Foundation Grant AST-0618398, NASA Grant NNG06GJ08G, The Simons Foundation, Natural Sciences and Engineering Research Council, Canadian Institute for Advanced Research, Japan Society for the Promotion of Science, and the CONICYT. Lithographed detectors, capacitors, and inductors were fabricated at Berkeley Marvell Nanofabrication Laboratory as well as the Lawrence Berkeley National Laboratory.

References

1. A. Suzuki et al., The Polarbear-2 and the Simons array. J. Low Temp. Phys. (LTD 16). doi:10.1007/s10909-015-1425-4
2. K. Hattori et al., Development of readout electronics for Polarbear-2 cosmic microwave background experiment. J. Low Temp. Phys. (LTD 16). doi:10.1007/s10909-015-1448-x
3. A.N. Bender et al., SPT-3G: the next generation receiver for the south pole telescope. J. Low Temp. Phys. (LTD 16)
4. H. Shawn, et al., Cryogenic detector arrays and readout for AdvACTPol. J. Low Temp. Phys. (LTD 16)
5. M. Dobbs et al., Frequency multiplexed superconducting quantum interference device readout of large bolometer arrays for cosmic microwave background measurements. Rev. Sci. Instrum. **83**, 073113 (2012). doi:10.1063/1.4737629
6. K. Hattori et al., Adaption of frequency-domain readout for transition edge sensor bolometers for the Polarbear-2 cosmic microwave background experiment. Nucl. Instrum. Methods A **732**, 200–302 (2013). doi:10.1016/j.nima.2013.07.052
7. M.P. Bruijn et al., High-Q LC filters for FDM read out of cryogenic sensor arrays. J. Low Temp. Phys. **167**, 695–700 (2012). doi:10.1007/s10909-011-0422-5
8. K. Hattori et al., Optimization of cold resonant filters for frequency domain multiplexed readout of Polarbear-2. SPIE Proc. **9153**(91531B) (2014). doi:10.1117/12.2057045